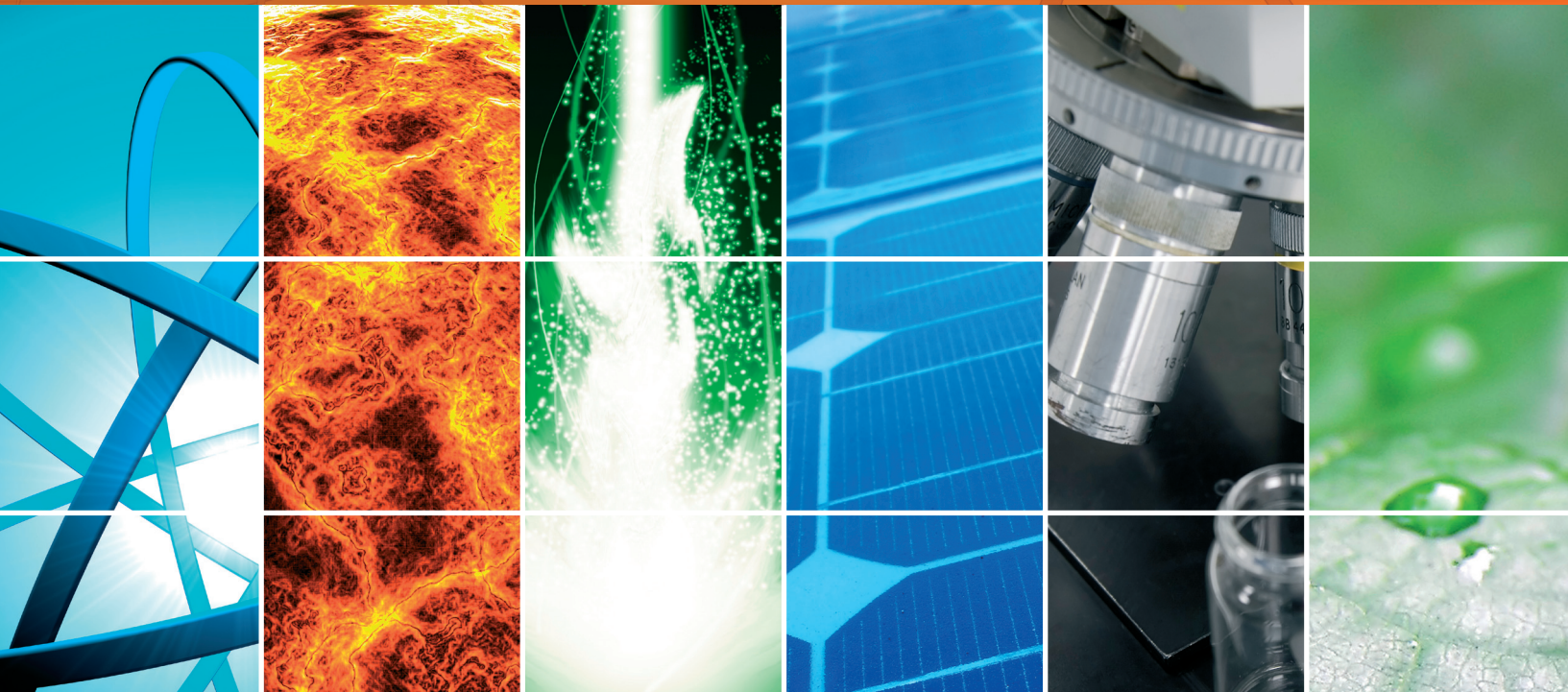


Solar Power Generation

Guest Editors: K. S. Reddy, T. K. Mallick, and D. Chemisana





Solar Power Generation

International Journal of Photoenergy

Solar Power Generation

Guest Editors: K. S. Reddy, T. K. Mallick, and D. Chemisana



Copyright © 2013 Hindawi Publishing Corporation. All rights reserved.

This is a special issue published in "International Journal of Photoenergy." All articles are open access articles distributed under the Creative Commons Attribution License, which permits unrestricted use, distribution, and reproduction in any medium, provided the original work is properly cited.

Editorial Board

M. Sabry Abdel-Mottaleb, Egypt
Nihal Ahmad, USA
Nicolas Alonso-Vante, France
Wayne A. Anderson, USA
Vincenzo Augugliaro, Italy
Detlef W. Bahnemann, Germany
Mohammad A. Behnajady, Iran
Ignazio Renato Bellobono, Italy
Raghu N. Bhattacharya, USA
Pramod H. Borse, India
Gion Calzaferri, Switzerland
Adriana G. Casas, Argentina
Wonyong Choi, Korea
Věra Cimrova, Czech Republic
Vikram Dalal, USA
D. (Dion) D. Dionysiou, USA
Mahmoud M. El-Nahass, Egypt
Ahmed Ennaoui, Germany
Chris Ferekides, USA
Beverley Glass, Australia
Shinya Higashimoto, Japan
Yadong Jiang, China
Chun-Sheng Jiang, USA

Shahed Khan, USA
Cooper Harold Langford, Canada
Yuexiang Li, China
Stefan Lis, Poland
Niyaz M. Mahmoodi, Iran
D. Mantzavinos, Greece
Ugo Mazzucato, Italy
Jacek Miller, Poland
Jarugu N. Moorthy, India
Franca Morazzoni, Italy
Fabrice Morlet-Savary, France
Ebinazar B. Namdas, Australia
Maria da Graça P. Neves, Portugal
Leonidas Palilis, Greece
Leonardo Palmisano, Italy
Ravindra K. Pandey, USA
David Lee Phillips, Hong Kong
Pierre Pichat, France
Gianluca Li Puma, UK
Xie Quan, China
Tijana Rajh, USA
Peter Robertson, UK
Avigdor Scherz, Israel

Lukas Schmidt-Mende, Germany
Panagiotis Smirniotis, USA
Zofia Stasicka, Poland
Juliusz Sworakowski, Poland
Nobuyuki Tamaoki, Japan
Gopal N. Tiwari, India
Nikolai V. Tkachenko, Finland
Veronica Vaida, USA
Roel van De Krol, Germany
M. van Der Auweraer, Belgium
Ezequiel Wolcan, Argentina
Man Shing Wong, Hong Kong
David Worrall, UK
F. Yakuphanoglu, Turkey
Minjoong Yoon, Korea
Hongtao Yu, USA
Jimmy C. Yu, Hong Kong
Jun-Ho Yum, Switzerland
Klaas Zachariasse, Germany
Lizhi Zhang, China
Jincai Zhao, China

Contents

Solar Power Generation, K. S. Reddy, T. K. Mallick, and D. Chemisana

Volume 2013, Article ID 950564, 2 pages

A Grid-Connected Multilevel Current Source Inverter and Its Protection for Grid-Disconnection,

Nimrod Vázquez, Luz del Carmen García, Claudia Hernández, Esli Vázquez, Héctor López, Ilse Cervantes, and Juan Iturria

Volume 2013, Article ID 575309, 10 pages

New Strategies and Simulation Tools to Optically Design a Field of Heliostats, Paola Sansoni,

Franco Francini, Daniela Fontani, Elisa Sani, Luca Mercatelli, and David Jafrancesco

Volume 2013, Article ID 523947, 7 pages

A Suitable Polysulfide Electrolyte for CdSe Quantum Dot-Sensitized Solar Cells, H. K. Jun,

M. A. Careem, and A. K. Arof

Volume 2013, Article ID 942139, 10 pages

Applying a Cerebellar Model Articulation Controller Neural Network to a Photovoltaic Power Generation System Fault Diagnosis, Kuei-Hsiang Chao, Bo-Jyun Liao, and Chin-Pao Hung

Volume 2013, Article ID 839621, 12 pages

The Evaluation of Solar Contribution in Solar Aided Coal-Fired Power Plant, Rongrong Zhai,

Yongping Yang, Yong Zhu, and Denggao Chen

Volume 2013, Article ID 197913, 9 pages

A Novel Extension Decision-Making Method for Selecting Solar Power Systems, Meng-Hui Wang

Volume 2013, Article ID 108981, 6 pages

Photovoltaic Power System with an Interleaving Boost Converter for Battery Charger Applications,

Sheng-Yu Tseng and Cheng-Tao Tsai

Volume 2012, Article ID 936843, 15 pages

On the Performance of Hybrid PV/Unitized Regenerative Fuel Cell System in the Tropics,

Salwan Dhrab, Tamer Khatib, Kamaruzzaman Sopian, Habeeb Al-Ani, and Saleem H. Zaidi

Volume 2012, Article ID 942784, 7 pages

Optical Design of a Solar Dish Concentrator Based on Triangular Membrane Facets, Hongcai Ma,

Guang Jin, Xing Zhong, Kai Xu, and Yanjie Li

Volume 2012, Article ID 391921, 5 pages

Performance of Grid-Connected Photovoltaic System in Two Sites in Kuwait, Ali Hajjah, Tamer Khatib,

K. Sopian, and M. Sebzali

Volume 2012, Article ID 178175, 7 pages

Economical Feasibility of Utilizing Photovoltaics for Water Pumping in Saudi Arabia, Ahmet Z. Sahin and Shafiqur Rehman

Volume 2012, Article ID 542416, 9 pages

Editorial

Solar Power Generation

K. S. Reddy,¹ T. K. Mallick,² and D. Chemisana³

¹ Heat Transfer and Thermal Power Laboratory, Department of Mechanical Engineering, Indian Institute of Technology Madras, Chennai 600 036, India

² Environment and Sustainability Institute, College of Engineering, Mathematics and Physical Sciences, University of Exeter, Campus, Penryn, Cornwall TR10 9EZ, UK

³ Applied Physics Section of the Environmental Science Department, Higher Polytechnic School, University of Lleida, C/Pere Cabrera S/n, 25001 Lleida, Spain

Correspondence should be addressed to K. S. Reddy; ksreddy@iitm.ac.in

Received 11 July 2013; Accepted 11 July 2013

Copyright © 2013 K. S. Reddy et al. This is an open access article distributed under the Creative Commons Attribution License, which permits unrestricted use, distribution, and reproduction in any medium, provided the original work is properly cited.

Solar power generation technologies are important for providing a major share of the clean and renewable energy needed in the future, because they are the cost-effective among renewable power generation technologies. Solar power generation becomes sustainable and competitive with fossil-fuel power generation within the next decade. Solar power generation has proven to be one most attractive option for electrical energy production in grid-connected and distributed modes. The solar power generation can be done both by photovoltaic (PV) and concentrating solar power (CSP) systems. The PV technologies such as single and multicrystalline, thin film cells, organic/inorganic dye-sensitized, and multijunction solar cells have seen an increasing trend for their utilities as backup energy generation systems for small-scale and rooftop applications. The CSP technologies such as solar dish, parabolic trough, linear Fresnel reflectors, and power tower are gaining momentum for large-scale solar power generation using power cycles/engines. This special issue on solar power generation is focused mainly various technologies, materials, and control strategies for effective solar energy conversion, energy storage, control, and implementation approaches.

Various novel solar PV systems are proposed for performance improvement and cost effectiveness. Development of materials plays major role in viable solar power generation. H. K. Jun et al. proposed a suitable polysulfide electrolyte for CdSe quantum dot-sensitized solar cells. With seven cyclic ionic layers, such system produces an efficiency of 1.41%. Energy storage plays a vital role in solar power systems for improving reliability and extended operation. S.-Y. Tseng and

C.-T. Tsai investigated a photovoltaic power system with an interleaving boost converter for battery charger applications with an efficiency of 88% under full-load condition. The control systems are very important in solar power generation for safety and ensuring load dispatchability. The solar power system stability can be attained by an accurate and fault tolerant control system. K.-H. Chao et al. developed a cerebellar model articulation controller neural network to the PV power system for fault diagnosis. N. Vázquez et al. have analysed a grid-connected multilevel current source inverter and its protection for grid disconnection. This paper shows both experimental operation and simulation analysis of the grid-connected system with multilevel current source inverter. A. Hajah et al. carried out performance analysis of a grid-connected photovoltaic power plant in two locations in Kuwait. The analysis showed that the annual capacity factor and the annual yield factor are lower for Multa compared to Warfa, although energy cost for both places remains the same.

Configuration, geometry, and material of reflector are very important in CSP plants for optical performance improvement. H. Ma et al. proposed a triangular membrane facets-based reflector for optical design of solar dish concentrator which will achieve 83.63% of radiative collection efficiency over a 15 cm radius disk located in the focal plane. Selection of appropriate solar power system is very crucial for execution and control strategies. A novel extension decision making method has been proposed for selection of suitable solar power systems by M.-H. Wang. New strategies and simulation tools are proposed to design a heliostats

field in solar power tower plant for estimation of optical performance.

Hybridization of fossil-fuel-based power plants with solar energy can improve the reliability and performance of large-scale solar power generation. The evaluation of solar fraction in solar-aided coal-fired power plants carried out by R. Zhai et al. The analysis showed that the solar power station can contribute up to 30 MW of electricity for the 600 MW coal-fired station for cost-effective operation. S. Dihrab et al. carried out performance analysis of hybrid PV-unitized regenerative fuel cell system in the tropics. Implementation of solar power system in agricultural sector can attain sustainable energy supply in rural areas. A. Z. Sahin and S. Rehman investigated the economic feasibility of solar PV water pumping in Saudi Arabia and found that the cost of water pumping can vary between 2 and 3 US cents per m³.

*K. S. Reddy
T. K. Mallick
D. Chemisana*

Research Article

A Grid-Connected Multilevel Current Source Inverter and Its Protection for Grid-Disconnection

Nimrod Vázquez,^{1,2} Luz del Carmen García,¹ Claudia Hernández,¹ Eslí Vázquez,³ Héctor López,¹ Ilse Cervantes,² and Juan Iturria⁴

¹ *Electronics Engineering Department, Technological Institute of Celaya, 38010 Celaya, GTO, Mexico*

² *Applied Mathematics Division, Potosino Institute of Scientific and Technological Research, 78216 San Luis Potosi, SLP, Mexico*

³ *Engineering Faculty, Veracruz University, 94294 Boca del Rio, VER, Mexico*

⁴ *CEO, Hawk Diverse Trailers, 38000 Celaya, GTO, Mexico*

Correspondence should be addressed to Nimrod Vázquez; n.vazquez@ieee.org

Received 4 November 2012; Revised 7 February 2013; Accepted 23 April 2013

Academic Editor: Tapas Mallick

Copyright © 2013 Nimrod Vázquez et al. This is an open access article distributed under the Creative Commons Attribution License, which permits unrestricted use, distribution, and reproduction in any medium, provided the original work is properly cited.

Traditionally DC-AC converters are considered with voltage source inverters (VSI); although less studied and discussed, it has started recently to be used current source inverters (CSI). Another possibility for DC/AC conversion is the multilevel configuration. This paper shows experimental operation and simulation analysis of a grid-connected multilevel current source inverter (MCSI), which includes a circuit for equipment safety reasons due to grid disconnections.

1. Introduction

Since fossil fuels are depleting day by day, research has started to focus on different alternatives in order to fulfill the required energy around the world. Nowadays, renewable energy is becoming more important. There exist some applications of renewable energy which employ hundreds of MW (high power), and there are also some of those, which uses hundreds of few W (low power). Applications may also be classified depending on if they are connected to the grid or not, and also it is well known as cogeneration and stand-alone systems.

Grid connected systems deliver the maximum obtainable power from the photovoltaic (PV) and/or wind system to the AC mains [1]; since energy supply changes according to weather conditions, then possible amount of released energy also changes. Algorithms such as improved perturbation and observation method [2], sliding mode observer technique [3], and some others [4–8] are employed to seek the maximum power point (MPP).

For increasing system efficiency, low voltages are used not only in solar cell arrays [9], but also in some wind systems. Hence, boosting type converters are required for

these systems. Different topologies which provide current to the AC mains are shown in Figures 1 and 2, based on VSI and CSI respectively.

A two-stage topology is illustrated in Figure 1(a): a DC/DC boost converter and a DC/AC converter [4]. For increasing input voltage, a DC/DC converter, which allows interaction to the AC mains, not only is used for constant output voltage but also is employed in order to perform the MPP, while inverter stage delivers a sinusoidal current to the utility line. Converter as illustrated in Figure 1(b) also includes two stages: multiple isolated DC/DC converters and a multilevel inverter [9]; first stage is mainly used for isolation purposes and the second one is used for providing sinusoidal current to the AC mains. Converter addressed in Figure 1(c) has also two stages: a DC/DC boost converter and a nontraditional multilevel inverter [10]; first stage is mainly used for increasing the input voltage, and the next one is used to provide sinusoidal current to the AC mains. Some other schemes are found in the literature [11–14].

Systems, which combine the power from two or more sources, are normally found in the literature [15–21]. Some authors [15] have suggested a converter which is able to obtain

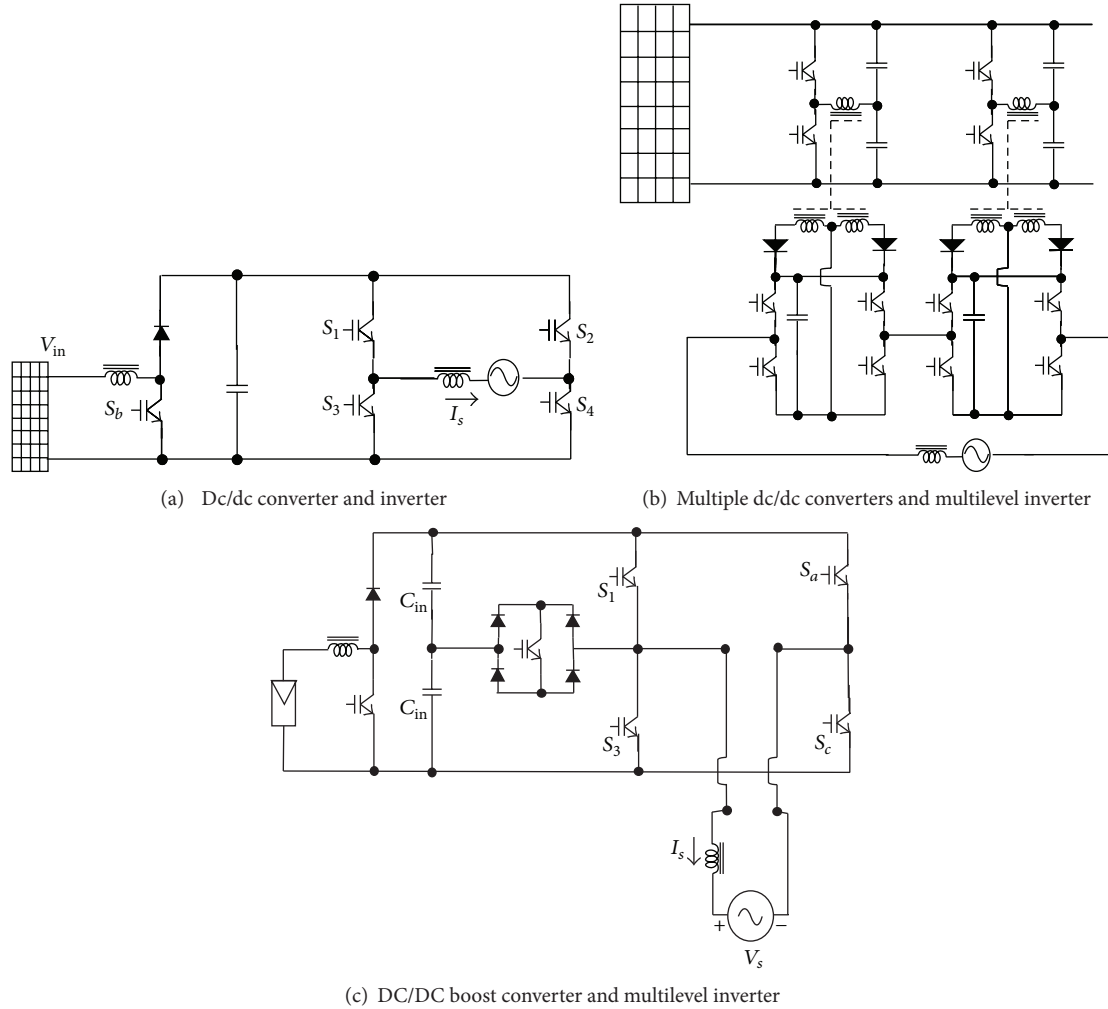


FIGURE 1: Topologies to inject current to the ac mains based on VSI.

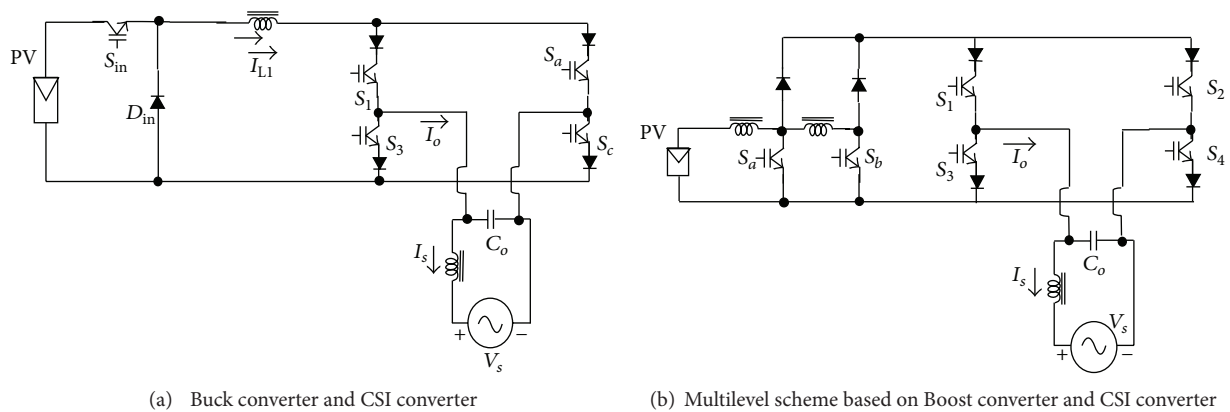


FIGURE 2: Topologies to inject current to the ac mains based on CSI.

energy from a PV array and the utility; however, for this particular case, there is not energy injected to the AC mains. Some others [16] have proposed a series of DC/DC converters connected when multiple photovoltaic panels are employed, a single converter for each panel, and also a DC/AC converter is

taken into account. In [17] has been proposed a system which considers photovoltaic panels and a wind turbine as main inputs, the photovoltaic voltage is higher than the output voltage, and the wind turbine voltage is lower than the output voltage.

Converters based on CSI, which are shown in Figure 2, are able to handle photovoltaic arrays [22–25], with the aid of DC/DC converters. Both buck and inverter are used to inject energy to the AC mains [22] as illustrated in Figure 2(a). For this topology in particular the input has to have high voltage. Figure 2(b) illustrates the use of DC/DC boost converter in order to produce a multilevel output [23]; the CSI is operated at low frequency, as a polarity inverter.

Some multilevel CSI, which are not applied to PV systems, are for general purpose [26, 27].

A comparative performance evaluation for PV system between VSI and CSI is shown in the literature [25]. Comparison is made under short-circuit fault conditions, and it demonstrates how CSI offers a better solution. However, grid disconnection is not considered, into account; as it will be shown next in this paper, this may cause damage in CSI if a protection circuit is not considered.

This paper discusses about a grid connected CSI of multilevel type, which combines CSI and multilevel converter features. Inverter topology is already found in the literature [27]; however, it did not consider grid connection. This converter is simple, and it uses fewer or equal amount of semiconductors than the multilevel CSI described in the literature [25–27]. The important part of this proposal is to include the protection circuit for grid disconnection, which differs from islanding protection. A CSI under grid connection must include this type of protection as will be shown.

The paper is organized as follows: the proposed converter is addressed in Section 2 it includes not only operation and waveforms but also implementation details; simulation and experimental results are discussed in Section 3, and finally some conclusions are given.

2. Proposed Grid Connected Multilevel Current Source Inverter

The proposed idea consists of a CSI, but a multilevel type allows producing an output current with a lower harmonic content with a relatively low semiconductors switching frequency. This converter injects current to the AC mains in parallel connection. A circuit for grid disconnection is considered for safety reasons. This multilevel converter topology is illustrated in Figure 3.

2.1. Operation of the Converter. For an easy explanation of how multilevel CSI operates, the input current is considered constant (large inductors); when switches S_1 , S_2 , and S_3 are turned on, the rest of switches are turned off; in fact the control signal of S_1 is exactly the opposite of S_a and the same for the others switches. In practice there exist a small overlapping in the control signals S_1 and S_a , this is because always a current path must be provided to the inductors in order to avoid the semiconductor damage.

Current generated by the MCSI is shown in Figure 4. These waveforms are at low frequency, and only the positive

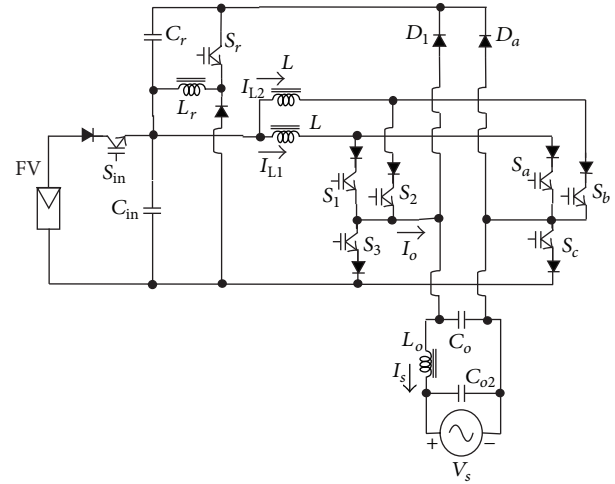


FIGURE 3: Proposed grid connected multilevel current source inverter.

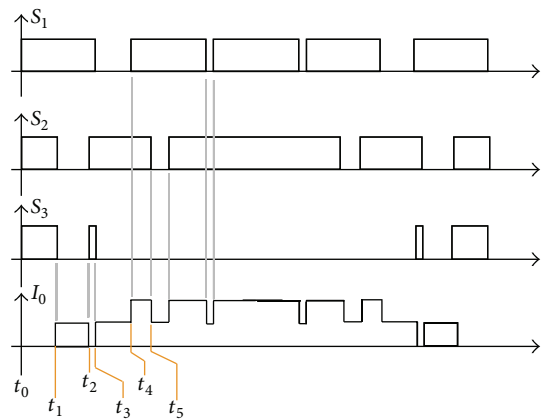


FIGURE 4: Control signals and output current. Top to down: control signal of S_1 , control signal of S_3 , control signal of S_2 , and output current.

semicycle is shown in order to illustrate the behavior. Control signals for switches S_1 , S_2 , and S_3 are also included. According to this Figure 4, the converter operates as follows:

- (1) During t_0 - t_1 , S_1 , S_2 , and S_3 are turned on, the equivalent subcircuit is shown in Figure 5(a), then zero current is injected (also a zero current may be produced when S_1 , S_2 and S_3 are turned off).
- (2) During t_1 - t_2 , S_1 is maintained on, S_2 and S_3 are turned off, the equivalent subcircuit is shown in Figure 5(b), and then a positive current is delivered.
- (3) During t_2 - t_3 . The same switches state used during t_0 - t_1 is considered during this stage; then a zero current output is obtained.

TABLE 1: Switching states of the converter.

Output current	Switches		
	S_1	S_2	S_3
Zero	1	1	1
	0	0	0
Positive	1	0	0
	0	1	0
Double positive	1	1	0
Negative	0	1	1
	1	0	1
Double negative	0	0	1

“1” means “on.”

“0” means “off.”

- (4) During t_3-t_4 , a positive current is injected to the load, but in this case the other combination is used. S_2 is turned on; S_1 and S_3 are turned off.
- (5) During t_4-t_5 , S_1 and S_2 are turned on, S_3 is turned off, the equivalent subcircuit is shown in Figure 5(c), and then a double magnitude of positive current is obtained.
- (6) After t_5 , during the rest of time, the converter operation is similar to that mentioned previously. In Table 1 summarized the different switching states to produce the required output current.

2.2. Circuit Protection for Grid Disconnection. An important part in this proposal is the protection circuit for grid disconnection. Elements for this circuit are a couple of diodes D_1 , D_a , a capacitor C_r , and a dc/dc buck-boost converter composed by S_r , L_r , and its diode (Figure 3).

The inverter may be described mathematically as a current source when it is connected to the ac mains in parallel; if grid disconnection occurs, for any circumstance (break protection, utility failure), an overvoltage will be generated, which certainly will damage not only the converter but also the other connected devices to it. For avoiding this situation, a current path must be provided to the current source, which prevents any damage to the system.

When grid disconnection occurs, the current of the inverter will charge the output capacitor, and then diode D_1 or D_a (depending on the AC mains semicycle) is able to conduce by charging the capacitor C_r . Figure 6 illustrates the subcircuit for the positive semicycle, by the time when diode D_1 start to conduce, then the capacitor voltage C_r will be increased; once the capacitor voltage increment is detected, the auxiliary switch (S_{in}) is turned off, and this will turn off the system; however the inductor is still transferring remaining energy to the capacitor C_r (Figure 6(b)). It should be noticed that, under normal condition S_{in} must be turned on.

Once, system starts to operate normally (after reconnection and detection of AC mains), the DC/DC buck-boost converter will recover the stored energy in capacitor C_r at the input of the multilevel inverter by delivering energy to the

capacitor C_{in} , then S_r will be commuted until the capacitor reach its steady-state voltage.

2.3. Controlling the System. The proposed power converter controller is shown in Figure 7. It is composed by a voltage detector, a PLL, a MPP tracker, and a current controller with its multilevel modulation technique.

Voltage detector is used in order to realize; if a detected grid disconnection occurs, during voltage increment, the switch S_{in} is turned off, which will assure a proper system operation. It is important to notice that grid voltage variation may occurs, because of this not any voltage increment should be considered as a grid disconnection; according to standard IEEE 929, a failure must be considered if the AC mains are 10% above its nominal value, which is evaluated as criteria for establishing that the system have failed.

PLL circuit is used to synchronize the injected current with the AC mains, this is necessary for delivering only real power to the AC mains; this means that current must be in phase with the AC mains.

For guaranty multilevel inverter operation not only PWM and current controller are used, but also the inductor current is balanced. For accomplishing this, switching state redundancy of the multilevel converter has to be taken into account; the technique is implemented by alternating both combinations in steady state and a simple controller, which is employed in order to regulate the inductor currents due to current unbalance, caused due to parasitic elements or disturbances in the system [27].

Waveforms of the PWM method employed at the inverter are shown in Figure 8; both two triangular carriers and a rectified reference signal are employed. Control signals for switches are obtained not only by comparing the carriers with the reference [27] but also by considering the AC mains semicycle and the information shown in Table 1; it is important to include the overlapping of switches control signal in order to assure the inductors current continuity.

2.4. Converter Gain. For carrying the analysis out, it is considered not only an averaged method but also that switching frequency is higher than the output voltage frequency. Then, the multilevel CSI is obtained as follows:

$$I_{op} = (n - 1) MI_L, \quad (1)$$

where I_{op} is the amplitude of the average output current; I_L is the inductor current; M is the modulation index; and n is the inverter output level.

By neglecting losses, we are able to make equal the input power and output power as follows:

$$P_{in} = P_o, \quad (2)$$

$$(n - 1) I_L V_{in} = \frac{V_{op} I_{op}}{2},$$

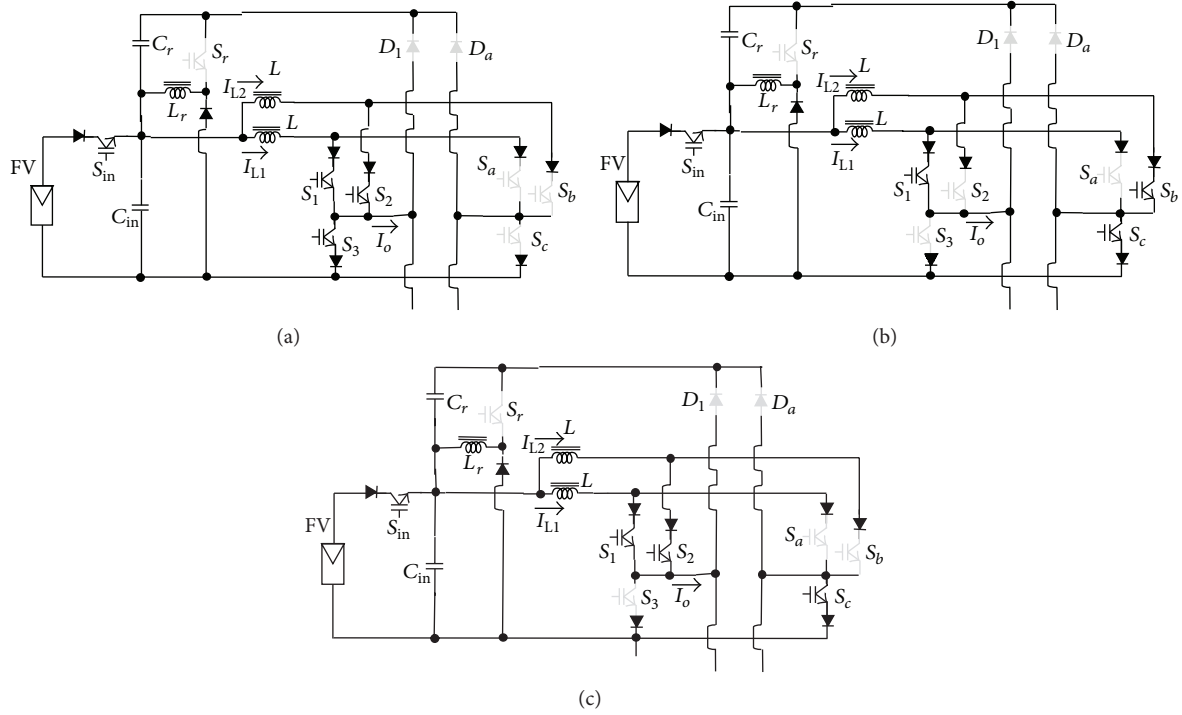


FIGURE 5: Subcircuits of the proposed multilevel CSI. (a) Subcircuit for zero current. (b) Subcircuit for positive current. (c) Subcircuit for double positive current.

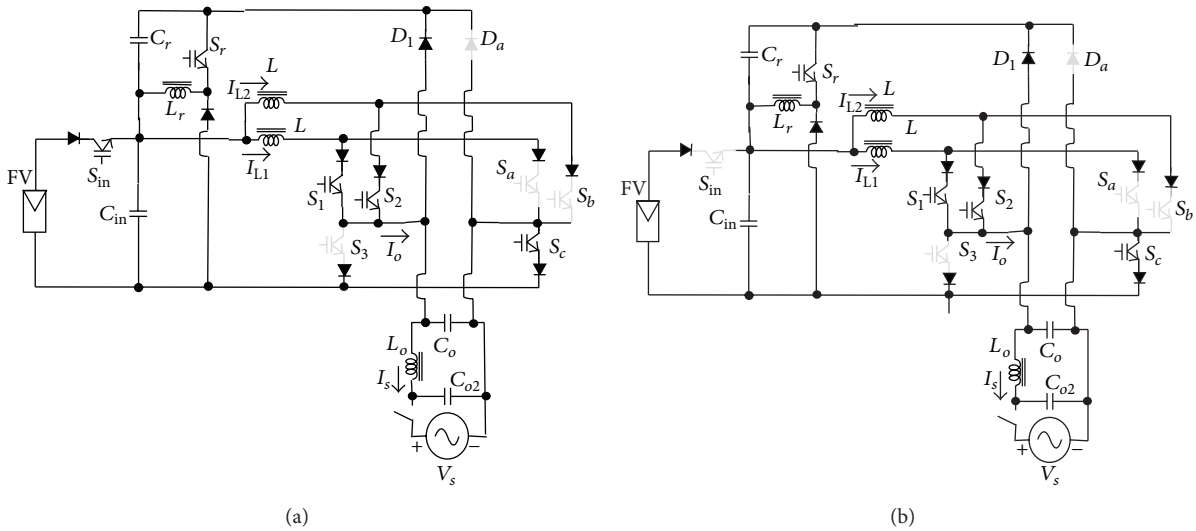


FIGURE 6: Subcircuit when the protection circuit is operating for positive semicycle.

where P_o is the output power, P_{in} is the input power, V_{in} is the input voltage, V_{op} is the peak of the output voltage.

Expressions (1) and (2) lead us to

$$\frac{V_{op}}{V_{in}} = \frac{2}{M}. \tag{3}$$

Voltage graph and current gain are shown in Figure 9, with $n = 3$; for a three-level inverter, it should be noticed that with $M = 1$ the current and voltage gain is equal to two

in both; this means that the inductors current contribution is optimal, but the boosting function is lower. This graph also shows the CSI boosting capability, which is not found in the VSI; actually it is a bucking system, essential feature in PV applications.

2.5. *Passive Elements Design.* For having good converter operation the DC link inductor (L) must be large, this guaranties a low harmonic distortion at the output. Let us

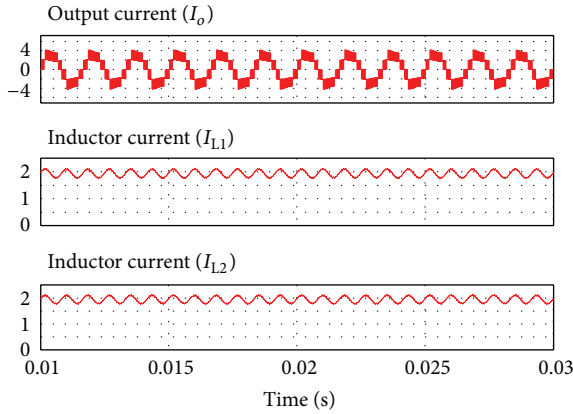


FIGURE 10: Steady-state operation of multilevel output current and inductors current. Top to bottom: multilevel output current (I_o , 2 A/div), inductor current (I_{L1} , 1 A/div).

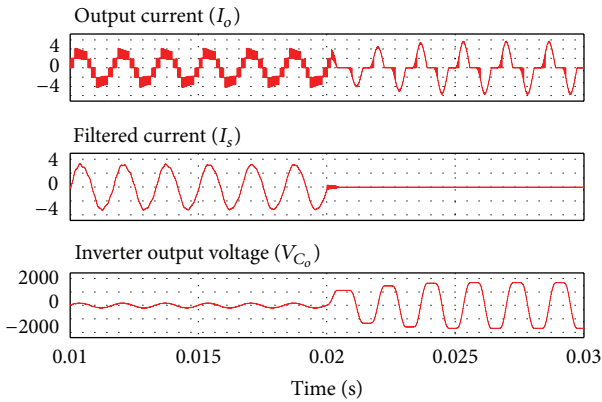


FIGURE 11: Operation of the system under a grid disconnection without the protection circuit. Top to bottom: output current (I_o , 2 A/div), filtered current (I_s , 2 A/div), and Inverter output voltage (V_{C_o} , 1000 V/div).

3. Simulation and Experimental Results

The functionality of the system was not only mathematically simulated but also an experimental prototype was built, so that the proposed idea was validated.

Numerical simulations, shown through Figures 10 to 12, were made at 600 Hz with an inductor of 40 mH due to the simulator time response. Figure 10 shows not only the inductors currents but also the output current with a modulation index of 0.82, it should be noticed that they are well balanced.

System performance under grid disconnection without the circuit protection is illustrated in Figure 11, where output current, filtered current and the capacitor C_o voltage are shown. It is easily seen that, when the AC mains is disconnected, the capacitor voltage increases higher than 1000 V, this would certainly causes damage to any circuit; therefore it is necessary the circuit protection.

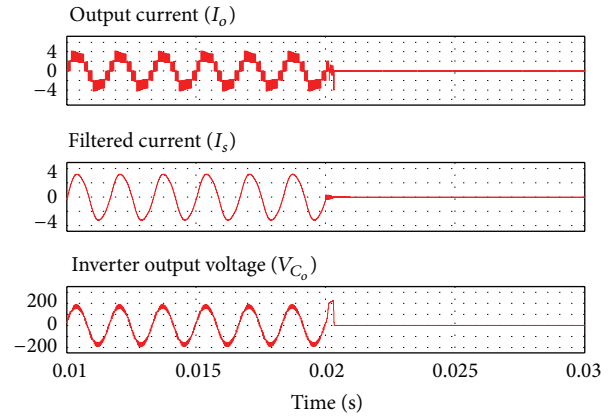


FIGURE 12: Operation of the system under a grid disconnection with the protection circuit. Top to bottom: output current (I_o , 2 A/div), Filtered current (I_s , 2 A/div), and inverter output voltage (V_{C_o} , 100 V/div).

Without protection for the grid disconnection, CSI energy is delivered to the output capacitor C_o , and then the capacitor increases its voltage until its destruction, as shown in Figure 10. Capacitor voltage reaches more than 1000 V in less time that a half semicycle of the AC mains.

It is also noticed that after failure, current is distorted and voltage is out of phase with respect to current; while current has zero value at certain times, the output capacitor voltage remains flat at this condition; however, this evolution in a the experimental prototype will not happen, because inverter damage occurs first.

A test for the system was carried out under grid disconnection, where the protection circuit was included, as it is shown in Figure 12. The output voltage for capacitor C_o increases when the grid is disconnected, until then diode D_1 starts to conduce, after the system shutdown is made. The Figure shows output voltage, output current, and filtered current and capacitor C_o voltage. It is clearly seen that the proposed scheme effectively avoids the system failure under a grid disconnection.

Figures 13–16 show experimental results: some of them are in steady-state, but some other were made to illustrated the operation of system under transitory. Input inductors are of 400 mH and switching devices are IRG4PC40. Steady state operations for the inverter control signals are shown in Figure 13; the sinusoidal reference with a higher frequency clearly illustrates the PWM operation and the control signals of S_a , S_b , and S_c of the multilevel inverter.

Some other waveforms for the converter at steady state are shown in Figure 14, which are related to the output. Two control signals, the output current and the sinusoidal reference, generate a multilevel output current. The current THD obtained in this test is lower than 5%, actually in order to be precise is 2.7%.

Experimental results under changing conditions are illustrated in Figures 15 and 16. PV panel power variations are illustrated in Figure 15, where the two evaluated conditions are shown in Table 2. This test was made under the same

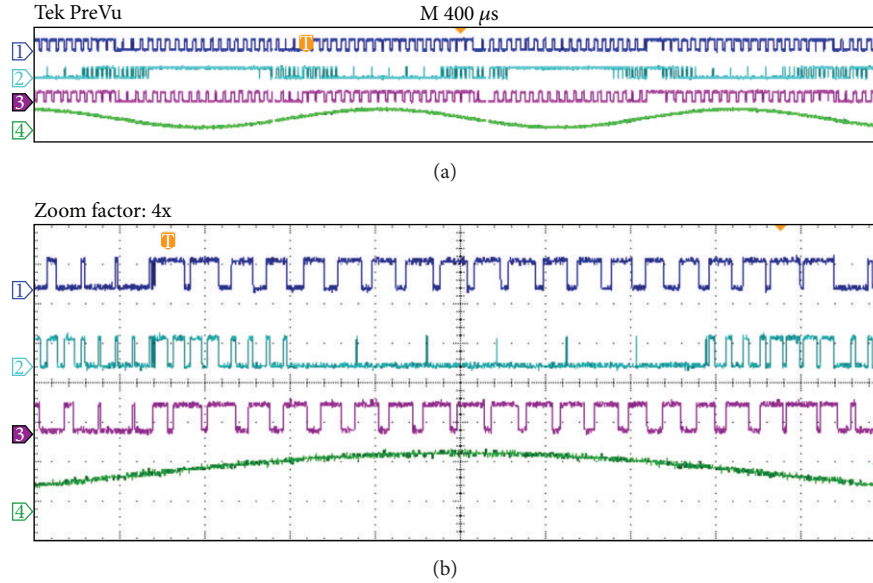


FIGURE 13: Control signals of the switches and sinusoidal reference. Top to bottom: control signal S_1 , S_3 , and S_2 , respectively, (5 V/div each) and sinusoidal reference (2 V/div each). Time: 400 $\mu\text{s}/\text{div}$; zoom time 100 $\mu\text{s}/\text{div}$.

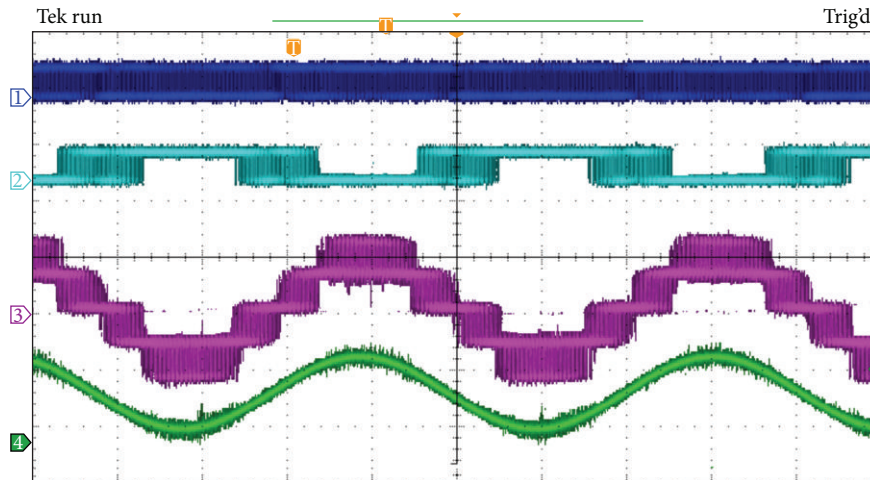


FIGURE 14: Operation of the system under a steady state. Top to bottom: control signals S_1 and S_3 , respectively, (5 V/div each), output current (2 A/div), sinusoidal reference (2 V/div). Time 4 ms/div.

irradiance condition; five or four PV panels are connected in series for each case; indeed one panel of the five is in short circuit to have four panels in operation. AC mains voltage, output current, sinusoidal reference and PV panel voltage are also shown. It is easily seen that delivered power to the AC mains changes according to power variation of the PV panel.

System operation under grid disconnection is illustrated in Figure 16; the capacitor C_o voltage, the filtered output current, the capacitor C_r voltage and the control signal which detects the grid disconnection (overvoltage for this capacitor) are included. It should be noticed that during AC mains disconnection not only the voltage of C_r increases, but also

TABLE 2: Conditions of the PV panel.

First condition	Second condition
$V_{mp} = 60 \text{ V}$	$V_{mp} = 80 \text{ V}$
$V_{oc} = 75 \text{ V}$	$V_{oc} = 100 \text{ V}$
$I_{mp} = 0.5 \text{ A}$	$I_{mp} = 0.5 \text{ A}$
$I_{sc} = 0.7 \text{ A}$	$I_{sc} = 0.7 \text{ A}$

the output voltage suddenly reaches the AC mains voltage peak due to the conduction of diode D_1 and connection with the capacitor C_r . When voltage for the capacitor C_r reaches the established value to determine grid disconnection, the

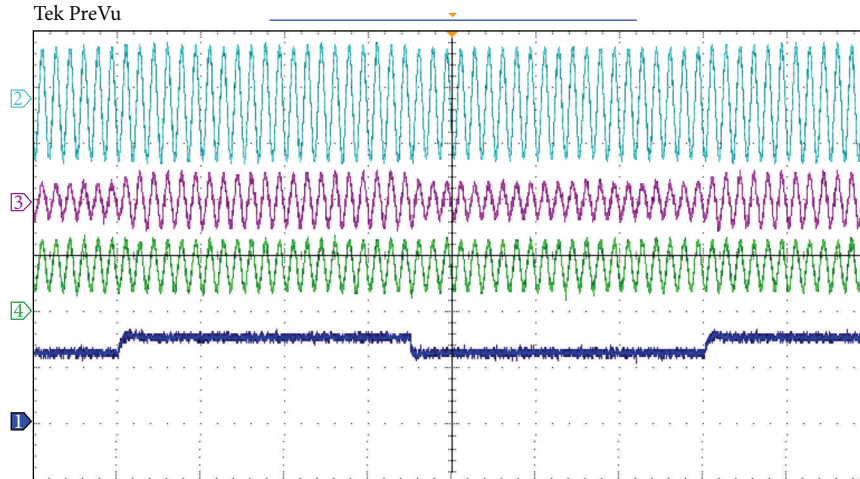


FIGURE 15: Operation of the system under PV perturbation. Top to bottom: Ac mains voltage (100 V/div), Output current (1 A/div), Sinusoidal reference (2 V/div), PV panel voltage (50 V/div). Time 100 ms/div.

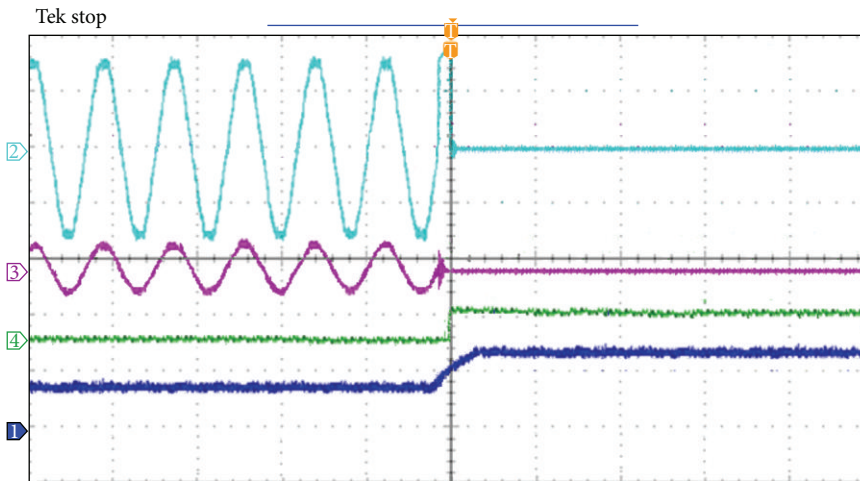


FIGURE 16: Operation of the system under grid disconnection. Top to down: Capacitor C_o voltage (100 V/div), Output current (1 A/div), grid disconnection detector by using overvoltage detector (5 V/div), and Capacitor voltage C_r (100 V/div). Time 20 ms/div.

detector defines when the switch S_{in} is turned off; however, the capacitor C_r will increase its voltage until the input inductors L_1 and L_2 are completely discharged. Protection circuit operates the system safely.

4. Conclusions

This paper presents a grid-connected multilevel current source inverter. It is proposed not only to operate under low PV panel voltage, due to the boosting capability of the CSI topology employed, but also a low THD at low switching frequency is obtained due to the multilevel operation.

The proposed converter considers a grid disconnection circuit for security reasons. When considering current sources, disconnection may damage not only some circuits connected to it but also the whole system; therefore it is necessary to include a method for alleviating this issue.

Operation, analysis, and implementation were exposed, and finally simulation and experimental results were discussed.

References

- [1] J. M. Carrasco, L. G. Franquelo, J. T. Bialasiewicz et al., "Power-electronic systems for the grid integration of renewable energy sources: a survey," *IEEE Transactions on Industrial Electronics*, vol. 53, no. 4, pp. 1002–1016, 2006.
- [2] N. Femia, G. Petrone, G. Spagnuolo, and M. Vitelli, "A technique for improving P&O MPPT performances of double-stage grid-connected photovoltaic systems," *IEEE Transactions on Industrial Electronics*, vol. 56, no. 11, pp. 4473–4482, 2009.
- [3] I. S. Kim, M. B. Kim, and M. J. Youn, "New maximum power point tracker using sliding-mode observer for estimation of solar array current in the grid-connected photovoltaic system," *IEEE Transactions on Industrial Electronics*, vol. 53, no. 4, pp. 1027–1035, 2006.

- [4] J. M. Kwon, K. H. Nam, and B. H. Kwon, "Photovoltaic power conditioning system with line connection," *IEEE Transactions on Industrial Electronics*, vol. 53, no. 4, pp. 1048–1054, 2006.
- [5] J. H. Park, J. Y. Ahn, B. H. Cho, and G. J. Yu, "Dual-module-based maximum power point tracking control of photovoltaic systems," *IEEE Transactions on Industrial Electronics*, vol. 53, no. 4, pp. 1036–1047, 2006.
- [6] N. Onat, "Recent developments in maximum power point tracking technologies for photovoltaic systems," *International Journal of Photoenergy*, vol. 2010, Article ID 245316, 11 pages, 2010.
- [7] R. Leyva, C. Olalla, H. Zazo et al., "MPPT based on sinusoidal extremum-seeking control in PV generation," *International Journal of Photoenergy*, vol. 2012, Article ID 672765, 7 pages, 2012.
- [8] P. Bhatnagar and R. K. Nema, "Maximum power point tracking control techniques: state-of-the-art in photovoltaic applications," *Renewable and Sustainable Energy Reviews*, vol. 23, pp. 224–241, 2013.
- [9] H. Ertl, J. W. Kolar, and F. C. Zach, "A novel multicell DC-AC converter for applications in renewable energy systems," *IEEE Transactions on Industrial Electronics*, vol. 49, no. 5, pp. 1048–1057, 2002.
- [10] J. Selvaraj and N. A. Rahim, "Multilevel inverter for grid-connected PV system employing digital PI controller," *IEEE Transactions on Industrial Electronics*, vol. 56, no. 1, pp. 149–158, 2009.
- [11] C. L. Shen and J. C. Su, "Grid-connection half-bridge PV inverter system for power flow controlling and active power filtering," *International Journal of Photoenergy*, vol. 2012, Article ID 760791, 8 pages, 2012.
- [12] S. Busquets-Monge, J. Rocabert, P. Rodríguez, S. Alepuz, and J. Bordonau, "Multilevel diode-clamped converter for photovoltaic generators with independent voltage control of each solar array," *IEEE Transactions on Industrial Electronics*, vol. 55, no. 7, pp. 2713–2723, 2008.
- [13] S. Sladic, S. Skok, and D. Nedeljkovic, "Efficiency considerations and application limits of single-phase active power filter with converters for photoenergy applications," *International Journal of Photoenergy*, vol. 2011, Article ID 643912, 8 pages, 2011.
- [14] C. T. Tsai and S. H. Chen, "PV power-generation system with a phase-shift PWM technique for high step-up voltage applications," *International Journal of Photoenergy*, vol. 2012, Article ID 838231, 11 pages, 2012.
- [15] K. Kobayashi, H. Matsuo, and Y. Sekine, "Novel solar-cell power supply system using a multiple-input DC-DC converter," *IEEE Transactions on Industrial Electronics*, vol. 53, no. 1, pp. 281–286, 2006.
- [16] G. R. Walker and P. C. Sernia, "Cascaded DC-DC converter connection of photovoltaic modules," *IEEE Transactions on Power Electronics*, vol. 19, no. 4, pp. 1130–1139, 2004.
- [17] Y. M. Chen, Y. C. Liu, S. C. Hung, and C. S. Cheng, "Multi-input inverter for grid-connected hybrid PV/wind power system," *IEEE Transactions on Power Electronics*, vol. 22, no. 3, pp. 1070–1077, 2007.
- [18] Y. M. Chen, Y. C. Liu, and S. H. Lin, "Double-input PWM DC/DC converter for high-/low-voltage sources," *IEEE Transactions on Industrial Electronics*, vol. 53, no. 5, pp. 1538–1545, 2006.
- [19] Y. M. Chen, Y. C. Liu, and F. Y. Wu, "Multi-input dc/dc converter based on the multiwinding transformer for renewable energy applications," *IEEE Transactions on Industry Applications*, vol. 38, no. 4, pp. 1096–1104, 2002.
- [20] T. T. Chow, G. N. Tiwari, and C. Menezo, "Hybrid solar: a review on photovoltaic and thermal power integration," *International Journal of Photoenergy*, vol. 2012, Article ID 307287, 17 pages, 2012.
- [21] J. S. Silva, A. R. Cardoso, and A. Beluco, "Consequences of reducing the cost of PV modules on a PV wind diesel hybrid system with limited sizing components," *International Journal of Photoenergy*, vol. 2012, Article ID 384153, 7 pages, 2012.
- [22] C. C. Chan and Y. M. Chang, "Current source inverter with energy clamp circuit and controlling method therefore having relatively better effectiveness," US patent No. US2007/0230220A1.
- [23] P. G. Barbosa, H. A. C. Braga, M. C. B. Rodrigues, and E. C. Teixeira, "Boost current multilevel inverter and its application on single-phase grid-connected photovoltaic systems," *IEEE Transactions on Power Electronics*, vol. 21, no. 4, pp. 1116–1124, 2006.
- [24] D. Amorndechaphon, S. Premrudeepreechacharn, K. Higuchi, and X. Roboam, "Modified grid-connected CSI for hybrid PV/wind power generation system," *International Journal of Photoenergy*, vol. 2012, Article ID 381016, 12 pages, 2012.
- [25] P. P. Dash and M. Kazerani, "Dynamic modeling and performance analysis of a grid-connected current-source inverter-based photovoltaic system," *IEEE Transactions on Sustainable Energy*, vol. 2, no. 4, pp. 443–450, 2011.
- [26] F. L. M. Antunes, H. A. C. Braga, and I. Barbi, "Application of a generalized current multilevel cell to current-source inverters," *IEEE Transactions on Industrial Electronics*, vol. 46, no. 1, pp. 31–38, 1999.
- [27] N. Vázquez, H. López, C. Hernández, E. Vázquez, R. Osorio, and J. Arau, "A different multilevel current source inverter," *IEEE Transactions on Industrial Electronics*, vol. 57, no. 8, pp. 2623–2632, 2010.

Research Article

New Strategies and Simulation Tools to Optically Design a Field of Heliostats

**Paola Sansoni, Franco Francini, Daniela Fontani, Elisa Sani,
Luca Mercatelli, and David Jafrancesco**

CNR-INO National Institute of Optics, Largo E. Fermi 6, 50125 Firenze, Italy

Correspondence should be addressed to Paola Sansoni; paola.sansoni@ino.it

Received 30 October 2012; Accepted 1 February 2013

Academic Editor: Kalvala Srinivas Reddy

Copyright © 2013 Paola Sansoni et al. This is an open access article distributed under the Creative Commons Attribution License, which permits unrestricted use, distribution, and reproduction in any medium, provided the original work is properly cited.

A heliostats field is an array of mirrors concentrating the solar power on a receiver, typically placed on a tower. Our research experience in the optical design of heliostats fields for Concentrating Solar Power plants suggested using apposite simulation procedures, which were especially developed to simplify the reproduction of heliostats fields and to support in the analysis of the tower plant performances. Our most practically useful simulation tools are presented in this paper with exemplificative application results. The proposed strategies are addressed to solve specific problems and to evidence particularly crucial features. The main program facilitates the heliostats field analysis, exploiting the integration between our software code and *Zemax*. A side program permits to assess effects of seasonal and daily variations of solar irradiation. Another dedicated side code simplifies the selection of a *Compound Parabolic Concentrator* as secondary optics.

1. Introduction

The paper proposes new simulation tools especially studied by our research group to facilitate the optical design of heliostats fields, which are typically employed in thermodynamic tower plants. Heliostats tower systems are Concentrating Solar Power (CSP) installations with principal components a heliostats field and a tower receiver. A heliostats field is an array of mirrors concentrating the solar power on a receiver, typically placed on a tower. The experience of our research group in the optical design of heliostats fields for CSP plants suggested developing specific software programs that can be used as assisting tools to facilitate the simulation of a multimirror field. This paper discusses applications and capabilities of our most practically useful tools. Their main purposes are to simplify the optical design of multimirror arrays and to support in the analysis of the solar plant performances.

Considering the optical point of view, for planning and simulating a multimirror plant it is necessary to use an optical design software package because it takes into account not only the interaction between luminous radiation and surfaces, the effects due to the whole solar spectrum, but also the effects

due to solar divergence that in this case are significant because of the large distances involved. The software codes developed for our optical analyses offer the possibility to perform detailed and extensive investigations entailing specialised simulation programs. Unfortunately the case of tower plants involves an elevated amount of system components, so the manual insertion of all mirrors parameters can cause errors, and it is typically very tedious and time-consuming.

Some software codes, especially dedicated to the optical design of heliostat fields, were elaborated by other research groups for specific requirements, obtaining very promising results [1–4]. Two examples of these codes are described in Erminia Leonardi's publications [1, 2]. Besides, our European colleagues of the *PROMES* group, within the French *CNRS*, developed a software, denominated *SOLFAST 4D* [3]. The Laboratory “PROcédés, Matériaux et Energie Solaire” (*PROMES*) is a Research Unity of the *CNRS* (*Centre National de la Recherche Scientifique*) located at Font Romeu Odeillo, France.

Our research group preferred to use commercial optical design packages for being able to exploit all the potentialities of these software programs. The utilization of optical design software improves the simulation procedure versatility. The

advantage is that the solar field, with its components, is seen as an element to be designed, whose development can utilize all the potentialities of these software packages, like automatic optimization and radiometric calculations. This strategy allowed us to obtain results with elevated graphic characteristics, high precision, and high reliability.

The aim of the proposed work was to simplify the analysis of the heliostats field behaviour, exploiting the possibility of interfacing optical design codes with programming systems, like *Octave*. Our integrated simulation tools were created for guiding the system analysis from the optical point of view, for managing the large data amount, and for extracting the essential parameters, with a particular attention to the quantities that are critical for the examined heliostats field.

The next sections propose three of our simulation tools: *Simulation Tool_1 (ST_1)* performs the optical design of a heliostats field; *Simulation Tool_2 (ST_2)* evaluates the power collected by the tower plant; *Simulation Tool_3 (ST_3)* examines a polar conical surface as secondary optics.

An accurate design (*ST_1*) of the multimirror field involves various aspects, but it is essential for being capable of correctly assessing the power collected on the tower receiver by the heliostats (*ST_2*). Several features are important for our optical studies: first of all, the mirrors disposition must be defined to optimise the concentration of the light on the target (*ST_1*). Beyond the receiver covering, there are other relevant aspects, like the study of seasonal and daily variations of solar irradiation (*ST_2*) on the tested CSP field, the shape and aperture of a possible CPC (*Compound Parabolic Concentrator*) receiver (*ST_3*), and the possibility to assess *vignetting* effects on the mirrors (*ST_1*).

The study of the interactions among solar rays, mirrors, and target is usually performed with the assistance of *Zemax* optical design software. The employment of this software package is justified owing to its capacity to manage and analyse a huge number of luminous rays, along with its possibility to generate irradiance maps (light distribution in W/m^2 unities) in predefined positions. The main application of the irradiance maps study is to analyse the behaviour of the radiation in proximity of the critical zones (*ST_1*): inside the target (a test surface placed in significant positions), within the furnace (the real receiving structure), and on the heliostats field. However the analysis of irradiance maps can also be useful to introduce potential modifications on the CSP plant geometry (*ST_1*). In practice, during the initial design phase, when the heliostats array geometry is defined, it is necessary to have the maximum freedom in the designation of the variables, taking into account that geometrical shape, azimuth, and elevation values must be identified for every mirror position. It is therefore essential to simplify the data insertion inside the software code (*ST_1*), which should not be manually done because the multimirror field can include up to thousands of collectors.

2. Simulation Tool_1: Optical Design of a Heliostats Field

Simulation tool_1 (ST_1) represents the main proposed code, and it was created with the aim of facilitating the insertion

of all the data pertaining to the multimirror tower plant, for being simulated in the optical design software package. We developed a software program, in *Octave* type language, which starting from the description of the CSP field is capable of interacting with *Zemax* to obtain an analysis of the beam distribution on the target.

Its application can be summarized as follows: *ST_1* prepares a file containing all the geometrical parameters of the mirrors and their positioning on the field; successively the file could be read by a *Zemax* macroinstruction that will automatically import all the optical components.

In practice the program accepts the following inputs:

- (i) geometrical position of the target;
- (ii) azimuth and elevation of the sun;
- (iii) positions of all mirrors composing the heliostat field, taken from a text format file;
- (iv) in alternation to the previous point it is possible to prepare a field with predefined dimensions, as an $N \times M$ heliostats matrix, oriented at a defined angle with respect to the tower.

The following parameters are determined for every mirror:

- (i) x , z , and y coordinates with respect to the tower, which is identified as axes origin;
- (ii) curvature radius as a function of furnace entrance position;
- (iii) local azimuth and elevation of every mirror to deviate the solar rays on the furnace in dependence of sun's azimuth and elevation;
- (iv) besides it is possible to insert an "angular noise" on the mirror position in order to simulate a tracking error.

The data contained in the matrix of $N \times M$ mirrors are transferred in automatic modality, and a *Zemax* program supplies the following results:

- (i) irradiance map on a suitable target plane;
- (ii) map of the solar irradiance on the plane located under the heliostats, to evaluate the influence of the tower shadow and of the relative mirrors shadows (*vignetting* effects).

In particular it is useful to remember that every programme that uses ray-tracing techniques automatically takes into account the *cosine effect* on the mirrors. This means that the software code considers the mutual shadows between the heliostats rows and the consequent effect of sunlight block that a heliostats line can cause on the next mirrors row. The results of the calculation are therefore very precise, and they can successfully simulate the real plant conditions.

Exemplificative results of the optical simulation of a multimirror tower plant are presented in Figures 1–3. Each heliostats plant simulation is obtained inserting in *Zemax* the data pertaining to the position of mirrors, through the *Octave* interface of *ST_1*. Then the *Zemax* software package

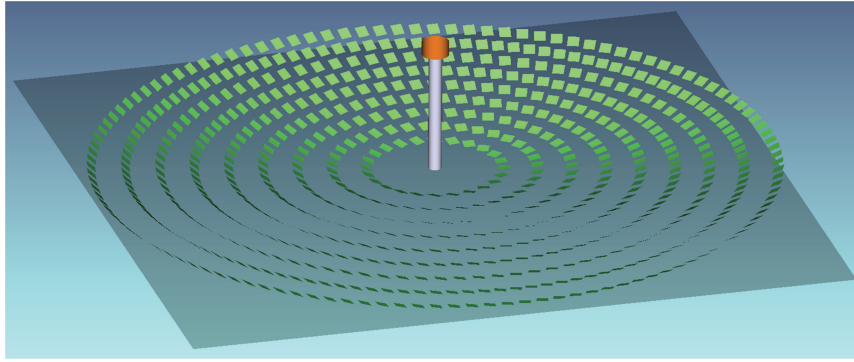


FIGURE 1: A 3D rendering of a multimirror tower plant.

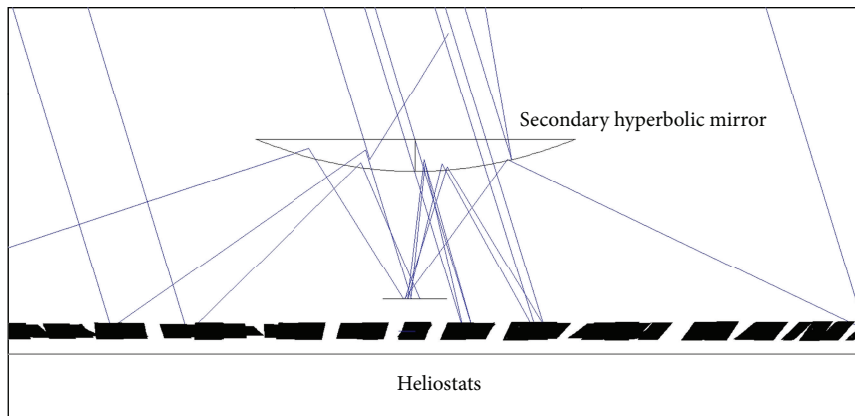


FIGURE 2: Scheme of a heliostats field of beam-down type, evidencing the rays reflected by the secondary hyperbolic mirror.

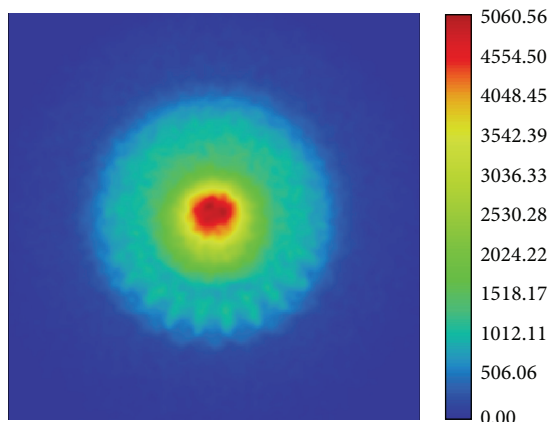


FIGURE 3: Example of a target irradiance map on a heliostat field.

can provide a 3D rendering of the solar plant, like Figure 1, a heliostats field scheme, like Figure 2, and irradiations maps, like the example shown in Figure 3. In the side view of Figure 2 the heliostats appear as dark quadrangles (often superimposed) in a bottom line, while the secondary optics is clearly visible at figure centre. The target irradiation map (in W/m^2) in Figure 3 presents the distribution over the

tower target of the light concentrated by the array of mirrors composing the CSP plant.

In addition to the optical design of a multimirror field, which is the principal function of *ST-I*, our main code allows additional functions: the first quantifies the effects of angular noise, while the second examines mutual shadows between mirrors.

In order to obtain a more realistic simulation of the actual practical realisation of the solar field, our program *ST-I* allows the insertion of an “angular noise.” In particular, a *Gaussian angular noise* can be introduced on every mirror to simulate the effect of random disturbances on the position of the collectors. The application of a *Gaussian angular noise* on the heliostats orientation consists in adding this angular noise to the azimuth and elevation values of each mirror.

These errors are actually due to several different causes, like the imperfect positioning of a real mirror, tracking errors, wind effects, and so forth. The code of *ST-I* permits to set the variance value of the *Gaussian noise*, in order to analyse how much an incorrect orientation of the mirrors affects the illumination on the target. An example of application of the *Gaussian angular noise* on the mirror orientations is numerically reported in Table 1 and graphically visualized in Figures 4 and 5. In particular Figure 4 presents the *Gaussian angular noise*, corresponding to the angular deviation of mirrors orientation, for a Gaussian distribution with variance 0.011.

TABLE 1: Mirror angular noise, as a function of the Gaussian noise variance, and effect on the furnace illumination.

Variance of the Gaussian angular noise	FWHM noise on the mirrors	FWHM error on the furnace
0.00625	$\pm 0,093^\circ$	$\pm 0,186^\circ$
0.011	$\pm 0,123^\circ$	$\pm 0,247^\circ$
0.0125	$\pm 0,132^\circ$	$\pm 0,263^\circ$
0.025	$\pm 0,186^\circ$	$\pm 0,372^\circ$
0.05	$\pm 0,263^\circ$	$\pm 0,527^\circ$

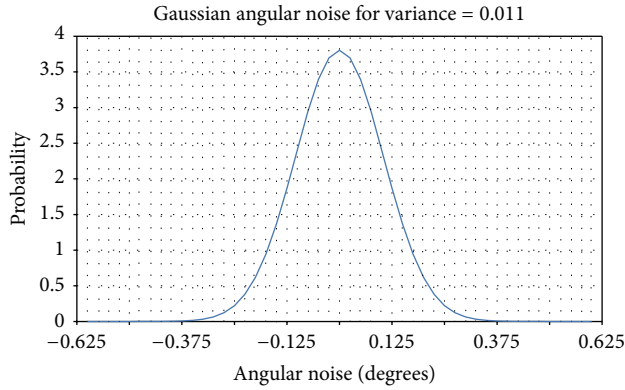


FIGURE 4: Angular deviation of mirrors orientation for a Gaussian distribution with variance 0.011.

Then Figure 5 illustrates the effect of the *Gaussian angular noise* on the perfect target image shown in Figure 3.

Table 1 presents the noise of mirror orientation and the consequent error on the target for different values of variance of the *Gaussian angular noise*. Columns 2 and 3 report the FWHM (full width at half maximum) of the angular deviation, in a Gaussian distribution statistic. Column 2 refers to the angular deviation on the mirrors orientation (azimuth and elevation), while Column 3 reports the angular deviation of the ray impinging on the furnace target. Because of the specular reflection, the values in Column 3 (target angular error) are double than those in Column 2 (mirror angular noise).

These design considerations can be practically advantageous, since they give indications about the robustness or sensitivity of our optical design with respect to angular variations.

The possible shadows between mirror rows, causing *vignetting effects*, are easily observable using a function that is available in the *ST_1* code. A detector, located under the heliostats plane and having the same dimension of the multimirror field, visualises the shadows that the sun generates between the collectors rings. Figure 6 presents an example of visualisation of this *vignetting effect*. If the image presents superimposed shadows, it is evident that the solar rays cannot completely illuminate all mirrors, therefore generating even significant reductions of the plant performances. For a correct optical design of the solar plant the *vignetting effect* simulation should be repeated for various

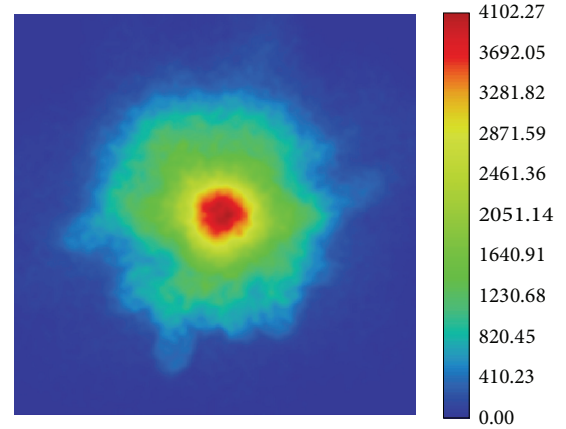


FIGURE 5: The target irradiance map of Figure 3 with the effect of a Gaussian angular noise.

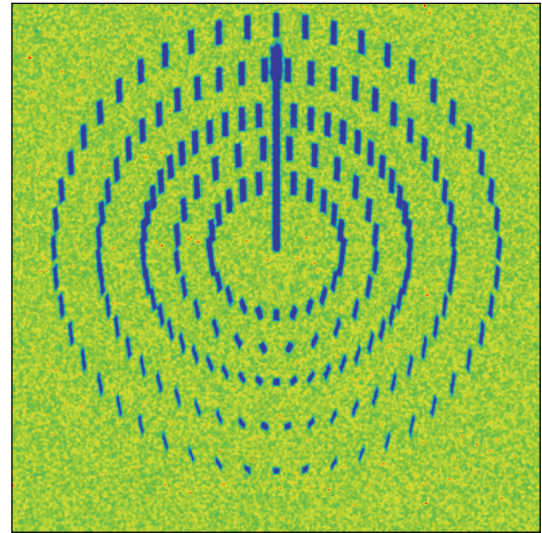


FIGURE 6: Example of the shadows of mirrors and tower in a circular field.

hours of the day, in order to optimise the multimirror array design for the whole working period.

3. Simulation Tool_2: Evaluation of the Power Collected by the Field

Another fundamental aspect in the analysis of heliostats plants is the capacity of the CSP field to collect solar energy. A dedicated program, indicated as *Simulation Tool_2* (*ST_2*), was developed for examining this multimirror field characteristic. This program, starting from the heliostats field geometry, calculates the solar power on each mirror composing the solar field. *ST_2* code permits to precisely evaluate the quantity of energy collected by the tower plant during the day and for each single day of the year. Conversely to *ST_1*, *ST_2* does not require the use of *Zemax*, and it is faster than *ST_1* in the calculation of the results.

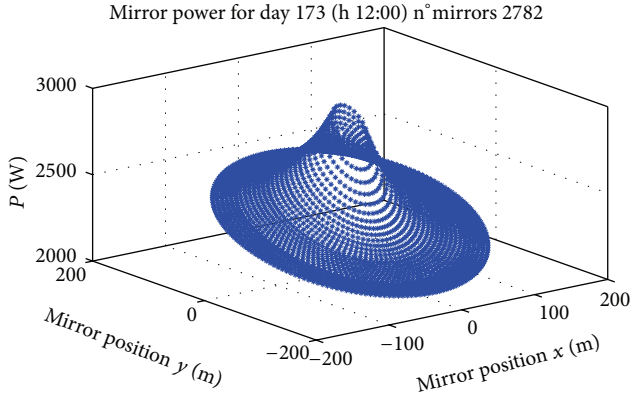


FIGURE 7: A 3D view of the power P collected by each mirror (3 m^2) in the solar field.

This type of evaluation (ST_2) is of extreme importance in the phase of optical design of a heliostats field, because it allows verifying performances and efficiency levels of the solar plant as a function of mirrors field geometry and furnace position.

The solar irradiance data I_s must be introduced as input data in *Simulation Tool_2*. However ST_2 includes an alternative automatic modality for the intensity calculation, as a function of the angle of sun's elevation, considering the effect of the air mass interposed between sun and heliostats. But the sunlight attenuation also depends on other parameters that are not easily predictable like water vapour content, aerosol, and pollution, which must be related with plant location, season, and atmospheric conditions [5]. Since it is impossible to take precisely into account all these aspects, we chose a simplified model that introduces an empirical coefficient $Q = 1.1$ to take into account also the diffused component [6, 7], and the solar irradiance I_s can be estimated as

$$I_s = Q \times I_0 \times 0.7^{(AM^{0.678})}. \quad (1)$$

$I_0 = 1.353 \text{ kW/m}^2$ represents the solar irradiance outside the Earth atmosphere, and AM is the *Air Mass* coefficient [8]. Considering that the field of heliostats reflects on the target only the direct radiation, the value of Q must necessarily be set to 1:

$$AM = \frac{1}{\cos z + 0.50572 \cdot (96.07995 - z)^{-1.6364}}, \quad (2)$$

where z represents the angle that the sun forms with the *zenith* (zenith angle).

The solar irradiance value I_r reflected towards the tower by the single mirror is determined by the following equation:

$$I_r = \mathbf{S} \cdot \mathbf{U} \cdot I_s \cdot R \cdot A_{sp},$$

$$\mathbf{S} = [S_x \ S_y \ S_z], \quad (3)$$

$$\mathbf{U} = [U_x \ U_y \ U_z],$$

where $S_x, S_y,$ and S_z represent the *unit vectors* of the solar ray and $U_x, U_y,$ and U_z represent the *unit vectors* of the mirror

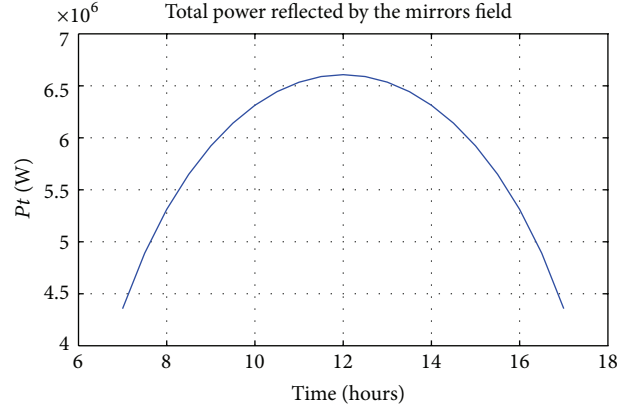


FIGURE 8: Total power reflected by the mirrors field at different hours of the day.

normal axis. Finally R and A_{sp} are reflectance and heliostat surface, respectively.

The main advantage of the application of ST_2 is to facilitate the definition of the initial geometry for the heliostats array and to permit the assessment of daily and seasonal fluctuations of collected power.

Examples of two types of results that can be obtained are presented in Figures 7 and 8. Figure 7 reports a 3D view of the power P collected by each mirror in the solar field, where the area of every mirror is 3 m^2 . Figure 8 presents the total power P_t reflected by the mirrors field toward the target at different hours of the day.

Besides it is possible to visualise the received solar power behaviour in a movie format.

4. Simulation Tool_3: Polar Conical Surface as Secondary Optics

The last software tool proposed in this paper refers to the utilisation of a secondary optics in the furnace: in particular *Simulation Tool_3* (ST_3) allows introducing a polar conical surface as secondary optics of the collection system.

The angular aperture θ of a possible secondary concentrator must be defined considering the position of all mirrors composing the solar tower plant. Consequently the value of θ affects the geometry of the multimirror field, and, conversely, the plant geometry affects the angular aperture of the secondary optics. A frequently employed secondary optics is the *Compound Parabolic Concentrator* (CPC).

ST_3 program allows simulating the field of view θ of a CPC to simplify the operations of optical design of heliostats fields. In this case the concentrator is no more considered as a receiver, but as a luminous source that projects a luminous cone on the ground. The interception between the cone and the ground defines the limitations that should contain the mirrors of the heliostats array.

Figure 9 presents an example of a calculation for a CPC placed at a height (h) of 25 m, at a horizontal coordinate ($dist$) of 20 m, with an inclination angle ($Alfa$) of 51.3° (of the cone axis with respect to the ground). The tower is

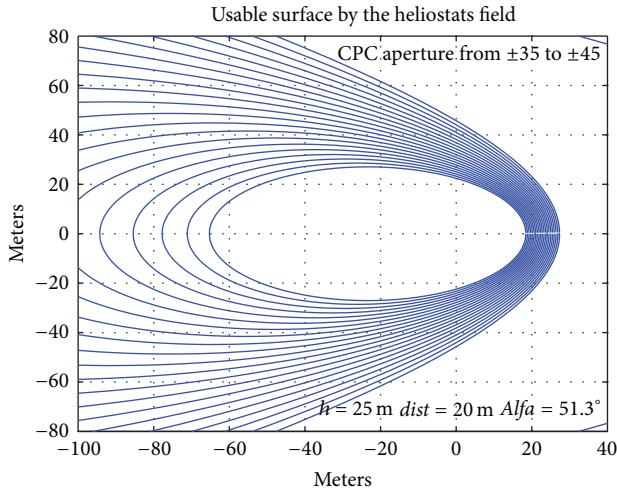


FIGURE 9: Useful surface in the heliostats field as a function of angular aperture and orientation of the CPC secondary optics.

located in position (20 m; 0) of the chosen coordinates. Every possible *CPC* aperture corresponds to a curve on the plot of Figure 9. The range for the total angular aperture θ of the *CPC* is between 70 degrees ($\pm 35^\circ$) and 90 degrees ($\pm 45^\circ$). The aperture of the *Compound Parabolic Concentrator*, selected as secondary optics, must be chosen in order that the mirrors of the solar plant are contained inside the corresponding area.

5. Conclusion

Other research groups chose to construct a software program dedicated to the optical design of heliostats fields, obtaining very good results. Our research group preferred to use commercial optical design packages for being able to exploit all the potentialities of these software programs. This strategy allowed us to utilise optimisation processes and radiometric calculations, finally obtaining results with elevated precision, advanced graphic characteristics, and high reliability.

The proposed simulation instruments are practically useful for developing optical designs of heliostats tower plants. Being derived from our experience in the research on solar plant design, they are addressed to solve specific problems and to evidence particularly crucial features. This paper presented the most advantageous tools, among our simulation programs for heliostats field design, and their practical applications were discussed showing examples of results.

The main code *ST_1* performs several functions: it provides a rapid and easy-to-manage optical design of a heliostats field; it gives the irradiance map on a target of the heliostats field; it estimates the effect of a *Gaussian angular noise* on the heliostats positions; it assesses the possible shadows (*vignetting effect*) between mirror rows. The aim of *ST_1* code is to facilitate the heliostats field analysis, exploiting the integration between our simulation code and ray-tracing software packages (*Zemax*). It simplifies optical design and ray-tracing simulation of the multimirror array, representing the key component of every thermodynamic tower plant. The heliostats field should be precisely shaped, placed, and

oriented to concentrate the sunlight on the tower receiver. The collection performances of the solar plant should be examined considering the solar variations during the day and during the year, finally selecting the optimal configuration.

The two side programs are more specific: *ST_2* evaluates the power collected by the heliostats field; *ST_3*, using a polar conical surface (a *CPC*) as secondary optics, selects the *CPC* aperture. The side-program *ST_2* permits to assess effects of seasonal and daily variations of solar irradiation. The dedicated side-code *ST_3* simplifies the selection of a *Compound Parabolic Concentrator (CPC)* as secondary optics of the furnace.

Our simulation tools and optical design strategies were developed for the application to a precise thermodynamic tower plant simulation, which we can consider as reference case for our studies. In our reference heliostat field, the study of interactions between solar rays, mirrors, and target was carried out employing *Zemax* as optical design software package. The utilization of this simulation program is justified on the base of its capacity to analyse a great amount of luminous rays and its possibility to use these characteristics for simulating irradiance maps in proximity of the critical zones: in the test target, within the furnace and on the heliostats plant.

In order to simplify the analysis of the solar plant features, we exploited the possibility of interfacing our optical design packages with codes in *Octave* style. These integrated simulation tools were developed for guiding the optical system analysis, for managing the large data amount, and for extracting the major and crucial parameters of the multimirror field.

Nomenclature

<i>Alfa</i> :	<i>CPC</i> inclination angle (between cone axis and ground)
<i>AM</i> :	Air mass coefficient
<i>A_{sp}</i> :	Heliostat surface
<i>CPC</i> :	Compound parabolic concentrator
<i>CSP</i> :	Concentrating solar power
<i>dist</i> :	Horizontal coordinate at which the <i>CPC</i> is placed
<i>h</i> :	Height at which the <i>CPC</i> is placed
<i>I₀</i> :	Solar irradiance outside the Earth atmosphere
<i>I_r</i> :	Solar irradiance reflected towards the tower by the single mirror
<i>I_s</i> :	Solar irradiance
<i>N × M</i> :	Heliostats matrix
<i>Octave</i> :	High-level programming language for numerical computations
<i>P</i> :	Power collected by each mirror in the solar field
<i>P_t</i> :	Total power reflected by the mirrors field toward the target
<i>Q</i> :	Empirical coefficient to take into account also the diffused component
<i>R</i> :	Reflectance
<i>ST_1</i> :	<i>Simulation Tool_1</i>
<i>ST_2</i> :	<i>Simulation Tool_2</i>
<i>ST_3</i> :	<i>Simulation Tool_3</i>

- S_x, S_y, S_z : Unit vectors of the solar ray
 U_x, U_y, U_z : Unit vectors of the mirror normal axis
 x, z, y : Coordinates with respect to the tower (origin)
 z : Angle that the sun forms with the zenith (zenith angle).
 $Zemax$: Optical design software by ray tracing
 θ : Field of view or total angular aperture of the CPC (as secondary collector).

References

- [1] E. Leonardi, "Detailed analysis of the solar power collected in a beam-down central receiver system," *Solar Energy*, vol. 86, no. 2, pp. 734–745, 2012.
- [2] E. Leonardi and B. D'Aguanno, "CRS4-2: a numerical code for the calculation of the solar power collected in a central receiver system," *Energy*, vol. 36, no. 8, pp. 4828–4837, 2011.
- [3] "SOLFAST 4D by the PROMES Group—CNRS (French National Research Council)," <http://www.hpc-sa.com/en/products/solfast4d>.
- [4] Tonatiuh 1.2.6, "Ray tracing for solar energy".
- [5] V. Badescu, Ed., *Modeling Solar Radiation at the Earth Surface*, Springer, Berlin, Germany, 2008.
- [6] A. B. Meinel and M. P. Meinel, *Applied Solar Energy*, Addison Wesley, New York, NY, USA, 1976.
- [7] PVCDROM, *Stuart Bowden and Christiana Honsberg*, Solar Power Labs, Arizona State University, 2011.
- [8] F. Kasten and A. T. Young, "Revised optical air mass tables and approximation formula," *Applied Optics*, vol. 28, no. 22, pp. 4735–4738, 1989.

Research Article

A Suitable Polysulfide Electrolyte for CdSe Quantum Dot-Sensitized Solar Cells

H. K. Jun, M. A. Careem, and A. K. Arof

Centre for Ionics University of Malaya, Department of Physics, University of Malaya, 50603 Kuala Lumpur, Malaysia

Correspondence should be addressed to A. K. Arof; akarof@um.edu.my

Received 22 November 2012; Revised 29 January 2013; Accepted 29 January 2013

Academic Editor: Daniel Chemisana

Copyright © 2013 H. K. Jun et al. This is an open access article distributed under the Creative Commons Attribution License, which permits unrestricted use, distribution, and reproduction in any medium, provided the original work is properly cited.

A polysulfide liquid electrolyte is developed for the application in CdSe quantum dot-sensitized solar cells (QDSSCs). A solvent consisting of ethanol and water in the ratio of 8 : 2 by volume has been found as the optimum solvent for preparing the liquid electrolytes. This solvent ratio appears to give higher cell efficiency compared to pure ethanol or water as a solvent. Na₂S and S give rise to a good redox couple in the electrolyte for QDSSC operation, and the optimum concentrations required are 0.5 M and 0.1 M, respectively. Addition of guanidine thiocyanate (GuSCN) to the electrolyte further enhances the performance. The QDSSC with CdSe sensitized electrode prepared using 7 cycles of successive ionic layer adsorption and reaction (SILAR) produces an efficiency of 1.41% with a fill factor of 44% on using a polysulfide electrolyte of 0.5 M Na₂S, 0.1 M S, and 0.05 M GuSCN in ethanol/water (8 : 2 by volume) under the illumination of 100 mW/cm² white light. Inclusion of small amount of TiO₂ nanoparticles into the electrolyte helps to stabilize the polysulfide electrolyte and thereby improve the stability of the CdSe QDSSC. The CdSe QDs are also found to be stable in the optimized polysulfide liquid electrolyte.

1. Introduction

Dye-sensitized solar cells (DSSCs) have been the focus of research in recent decade due to their low cost and ease of fabrication [1, 2]. Recently quantum dot-sensitized solar cells (QDSSCs) are emerging as an alternative to DSSCs to overcome the stability issues of the latter. A QDSSC uses a semiconductor quantum dot (QD) as the light absorber instead of the usual inorganic dyes [3–5]. QDSSCs are being investigated as promising low-cost solar cells as they offer more advantages compared to DSSCs. Notable advantages of QDs include easy preparation, tunable band gap energy, high extinction coefficient, and multiple exciton generation [6–10]. Among the semiconductor QD choices, CdS and CdSe are the widely used QDs in QDSSCs.

For the operation of a DSSC or QDSSC, a good electrolyte with a redox mediator is required. The redox mediator regenerates the oxidized sensitizer by donating an electron. Unfortunately, there are not many electrolyte/redox mediator systems which can function in both DSSCs and QDSSCs. DSSCs work best with iodide-based electrolyte systems [11]. However, in QDSSCs, iodide-based electrolytes produce very

poor results [12–15]. Nevertheless, with appropriate coating on the QDs surface, a good efficiency result can be obtained with I⁻/I₃⁻ redox electrolyte as shown by Shalom et al. [14]. Therefore, the electrolyte chosen has played a major role in determining the QDSSCs' performance [15]. In general, polysulfide electrolytes have been used by many researchers as an electrolyte of choice for QDSSCs [16, 17]. An optimized polysulfide electrolyte system has been reported for use in CdS QDSSCs by Lee and Chang [18]. We have used the same polysulfide electrolyte in a QDSSC based on CdSe QD prepared using 6 cycles of successive ionic layer adsorption and reaction (SILAR), and the cell showed a very low efficiency of 0.65%. There are many different polysulfide compositions reported in the literature which give reasonable efficiencies for CdSe QDSSCs [16, 19–21]. The compositions reported range from pure aqueous solutions to solutions containing various amounts of KCl, NaOH, or KOH as additives. Lee et al. reported an efficiency of 2.9% in a CdSe QDSSC by using an electrolyte consisting of Na₂S, S and KCl in water/methanol mixture [16]. Meanwhile, Diguna et al. obtained an efficiency of 2.7% with just Na₂S and S in the liquid electrolyte [19]. However, a lower efficiency of

1.83% has been reported with an electrolyte composition of Na_2S , S, and NaOH [20]. A somewhat lower efficiency was obtained by Salant et al. with an electrolyte composition of Na_2S , S, and KOH [21]. The different conversion energy efficiencies ranging from 1.50% to about 3.00% reported by the above researchers may have arisen due to different QDSSC system involved such as variation in the electrolytes used, the way the QDs were prepared, and the surface treatment of the photoanode. The discrepancies in the results reported motivated us to undertake a systematic study to find a suitable polysulfide-based electrolyte system that can result in optimum performance in CdSe-based QDSSCs.

In this study, we have fabricated a standard CdSe QDSSC with platinum as the counter electrode. CdSe QD-sensitized electrode was prepared using SILAR method. The thickness of TiO_2 layer was kept constant in all QDSSCs with no surface treatment. Various compositions of polysulfide liquid electrolyte were prepared and then tested in the QDSSCs to determine the optimum performing electrolyte. The performance of the QDSSC with the optimized polysulfide electrolyte was then evaluated over two hours to assess the stability of the cell. To the authors' best knowledge, there is no report in the literature on the optimization of polysulfide electrolyte for use in CdSe QDSSC prepared from SILAR method. Hence, the outcome of this study may lead to a basic electrolyte of the polysulfide system for application in CdSe QDSSCs.

2. Experimental

2.1. Materials. Titanium dioxide (TiO_2) paste (18NR) was purchased from JGC C&C, Japan. Platinum catalyst solution (Plastisol) and fluorine-doped tin oxide (FTO) conducting glass ($8 \Omega/\text{sq}$ sheet resistance) were obtained from Solaronix, Switzerland. Compact layer solution, diisopropoxy titanium bis(acetylacetonate) was procured from Sigma-Aldrich and diluted with ethanol to obtain a 0.38 M solution. Cadmium nitrate tetrahydrate, selenium dioxide, sodium borohydride, potassium chloride, sulfur, guanidine thiocyanate (GuSCN), and TiO_2 nanoparticles powder were all procured from Sigma-Aldrich, while sodium sulfide nonahydrate was obtained from Bendosen, Germany.

2.2. Preparation of TiO_2 Film Photoanodes and Counter Electrodes. FTO conducting glasses were used as substrates for both working and counter electrodes. For the working electrode or photoanode, a compact layer of TiO_2 was first prepared by spin coating diisopropoxy titanium bis(acetylacetonate) solution on the substrate surface. Spin coating was performed at 3000 rpm for 10 seconds. Then the solution coated FTO glass was sintered at 450°C for 30 minutes. The acquired TiO_2 compact layer will improve the adhesion of TiO_2 to the substrate and at the same time provide a larger TiO_2 /FTO contact area ratio. The compact layer also prevents the electron recombination in the solar cell by minimizing the contact between the redox electrolyte and the conductive FTO surface [22]. TiO_2 paste was subsequently deposited on top of the compact layer using doctor-blade method. The newly deposited layer was sintered at 450°C for 30 minutes in order to remove any organic residues and moisture as well

as to obtain a mesoporous TiO_2 layer. The SEM image showed that mesoporous TiO_2 layer has a thickness of about $5 \mu\text{m}$.

Counter electrodes were prepared by spin coating a thin layer of Plastisol solution on FTO conducting surfaces. The electrodes were then sintered at 450°C for 30 minutes.

2.3. Fabrication of CdSe QD-Sensitized Electrodes. CdSe QDs were prepared using the SILAR deposition method. The QD synthesis process was performed in a glove box filled with argon gas following the procedure reported in the literature [23]. TiO_2 -coated electrode was first dipped into 0.03 M $\text{Cd}(\text{NO}_3)_2$ ethanol solution for 30 s followed by ethanol rinsing and drying. Then the electrode was dipped into Se^{2-} solution for 30 s followed by ethanol rinsing and drying. Se^{2-} solution was prepared by reacting 0.03 M SeO_2 ethanolic solution with 0.06 M NaBH_4 . The mixture was stirred for about an hour before it was used for SILAR dipping process. This two-step dipping process is termed as 1 SILAR cycle. All QDs used were deposited using 7 SILAR cycles (based on optimization study performed by the author).

2.4. Assembly of QDSSCs. A sandwich-type cell was fabricated by clamping the working electrode with the counter electrode. Parafilm ($130 \mu\text{m}$ thickness) was used as a spacer. A droplet of the electrolyte was dropped onto the surface of QD-sensitized TiO_2 film prior to cell assembly. The procedure was repeated until the QD-sensitized TiO_2 film was covered with the electrolyte. The effective working area used was 0.25 cm^2 . This assembly method is slightly different from the common method where Surlyn tape is used as spacer with proper sealing. In our case, careful attention was given to ensure that the electrolyte has covered the aperture of the parafilm spacer before the cell assembly. There was no external sealing applied as the parafilm spacer was adequate to prevent the electrolyte from leaking. Polysulfide electrolyte solution was prepared from Na_2S , S, KCl, GuSCN, and TiO_2 in water-ethanol mixture. The concentration of each material in the electrolyte is given in detail in Section 3.

2.5. Photoresponse Measurements. Photocurrent-voltage (I - V) characteristics of the QDSSCs were measured using a Keithley 2400 electrometer under illumination from a xenon lamp at the intensity of $100 \text{ mW}/\text{cm}^2$. Efficiency was calculated from

$$\eta = \frac{J_{\text{SC}} \times V_{\text{OC}} \times \text{FF}}{P_{\text{in}}}, \quad (1)$$

where J_{SC} is photocurrent density measured at short-circuit, V_{OC} is open-circuit voltage, FF is fill factor, and P_{in} is the intensity of the incident light. Measurement on each cell was repeated three times to ensure the consistency of the data. In order to confirm the best performance, measurements were repeated on another identical cell, and reproducibility of the results was checked.

3. Results and Discussion

3.1. Determining the Optimum Solvent for the Electrolyte. Most of the polysulfide electrolytes were prepared as aqueous

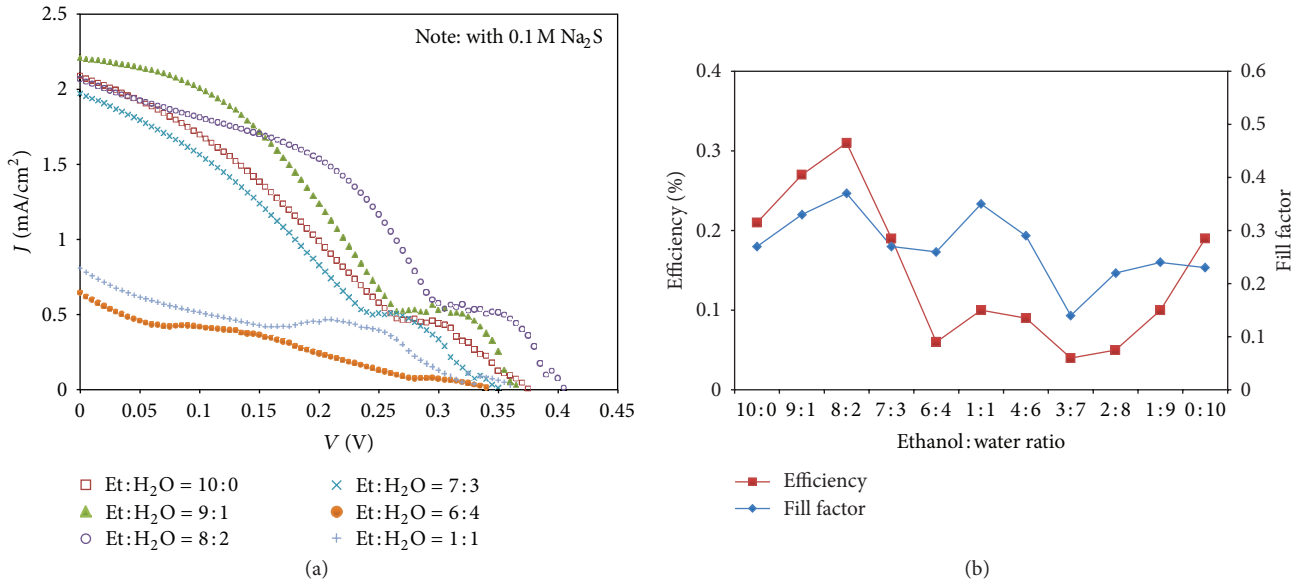


FIGURE 1: (a) J - V curves of CdSe QDSSCs with $0.1 \text{ M Na}_2\text{S}$ electrolyte having various solvent ratio. (b) Variation of efficiency and fill factor of the cells with different solvent ratio in the electrolyte.

TABLE 1: Performance parameters of CdSe QDSSCs with $0.1 \text{ M Na}_2\text{S}$ electrolytes having various solvent ratio.

Solution composition of the electrolyte	J_{SC} (mA/cm^2)	V_{OC} (V)	Fill factor (%)	Efficiency, η (%)
Methanol 100%	0.42	0.305	16.0	0.02
Ethanol 100%	2.09	0.375	27.0	0.21
Ethanol : water = 9 : 1	2.21	0.365	33.0	0.27
Ethanol : water = 8 : 2	2.07	0.405	37.0	0.31
Ethanol : water = 7 : 3	1.97	0.350	27.0	0.19
Ethanol : water = 6 : 4	0.65	0.340	26.0	0.06
Ethanol : water = 1 : 1	0.81	0.360	35.0	0.10
Ethanol : water = 4 : 6	0.85	0.345	29.0	0.09
Ethanol : water = 3 : 7	0.82	0.340	14.0	0.04
Ethanol : water = 2 : 8	0.62	0.360	22.0	0.05
Ethanol : water = 1 : 9	1.21	0.340	24.0	0.10
Water 100%	2.09	0.395	23.0	0.19

solutions. However, recently Lee and Chang proposed to mix methanol with water for the electrolyte preparation [18]. The use of alcohol was suggested to reduce the high surface tension of the aqueous solution. High surface tension will result in a low penetration and poor wetting of the solution in the mesoporous TiO_2 film. To overcome this problem, alcohol (methanol or ethanol) solution is used as cosolvent for the electrolyte solution.

We start with the comparison of pure alcohol and aqueous solution as a solvent for the electrolyte. Appropriate amount of Na_2S only was used to prepare the 0.1 M electrolyte solution. Figure 1(a) shows the J - V curves of QDSSCs fabricated with electrolytes having selected ratio of cosolvents, and Figure 1(b) shows the variation of efficiencies and fill factors of all cells investigated with the ethanol/water ratio in the electrolyte. Table 1 shows the summary of the performance parameters of all cells investigated, which were prepared with electrolytes having different ratio of cosolvents.

With the pure water aqueous electrolyte solution (water 100%), the efficiency of the QDSSC is found to be 0.19% with a short-circuit photocurrent density of $2.09 \text{ mA}/\text{cm}^2$. However, with pure methanol electrolyte solution (methanol 100%), the solar cell does not perform well. The efficiency is only 0.02% with a short-circuit photocurrent density of $0.2 \text{ mA}/\text{cm}^2$. Both solutions produce an open-circuit voltage above 0.3 V . Fill factor is rather low, that is, 23% for the water solution and 16% for the methanol solution. With another alcohol-based solution, pure ethanol solution (ethanol 100%), a cell efficiency of 0.21% with a short-circuit photocurrent density of $2.09 \text{ mA}/\text{cm}^2$ is observed. Ethanol seems to be a better solvent compared with methanol as it yields a better fill factor value of 27%. Ethanol has a surface tension of $21.82 \text{ mN}/\text{m}$ at room temperature compared with $22.51 \text{ mN}/\text{m}$ of methanol [24]. However, surface tension is only part of the contributing factors for the solar cell performance. The ethanol can also serve as a sacrificial hole scavenger that allows easy hole

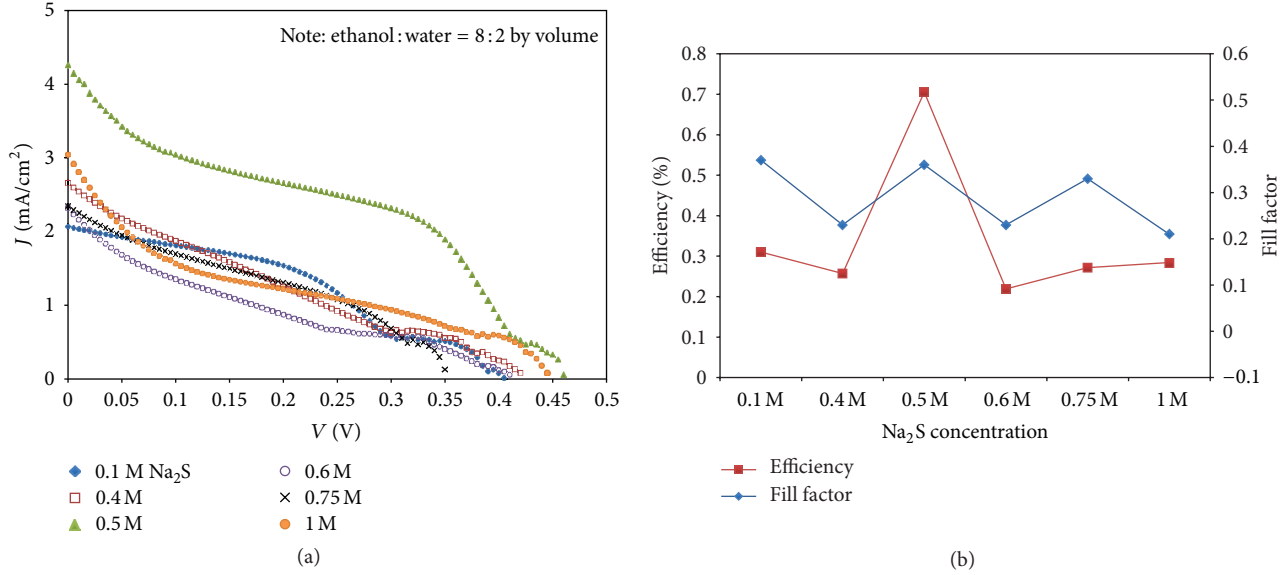


FIGURE 2: (a) J - V curves of CdSe QDSSCs with electrolytes having various amounts of Na₂S. (b) Variation of efficiency and fill factor of the cells with the amount of Na₂S in the electrolyte.

transfer from the excited CdSe QDs and prevents the recombination of the charge carriers [25]. Therefore, a mixture of water and ethanol is chosen as the solvent in our subsequent investigations. The ratio of ethanol and water is varied to prepare the co-solvent solution for the electrolyte.

From the results, we can see that the best cell performance is obtained when the solution consists of ethanol/water ratio of 8/2 (by volume). The cell with this electrolyte has the best efficiency of 0.31% with a short-circuit photocurrent density of 2.07 mA/cm². This result is better than the results obtained for cells with single solvent-based electrolytes. This cell also has the highest fill factor (37%) among the cells prepared with other electrolyte solutions. As the ratio of the ethanol part in the electrolyte solution decreases, efficiency of the cell is found to decrease. It is clear that electrolytes having ratio of ethanol to water greater than 7 give better performance. This indicates the importance of ethanol in making the electrolyte penetrate deep into the mesoporous TiO₂ film and wet the pores. The penetration and wetting depends on the combination of viscosity and surface tension of the electrolyte solution. As the maximum performance is obtained with the electrolyte having ethanol/water ratio of 8/2, this composition is used for further studies to enhance the performance of the QDSSCs. It is interesting to note that QDSSCs work without S in the Na₂S electrolyte, but the J - V curves of the cell appear to be different in that the curves level off at higher applied voltage in the range 0.25–0.35 V before eventually dropping to zero photocurrent density. We attribute this effect to the absence of regenerative species of S_x^{2-} in the electrolyte and the hole scavenging effect from alcohol which results in nonregenerative cells [25–27]. The use of alcohol in the solar cell electrolyte will lead to alcohol oxidation at the photoanode and at the same time it itself is a sacrificial donor by scavenging photogenerated holes. It is therefore of great importance to further optimize

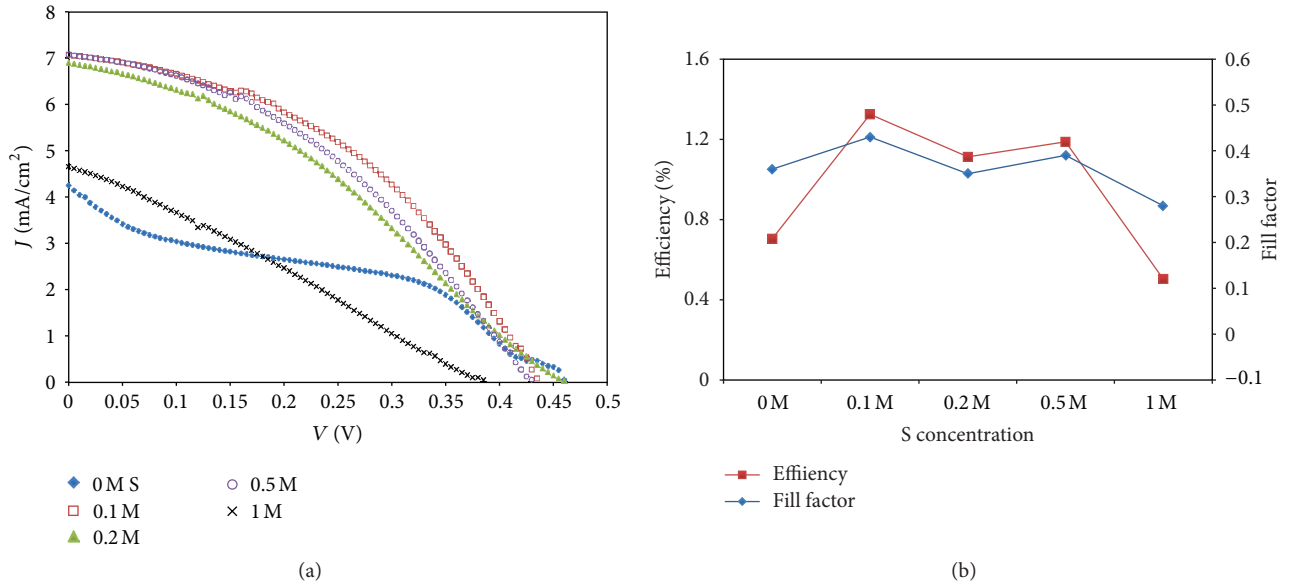
the Na₂S concentration as well as the inclusion of regenerative species S_x^{2-} in the optimized solvent of ethanol/water (8/2 by volume). Further investigations are necessary to understand the exact reasons for the unusual shape of the J - V curves when S is absent in the electrolytes.

3.2. Determining the Optimum Na₂S Salt Concentration for the Electrolyte. As the efficiency of the cell obtained with 0.1 M Na₂S electrolyte is low, it is imperative to optimize the Na₂S concentration in the electrolyte solution. The amount of Na₂S is varied in the solution having ethanol/water: 8/2 (by volume) to obtain electrolyte solutions of different concentrations ranging from 0.1 to 1.0 M. The corresponding J - V curves of the cells having different concentration of Na₂S are shown in Figure 2(a), while the variation of the efficiencies and fill factors with the concentrations are shown Figure 2(b). Table 2 summarizes the performance parameters of the cells prepared with electrolytes having different concentration of Na₂S. From the results, optimum performance is obtained for the cells with an electrolyte having 0.5 M of Na₂S. This cell has an efficiency of 0.71% with an improved short-circuit photocurrent density of 4.26 mA/cm² as well as a better open-circuit voltage of 0.46 V. However, there is not much change in the fill factor value.

Further increase of Na₂S in the electrolyte solution above 0.5 M does not improve the cell performance. It should be noted that Na₂S is only slightly soluble in alcohol but well soluble in water. As such, higher concentration of salt may not incur full solubility in the co-solvent. The results obtained suggest that for the best performance of the QDSSC the electrolyte must have an optimum Na₂S concentration of 0.5 M. With higher salt concentration, charge recombination at the photo electrode and electrolyte interface is enhanced as evidenced by the low fill factor value. This also implies a slow

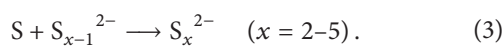
TABLE 2: Performance parameters of CdSe QDSSCs with electrolytes having various amounts of Na₂S in ethanol/water (8 : 2 by volume) solution.

Na ₂ S concentration in the electrolyte	J_{SC} (mA/cm ²)	V_{OC} (V)	Fill factor (%)	Efficiency, η (%)
0.1 M	2.07	0.405	37.0	0.31
0.4 M	2.66	0.420	23.0	0.26
0.5 M	4.26	0.460	36.0	0.71
0.6 M	2.32	0.410	23.0	0.22
0.75 M	2.35	0.350	33.0	0.27
1.0 M	3.04	0.445	21.0	0.28

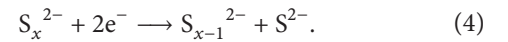
FIGURE 3: (a) J - V curves of CdSe QDSSCs with electrolytes having various amount of S. (b) Variation of efficiency and fill factor of the cells with the amount of S in the electrolyte. The electrolyte used: 0.5 M Na₂S in ethanol/water (8 : 2 by volume).

hole recovery rate from the oxidized QD by the high concentration electrolytes. It is interesting to note that the QDSSC works with only Na₂S in the electrolyte, but the J - V curves have somewhat irregular shapes (Figure 1(b)). The absence of regenerative S species in the electrolyte may have resulted in these irregular shapes as indicated in Section 3.1. This problem can be mitigated by the addition of sulfur to form the polysulfide redox couple (see Section 3.3). It should be noted that without the sulfur in the electrolyte the QDCCs will not function continuously.

3.3. Determining the Sulfur Content Needed for the Best Performance of the Cells. In order to obtain a regenerative redox couple, a second element is needed to couple with S²⁻ from the Na₂S. In most studies, sulfur is added to the sulfide salt to form a polysulfide (S²⁻/S_{*x*}²⁻) redox couple. From the perspective of chemical reaction, oxidation occurs at the photoanode-electrolyte interface according to [28]



At the counter electrode, reduction occurs where S_{*x*}²⁻ is reverted back to S²⁻:



This chemical reaction is thought to enhance the hole recovery rate which results in a higher performance of solar cell [29]. Ardoin and Winnick suggested that the active species at the photoanode would be the disulfide ion [30].

In this study, we have added sulfur into the 0.5 M Na₂S solution. The amount of the sulfur added is varied, and the efficiency of the cell utilizing each electrolyte is obtained. Due to limited solubility of sulfur in alcohol, the amount of the sulfur added is limited to 1.0 M. The performance trend along with J - V curves of cells having different amount of S are shown in Figure 3, and the performance parameters of the cells are summarized in Table 3. The results show that addition of 0.1 M of sulfur to the electrolyte enhances the cell efficiency to a best value of 1.32% and produces the best fill factor of 43%. Photocurrent density is also improved to a higher value of 7.08 mA/cm². The overall efficiency has more than 80% improvement which is largely attributed to the enhancement of photocurrent density. This shows that

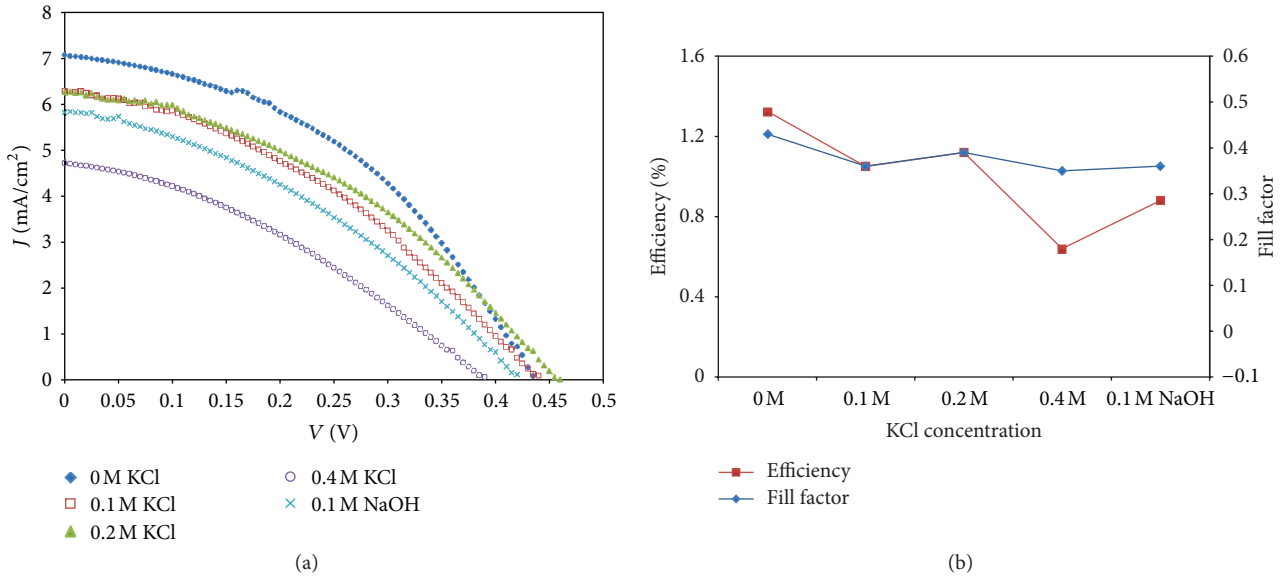


FIGURE 4: (a) J - V curves of CdSe QDSSCs with electrolytes having various amounts of KCl additive. (b) Variation of efficiency and fill factor of the cells with the amount of KCl in the electrolyte. Electrolyte used: 0.5 M Na₂S, 0.1 M S in ethanol/water (8 : 2 by volume).

TABLE 3: Performance parameters of CdSe QDSSCs with electrolytes having various amounts of S. The electrolyte used: 0.5 M Na₂S in ethanol/water (8 : 2 by volume).

S concentration in the electrolyte	J_{SC} (mA/cm ²)	V_{OC} (V)	Fill factor (%)	Efficiency, η (%)
0 M	4.26	0.460	36.0	0.71
0.1 M	7.08	0.435	43.0	1.32
0.2 M	6.91	0.460	35.0	1.11
0.5 M	7.08	0.430	39.0	1.19
1.0 M	4.66	0.385	28.0	0.50

addition of sulfur in small amount up to 0.1 M concentration increases the cell performance. However, further increase of sulfur amount does not yield better performance. We attribute this to the solubility limit of sulfur in the solvent. Note that with the addition of sulfur in the electrolyte, the J - V curves take the regular shapes.

3.4. Determining Additives Needed in the Electrolyte for the Optimum Performance of Cells. The introduction of additives to the electrolyte has been shown to enhance the photocurrent generated and thereby improve the performance of QDSSCs [18, 31]. Lee and Chang have added KCl to the electrolyte to further enhance the performance of CdS QDSSCs [18]. The presence of KCl increased the performance of the cell as well as the electrolyte solution conductivity. In the present study, we have added different amounts of KCl to the optimized 0.5 M Na₂S and 0.1 M S solution. However, we noticed that the performance of the cells did not improve. The electrolyte without KCl appears to be superior in our case (see Figure 4(a)). Addition of KCl actually decreased the photocurrent density in contradiction to Lee and Chang's work. The difference may be due to different solvent mixtures as they have used a mixture of methanol and water as co-solvent. The presence of anion Cl⁻ in the electrolyte may have altered the CdSe QDs surface which could have resulted in a

lower cell performance. At present, the mechanism of the Cl⁻ effect is not well understood.

Replacement of KCl with NaOH also did not produce any improvement either in the performance of QDSSCs (see Figure 4(a)). This is expected as KCl is more electropositive than NaOH. Thus the conductivity of the electrolyte with added NaOH should be lower compared with that of the electrolyte with added KCl. The performance parameters of CdSe-sensitized solar cells with electrolytes having KCl or NaOH additive are summarized in Table 4. Figure 4(a) shows the corresponding J - V curves, and the trend of the variation of parameters with KCl additive is shown in Figure 4(b).

In a DSSC work reported by Zhang et al., guanidine thiocyanate (GuSCN) was added to the I⁻/I₃⁻ electrolyte system for the improvement of performance and stability [32]. Following this report, Chou et al. have tried GuSCN additive in CdS QDSSC and obtained enhancement in current density and efficiency [31]. In order to try this additive to the CdSe QDSSC, we have added different amounts of GuSCN into our optimized electrolyte solution having 0.5 M Na₂S and 0.1 M S in ethanol/water (8/2 by volume). The presence of GuSCN decreases the photocurrent density but increases the open-circuit voltage in contrast to the significant improvement in photocurrent density reported by Chou et al. [31]. This difference

TABLE 4: Performance parameters of CdSe QDSSCs with electrolytes having various amounts of KCl additive. Electrolyte used: 0.5 M Na₂S, 0.1 M S in ethanol/water (8 : 2 by volume).

KCl concentration in the electrolyte	J_{sc} (mA/cm ²)	V_{oc} (V)	Fill factor (%)	Efficiency, η (%)
0 M	7.08	0.435	43.0	1.32
0.1 M	6.60	0.440	36.0	1.05
0.2 M	6.27	0.460	39.0	1.12
0.4 M	4.22	0.390	35.0	0.64
0.1 M NaOH	5.83	0.420	36.0	0.88

TABLE 5: Performance parameters of CdSe QDSSC with electrolytes having various amounts of GuSCN additive. Electrolyte used: 0.5 M Na₂S, 0.1 M S in ethanol/water (8 : 2 by volume).

GuSCN concentration in the electrolyte	J_{sc} (mA/cm ²)	V_{oc} (V)	Fill factor (%)	Efficiency, η (%)
0 M	7.08	0.435	43.0	1.32
0.05 M	6.80	0.470	44.0	1.41
0.1 M	6.98	0.455	37.0	1.18
0.2 M	6.95	0.445	42.0	1.30

could be attributed to the different electrolyte compositions and QD-sensitized photoanodes involved. Only a small amount of GuSCN is required to enhance our polysulfide electrolyte. In our case, 0.05 M of GuSCN can boost the cell performance to a best efficiency of 1.41% with the best fill factor of 44% and the best open-circuit voltage of 0.470 V (see Table 5). The performance parameters of the cells with electrolytes having various amounts of GuSCN are summarized in Table 5, and the J - V curves of the cells and performance trend are shown in Figures 5(a) and 5(b). It should be noted that the addition of GuSCN does not result in a distinct improvement on the cell performance. An initial increase of GuSCN concentration produces a slight improvement on the cell performance as the additive assists in decreasing the interfacial recombination at the photoanode by patching up the TiO₂ surface not covered by the QDs [32]. However, at higher concentration of GuSCN, cyanide may have adsorbed strongly on the CdSe QDs surface. This phenomenon may have negative effect on the electrolyte regenerative cycle, though the precise mechanism may need to be further investigated [33].

So far, we are able to reproduce the performance of the optimized electrolyte by using few similar cell assemblies with performance variance of $\pm 0.05\%$. Our optimized polysulfide electrolyte composition is different from that of Lee and Chang as they have obtained an optimized polysulfide electrolyte consisting of 0.5 M Na₂S, 2 M S, and 0.2 M KCl in methanol/water (7 : 3 by volume) solution [18]. It should be noted that their electrolyte is efficient in CdS QDSSCs. When the same electrolyte was applied in CdSe QDSSC (as in our study), the efficiency did not match with what has been reported. Clearly both electrolytes are sensitive to the material type involved. It is also noted that the efficiency obtained in this study for CdSe QDSSCs is lower compared to the values reported in the recent literatures where efficiency of more than 2.0% was obtained [34–36]. Table 6 lists the performance parameters of some CdSe QDSSCs from other groups for comparison. Beside different polysulfide electrolyte

composition, the performance differences are largely due to different photoanode configuration, surface treatment, QD deposition method, and type of counter electrode. We acknowledge our best result is lower as our photoanode has not been fully optimized. We anticipate a better result if all the photoanode parameters are optimized (i.e., TiO₂ film thickness, ZnS passive layer, scattering layer, and volume and size of QD deposited). The choice of counter electrode also plays an important role in the cell performance. Commonly used platinum electrode may not be suitable with polysulfide electrolyte as the S compound will adsorb on the surface affecting the electrode performance [37]. The alternative will be Cu₂S electrode which has better catalytic activity for the reduction of S_x²⁻ species [20, 35].

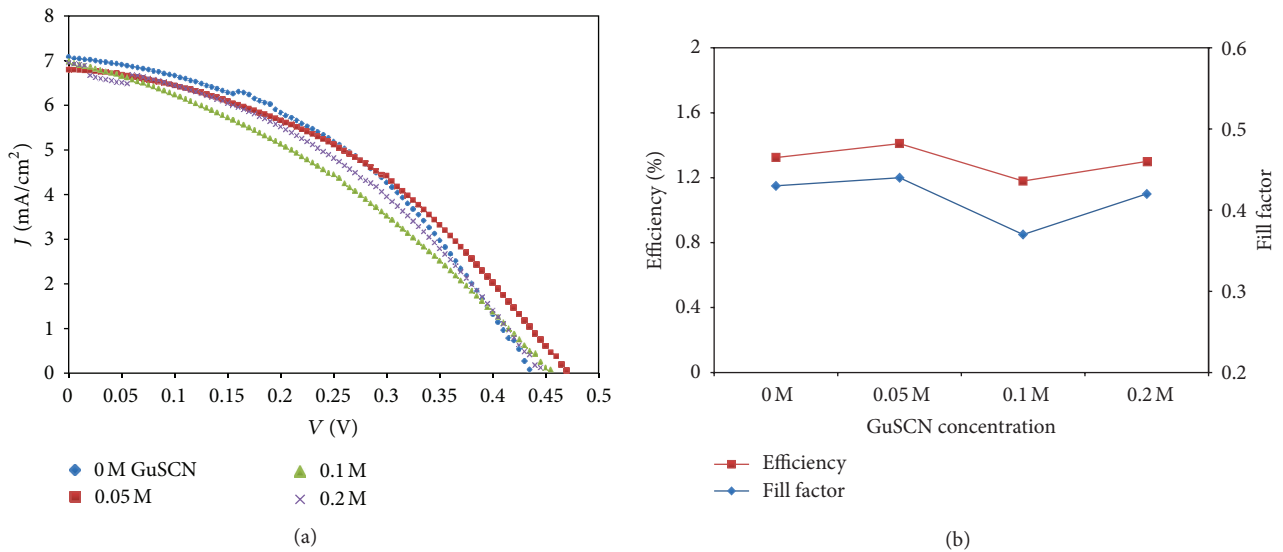
3.5. Stability of the Electrolyte and the QDSSC. From our study as discussed in previous sections, the optimum polysulfide electrolyte for CdSe QDSSC consists of 0.5 M Na₂S, 0.1 M S, and 0.05 M GuSCN in ethanol/water solution (8/2 by volume). To improve the stability of the electrolyte, we have added 1 wt% of TiO₂ nanoparticles (<400 nm) into the solution. TiO₂ is usually used as a filler in the preparation of stable high conducting polymer electrolytes. We have investigated the performance of CdSe QDSSCs having electrolytes with and without TiO₂ nanoparticles under continuous soaking of light for two hours with a light intensity of 100 mW/cm². Initially the cell with the electrolyte having added TiO₂ shows an efficiency of 1.39% which is slightly lower than that of the cell without TiO₂ added (refer Table 7). Nevertheless, it has an improved photocurrent density of 7.70 mA/cm². When the illumination is continued, the efficiencies of both cells decrease with time. The efficiency of the cell using polysulfide electrolyte without added TiO₂ appears to decrease at a faster rate compared to that of the cell using electrolyte with added TiO₂. After two hours, the former reaches an efficiency of 0.72%, a decrease of about 50% from initial value. For the cell using polysulfide electrolyte with added TiO₂, the efficiency obtained after two hours of continuous light soaking is 1.02%.

TABLE 6: Performance parameters of CdSe QDSSC with different polysulfide electrolyte compositions reported by various groups.

Photoanode configuration	Electrolyte composition	J_{SC} (mA/cm ²)	V_{OC} (V)	Fill factor (%)	Efficiency η (%)	Reference
TiO ₂ /CdSe	0.5 M Na ₂ S, 0.1 M S, 0.05 M GuSCN in ethanol/water (8 : 2 by volume)	6.80	0.470	44.0	1.41	This work
TiO ₂ /CdSe	0.5 M Na ₂ S, 0.1 M S, 0.2 M KCl in methanol/water (3 : 7 by volume)	10.61	0.378	36.0	1.40	[16]
TiO ₂ /CdS/CdSe/ZnS	0.5 M Na ₂ S, 0.1 M S, 0.2 M KCl in methanol/water (3 : 7 by volume)	11.66	0.503	49.0	2.90	[16]
TiO ₂ /CdSe	1 M Na ₂ S, 1 M S in aqueous	6.03	0.680	39.0	1.60	[19]
TiO ₂ /F/CdSe/F/ZnS	1 M Na ₂ S, 1 M S in aqueous	7.51	0.710	50.0	2.70	[19]
TiO ₂ /CdSe	1 M Na ₂ S, 0.1 M S, 0.1 M NaOH in ultrapure water	3.06	0.430	21.0	0.28	[20]
TiO ₂ /CdSe/ZnS	1 M Na ₂ S, 0.1 M S, 0.1 M NaOH in ultrapure water	7.13	0.510	48.0	1.83	[20]
TiO ₂ /CdSe	1 M Na ₂ S, 0.1 M S, 0.1 M KOH in aqueous	2.70	0.554	26.0	0.40	[21]
TiO ₂ /CdSe/ZnS	1 M Na ₂ S, 0.1 M S, 0.1 M KOH in aqueous	9.00	0.554	35.0	1.70	[21]

TABLE 7: Performance parameters of CdSe QDSSCs with and without TiO₂ nanoparticles in the electrolyte. Electrolyte used: 0.5 M Na₂S, 0.1 M S, 0.05 M GuSCN in ethanol/water (8 : 2 by volume).

Composition	Time (min)	J_{SC} (mA/cm ²)	V_{OC} (V)	Fill factor (%)	Efficiency, η (%)
0.5 M Na ₂ S + 0.1 M S + 0.05 M GuSCN	0	6.80	0.470	44.0	1.41
	120	4.36	0.40	41.0	0.72
0.5 M Na ₂ S + 0.1 M S + 0.05 M GuSCN + 1 wt% TiO ₂	0	7.70	0.475	38.0	1.39
	120	5.27	0.430	45.0	1.02

FIGURE 5: (a) J - V curves of CdSe QDSSCs with electrolytes having various amounts of GuSCN additive. (b) Variation of efficiency and fill factor of the cells with the amount of GuSCN in the electrolyte. Electrolyte used: 0.5 M Na₂S, 0.1 M S in ethanol/water (8 : 2 by volume).

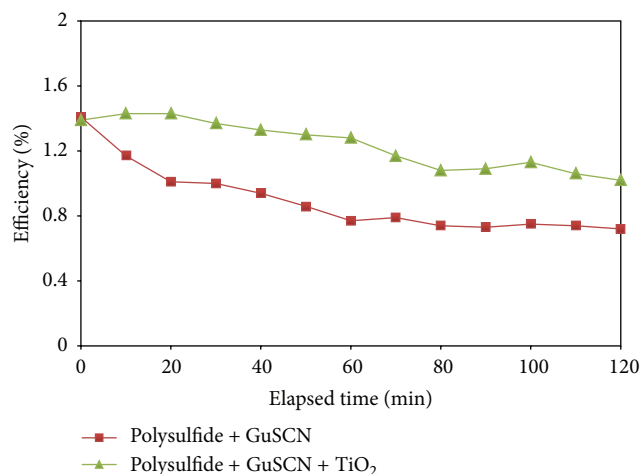


FIGURE 6: Efficiency variation of CdSe QDSSCs with time under two-hour light soaking. The polysulfide electrolytes used in the cells were with and without added TiO₂ nanoparticles.

This translates to about 27% decrease from initial value. The decrease in performance is also noted, and this can be attributed to the decrease of photocurrent density and open-circuit voltage. With the addition of TiO₂ to the electrolyte solution, stability of the cell has improved substantially presumably due to enhanced stability of the electrolyte. The efficiency variation of the two cells in the two-hour light soaking period is presented in Figure 6. The presence of TiO₂ is thought to have adsorbed on the QD surface and thus passivating the QD surface states which in turn decrease the recombination electrons from the photoanode into the electrolyte [14]. Thus, an improved performance and better stability are achieved. Although the mechanism involved in the stability improvement of the cell due to addition of TiO₂ in the polysulfide electrolyte needs further investigation to understand, this method seems noteworthy for improving the stability of the QDSSCs using polysulfide liquid electrolytes.

When a CdSe-sensitized photoanode is dipped in the optimized polysulfide electrolyte solutions, UV-vis spectra obtained for the CdSe-sensitized photoanode before and after dipping into the electrolyte do not show any deviation. The results obtained are shown in Figure 7. There is no significant change of absorbance before and after dipping of the electrode. The CdSe-sensitized TiO₂ film appears to be having the same colour of dark brown before and after dipping (see inset in Figure 7). This signifies that no major chemical reaction occurs in the CdSe-sensitized TiO₂ film upon exposure to polysulfide electrolyte. These results emphasize that polysulfide electrolytes are a better choice for CdSe QDSSCs as the electrolytes do not produce any serious deterioration of the QDs.

4. Conclusions

A suitable polysulfide electrolyte has been investigated for use in CdSe-based QDSSCs. The optimum cell performance was obtained with polysulfide electrolyte consisting of 0.5 M Na₂S, 0.1 M S, and 0.05 M GuSCN in ethanol/water (8/2

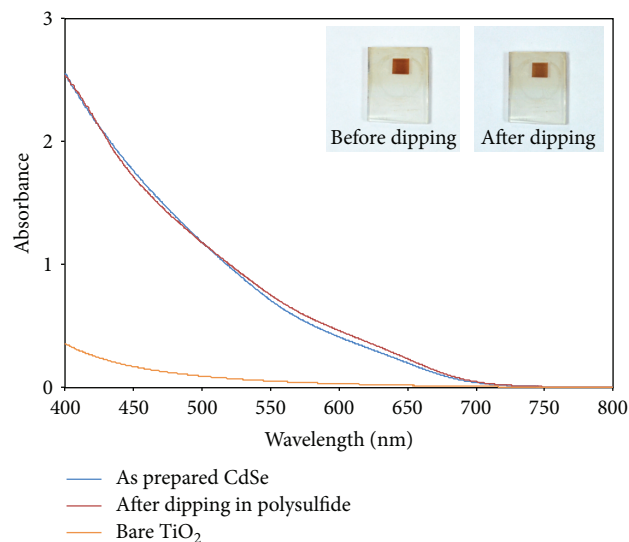


FIGURE 7: UV-vis spectra of CdSe-sensitized TiO₂ electrodes before and after dipping in polysulfide electrolytes (inset: photograph of CdSe-sensitized electrodes before dipping and after dipping in polysulfide electrolyte).

by volume) solution. The CdSe QDSSC with this optimized polysulfide electrolyte has an efficiency of 1.41%, a short circuit current density of 6.80 mA/cm², an open-circuit voltage of 0.47 V and a fill factor of 44%. With the addition of TiO₂ nanoparticles to the electrolyte, the stability of the cell is enhanced. A higher photocurrent density was also obtained with the inclusion of TiO₂ nanoparticles. The polysulfide electrolyte has the potential to give good long-term stability for the CdSe QDSSCs as the QDs do not appear to undergo any serious deterioration.

Acknowledgment

The authors would like to thank University of Malaya for the IPPP Grant no. PV094-2012A. H. K. Jun thanks University of Malaya for a Fellowship Scheme scholarship award.

References

- [1] B. O'Regan and M. Grätzel, "A low-cost, high-efficiency solar cell based on dye-sensitized colloidal TiO₂ films," *Nature*, vol. 353, no. 6346, pp. 737–740, 1991.
- [2] M. Grätzel, "Dye-sensitized solar cells," *Journal of Photochemistry and Photobiology C*, vol. 4, no. 2, pp. 145–153, 2003.
- [3] R. Vogel, K. Pohl, and H. Weller, "Sensitization of highly porous, polycrystalline TiO₂ electrodes by quantum sized CdS," *Chemical Physics Letters*, vol. 174, no. 3-4, pp. 241–246, 1990.
- [4] R. Vogel, P. Hoyer, and H. Weller, "Quantum-sized PbS, CdS, Ag₂S, Sb₂S₃, and Bi₂S₃ particles as sensitizers for various nanoporous wide-bandgap semiconductors," *Journal of Physical Chemistry*, vol. 98, no. 12, pp. 3183–3188, 1994.
- [5] P. V. Kamat, "Quantum dot solar cells. Semiconductor nanocrystals as light harvesters," *Journal of Physical Chemistry C*, vol. 112, no. 48, pp. 18737–18753, 2008.
- [6] W. W. Yu, L. H. Qu, W. Z. Guo, and X. G. Peng, "Experimental determination of the extinction coefficient of CdTe, CdSe, and

- CdS Nanocrystals,” *Chemistry of Materials*, vol. 15, no. 14, pp. 2854–2860, 2003.
- [7] V. González-Pedro, X. Xu, I. Mora-Seró, and J. Bisquert, “Modeling high-efficiency quantum dot sensitized solar cells,” *ACS Nano*, vol. 4, no. 10, pp. 5783–5790, 2010.
- [8] G. Zhu, L. Pan, T. Xu, and Z. Sun, “CdS/CdSe-cosensitized TiO₂ photoanode for quantum-dot-sensitized solar cells by a microwave-assisted chemical bath deposition method,” *ACS Applied Materials and Interfaces*, vol. 3, no. 8, pp. 3146–3151, 2011.
- [9] A. J. Nozik, “Quantum dot solar cells,” *Physica E*, vol. 14, no. 1-2, pp. 115–120, 2002.
- [10] A. J. Nozik, M. C. Beard, J. M. Luther, M. Law, R. J. Ellingson, and J. C. Johnson, “Semiconductor quantum dots and quantum dot arrays and applications of multiple exciton generation to third-generation photovoltaic solar cells,” *Chemical Reviews*, vol. 110, no. 11, pp. 6873–6890, 2010.
- [11] Y. Chiba, A. Islam, Y. Watanabe, R. Komiya, N. Koide, and L. Han, “Dye-sensitized solar cells with conversion efficiency of 11.1%,” *Japanese Journal of Applied Physics*, vol. 45, no. 24–28, pp. L638–L640, 2006.
- [12] M. Samadpour, A. Irajizad, N. Taghavinia, and M. Molaei, “A new structure to increase the photostability of CdTe quantum dot sensitized solar cells,” *Journal of Physics D*, vol. 44, no. 4, Article ID 045103, 2011.
- [13] V. Jovanovski, V. Gonzalez-Pedro, S. Gimenez et al., “A sulfide/polysulfide-based ionic liquid electrolyte for quantum dot-sensitized solar cells,” *Journal of the American Chemical Society*, vol. 133, no. 50, pp. 20156–20159, 2011.
- [14] M. Shalom, S. Dor, S. Rühle, L. Grinis, and A. Zaban, “Core/CdS quantum dot/shell mesoporous solar cells with improved stability and efficiency using an amorphous TiO₂ coating,” *Journal of Physical Chemistry C*, vol. 113, no. 9, pp. 3895–3898, 2009.
- [15] G. Hodes, “Comparison of dye- and semiconductor-sensitized porous nanocrystalline liquid junction solar cells,” *Journal of Physical Chemistry C*, vol. 112, no. 46, pp. 17778–17787, 2008.
- [16] Y.-L. Lee, B.-M. Huang, and H.-T. Chien, “Highly efficient CdSe-sensitized TiO₂ photoelectrode for quantum-dot-sensitized solar cell applications,” *Chemistry of Materials*, vol. 20, no. 22, pp. 6903–6905, 2008.
- [17] S. Rühle, M. Shalom, and A. Zaban, “Quantum-dot-sensitized solar cells,” *Chemical Physics and Physical Chemistry*, vol. 11, no. 11, pp. 2290–2304, 2010.
- [18] Y.-L. Lee and C.-H. Chang, “Efficient polysulfide electrolyte for CdS quantum dot-sensitized solar cells,” *Journal of Power Sources*, vol. 185, no. 1, pp. 584–588, 2008.
- [19] L. J. Diguna, Q. Shen, J. Kobayashi, and T. Toyoda, “High efficiency of CdSe quantum-dot-sensitized TiO₂ inverse opal solar cells,” *Applied Physics Letters*, vol. 91, no. 2, Article ID 023116, 2007.
- [20] S. Giménez, I. Mora-Seró, L. Macor et al., “Improving the performance of colloidal quantum-dot-sensitized solar cells,” *Nanotechnology*, vol. 20, no. 29, Article ID 295204, pp. 4208–4214, 2009.
- [21] A. Salant, M. Shalom, I. Hod, A. Faust, A. Zaban, and U. Banin, “Quantum dot sensitized solar cells with improved efficiency prepared using electrophoretic deposition,” *ACS Nano*, vol. 4, no. 10, pp. 5962–5968, 2010.
- [22] Y. Tachibana, K. Umekita, Y. Otsuka, and S. Kuwabata, “Performance improvement of CdS quantum dots sensitized TiO₂ solar cells by introducing a dense TiO₂ blocking layer,” *Journal of Physics D*, vol. 41, no. 10, Article ID 102002, 2008.
- [23] H. Lee, M. Wang, P. Chen et al., “Efficient CdSe quantum dot-sensitized solar cells prepared by an improved successive ionic layer adsorption and reaction process,” *Nano Letters*, vol. 9, no. 12, pp. 4221–4227, 2009.
- [24] G. Vázquez, E. Alvarez, and J. M. Navaza, “Surface tension of alcohol + water from 20 to 50°C,” *Journal of Chemical and Engineering Data*, vol. 40, no. 3, pp. 611–614, 1995.
- [25] R. Costi, A. E. Saunders, E. Elmalem, A. Salant, and U. Banin, “Visible light-induced charge retention and photocatalysis with hybrid CdSe-Au nanodumbbells,” *Nano Letters*, vol. 8, no. 2, pp. 637–641, 2008.
- [26] I. Mora-Seró and J. Bisquert, “Breakthroughs in the development of semiconductor-sensitized solar cells,” *Journal of Physical Chemistry Letters*, vol. 1, no. 20, pp. 3046–3052, 2010.
- [27] B. R. Müller, S. Majoni, D. Meissner, and R. Memming, “Photocatalytic oxidation of ethanol on micrometer- and nanometer-sized semiconductor particles,” *Journal of Photochemistry and Photobiology A*, vol. 151, no. 1–3, pp. 253–265, 2002.
- [28] Z. Yang, C.-Y. Chen, P. Roy, and H.-T. Chang, “Quantum dot-sensitized solar cells incorporating nanomaterials,” *Chemical Communications*, vol. 47, no. 34, pp. 9561–9571, 2011.
- [29] S. Licht, “A description of energy conversion in photoelectrochemical solar cells,” *Nature*, vol. 330, no. 6144, pp. 148–151, 1987.
- [30] N. Ardoin and J. Winnick, “Polysulfide solution chemistry at a CdSe photoanode,” *Journal of the Electrochemical Society*, vol. 135, no. 7, pp. 1719–1722, 1988.
- [31] C.-Y. Chou, C.-P. Lee, R. Vittal, and K.-C. Ho, “Efficient quantum dot-sensitized solar cell with polystyrene-modified TiO₂ photoanode and with guanidine thiocyanate in its polysulfide electrolyte,” *Journal of Power Sources*, vol. 196, no. 15, pp. 6595–6602, 2011.
- [32] C. Zhang, Y. Huang, Z. Huo, S. Chen, and S. Dai, “Photoelectrochemical effects of guanidinium thiocyanate on dye-sensitized solar cell performance and stability,” *Journal of Physical Chemistry C*, vol. 113, no. 52, pp. 21779–21783, 2009.
- [33] S. K. Sarkar, N. Chandrasekharan, S. Gorer, and G. Hodes, “Reversible adsorption-enhanced quantum confinement in semiconductor quantum dots,” *Applied Physics Letters*, vol. 81, no. 26, pp. 5045–5047, 2002.
- [34] T. Zewdu, J. N. Clifford, J. P. Hernandez, and E. Palomares, “Photo-induced charge transfer dynamics in efficient TiO₂/CdS/CdSe sensitized solar cells,” *Energy and Environmental Science*, vol. 4, no. 11, pp. 4633–4638, 2011.
- [35] M. A. Hossain, J. R. Jennings, C. Shen et al., “CdSe-sensitized mesoscopic TiO₂ solar cells exhibiting >5% efficiency: redundancy of CdS buffer layer,” *Journal of Materials Chemistry*, vol. 22, no. 32, pp. 16235–16242, 2012.
- [36] H. J. Lee, J. Bang, J. Park, S. Kim, and S.-M. Park, “Multilayered semiconductor (CdS/CdSe/ZnS)-sensitized TiO₂ mesoporous solar cells: all prepared by successive ionic layer adsorption and reaction processes,” *Chemistry of Materials*, vol. 22, no. 19, pp. 5636–5643, 2010.
- [37] P. V. Kamat, “Boosting the efficiency of quantum dot sensitized solar cells through modulation of interfacial charge transfer,” *Accounts of Chemical Research*, vol. 45, no. 11, pp. 1906–1915, 2012.

Research Article

Applying a Cerebellar Model Articulation Controller Neural Network to a Photovoltaic Power Generation System Fault Diagnosis

Kuei-Hsiang Chao, Bo-Jyun Liao, and Chin-Pao Hung

Department of Electrical Engineering, National Chin-Yi University of Technology, No. 57, Section 2, Zhongshan Road, Taiping District, Taichung 41170, Taiwan

Correspondence should be addressed to Kuei-Hsiang Chao; chaokh@ncut.edu.tw

Received 4 November 2012; Revised 31 December 2012; Accepted 14 January 2013

Academic Editor: Daniel Chemisana

Copyright © 2013 Kuei-Hsiang Chao et al. This is an open access article distributed under the Creative Commons Attribution License, which permits unrestricted use, distribution, and reproduction in any medium, provided the original work is properly cited.

This study employed a cerebellar model articulation controller (CMAC) neural network to conduct fault diagnoses on photovoltaic power generation systems. We composed a module array using 9 series and 2 parallel connections of SHARP NT-R5E3E 175 W photovoltaic modules. In addition, we used data that were outputted under various fault conditions as the training samples for the CMAC and used this model to conduct the module array fault diagnosis after completing the training. The results of the training process and simulations indicate that the method proposed in this study requires fewer number of training times compared to other methods. In addition to significantly increasing the accuracy rate of the fault diagnosis, this model features a short training duration because the training process only tunes the weights of the exited memory addresses. Therefore, the fault diagnosis is rapid, and the detection tolerance of the diagnosis system is enhanced.

1. Introduction

Photovoltaic power generation system is one of the renewable energy sources, which produces less pollution. To enhance their power generation efficiency, the proposed system was installed in vast and boundless spaces without a shadow. However, when the system operation time increased, the power could be reduced because of module aging. In addition, prolonged outdoor use of the system can result in module faults from natural disasters. Faults in one of the modules in photovoltaic power generation systems significantly decrease the output power of the system [1–4]. Furthermore, photovoltaic power module faults are difficult to determine and detect by sight, and manual, individual inspection of the modules is time consuming.

Therefore, fault diagnosis techniques for photovoltaic systems not only increase maintenance efficiency and enhance system power generation reliability, but also effectively decrease operation costs. Currently, photovoltaic science applications and technology (PVSAT) projects for fault

diagnosis are being explored in Germany, The Netherlands, and Switzerland [5, 6]. These projects primarily focus on establishing a self-fault detection system for grid-connected systems to detect system errors and analyze their causes. However, the development of grid-connected photovoltaic systems relies on meteorological satellites to transmit atmospheric data, and the reference data are measured by ground weather stations as the atmospheric parameters for simulation analyses, further enhancing the overall recognition rate. Regarding the stand-alone systems, adopting this fault detection system is costly, resulting in limited application range and reduced practicality. In addition, experts have proposed employing high frequency reaction measurement [7] and time domain reflectometry (TDR) methods [8] to conduct fault diagnoses. By identifying the reflected feedback signal, the diagnosis method discriminates whether a fault has occurred in the reported area. However, this diagnosis technique relies on additional measurement equipments, such as a network analyzer. Furthermore, the techniques applied in both methods require detailed calculations of

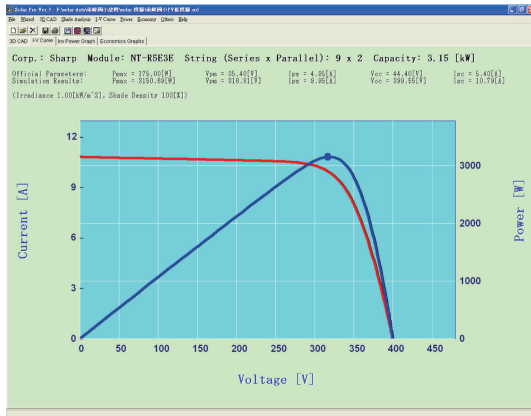


FIGURE 1: The P-V and I-V characteristic curves of a 3.15 kW photovoltaic power generation system simulated by Solar Pro under $1,000 \text{ W/m}^2$ irradiation and a module temperature of 25°C .

the conducting wire length within the photovoltaic power module. Therefore, system maintenance personnel must possess sufficient knowledge related to photovoltaic power generation systems. To apply fault diagnosis to large-scale versions of these systems, the accuracy of the wire length calculation must be ensured; otherwise, module fault areas can be misjudged. Therefore, applying this fault diagnosis technique does not significantly enhance system maintenance convenience. Chouder and Silvestre [9] used the fact that whether the calculated system power loss is a fixed value or a value occurring in a short period as a criterion to determine possible fault types. However, the cause of the fault and whether the fault point occurred on the side of the direct or alternating current cannot be accurately determined. Researchers have previously proposed a simple system performance model [10] to perform fault diagnoses for photovoltaic systems; however, this model was based on statistics of the power output of the power conditioner and categorized system faults into only three types: (1) ideal operating conditions, (2) normal operating conditions, and (3) actual operating conditions where possible faults and additional power loss may occur. Therefore, this simplified method does not significantly save maintenance labor. Vergura et al. [11] employed statistical methods to determine the number of power conditioner faults by referencing the power generation amount of the power conditioner's alternating current side. However, the most prevalent object in the photovoltaic power generation system with faults that cannot be determined visually is the photovoltaic module, rather than the power conditioner. Therefore, the effects of this method regarding the reduction of maintenance labor are limited.

Based on these mentioned facts, we used the CMAC to conduct fault diagnoses for the module arrays of photovoltaic power generation systems to increase the efficiency and accuracy of fault diagnosis and reduce system maintenance labor. In fault diagnoses, the CMAC application exhibits an excellent accuracy rate, high detection tolerance, and a multi-fault diagnosis function. The framework and diagnosis

steps of the CMAC-based fault diagnosis proposed in this study sampled data from existing photovoltaic systems as the information for conducting training. After the training was complete, the system was equipped with a suitable memory weight to conduct fault diagnoses on the test data.

2. Retrieval of Fault Data from the Photovoltaic Power Generation System

Solar Pro packaged software is a photovoltaic power system analysis simulation software developed by Laplace System Co., Ltd. [12]. Solar Pro can establish the module types, model numbers, and installation angles of photovoltaic power generation systems and can simulate the P-V and I-V curves of shaded or faulted photovoltaic power generation systems. Furthermore, this software can simulate system power generation situations ranging from one day, one month to one year. Figure 1 shows the P-V and I-V curves of a 3.15 kW photovoltaic power generation system simulated by Solar Pro under $1,000 \text{ W/m}^2$ sunlight irradiation and a module temperature of 25°C . Figure 1 shows that, in addition to indicating the maximum power point voltage, maximum power point current, and maximum power under a particular irradiation and module temperature, Solar Pro can indicate the open-circuit voltage (V_{oc}) and the short-circuit current (I_{sc}) of a system.

Figure 2 shows the I-V and P-V curves of the SHARP NT-R5E3E photovoltaic module datasheet under irradiation between 200 and $1,000 \text{ W/m}^2$ with a PV module surface temperature of 25°C . Figure 3 shows the simulated I-V and P-V curves of the SHARP NT-R5E3E photovoltaic power module using the Solar Pro photovoltaic power system analysis and simulation software under an irradiation between 200 and $1,000 \text{ W/m}^2$ and a PV module surface temperature at 25°C . By comparing Figures 2 and 3, we observed that the simulation results of Solar Pro are identical to those of the datasheet, confirming that the characteristic curve simulated by Solar Pro was identical to the performance curve of the actual module and the power generation data.

Figure 4 shows the P-V and I-V simulation curve of the 3.15 kW photovoltaic power generation system composed using NT-R5E3E photovoltaic power modules featuring 9 series and 2 parallel connections under 900 W/m^2 irradiation and a PV module surface temperature at 51.6°C . Figure 5 shows the simulated I-V and P-V curves of a series of photovoltaic power module arrays when two modules were shaded, and the irradiation and PV module surface temperature were identical to those shown in Figure 4. From the information shown in Figure 5, we observed that when the photovoltaic power modules were shaded, the I-V curve was not smooth, and multiple peaks occurred in the P-V curve. Figure 6 shows the measurement results obtained under 945 W/m^2 and a PV module surface temperature of 51.6°C , when two modules in a photovoltaic power module array were shaded. We observed that, when the photovoltaic power generation system was shaded, the actually measured I-V curve altered, and multiple peaks occurred in the P-V curve. Figures 5 and 6 show that the simulation and measurement results exhibited

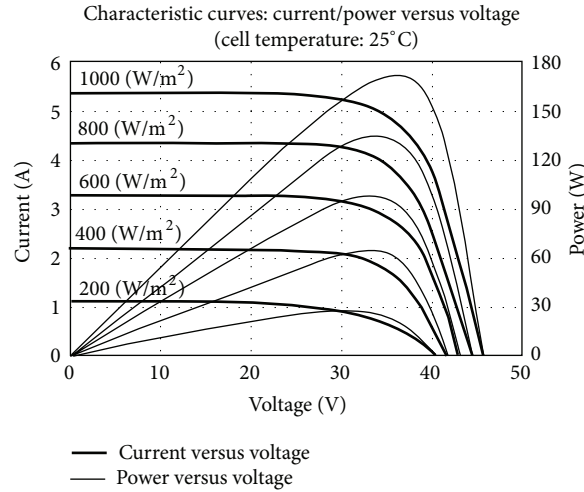


FIGURE 2: The I-V and P-V curves of the SHARP NT-R5E3E photovoltaic power module datasheet.

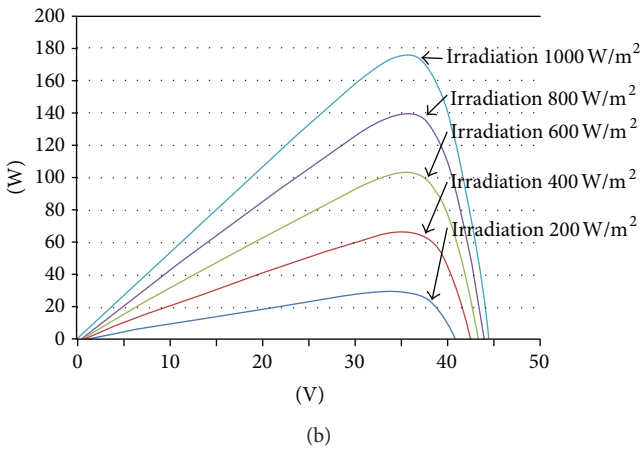
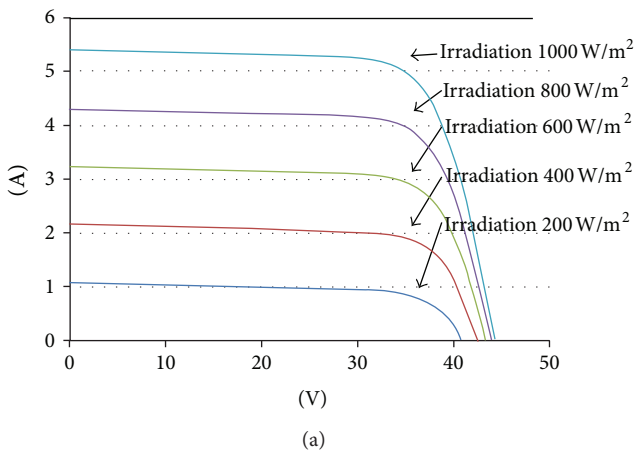


FIGURE 3: The simulated I-V and P-V curves of the SHARP NT-R5E3E photovoltaic power module using Solar Pro software with an irradiation between 200 and 1,000 W/m² and a PV module surface temperature less than 25°C; (a) I-V curve and (b) P-V curve.

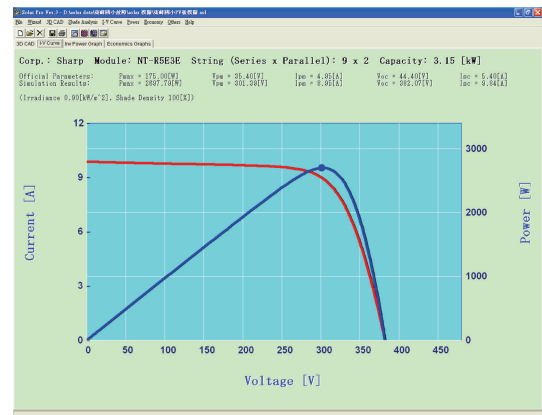


FIGURE 4: Simulated P-V and I-V curves under 900 W/m² irradiation and a PV module surface temperature of 51.6°C.

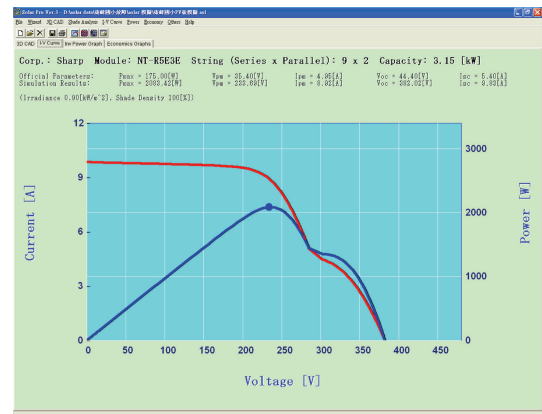


FIGURE 5: Simulated I-V and P-V curves of a photovoltaic power module array when two modules were shaded, the irradiation was 900 W/m², and the PV module surface temperature was at 51.6°C.

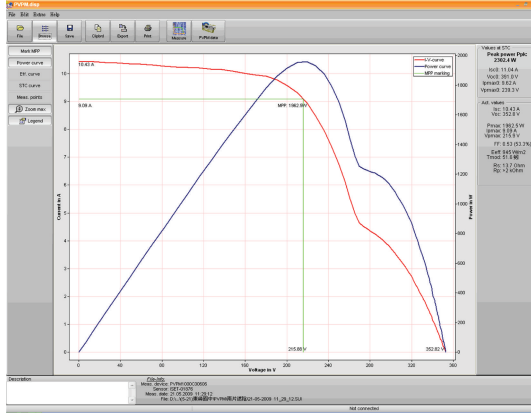
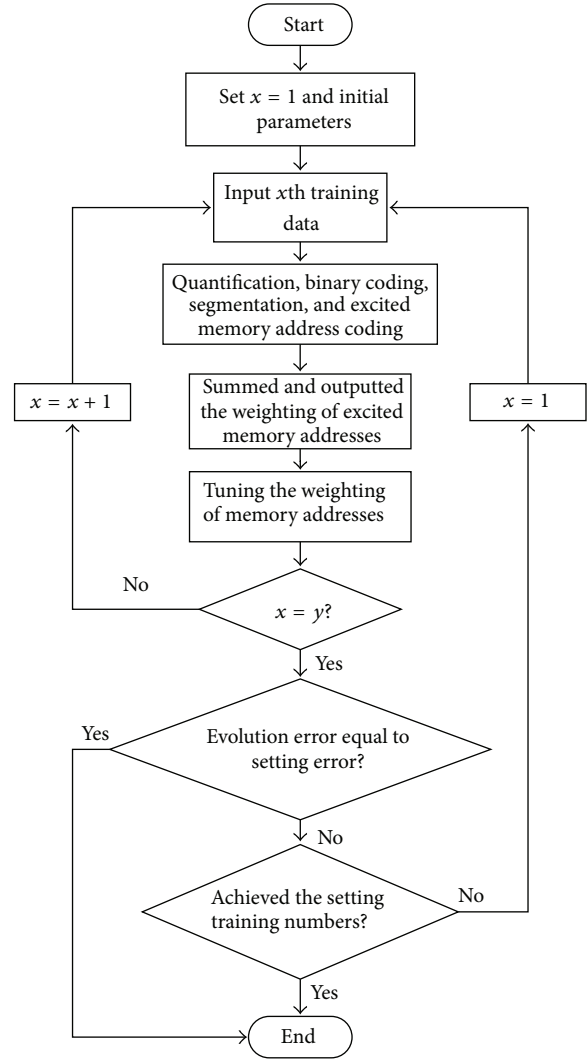


FIGURE 6: Measured P-V and I-V curves of a photovoltaic power module array when two modules were shaded, the irradiation was 945 W/m^2 , and the PV module surface temperature was at 51.6°C .

an excellent match, verifying that the I-V and P-V curves of a photovoltaic power generation system change, when a photovoltaic power module is shaded or faulted. In addition, the voltage, current, and power of the maximum power point can be altered. Therefore, we selected the voltage, current, and power of the maximum power point and open-circuit voltage as the characteristics for the fault diagnosis to examine the photovoltaic power generation system's fault conditions and types.

3. The Theory Regarding Cerebellar Model Articulation Controllers (CMACs)

The CMAC theory was proposed by Albus in the 1970s [13] to imitate the neurological structure of the human cerebellum for achieving rapid learning and reactions. The CMAC stimulates related memory based on the varying sizes and levels of received input signals. Therefore, memory that is stimulated by relative input signals is approximated. There is no multilayer memory algorithmic framework for articulating controller frameworks. Conversely, memory cells are directly used to store mapping relationships between the input and output signals. The CMAC possesses substantial memory capacity, but the memory stimulated by each input signal can only be a minimal unit. Therefore, not all of the memory is used. This characteristic is identical to the structure of the human cerebellum. Although the human cerebellum has a large memory capacity, it uses a minimal portion of the memory that regards specific input signals. During the CMAC mapping process, each memory address stores a weight. When a set of input signals is inputted, a set of memory addresses is excited through a combination of quantification, coding, and segmentation addresses. Thereafter, the output for this set of input signals can be mapped by summing the weights within a set of excited memory addresses. By comparing the obtained output value to an ideal output value and averagely distributing the output values based on the size of the error value into a set of segmentation memory addresses for tuning, the training process for the data set is completed. The CMAC, similar to other neural



x : numbers of training data till now
 y : total number of training data

FIGURE 7: Flowchart of the CMAC training process.

networks, is divided into a training stage and a diagnosis stage [14]. A detailed description of the learning and training stage is provided below. The flowchart of the CMAC training process is shown in Figure 7.

3.1. Quantification. To successfully perform coding on the inputted analog signal, the inputted signal should be quantified. The concept of quantification is similar to that of the function implemented by general analog-to-digital integrated circuits (IC). The implemented conversion is represented by

$$Q_x(x) = \text{ceil} \left(\frac{(x - x_{\min})}{[(x_{\max} - x_{\min})/Q_{\max}]} \right). \quad (1)$$

In (1), x represents the quantified input, Q_{\max} denotes the maximum quantization level, $\text{ceil}(\cdot)$ is the maximum integer

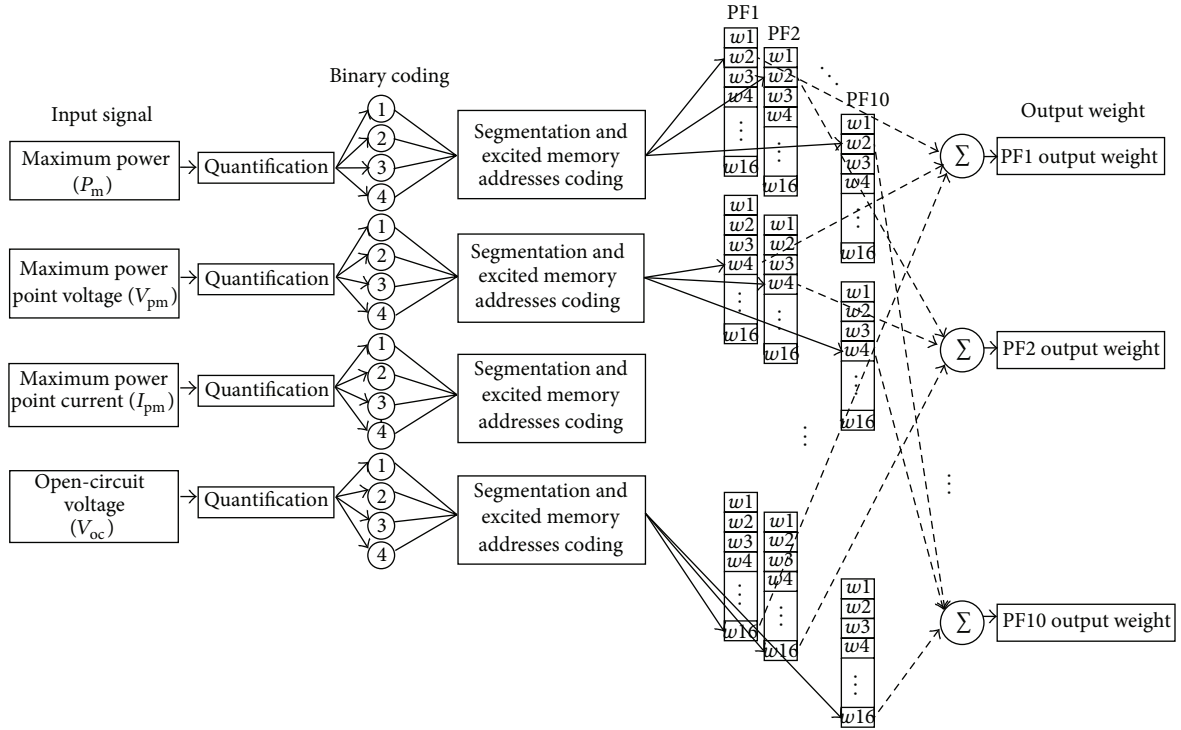


FIGURE 8: CMAC fault diagnosis framework.

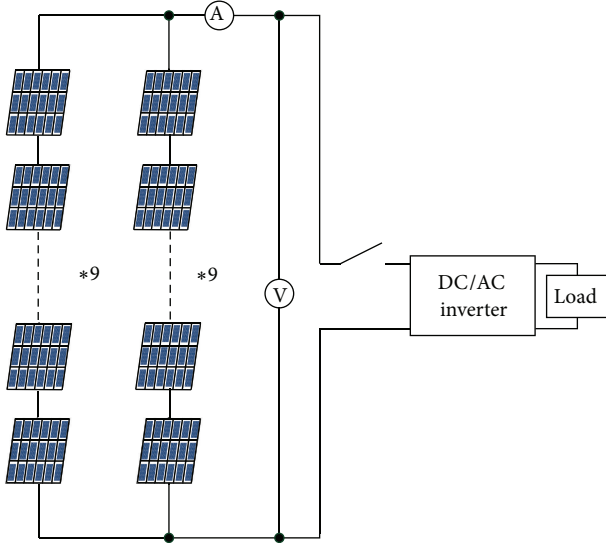


FIGURE 9: The photovoltaic power generation system featuring 9 series and 2 parallel connections.

instruction, and $[x_{\min}, x_{\max}]$ indicates the minimum and maximum values of the training sample. Numerous quantification levels are delineated by the equidistance between the maximum and minimum values of all of the input data. Quantification levels with a high resolution produce comparatively precise quantification codes, although they require additional memory spaces [15].

3.2. *Excited Address Coding.* Performing coding on the quantified values involves the hypotheses of, the following quantification: (1) a set of input signals exhibits quantification levels of 5, 10, 8, and 12; (2) the quantization levels are converted to a binary code of 0101_b, 1010_b, 1000_b, and 1100_b; and (3) a series of binary codes are combined for coding. Therefore, a 16-bit coding of 1100100010100101_b is acquired.

By grouping the obtained coding 3 bits per group, 6 groups are established. By sequentially coding the least significant bit to the most significant bit, 6 segmentation addresses are obtained: $a_1 = 101_b = 5$, $a_2 = 100_b = 4$, $a_3 = 010_b = 2$, $a_4 = 100_b = 4$, $a_5 = 100_b = 4$, and $a_6 = 001_b = 1$. Based on the correspondence of these decimal values to the relative memory addresses and from hypothesizing that the preliminary weight of all memory is 0, the summed memory weight of the first stimulation is 0.

3.3. *Weight Tuning.* Hypothesizing that the summed output weight value of a specific fault type is 1, showing that a specific datum is categorized as a fault type. Therefore, when the sum of the memory is not 1, weight tuning is required. The process of weight tuning is shown by [16, 17]

$$w_{\text{new}}^{a_i} = w_{\text{old}}^{a_i} + \beta \frac{Y_d - Y}{A^*}. \quad (2)$$

In (2), a_i represents the strobe memory address and β denotes the learning constant (with a value between 0 and 1). Assuming that all fault types only have one set of training samples, β can be directly established as 1. The β value of more than one sample of data is typically slightly less than 1. Y_d

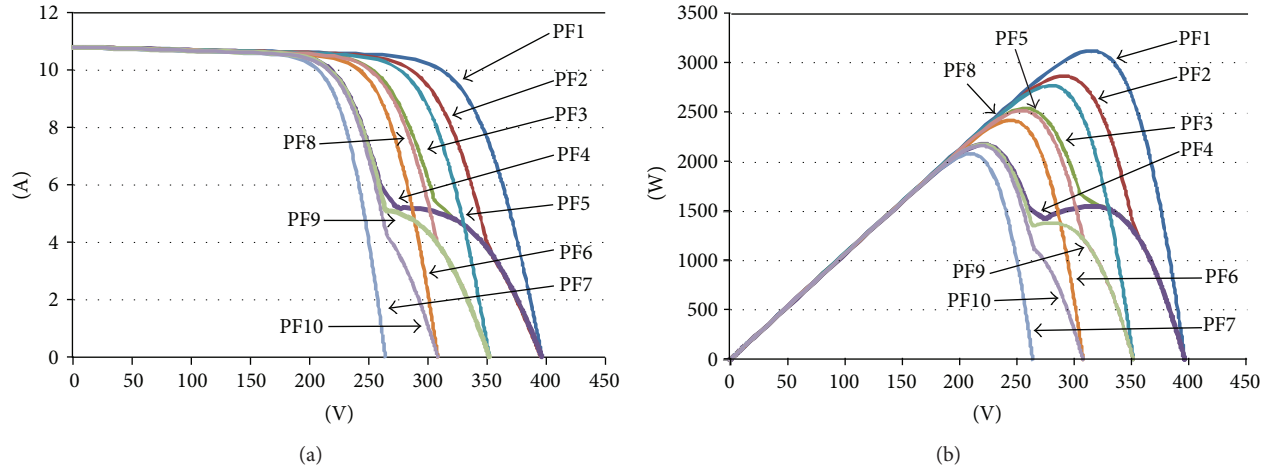


FIGURE 10: The simulation curves of the normal operations and various faults under a module temperature of 31°C and $1,000\text{ W/m}^2$ irradiation: (a) I-V characteristic curve and (b) P-V characteristic curve.

represents the target value (set as 1 in this study), Y indicates the actual output value, and A^* is the number of segmentation memory addresses. This formula evenly distributes weight values that require learning to separate memory addresses.

3.4. Detection Tolerance. The CMAC proposed in this study exhibited excellent anti-interference. For example, if a 16-bit original code (1100100010100101_b) coded in Section 3.2 is interfered and converted into ($110110001010-0101_b$), the excited addresses, that is, $(a_6, a_5, a_4, a_3, a_2, a_1)$, convert from $(1, 4, 4, 2, 4, 5)$ to $(1, 5, 4, 2, 4, 5)$. Except for a_5 , which exhibited an error, the other parts possessed normal outputs, thereby exhibiting tolerance. If expanded, the number of groups can be distributed and stored in additional addresses, resulting in a low error detection influential level on the adjacent bits, further enhancing accuracy.

4. Diagnosis Framework Establishment

To perform a fault diagnosis of the photovoltaic power generation system proposed in this study, the present irradiation and PV module temperature of the photovoltaic power generation system are required. Inputting this data, combined with the retrieved characteristic data of the photovoltaic power generation system (e.g., the maximum power, (P_m) , maximum power point voltage (V_{pm}) , maximum power point current (I_{pm}) , and open-circuit voltage (V_{oc}) during operation) into the CMAC, determines whether the photovoltaic power generation system is operating normally or is faulted. Figure 8 shows the framework of the CMAC fault diagnosis method proposed in this study. The input signals of this framework were the four detection signals mentioned. The CMAC fault diagnosis framework contained 10 weighted output values, representing the 10 fault types. Therefore, a total of 10 trained memory layers exist. The memory address number of each layer consisted of 2-bit groups. In this study, we used 4 bits per group for a total of four groups. Therefore, each layer had 64 memory addresses. Following

TABLE 1: Photovoltaic power generation system fault types.

Fault type	Fault condition
PF1	Operating normally.
PF2	Faults occurring in one module in one circuit branch.
PF3	Faults occurring in two modules in one circuit branch.
PF4	Faults occurring in three modules in one circuit branch.
PF5	Faults occurring in one module in both circuit branches.
PF6	Faults occurring in two modules in both circuit branches.
PF7	Faults occurring in three modules in both circuit branches.
PF8	Faults occurring in one module in one circuit branch, as well as in two modules in the other circuit branch.
PF9	Faults occurring in one module in one circuit branch, as well as in three modules in the other circuit branch.
PF10	Faults occurring in two modules in one circuit branch, as well as in three modules in the other circuit branch.

input value quantification, grouping, excited address coding, and summing all of the weight values of the excited addresses, a weighted output value was obtained. The diagnosed system used photovoltaic power modules featuring 9 series and 2 parallel connections. The connections are shown in Figure 9.

4.1. Fault Type. This study divided the faults of the photovoltaic power generation system into 10 types (under identical irradiation and PV module temperatures), as listed in Table 1. Figure 10 shows the I-V and P-V characteristic curves of the photovoltaic power generation system that were simulated based on the various fault types in Table 1 and under a PV module temperature of 31°C and $1,000\text{ W/m}^2$ irradiation.

TABLE 2: CMAC-related parameters.

Total types of input	4
Total types of output	10
Quantification levels	16
Number of bits per group	4
Number of clusters	4
Learning constant (β)	0.9
Number of training times	5

TABLE 3: The 21 intervals differentiated by temperature and irradiation.

Irradiation	Module temperature
301–400 W/m ²	31–40°C
	41–50°C
	51–60°C
401–500 W/m ²	31–40°C
	41–50°C
	51–60°C
501–600 W/m ²	31–40°C
	41–50°C
	51–60°C
601–700 W/m ²	31–40°C
	41–50°C
	51–60°C
701–800 W/m ²	31–40°C
	41–50°C
	51–60°C
801–900 W/m ²	31–40°C
	41–50°C
	51–60°C
901–1000 W/m ²	31–40°C
	41–50°C
	51–60°C

4.2. Diagnosis Process. The CMAC fault diagnosis process of the photovoltaic power generation system proposed in this study is given below.

Step 1. Conducting the initialization of the relevant parameters, as shown in Table 2 the maximum power P_m , maximum power point voltage V_{pm} , maximum power point current I_{pm} , and open-circuit voltage V_{oc} were used as input signals to conduct quantification procedure.

Step 2. Following quantification, the quantified values were converted into binary codes and combined. Thereafter, the combined codes were grouped. This study distributed 4 bits per group, and there were 4 groups.

Step 3. The grouped codes were used to search for corresponding memory addresses, and the weighted value within the memory was summed. This study used a 10-layer memory

space. Therefore, memory that had identical addresses in the 10 layers is excited, resulting in 10 outputs.

Step 4. The weight values of the 10 outputs are determined. The greater a weight value or the closer a weight value approximates to 1, the greater fault probability rate it exhibits.

5. Test Results

Irradiation and temperature can change over time. Therefore, the potential PV module temperatures and irradiation ranges within one day were divided into 21 types. Irradiations between 300 and 1,000 W/m² were divided every 100 W/m², and PV module surface temperature between 31 and 60°C was further separated every 10°C into three subintervals. These categorizations are listed in Table 3. We obtained 200 data sets for each interval as the training data for photovoltaic power generation system fault diagnosis. A total of 4,200 sets of training data were retrieved from 21 intervals. We used 20 data sets as the test data based on the data obtained from the categorizations in Table 3 (300–1000 W/m² irradiation and temperature intervals of 31–40, 41–50, and 51–60°C). Tables 4 and 6 contain detailed lists of the test data. The test data comprised the operating maximum power P_m , maximum power point voltage V_{pm} , maximum power point current I_{pm} , and open-circuit voltage V_{oc} of the photovoltaic power array module, which were acquired by inputting the parameters (i.e., irradiation, PV module temperature, and a number of selected fault modules) into Solar Pro for simulation. In addition, operating voltage, current, power, and open-circuit voltage are four critical characteristics in photovoltaic power generation system fault diagnosis. Tables 5 and 7 show the diagnosis results of the fault diagnosis method proposed in this study. The tables show observations of the fault types that can be accurately diagnosed using the method proposed in this study. In addition, the proposed fault diagnosis method does not only diagnose the main fault type of the PV system, but also can diagnose that the possibilities of other fault types have been revealed by the output weights. For example, in Table 5, the output weight index of PF4 is 1.0 in tested number 7, which means that the PV system has a 100% possibility on fault type PF4. And the tested number 7 has the lowest possibility for PF7, because its output weight index is 0.14 (or minimum). This information will be useful to find the hidden fault of the tested object for a maintenance engineer.

Furthermore, to verify the anti-interference ability of the proposed fault diagnosis framework, we altered the test samples, situating (1) a 5% maximum power reduction, (2) a 10% maximum power point voltage increase, (3) a 20% maximum power point current decrease, and (4) a 10% open-circuit voltage increase, and the data that contained additional errors are, respectively, listed in Tables 8 and 10. Based on the detection results in Tables 9 and 11, after adding the errors, the proposed fault diagnosis system still can correctly detect the fault types all of the data sets. Although the output weight values of various fault types for each test data have been changed in Tables 9 and 11 due to error interference, the most possibility occurrence on fault type is

TABLE 4: Test data under 300–1000 W/m² irradiation and PV module surface temperatures between 31 and 40°C.

Test no.	P_m (W)	V_{pm} (V)	I_{pm} (A)	V_{oc} (V)	Temperature (°C)	Irradiation (W/m ²)	Known fault type
1	869.43	310.84	2.8	372.56	31.5	300	PF1
2	1195.23	313.34	3.81	377.94	32.5	400	PF1
3	1399.53	289.25	4.84	381.82	33.5	500	PF2
4	1695.32	290.62	5.83	384.93	34.5	600	PF2
5	1758.35	255.11	6.89	387.41	35.5	700	PF3
6	2013.52	256.87	7.84	389.52	36.5	800	PF3
7	1949.64	219.32	8.89	391.26	37.5	900	PF4
8	2164.02	217.65	9.94	392.78	38.5	1000	PF4
9	761.64	268.98	2.83	326.78	39.5	300	PF5
10	1064.23	277.81	3.83	336.43	31.5	400	PF5
11	1183.78	244.95	4.83	297.45	32.5	500	PF6
12	1433.72	246.19	5.82	299.85	33.5	600	PF6
13	1441.41	209.59	6.88	258.68	34.5	700	PF7
14	1650.25	207.82	7.94	260.08	35.5	800	PF7
15	2251.15	251.19	8.96	348.29	36.5	900	PF8
16	2498.68	253.42	9.86	349.63	37.5	1000	PF8
17	602.75	211.32	2.85	327.28	38.5	300	PF9
18	826.64	212.81	3.88	332.09	39.5	400	PF9
19	1057.41	216.95	4.87	297.84	31.5	500	PF10
20	1281.44	218.22	5.87	300.23	32.5	600	PF10

TABLE 5: Diagnosis results of the test data under 300–1000 W/m² irradiation and PV module surface temperatures between 31 and 40°C.

Test no.	Output weight for various fault types										Known fault type	Diagnosed results
	PF1	PF2	PF3	PF4	PF5	PF6	PF7	PF8	PF9	PF10		
1	1	0.6	0.55	0.58	0.29	0.19	0.23	0.24	0.1	0.2	PF1	PF1
2	1	0.6	0.66	0.61	0.23	0.23	0.2	0.28	0.22	0.23	PF1	PF1
3	0.5	0.97	0.59	0.65	0.31	0.21	0.22	0.23	0.23	0.2	PF2	PF2
4	0.5	0.99	0.6	0.5	0.25	0.27	0.2	0.25	0.14	0.19	PF2	PF2
5	0.5	0.66	1	0.55	0.14	0.18	0.2	0.65	0.18	0.14	PF3	PF3
6	0.44	0.66	1	0.42	0.09	0	0.05	0.58	0.09	0.1	PF3	PF3
7	0.5	0.61	0.76	1	0.16	0.23	0.14	0.25	0.57	0.52	PF4	PF4
8	0.87	0.84	0.83	0.99	0.5	0.59	0.46	0.47	0.63	0.53	PF4	PF4
9	0.16	0.2	0.11	0.12	1	0.19	0.23	0.47	0.33	0.27	PF5	PF5
10	0.16	0.2	0.22	0.15	1	0.23	0.2	0.58	0.51	0.23	PF5	PF5
11	0.33	0.24	0.14	0.19	0.31	1	0.22	0.23	0.23	0.46	PF6	PF6
12	0.16	0.22	0.18	0.14	0.25	1	0.2	0.36	0.14	0.45	PF6	PF6
13	0.16	0.19	0.22	0.18	0.14	0.42	1	0.18	0.18	0.14	PF7	PF7
14	0.09	0.22	0.13	0.18	0.13	0.41	1	0.08	0.11	0.08	PF7	PF7
15	0.14	0.32	0.51	0.17	0.58	0.12	0.14	1	0.6	0.11	PF8	PF8
16	0.5	0.58	0.66	0.55	0.09	0.51	0.46	1	0.01	0.43	PF8	PF8
17	0	0	0.1	0.54	0.25	0	0.39	0.23	1	0.51	PF9	PF9
18	0.16	0.2	0.22	0.53	0.5	0.23	0.41	0.58	1	0.71	PF9	PF9
19	0.16	0.24	0.14	0.53	0.53	0.52	0.34	0.23	0.65	1	PF10	PF10
20	0.16	0.22	0.18	0.64	0.25	0.59	0.2	0.25	0.74	1	PF10	PF10

TABLE 6: Test data under 300–1000 W/m² irradiation and PV module surface temperatures between 51 and 60°C.

Test no.	P_m (W)	V_{pm} (V)	I_{pm} (A)	V_{oc} (V)	Temperature (°C)	Irradiation (W/m ²)	Known fault type
1	834.4	293.69	2.84	358.83	51.5	300	PF1
2	1146.19	297.99	3.85	364.3	52.5	400	PF1
3	1343.63	274.46	4.9	368.22	53.5	500	PF2
4	1627.07	275.99	5.9	371.31	54.5	600	PF2
5	1689.67	244.75	6.9	373.75	55.5	700	PF3
6	1934.57	243.17	7.96	375.79	56.5	800	PF3
7	1872.46	210.42	8.9	377.46	57.5	900	PF4
8	2077.41	208.71	9.95	378.86	58.5	1000	PF4
9	726.03	255.95	2.84	312.88	59.5	300	PF5
10	1021.06	263.33	3.88	324.53	51.5	400	PF5
11	1134.87	231.04	4.91	287.06	52.5	500	PF6
12	1374.59	232.48	5.91	289.46	53.5	600	PF6
13	1380.6	200.41	6.89	249.74	54.5	700	PF7
14	1580.05	198.79	7.95	251.09	55.5	800	PF7
15	2158.96	241.32	8.95	336.22	56.5	900	PF8
16	2393.71	239.48	10	337.47	57.5	1000	PF8
17	577.06	200.23	2.88	313.59	58.5	300	PF9
18	791.4	203.64	3.89	318.54	59.5	400	PF9
19	1017.84	208.04	4.89	287.63	51.5	500	PF10
20	1232.58	209.42	5.89	290.01	52.5	600	PF10

TABLE 7: Diagnosis results of the test data under 300–1000 W/m² irradiation and PV module surface temperatures between 51 and 60°C.

Test no.	Output weight for various fault types										Known fault type	Diagnosed results
	PF1	PF2	PF3	PF4	PF5	PF6	PF7	PF8	PF9	PF10		
1	1	0.66	0.62	0.67	0.34	0.28	0.23	0.26	0.2	0.28	PF1	PF1
2	1	0.64	0.65	0.66	0.34	0.37	0.2	0.32	0.22	0.26	PF1	PF1
3	0.5	1	0.67	0.66	0.24	0.24	0.32	0.22	0.25	0.22	PF2	PF2
4	0.5	1	0.6	0.6	0.28	0.26	0.22	0.24	0.22	0.27	PF2	PF2
5	0.61	0.66	0.99	0.66	0.25	0.28	0.23	0.71	0.28	0.22	PF3	PF3
6	0.5	0.89	1	0.66	0.19	0.14	0.14	0.68	0.15	0.08	PF3	PF3
7	0.5	0.63	0.62	1	0.22	0.35	0.15	0.44	0.66	0.64	PF4	PF4
8	0.41	0.58	0.57	1	0.17	0.55	0.31	0.37	0.66	0.68	PF4	PF4
9	0.16	0.22	0.19	0.1	1	0.28	0.23	0.44	0.44	0.28	PF5	PF5
10	0.16	0.32	0.23	0.19	0.98	0.37	0.2	0.52	0.4	0.26	PF5	PF5
11	0.33	0.24	0.19	0.22	0.24	1	0.32	0.43	0.25	0.58	PF6	PF6
12	0.15	0.22	0.18	0.17	0.28	1	0.22	0.35	0.22	0.59	PF6	PF6
13	0.12	0.19	0.19	0.22	0.25	0.56	1	0.28	0.28	0.22	PF7	PF7
14	0.12	0.22	0.12	0.22	0.19	0.37	1	0.19	0.15	0.08	PF7	PF7
15	0.12	0.28	0.52	0.11	0.6	0.18	0.15	1	0.48	0.15	PF8	PF8
16	0.02	0.26	0.55	0.19	0.84	0.4	0.12	1	0.53	0.15	PF8	PF8
17	0	0	0	0.52	0.2	0	0.18	0.17	1	0.56	PF9	PF9
18	0.16	0.2	0.23	0.52	0.61	0.37	0.2	0.55	1	0.81	PF9	PF9
19	0.16	0.42	0.19	0.55	0.38	0.59	0.32	0.22	0.7	1	PF10	PF10
20	0.15	0.22	0.18	0.57	0.28	0.54	0.22	0.24	0.72	1	PF10	PF10

TABLE 8: Test data with an additional error and under 300–1000 W/m² irradiation and PV module surface temperatures between 31 and 40°C.

Test no.	P_m (W)	V_{pm} (V)	I_{pm} (A)	V_{oc} (V)	Temperature (°C)	Irradiation (W/m ²)	Known fault type
1	825.96*	341.92*	2.8	372.56	31.5	300	PF1
2	1195.23	313.34	3.04*	415.73*	32.5	400	PF1
3	1399.53	289.25	3.87*	420*	33.5	500	PF2
4	1695.32	319.68*	5.83	423.42*	34.5	600	PF2
5	1670.43*	255.11	5.51*	387.41	35.5	700	PF3
6	2013.52	282.55*	6.27*	389.52	36.5	800	PF3
7	1949.64	219.32	7.11*	430.38*	37.5	900	PF4
8	2055.82*	217.65	7.95*	392.78	38.5	1000	PF4
9	761.64	295.88*	2.83	359.45*	39.5	300	PF5
10	1011.02*	305.59*	3.83	336.43	31.5	400	PF5
11	1124.59*	244.95	4.83	327.19*	32.5	500	PF6
12	1362.03*	270.81*	5.82	299.85	33.5	600	PF6
13	1441.41	209.59	5.5*	284.55*	34.5	700	PF7
14	1567.73*	228.6*	7.94	260.08	35.5	800	PF7
15	2251.15	276.31*	7.16*	348.29	36.5	900	PF8
16	2373.74*	253.42	9.86	384.59*	37.5	1000	PF8
17	602.75	232.45*	2.28*	327.28	38.5	300	PF9
18	785.31*	234.09*	3.88	332.09	39.5	400	PF9
19	1057.41	238.64*	4.87	327.62*	31.5	500	PF10
20	1281.44	218.22	4.69*	330.25*	32.5	600	PF10
Variance	-5%	+10%	-20%	+10%			

*Indicates the addition of variance in the test data.

TABLE 9: Diagnosis results of the test data with additional errors and under 300–1000 W/m² irradiation and PV module surface temperatures between 31 and 40°C.

Test no.	Output weight for various fault types										Known fault type	Diagnosed results
	PF1	PF2	PF3	PF4	PF5	PF6	PF7	PF8	PF9	PF10		
1	0.83	0.6	0.55	0.74	0.29	0.19	0.23	0.24	0.32	0.5	PF1	PF1
2	0.83	0.4	0.44	0.46	0	0	0	0	0	0	PF1	PF1
3	0.33	0.73	0.63	0.6	0	0	0	0	0.24	0.17	PF2	PF2
4	0.77	0.83	0.6	0.5	0.25	0.27	0.2	0.25	0.14	0.19	PF2	PF2
5	0.33	0.61	0.67	0.36	0.27	0.18	0	0.36	0	0	PF3	PF3
6	0.36	0.63	0.66	0.42	0.33	0	0.21	0.25	0	0	PF3	PF3
7	0.35	0.45	0.62	0.82	0	0.1	0.1	0.13	0.39	0.41	PF4	PF4
8	0.74	0.76	0.66	0.83	0.37	0.38	0.65	0.38	0.36	0.24	PF4	PF4
9	0.16	0.2	0.11	0.12	0.58	0.19	0.23	0.24	0.1	0.27	PF5	PF5
10	0.5	0.2	0.22	0.15	0.6	0.2	0.5	0.51	0.23	0.2	PF5	PF5
11	0.16	0.24	0.14	0.19	0.47	0.62	0.22	0.45	0.48	0.2	PF6	PF6
12	0.16	0.22	0.18	0.14	0.56	0.69	0.2	0.25	0.14	0.45	PF6	PF6
13	0	0	0	0	0.09	0.24	0.5	0	0	0	PF7	PF7
14	0.09	0.22	0.13	0.18	0.13	0.17	0.52	0.08	0.11	0.08	PF7	PF7
15	0	0.16	0.14	0	0.56	0	0.1	0.67	0.42	0	PF8	PF8
16	0.43	0.55	0.47	0.46	0.61	0.5	0.73	0.91	0.74	0.77	PF8	PF8
17	0	0	0	0.14	0.25	0	0.38	0.23	0.54	0.27	PF9	PF9
18	0.16	0.4	0.22	0.15	0.61	0.23	0.41	0.58	0.62	0.23	PF9	PF9
19	0.16	0.24	0.14	0.27	0.41	0.47	0.34	0.45	0.58	0.84	PF10	PF10
20	0	0	0	0.5	0.34	0	0	0.2	0.57	0.78	PF10	PF10

TABLE 10: Test data with additional errors under 300–1000 W/m² irradiation and PV module surface temperatures between 51 and 60°C.

Test no.	P_m (W)	V_{pm} (V)	I_{pm} (A)	V_{oc} (V)	Temperature (°C)	Irradiation (W/m ²)	Known fault type
1	792.68*	323.06*	2.84	358.83	51.5	300	PF1
2	1146.19	327.78*	3.08*	364.3	52.5	400	PF1
3	1276.44*	301.9*	4.9	368.22	53.5	500	PF2
4	1545.71*	275.99	5.9	408.44*	54.5	600	PF2
5	1689.67	269.22*	5.52*	373.75	55.5	700	PF3
6	1837.84*	243.17	7.96	413.36*	56.5	800	PF3
7	1872.46	231.46*	7.12*	377.46	57.5	900	PF4
8	1973.53*	229.58*	9.95	378.86	58.5	1000	PF4
9	726.03	255.95	2.27*	344.16*	59.5	300	PF5
10	1021.06	289.66*	3.88	356.98*	51.5	400	PF5
11	1078.12*	231.04	3.92*	287.06	52.5	500	PF6
12	1305.86*	255.72*	5.91	289.46	53.5	600	PF6
13	1380.6	200.41	5.51*	274.71*	54.5	700	PF7
14	1580.05	218.66*	6.36*	251.09	55.5	800	PF7
15	2051.01*	241.32	8.95	369.84*	56.5	900	PF8
16	2393.71	239.48	8*	371.21*	57.5	1000	PF8
17	577.06	220.25*	2.3*	313.59	58.5	300	PF9
18	751.83*	224*	3.89	318.54	59.5	400	PF9
19	1017.84	228.84*	3.91*	287.63	51.5	500	PF10
20	1232.58	209.42	4.71*	319.01*	52.5	600	PF10
Variance	-5%	+10%	-20%	+10%			

*Indicates the addition of variance in the test data.

TABLE 11: Diagnosis results of the test data with additional errors and under 300–1000 W/m² irradiation and PV module surface temperatures between 51 and 60°C.

Test no.	Output weight for various fault type										Known fault type	Diagnosed results
	PF1	PF2	PF3	PF4	PF5	PF6	PF7	PF8	PF9	PF10		
1	0.83	0.66	0.62	0.68	0.34	0.28	0.23	0.26	0.43	0.54	PF1	PF1
2	0.83	0.43	0.42	0.47	0	0	0	0	0	0	PF1	PF1
3	0.66	0.83	0.67	0.66	0.34	0.24	0.32	0.22	0.25	0.22	PF2	PF2
4	0.5	0.89	0.6	0.6	0.4	0.26	0.22	0.24	0.22	0.27	PF2	PF2
5	0.49	0.47	0.56	0.44	0.31	0	0.11	0.17	0	0	PF3	PF3
6	0.5	0.66	0.87	0.66	0.4	0.39	0.14	0.49	0.15	0.08	PF3	PF3
7	0.37	0.48	0.47	0.66	0	0.46	0	0.25	0.24	0.24	PF4	PF4
8	0.41	0.58	0.57	0.8	0.17	0.77	0.31	0.37	0.39	0.41	PF4	PF4
9	0	0	0	0	0.44	0	0.2	0	0	0	PF5	PF5
10	0.53	0.64	0.65	0.66	0.83	0.37	0.2	32	0.22	0.26	PF5	PF5
11	0	0	0.12	0.12	0	0.64	0	42	0.19	0.45	PF6	PF6
12	0.15	0.22	0.18	0.17	0.54	0.82	0.22	0.24	0.22	0.59	PF6	PF6
13	0	0	0	0	0	0.28	0.5	0	0	0	PF7	PF7
14	0	0	0	0	0	0.37	0.59	0	0	0	PF7	PF7
15	0.5	0.63	0.47	0.56	0.22	0.27	0.15	0.85	0.12	0.15	PF8	PF8
16	0.38	0.64	0.47	0.41	0.27	0.14	0.09	0.87	0	0.05	PF8	PF8
17	0	0	0	0.13	0.2	0.18	0.38	0.17	0.46	0.28	PF9	PF9
18	0.16	0.43	0.23	0.19	0.45	0.45	0.55	0.41	0.75	0.26	PF9	PF9
19	0	0.17	0.12	0.22	0.14	0.57	0	0.42	0.33	0.64	PF10	PF10
20	0	0	0	0.39	0.22	0	0.25	0.29	0.43	0.75	PF10	PF10

unaltered. Furthermore, the order of possibility occurrence on fault type for each test data is almost one and all as shown in Tables 5 and 7 (without error addition). Therefore, whether an error or error interference was added did not influence the proposed method's ability to correctly detect the fault types of the test data.

6. Conclusion

This study proposed a photovoltaic power generation system fault diagnosis method based on the CMAC. Following training, the CMAC diagnosis framework conducts fault diagnoses on the data of operating photovoltaic power module arrays. The CMAC can associate, summarize, and possesses the characteristic of similar input signals exciting similar memory. Therefore, it exhibits an excellent classification accuracy rate. Furthermore, the CMAC can automatically associate and output the most probable fault type based on the similarity of the test data and specific fault patterns. Despite the presence of additional noise interference in the test data, the diagnosis results verified the accuracy and robustness of the diagnosis framework. In addition, the reduced amount of used memory, increased learning speed, and enhanced tolerance further verifies the CMAC's superior performance.

Conflict of Interests

The authors of the paper declare that there is no conflict of interests with any of the commercial identities mentioned in the paper.

Acknowledgment

This work was supported by the National Science Council, Taiwan, under Grant NSC 101-2221-E-167-030.

References

- [1] H. Patel and V. Agarwal, "MATLAB-based modeling to study the effects of partial shading on PV array characteristics," *IEEE Transactions on Energy Conversion*, vol. 23, no. 1, pp. 302–310, 2008.
- [2] L. Gao, R. A. Dougal, S. Liu, and A. P. Iotova, "Parallel-connected solar PV system to address partial and rapidly fluctuating shadow conditions," *IEEE Transactions on Industrial Electronics*, vol. 56, no. 5, pp. 1548–1556, 2009.
- [3] H. Patel and V. Agarwal, "Maximum power point tracking scheme for PV systems operating under partially shaded conditions," *IEEE Transactions on Industrial Electronics*, vol. 55, no. 4, pp. 1689–1698, 2008.
- [4] K. H. Chao, C. T. Chen, M. H. Wang, and C. F. Wu, "A novel fault diagnosis method based-on modified neural networks for photovoltaic systems," in *Proceedings of the 1st International Conference on Advances in Swarm Intelligence*, pp. 531–539, June 2010.
- [5] J. Betcke, V. V. Dijk, C. Reise et al., "PVSAT: remote performance check for grid connected PV systems using satellite data, evaluation of one year field-testing," in *Proceedings of the 17th European Photovoltaic Solar Energy Conference*, October 2001.
- [6] E. Lorenz, J. Betcke, A. Drews et al., "PVSAT-2: intelligent performance check of PV system operation based on satellite data," in *Proceedings of the 19th European Photovoltaic Solar Energy Conference*, June 2004.
- [7] L. Schirone, F. P. Califano, U. Moschella, and U. Rocca, "Fault finding in a 1 MW photovoltaic plant by reflectometry," in *Proceedings of the 1st World conference on Photovoltaic Energy Conversion*, vol. 1, pp. 846–849, December 1994.
- [8] T. Takashima, K. Otani, K. Sakuta et al., "Electrical detection and specification of failed modules in PV array," in *Proceedings of the 3rd World Conference on Photovoltaic Energy Conversion*, pp. 2276–2279, May 2003.
- [9] A. Chouder and S. Silvestre, "Automatic supervision and fault detection of PV systems based on power losses analysis," *Energy Conversion and Management*, vol. 51, no. 10, pp. 1929–1937, 2010.
- [10] S. K. Firth, K. J. Lomas, and S. J. Rees, "A simple model of PV system performance and its use in fault detection," *Solar Energy*, vol. 84, no. 4, pp. 624–635, 2010.
- [11] S. Vergura, G. Acciani, V. Amoroso, G. E. Patrono, and F. Vacca, "Descriptive and inferential statistics for supervising and monitoring the operation of PV plants," *IEEE Transactions on Industrial Electronics*, vol. 56, no. 11, pp. 4456–4464, 2009.
- [12] Solar Pro Brochure, http://www.lapsys.co.jp/english/e-products/e_pamphlet/sp_e.pdf.
- [13] J. S. Albus, "A new approach to manipulator control: the cerebellar model articulation controller," *Journal of Dynamic Systems, Measurement and Control, Transactions of the ASME*, vol. 97, no. 3, pp. 220–227, 1975.
- [14] C. P. Hung, W. G. Liu, and H. Z. Su, "Fault diagnosis of steam turbine-generator sets using CMAC neural network approach and portable diagnosis apparatus implementation," *Lecture Notes in Computer Science*, vol. 5754, pp. 724–734, 2009.
- [15] C. P. Hung and K. H. Chao, "CMAC neural network application on lead-acid batteries residual capacity estimation," *Lecture Notes in Computer Science*, vol. 4682, pp. 961–970, 2007.
- [16] C. P. Hung, H. J. Su, and S. L. Yang, "Melancholia diagnosis based on GDS evaluation and meridian energy measurement using CMAC neural network approach," *WSEAS Transactions on Information Science and Applications*, vol. 6, no. 3, pp. 500–509, 2009.
- [17] C. P. Hung and M. H. Wang, "Diagnosis of incipient faults in power transformers using CMAC neural network approach," *Electric Power Systems Research*, vol. 71, no. 3, pp. 235–244, 2004.

Research Article

The Evaluation of Solar Contribution in Solar Aided Coal-Fired Power Plant

Rongrong Zhai, Yongping Yang, Yong Zhu, and Denggao Chen

School of Energy Power and Mechanical Engineering, North China Electric Power University, Beijing 102206, China

Correspondence should be addressed to Rongrong Zhai; zhairongrong@gmail.com

Received 17 October 2012; Revised 11 January 2013; Accepted 29 January 2013

Academic Editor: Kalvala Srinivas Reddy

Copyright © 2013 Rongrong Zhai et al. This is an open access article distributed under the Creative Commons Attribution License, which permits unrestricted use, distribution, and reproduction in any medium, provided the original work is properly cited.

Solar aided coal-fired power plants utilize various types of solar thermal energy for coupling coal-fired power plants by using the characteristics of various thermal needs of the plants. In this way, the costly thermal storage system and power generating system will be unnecessary while the intermittent and unsteady way of power generation will be avoided. Moreover, the large-scale utilization of solar thermal power and the energy-saving aim of power plants will be realized. The contribution evaluating system of solar thermal power needs to be explored. This paper deals with the evaluation method of solar contribution based on the second law of thermodynamics and the principle of thermoeconomics with a case of 600 MW solar aided coal-fired power plant. In this study, the feasibility of the method has been carried out. The contribution of this paper is not only to determine the proportion of solar energy in overall electric power, but also to assign the individual cost components involving solar energy. Therefore, this study will supply the theoretical reference for the future research of evaluation methods and new energy resource subsidy.

1. Introduction

Since the energy crisis in the 1970s, the major developed countries of the world started a series of projects involving solar thermal power generation for energy substitution. Among the developments in this field, the research of America, Israel, Spain, Germany, and Italy began first and are consequently the most mature [1]. Solar energy as a form of clean energy has broad application prospects. Moreover, coupling with coal-fired power plants as a type of solar power utilization has been presented and investigated by many researchers.

Pai proposed the integration of a solar concentrator field to a 210 MWe coal-fired power plant [2]. Gupta and Kaushik found that using solar energy as a substitute for feed water heaters is more advantageous than using solar energy alone for power generation [3]. From a theoretical perspective, the solar aided coal-fired power generation system has many advantages when compared with a photovoltaic power generation system. However, the popular utilization

of this technology has been relatively slow. The reasons for this apathetic uptake have been concluded as follows: (a) variations of solar radiation can cause operation difficulties and (b) no reasonable evaluating systems have been built for the contribution of solar energy in the integrated system. The study about solar aided coal-fired power generation system mostly concentrates on performance analyses, integration modes, operations optimization, and so on. Since Gaggioli and El-Sayed comprehensively concluded the history of second law costing method, thermoeconomic analysis has become a powerful scheme applied extensively in design, operation, and reform of energy systems [4, 5]. Though thermoeconomic methods are multitudinous, the objectives of most existing analysis techniques still can be included in the determination of (a) the appropriate allocation of economic resources to optimize the design and operation of a system and (b) the economic feasibility and profitability of a system [6]. The methods can be roughly divided into two classes: algebraic methods and calculus methods [4, 5]. The thermoeconomic analysis of solar aided coal-fired power

generation system has already begun. Suresh and Reddy dealt with the 4-E (namely, energy, exergy, environment, and economic) analysis of solar aided coal-fired power plants with a subcritical and a supercritical power plant as references [7]; Baghernejad and Yaghoubi presented a new thermoeconomic method applying a genetic algorithm for optimization of an integrated solar combined cycle system [8].

The previous research as mentioned above has investigated the integration of a solar concentrator field with a power plant. However the integrated system introduces solar energy into the individual components in the traditional power plants, the researches about how to evaluate the contribution of solar energy in the system are hardly found.

A thermoeconomic method of evaluating solar contribution in the integrated system is firstly proposed in this paper. A new built 600 MW solar aided coal-fired power generation unit is considered as a reference power plant. According to the design parameters, the contribution proportion has been achieved, and the generation cost has also been explored by using sensitivity analysis method.

2. System Descriptions and the Proposed Problem

Figure 1 shows the diagram of the solar aided coal-fired power plant. In the solar field, several parabolic trough collectors are connected and the heating material is heat transfer oil. The oil-heat exchanger is a tube-shell heat exchanger. The parabolic trough collectors and the oil-heat exchanger together are called solar driven oil-water heat exchanger in this paper.

In a typical reheated steam coal-fired power plant, the combustion of coal takes place in the boiler. The unsaturated boiler feedwater from the condenser enters the boiler after going through four low-pressure reheaters (HTR1, HTR2, HTR3, and HTR4), three high-pressure reheaters (HTR5, HTR6, and HTR7), and a deaerator (Deaerator). The outlet superheated steam from the boiler is transported to the high-pressure cylinder to produce power, then, after being reheated in the boiler, drives the intermediate and lower pressure cylinders. Finally, the exhaust is condensed in the condenser. It can be seen from Figure 1 that the extractions from different positions of the cylinders ((1)–(8)) are used to heat the feedwater via feedwater reheaters. The 600 MW solar aided coal-fired power plant is similar to the reheated steam cycle system. The difference lies in that a solar aided oil-water heat exchanger has been added. When the solar radiation is strong (e.g., in the day), the steam extraction (1) is cut off and HTR7 will not be in operation; the feedwater will be heated in the oil-heat exchanger. Conversely, when the solar radiation is weak (e.g., in the night), the oil-heat exchanger will not be in operation and the plant will operate in the same manner as the base plant. In the solar field (as shown in the dash block in Figure 1), several parabolic collectors are connected using heat transfer oil as the heating medium in a tube-shell heat exchanger. The parabolic collectors and the oil-heat exchanger together are called solar driven oil-water heat exchanger (SDOHE) in this paper.

It can be seen from Figure 1 that the solar contribution concentrates on providing heat to the feedwater. After heating, the feedwater flows into the boiler, then, after a series of processes, the thermal energy is finally translated into electrical power.

The principle behind the solar aided coal-fired power generation system is to supply thermal energy by substituting high pressure feedwater heaters with oil-water heat exchangers. During a series of circulation, the energy contributes to the system power output indirectly. Therefore, it is meaningful to discuss how to evaluate the solar energy contribution in the solar aided coal-fired power plant.

3. Evaluation Model of Solar Energy Contribution

According to the first and second laws of thermodynamics, evaluation models based on energy balance and exergy balance are the possible methods for evaluating energy contribution such as solar energy and fuel. The method based on energy balance just considers the magnitude of energy without taking energy grade into account. The evaluation based on exergy balance has added energy grade to the system, while the nonequivalence of the same value of exergy at different points in the system has never been considered. Therefore, the evaluation based on the index of technical economics and energy equivalence has been explored in this study. The approach proposed in this paper is called the thermoeconomic cost method, considering both the energy grade and the nonequivalence.

The thermoeconomic cost method includes three steps as shown in Figure 2. Firstly, the contribution proportions of solar energy and coal in every exergy flow needs to be confirmed. Secondly, according to the thermoeconomic concept, the values of each cost flow can be achieved. Thirdly, the contribution of solar economic cost will be calculated with the above data.

3.1. Confirming the Ratio of Solar Energy against Coal according to Each Exergy Flow. This part is shown in Figure 2, Box 1. For the convenience of the analysis, Figure 1 has been simplified as shown in Figure 3. The system includes six subsystems: (1) oil-water heat exchanging driven by solar energy; (2) boiler preheating, steam generating, and superheating; (3) high-pressure cylinder of turbine; (4) boiler reheating; (5) intermediate- and low-pressure cylinder of turbine; and (6) heat exchanging. The main parameters of the system such as the temperature, enthalpy, and flow rate are listed in Figure 3.

The exergy balance equation of each subsystem is as follows.

(1) The exergy loss of oil-water heat exchanging is given by $E_9 + E_6 - E_1$.

The proportion of solar exergy loss assumed to be δ_1 . Then the loss will be, $\delta_1(E_9 + E_6 - E_1)$, and the exergy loss of feedwater will be, $(1 - \delta_1)(E_9 + E_6 - E_1)$.

The exergy achieved by water will be written as follows: $E_1 - E_6 + (1 - \delta_1)(E_9 + E_6 - E_1)$.

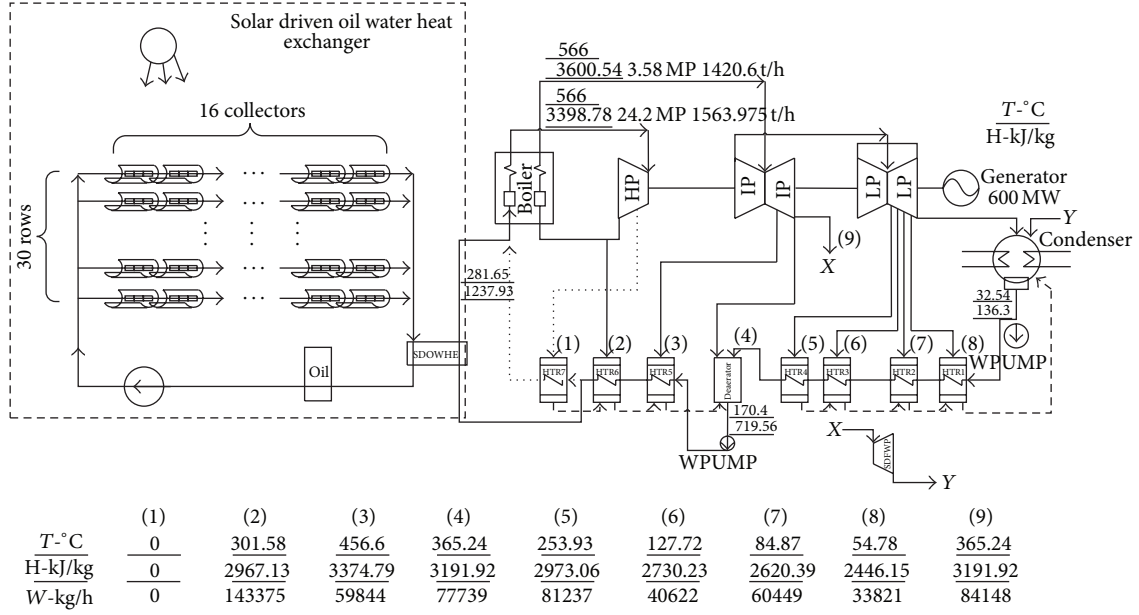


FIGURE 1: Layout of the solar aided coal-fired power plant.

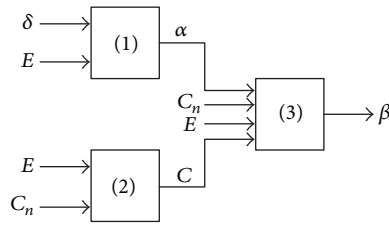


FIGURE 2: Schematic representation of the calculating process of the thermoeconomic cost evaluation.

It equals the exergy released by solar energy, which may be written as follows: $E_9 - \delta_1(E_9 + E_6 - E_1)$.

The proportion of solar energy at point 1 may become as follows:

$$\alpha_1 = (\alpha_6 [-(1 - \delta_1)E_9 + \delta_1 E_6 + (1 - \delta_1)E_1] + (1 - \delta_1)E_9 - \delta_1 E_6 + \delta_1 E_1)(E_1)^{-1}. \quad (1)$$

(2) The total exergy loss of preheater, steam generator and superheater is given by $E_{10} + E_1 - E_2$.

The proportion of coal exergy loss assumed to be δ_2 .

Then the exergy loss of water will be, $(1 - \delta_2)(E_{10} + E_1 - E_2)$, and the exergy achieved by water will be written as follows: $E_2 - E_1 + (1 - \delta_2)(E_{10} + E_1 - E_2)$.

It equals the exergy released by coal, which may be written as follows: $E_{10} - \delta_2(E_{10} + E_1 - E_2)$.

The proportion of solar energy at point 2 may become as follows:

$$\alpha_2 = \frac{\alpha_1 [-(1 - \delta_2)E_{10} + \delta_2 E_1 + (1 - \delta_2)E_2]}{E_2}. \quad (2)$$

(3) The proportions of solar energy at the import and export of turbine are equal.

For the third subsystem, the equation will be given by

$$\alpha_3 = \alpha_2 = \alpha_7. \quad (3)$$

For the fifth subsystem, the equation will be given by

$$\alpha_5 = \alpha_4 = \alpha_8. \quad (4)$$

(4) The total exergy loss of reheater is given by $E_{11} + E_3 - E_4$.

The proportion of coal exergy loss assumed to be δ_3 .

Then the exergy loss of coal will be $\delta_3(E_{11} + E_3 - E_4)$, and the exergy loss of water will be $(1 - \delta_3)(E_{11} + E_3 - E_4)$.

The exergy achieved by water will be written as follows: $E_4 - E_8 + (1 - \delta_3)(E_{11} + E_3 - E_4)$.

It equals the exergy released by coal, which may be written as follows: $E_{11} - \delta_3(E_{11} + E_3 - E_4)$.

The proportion of solar energy may become as follows:

$$\alpha_4 = \frac{\alpha_3 [-(1 - \delta_3)E_{11} + \delta_3 E_3 + (1 - \delta_3)E_4]}{E_4}. \quad (5)$$

(5) The total exergy loss is given by $E_5 + E_7 + E_8 - E_6$.

The proportions of exergy loss at point 7 and 8 are assumed to be δ_4 and δ_5 .

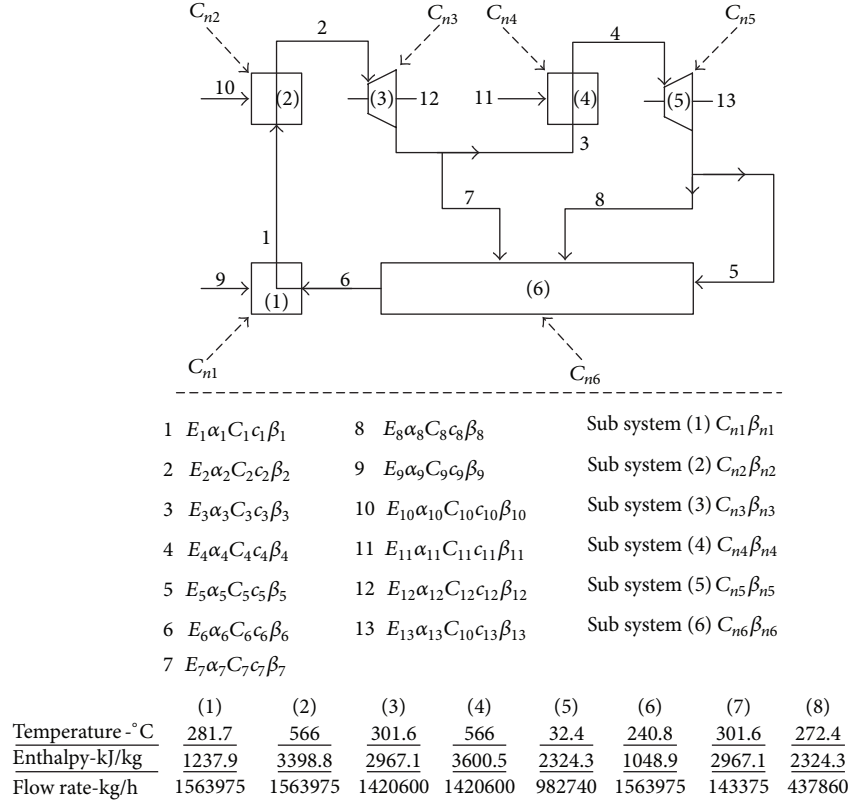


FIGURE 3: Schematic representation of solar aided coal-fired power generation system.

Then, the exergy loss at point 7 will be $\delta_4(E_5 + E_7 + E_8 - E_6)$.

The exergy loss at point 8 will be $\delta_5(E_5 + E_7 + E_8 - E_6)$, and the exergy loss at point 5 will be $(1 - \delta_4 - \delta_5)(E_5 + E_7 + E_8 - E_6)$.

The equation will be written as follows:

$$\begin{aligned} \alpha_6 = & (\alpha_7 [E_7 - \delta_4 (E_5 + E_7 + E_8 - E_6)] \\ & + \alpha_8 [E_8 - \delta_5 (E_5 + E_7 + E_8 - E_6)] \\ & + \alpha_5 [E_5 - (1 - \delta_4 - \delta_5) \\ & \times (E_5 + E_7 + E_8 - E_6)]) (E_6)^{-1}. \end{aligned} \quad (6)$$

The proportion of solar energy will be ensured by using (1)–(6).

3.2. The Exergy Follow Cost C Will Be Ensured by Thermoeconomic Analysis. This part is shown in Figure 2, Box 2. According to Figure 3, the system includes 6 subsystems and 13 exergy flows. The equation satisfied by each subsystem is given by:

$$C_{in} + C_n = C_{out}, \quad (7)$$

where C_{in} and C_n are, respectively, the energy cost of import and the cost of others, and C_{out} is the energy cost of export.

Then, for the first subsystem, the equation is given by the following:

$$C_6 + C_9 + C_{n1} = C_1. \quad (8)$$

For the second subsystem, the equation is given by the following:

$$C_1 + C_{10} + C_{n2} = C_2. \quad (9)$$

For the third subsystem, the equation is given by the following:

$$C_2 + C_{n3} = C_3 + C_7 + C_{12}. \quad (10)$$

For the fourth subsystem, the equation is given by the following:

$$C_3 + C_{11} + C_{n4} = C_4. \quad (11)$$

For the fifth subsystem, the equation is given by the following:

$$C_4 + C_{n5} = C_5 + C_8 + C_{13}. \quad (12)$$

For the sixth subsystem, the equation is given by the following:

$$C_5 + C_7 + C_8 + C_{n6} = C_6. \quad (13)$$

The cost of solar exergy flow E_9 is given data, and then we will get the equation as follows:

$$\frac{C_9}{E_9} = c_9. \quad (14)$$

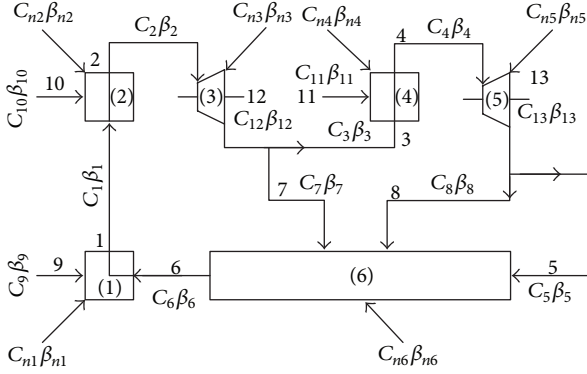


FIGURE 4: The schematic of cost flows.

The costs of coal exergy flows E_{10} and E_{11} are given data, and then the equation will be as follows:

$$\frac{C_{10}}{E_{10}} = \frac{C_{11}}{E_{11}} = c_{10} = c_{11}. \quad (15)$$

The costs of E_2 , E_3 , and E_7 have been given, and then the equation may be as follows:

$$\frac{C_2}{E_2} = \frac{C_3}{E_3} = \frac{C_7}{E_7}. \quad (16)$$

The costs of E_4 , E_5 , and E_8 have been given, and then the equation will be as follows:

$$\frac{C_4}{E_4} = \frac{C_5}{E_5} = \frac{C_8}{E_8}. \quad (17)$$

According to (8)–(17), the cost of each exergy flow will be ensured.

3.3. According to the Thermoeconomic Analysis of the Solar Part, the Cost Proportions of Solar Energy in Each Exergy Flow Will Be Ensured. This part is shown in Figure 2, Box 3. For the convenience of analysis, Figure 3 has been simplified as shown in Figure 4. The system still includes six subsystems.

According to the data above, the solar energy parts in each exergy flow have just been considered alone, and the cost proportions of solar energy will be explored.

Equations of each subsystem have been given as follows.

(1) The cost equation of oil-water heat exchanging is given by the following:

$$C_6\beta_6 + C_9\beta_9 + C_{m1}\beta_{m1} = C_1\beta_1. \quad (18)$$

(2) The cost equation of preheating, steam generating, and superheating is given by the following:

$$C_1\beta_1 + C_{10}\beta_{10} + C_{n2}\beta_{n2} = C_2\beta_2. \quad (19)$$

(3) The cost equation of turbine is given by the following:

$$C_2\beta_2 + C_{n3}\beta_{n3} = C_3\beta_3 + C_7\beta_7 + C_{12}\beta_{12}. \quad (20)$$

TABLE 1: Main designed parameters of coal-fired power plant.

Parameters	Values	Units
Capacity	600	MW
Parameters of main steam	24.2/566/566	MPa/°C/°C
Feedwater mass flow rate	1645.15	t/h
Condenser pressure	4.9	kPa
Feedwater temperature	272.3	°C
Coal consumption rate	257.4	g/kWh

(4) The cost equation of reheating is given by the following:

$$C_3\beta_3 + C_{11}\beta_{11} + C_{n4}\beta_{n4} = C_4\beta_4. \quad (21)$$

(5) The cost equation of turbine is given by the following:

$$C_4\beta_4 + C_{n5}\beta_{n5} = C_5\beta_5 + C_8\beta_8 + C_{13}\beta_{13}. \quad (22)$$

(6) The cost equation of heat exchanging is given by the following:

$$C_5\beta_5 + C_7\beta_7 + C_8\beta_8 + C_{n6}\beta_{n6} = C_6\beta_6. \quad (23)$$

Since the cost of solar energy achieving is free, we assume $C_9 = 0$ and $\beta_9 = 0$.

For the second and third subsystems, the import exergy flows of 10 and 11 will be 0, which means the solar parts in 10 and 11 will be 0:

$$\beta_{10} = \beta_{11} = 0. \quad (24)$$

Since the costs of E_2 , E_3 , and E_7 are equal, (25) can be obtained as follows:

$$\beta_2 = \beta_3 = \beta_7. \quad (25)$$

Since the flow rates of E_4 , E_5 , and E_8 are equal, (26) can be obtained as follows:

$$\beta_4 = \beta_5 = \beta_8. \quad (26)$$

The cost proportions of solar energy β will be ensured by using (18)–(26).

4. Case Study

4.1. Main Parameters. A coal-fired power plant of 600 MW in China has been chosen as the base plant, with the main designed parameters shown in Table 1. Coal is the supply fuel of the power plant, with the following components: moisture = 9.9%, ash = 23.7%, hydrogen = 3.11%, nitrogen = 1.01%, sulphur = 2%, oxygen = 2.78%, carbon = 57.5%, and LHV = 21981 kJ/kg.

The solar aided coal-fired power plant is using the same coal as the base case, except for the solar driven oil-water heat exchanger and the steam cut-off, other structures are the same as the base case. The data of solar field is based on real data from the GEGS-VI station in USA [9–11]. Some modifications have been made to make it suitable for the case in this

TABLE 2: Main parameters of the collector field.

Parameters	Values	Units
Solar irradiation	925	W/m ²
Area of per collector	235	m ²
Number of collector in each row	16	
Rows of collectors	30	Rows
Inlet temperature of heat transfer oil	250	°C
Outlet temperature of heat transfer oil	328	°C

TABLE 3: Main designed parameters of solar aided power plant.

Parameters	Values	Units
Capacity	600	MW
Feedwater temperature	281.65	°C
Coal consumption rate	243.7	g/kWh
Thermal efficiency	50.41	%
Exergy efficiency	48.07	%
Area of all collectors	112800	m ²

paper. The collectors are LS-2 parabolic trough collectors from LUZ Company [9], and the diagram and main parameters of the collectors are shown in Table 2. The collector field is composed of 30 rows of 16 solar collectors which are parallelly installed. The heated heat transfer oil flows into the oil-water heat exchanger and the cooled heat transfer oil will be pumped back into the oil cycle.

The main designed parameters of solar aided power plant are shown in Table 3.

For the solar aided coal-fired power plant, the energy efficiency and exergy efficiency can be defined as follows:

$$\eta_{\text{energy}} = \frac{w_{\text{output}}}{Q_{\text{coal}} + Q_{\text{solar}}}, \quad (27)$$

where η_{energy} is the energy efficiency, w_{output} is work output, Q_{coal} is the energy of coal, and Q_{solar} is the energy of solar.

$$\eta_{\text{exergy}} = \frac{w_{\text{output}}}{E_{\text{coal}} + E_{\text{solar}}}, \quad (28)$$

where η_{exergy} is the exergy efficiency, E_{coal} is the exergy of coal, and E_{solar} is the solar exergy.

It can be seen from Tables 1 and 3 that the coal consumption rate of solar aided coal-fired power plant is less than that of the coal-fired power plant.

The capital cost of the plant is shown in Table 4 [12–18]. The investment includes the cost of facilities and the maintaining cost. The cost of coal is 140 dollars/ton [19].

4.2. Results and Sensitivity Analysis. Based on the methodology proposed in Section 3, the solar contributions in 600 MW solar aided coal-fired power plant have been evaluated. The results of solar exergy proportion and solar cost proportion have been shown in Tables 5 and 6, respectively.

The overall exergy proportion of solar power in the plant can be calculated using $\alpha = (\alpha_{12} \times E_{12} + \alpha_{13} \times E_{13}) / (E_{12} + E_{13})$ and the result is 4.84%.

TABLE 4: The investment of the plant.

Items	Cost (dollars)
Solar concentration field	37528560.00
Oil-water heat exchangers	4192170.00
Super heaters of the boiler	168235561.38
Reheaters of the boiler	22941212.92
High-pressure turbine	24723323.22
Intermediate-pressure turbine	26877786.50
Low-pressure turbine	42734428.98
Condenser	14550480.00
Other heat exchangers	21149680.00
Deaerator	3156810.00
Pumps	673317.35

TABLE 5: Exergy value of each flow and the proportion of solar power.

Exergy flows	Exergy value (MJ/h)	Exergy Proportion of solar α	Percent
E_1	555712.8	α_1	48.39
E_2	2447325	α_2	6.55
E_3	1563747	α_3	6.55
E_4	2065157	α_4	4.09
E_5	89036.6	α_5	4.09
E_6	422330.4	α_6	4.72
E_7	157822.2	α_7	6.55
E_8	362203.9	α_8	4.09
E_9	357271.6	α_9	100
E_{10}	3551430	α_{10}	0
E_{11}	941377.7	α_{11}	0
E_{12}	664758.2	α_{12}	6.55
E_{13}	1495293	α_{13}	4.09

TABLE 6: Exergy cost of each flow and the proportion of solar power.

Cost flow	values	Cost proportion of solar β	Percent
C_1	5903	β_1	1.98
C_2	22724	β_2	0.70
C_3	14520	β_3	0.70
C_4	18896	β_4	0.56
C_5	815	β_5	0.56
C_6	5745	β_6	0.70
C_7	1465	β_7	0.70
C_8	3314	β_8	0.56
C_9	0	β_9	100
C_{10}	16181	β_{10}	0
C_{11}	4289	β_{11}	0
C_{12}	6833	β_{12}	0.78
C_{13}	15032	β_{13}	0.62

It can be seen from Table 5 that the proportion of solar exergy is 100 percent in the ninth exergy flow. This is due to the solar energy from the solar exergy flow sharing a contribution ratio of 100 percent. As exergy flows, the proportion of solar exergy shows a decreasing trend. The twelfth and the thirteenth exergy flows shown in Table 5 represent the exergy in system work (i.e., electric power). The proportions of solar power are 6.55% and 4.09%. The overall exergy proportion of solar power is 4.84% by weighing the proportions in the twelfth and thirteenth exergy flows. In the system, considering the proportion of exergy flows, the contribution of solar power can be measured by its proportion of 4.84% in the overall electric power. For the system with a rated capacity of 600 MW, in this case, about 29.04 MW of electric power is contributed to solar power and the rest 570.96 MW is contributed to coal-fired.

The overall cost proportion of solar power in the plant can be calculated using $\beta = (\beta_{12} \times C_{12} + \beta_{13} \times C_{13}) / (C_{12} + C_{13})$ and the result is 0.67%.

It can be seen from Table 6 that the cost of solar exergy flow is zero in the exergy cost of the ninth flow. This is because the solar energy has been considered to be free in the analysis. The exergy cost of the twelfth and thirteenth flows in Table 6 shows the exergy costs of electricity, and the proportions of solar power are 0.78% and 0.62% in them. By weighing the proportions of solar power in the twelfth and thirteenth flows, we can obtain that the proportion of solar power in the electric exergy cost is 0.67%. In this system, considering the exergy cost of flows, the proportion of the cost of solar power and solar equipments is 0.67%. For the system, a rated capacity of 600 MW, in this case, the cost of solar energy, and solar equipment share a proportion of 0.67% in the cost of electric power, and the rest (99.33%) comes from coal and other equipment. Comparing the calculated solar power exergy generated with the proportion of cost of solar power exergy generated, the proportion of 4.48% of solar power exergy generated is much larger than the proportion of 0.67% of cost of solar power exergy generated.

(1) *Sensitivity Analysis of Coal Cost.* When the coal cost changes from 100 to 180 dollars/ton, the trend of cost of electricity is shown in Figure 5 and the trend of the overall cost proportion of solar is shown in Figure 6.

The power generation cost is calculated as follows:

$$c_{\text{electricity}} = \frac{C_{\text{electricity}}}{E_{\text{electricity}}}, \quad (29)$$

where $c_{\text{electricity}}$ is the cost of power generation, $C_{\text{electricity}}$ is the exergy cost of electricity, and $E_{\text{electricity}}$ is the generating capacity.

The exergy cost of electricity includes two aspects, namely, fixed costs and variable costs. The fixed costs include equipment costs, material costs, depreciation costs, operation, and maintenance fees, and the variable costs include fuel costs, environmental costs, water charges. In order to take advantage of the calculation method proposed in this paper, all of the costs (except the fuel costs) have been converted to

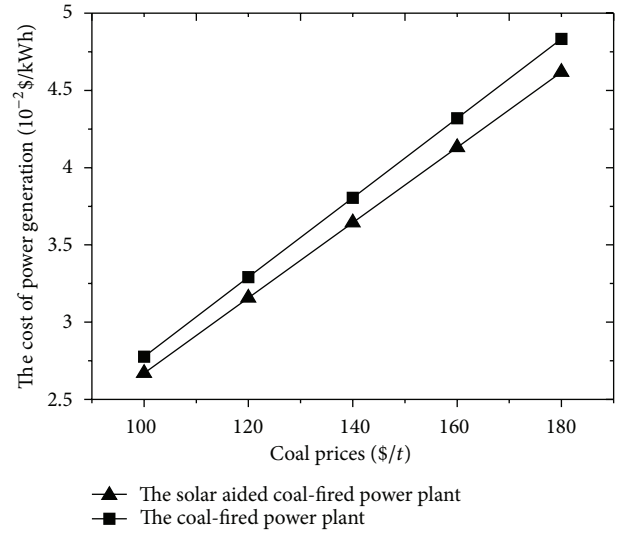


FIGURE 5: The change of cost of electricity with coal cost.

the equipment costs. Therefore, in this case, the cost of power generation is calculated as follows:

$$c_{\text{electricity}} = \frac{C_{12} + C_{13}}{E_{12} + E_{13}}. \quad (30)$$

It can be seen from Figure 5 that the cost of electricity increases from 2.67 cents/kWh to 4.62 cents/kWh in the solar aided coal-fired power plant with the coal prices increase from 100\$/t to 180\$/t. The power generation cost of 600 MW power plant is 3.81 cents/kWh, and that of the coupled power plant power is 3.64 cents/kWh when the coal price is 140\$/t. In the terms of coal price, the COE of a solar aided power plant is less than the one of coal-fired power plant. As solar energy is added to the solar aided system, in the condition of saving coal (with lower coal consumption rate), considering the solar energy is free, the COE of a coupled power plant will be lower than the original thermal power plant. However, compared to the pure solar power generation system, the coupled system uses the turbines, generators and other key equipment of the original thermal power system, and the work efficiency of the replaced high-temperature high-pressure high-grade steam is much higher than the pure solar thermal power generation. Therefore, the COE of the coupled power generation system is less than the pure solar power generation system.

It can be seen from Figure 6 that with the coal price increasing from 100\$/t to 180\$/t, the β is reduced from 0.92% to 0.51%, about 0.41 points. The reduction trend tends to be slower with the increase of the coal price.

(2) *Sensitivity Analysis of Solar Facilities' Investment.* When the investment of solar facilities changes from 60% to 140%, the trend of the cost of electricity is shown in Figure 7 and the trend of the overall cost proportion of solar is shown in Figure 8.

Figure 7 shows that, with the solar equipment price increase, the proportion of solar equipment increases in the

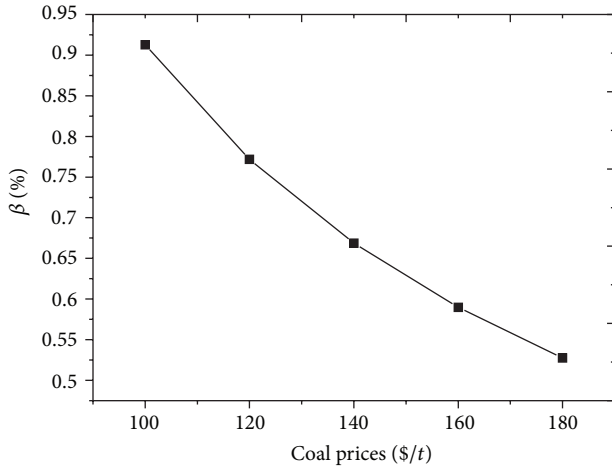


FIGURE 6: The change of the overall cost proportion of solar with coal cost.

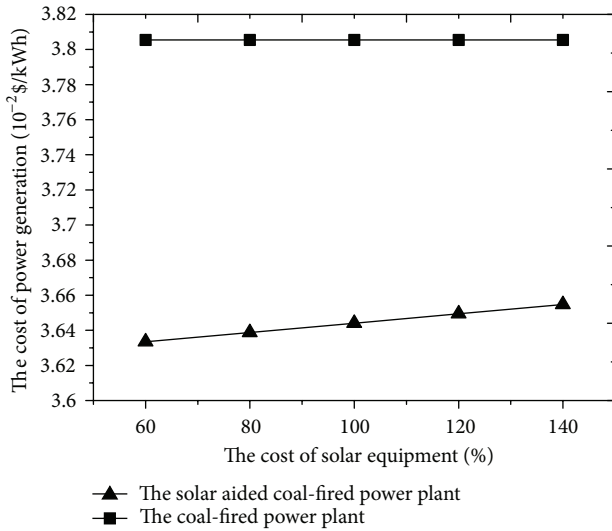


FIGURE 7: The change of the cost of electricity with the solar facilities' investment.

equipment costs, so the COE of solar aided power plant increases. Therefore, the production of cheap solar collector devices is good for power plant in low-cost operation.

It can be seen from Figures 7 and 8, with the change of the cost of solar equipment from 60% of the calculation cost to 140% of the calculation cost, that the cost of power generation increases from 3.63 cents/kWh to 3.65 cents/kWh; the β increases from 0.53% to 0.79%, which is about 0.26 points.

5. Conclusions

This paper proposed thermoeconomic cost method for solar contribution study in solar aided coal-fired power plant and analyzed the plant based on the newly constructed and reconstructed 600 MW power plant.

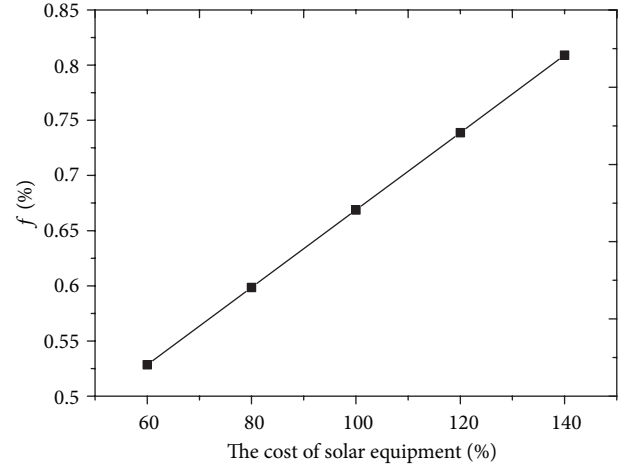


FIGURE 8: The change of the overall cost proportion of solar with the solar facilities' investment.

Based on the second law of thermodynamics and the principle of thermoeconomics, this paper proposed the evaluation of solar contribution in the solar aided coal-fired power plant, which can be used to assign the individual cost components involving solar energy. Its feasibility has been proven by analyzing a newly constructed power plant. The result shows: that when operating at the rated capacity, the proportion of solar power in overall electric power is 4.84%, which is about 29.04 MW.

Nomenclature

- E_i : The exergy value of the i th exergy flow
- δ_i : The ratio of solar exergy loss in the total exergy loss when running the i th equipment
- α_i : The ratio of solar exergy flow in the i th exergy flow
- c_i : The unit cost of the i th exergy flow
- C_i : $C_i = c_i \cdot E_i$. The cost of the i th exergy flow, as the energy cost
- C_{γ_i} : The nonenergy cost of the i th subsystem
- β_i : The exergy cost ratio of the solar contribution in the i th exergy flow
- β_{γ_i} : The ratio of the solar side of the nonenergy costs of the i th subsystem.

Acknowledgments

The research work is supported by China National Natural Science Foundation (no. 51106048), the Fundamental Research Funds for the Central Universities and the Program for 863 Project (2012AA050604). The authors have no other relevant affiliations or financial involvement with any organization or entity with a financial interest in or financial conflict with the subject matter or materials discussed in the paper apart from the one disclosed.

References

- [1] D. Mills, "Advances in solar thermal electricity technology," *Solar Energy*, vol. 76, no. 1-3, pp. 19-31, 2004.
- [2] B. R. Pai, "Augmentation of thermal power stations with solar energy," *Sādhanā*, vol. 16, no. 1, pp. 59-74, 1991.
- [3] M. K. Gupta and S. C. Kaushik, "Exergetic utilization of solar energy for feed water preheating in a conventional thermal power plant," *International Journal of Energy Research*, vol. 33, no. 6, pp. 593-604, 2009.
- [4] Y. M. El-Sayed and R. A. Gaggioli, "Critical review of second law costing methods—I: background and algebraic procedures," *Journal of Energy Resources Technology*, vol. 111, no. 1, pp. 1-7, 1989.
- [5] R. A. Gaggioli and Y. M. El-Sayed, "Critical review of second law costing methods—II: calculus procedures," *Journal of Energy Resources Technology*, vol. 111, no. 1, pp. 8-15, 1989.
- [6] M. A. Rosen and I. Dincer, "Thermoeconomic analysis of power plants: an application to a coal fired electrical generating station," *Energy Conversion and Management*, vol. 44, no. 17, pp. 2743-2761, 2003.
- [7] M. V. J. J. Suresh, K. S. Reddy, and A. K. Kolar, "4-E (energy, exergy, environment, and economic) analysis of solar thermal aided coal-fired power plants," *Energy for Sustainable Development*, vol. 14, no. 4, pp. 267-279, 2010.
- [8] A. Baghernejad and M. Yaghoubi, "Exergoeconomic analysis and optimization of an Integrated Solar Combined Cycle System (ISCCS) using genetic algorithm," *Energy Conversion and Management*, vol. 52, no. 5, pp. 2193-2203, 2011.
- [9] A. M. Patnode, *Simulation and performance evaluation of parabolic trough solar power plants [Ph.D. thesis]*, University of Wisconsin, Madison, Wis, USA, 2006.
- [10] T. Stuetzle, *Automatic control of the 30MWe SEGS VI parabolic trough plant [M.S. thesis]*, University of Wisconsin, Madison, Wis, USA, 2002.
- [11] T. Stuetzle, N. Blair, J. W. Mitchell, and W. A. Beckman, "Automatic control of a 30 MWe SEGS VI parabolic trough plant," *Solar Energy*, vol. 76, no. 1-3, pp. 187-193, 2004.
- [12] M. A. Lozano, A. Valero, and L. Serra, "Theory of the exergetic cost and thermoeconomics optimization," in *Proceedings of the International Symposium on International Conference on Energy Systems and Ecology (ENSEC '93)*, Cracow, Poland, 1993.
- [13] C. Frangopoulos, *Thermoeconomic functional analysis: a method for optimal design or improvement of complex thermal systems [Ph.D. thesis]*, Georgia Institute of Technology, 1983.
- [14] M. R. von Spakovsky, *A practical generalized analysis approach to the optimal thermoeconomic design and improvement of real-world thermal systems [Ph.D. thesis]*, Georgia Institute of Technology, 1986.
- [15] J. Uche, *Thermoeconomic analysis and simulation of a combined power and desalination plant [Ph.D. thesis]*, Department of Mechanical Engineering, University of Zaragoza, 2000.
- [16] J. Uche, L. Serra, and A. Valero, "Thermoeconomic optimization of a dual-purpose power and desalination plant," *Desalination*, vol. 136, no. 1-3, pp. 147-158, 2001.
- [17] J. L. Silveira and C. E. Tuna, "Thermoeconomic analysis method for optimization of combined heat and power systems. Part I," *Progress in Energy and Combustion Science*, vol. 29, no. 6, pp. 479-485, 2003.
- [18] Y. Yang, Y. Cui, H. Hou, X. Guo, Z. Yang, and N. Wang, "Research on solar aided coal-fired power generation system and performance analysis," *Science in China, Series E*, vol. 51, no. 8, pp. 1211-1221, 2008.
- [19] B. Zhang and J. Ma, "Coal price index forecast by a new partial least-squares regression," *Procedia Engineering*, vol. 15, pp. 5025-5029, 2011.

Research Article

A Novel Extension Decision-Making Method for Selecting Solar Power Systems

Meng-Hui Wang

Department of Electrical Engineering, National Chin-Yi University of Technology, Taichung 41110, Taiwan

Correspondence should be addressed to Meng-Hui Wang; wangmh@ncut.edu.tw

Received 29 October 2012; Accepted 16 January 2013

Academic Editor: Tapas Mallick

Copyright © 2013 Meng-Hui Wang. This is an open access article distributed under the Creative Commons Attribution License, which permits unrestricted use, distribution, and reproduction in any medium, provided the original work is properly cited.

Due to the complex parameters of a solar power system, the designer not only must think about the load demand but also needs to consider the price, weight, and annual power generating capacity (APGC) and maximum power of the solar system. It is an important task to find the optimal solar power system with many parameters. Therefore, this paper presents a novel decision-making method based on the extension theory; we call it extension decision-making method (EDMM). Using the EDMM can make it quick to select the optimal solar power system. The paper proposed this method not only to provide a useful estimated tool for the solar system engineers but also to supply the important reference with the installation of solar systems to the consumer.

1. Introduction

In recent years, global warming caused the sea levels rising. As a result, the loss of coastal wetlands causes the erosion of the coastline and the continued flooding in the low-lying area. Regional climate changes also caused serious striking against the environmental ecology and agriculture. The greenhouse effect and global warming are becoming increasingly apparent. In the past two decades, the economy has grown rapidly in Taiwan, and it made the energy requirement increase greatly. However, there is an extreme shortage of energy resources in Taiwan. Also, 99 percent of the energy must rely on import from the foreign countries. Facing the fossil-fuel shortage crisis, Taiwan is actively opening up the renewable energy at present. The solar energy is one of the renewable energy resources with the highest acceptance in Taiwan.

Because Taiwan is located in subtropics, the temperature and the sunlight suit to develop the solar power system. Solar power system has high potential. When the solar power system operates, it neither produces the air pollution nor generates a large number of CO₂. Therefore, this system is very helpful to reduce the global warming and the demand of fossil energy. The solar power system is also a clean and safe power supply system for businesses and families [1, 2].

The semiconductor industry fairly matures in Taiwan. The electronic power technology development is stepping

into a new stage. There is a quite good basis on manufacturing technology and R&D manpower. By the global photovoltaic (PV) industry growth trends, it is high competition to develop the solar power system in Taiwan. According to the industry statistics until 2007, there are more than 70 solar power system companies and solar power system output is 430 MW which is the fourth in the world. The PVs industry production is worth 53.5 billion dollars. It is beneficial to save the energy and reduce CO₂ and the industrial development. In part of the solar development, the single crystal silicon solar cell efficiency has reached 21%, and the polysilicon solar cell efficiency is up to 18.5%. The high efficient design and the packaging technologies in the PV module technology have been established. In 2012, we expect to be completed to install 20,000 families, and the capacity of 60 MW installations. The solar energy system can generate 7,200 million kWh per year. It promotes the development of the domestic PV industry, creates the domestic markets, and develops the industries.

When the solar power system is installed, it needs to consider the loading demand and the installing area. For the user, it is important to consider with the recovered cost, APGC, and the total weight of solar power system [3]. Confronting the variety of solar power system in the market, the solar system is an important task of how to select the best option from the specifications provided. Therefore, this

paper presents a novel decision-making method based on the extension theory [4–6]; we call it extension decision-making method (EDMM). First, according to the specifications of PV cell provided by the manufacturer, this paper uses the commercial software to simulate every solar power system and to compute the APGC of solar system. Then, this paper uses the proposed EDMM to count the evaluation index of every system. Using the evaluation index can make it easy to select the optimal system. This proposed method not only provides the system engineers with as a very useful assessment tool, but also supplies the users with the important reference when setting a solar power system. In addition, this paper proposes the method which can be added or subtracted to the characteristic and weight by the user's requirement. We hope that the proposed method will lead to further investigation for other renewable energy systems.

2. Review of Extension Theory

In the standard set, an element either belongs to or not belongs; so, the range of the standard set is $\{0, 1\}$, which can be used to solve a two-valued problem. In contrast to the standard set, the fuzzy set allows the description of concepts in which the boundary is not explicit. It concerns not only whether an element belongs to the set but also to what degree it belongs to the set. The range of a fuzzy set is $[0, 1]$. The extension set extends the fuzzy set from $[0, 1]$ to $(-\infty, \infty)$. As a result, it allows us to define a set that includes any data in the domain. Extension theory tries to solve the incompatibility or contradiction problems by the transformation of the matter element [7, 8]. The comparisons of the standard sets, fuzzy sets, and extension sets are shown in Table 1. Some definitions of extension theory are introduced in the next section.

2.1. Matter-Element Theory

2.1.1. Definition of Matter-Element. Defining the name of matter as N , the characteristics of the matter as c , and the value of c as v , a matter-element in extension theory can be described as follows:

$$R = (N, c, v), \quad (1)$$

where N , c , and v were called the three fundamental elements of the matter-element. If the value of the characteristic has a classical domain or a range, then we define the matter-element for the classical domain as follows:

$$R = (N, c, v) = (N, c, \langle v^L, v^U \rangle), \quad (2)$$

where v^L and v^U are the lower bound and upper bound of a classical domain.

2.1.2. Multidimensional Matter-Element. Assuming $R = (N, C, V)$ to be a multidimensional matter-element, $C = [c_1, c_2, \dots, c_n]$ a characteristic vector, and $V = [v_1, v_2, \dots, v_n]$

a value vector of C , then a multidimensional matter-element is defined as

$$R = \begin{bmatrix} N, c_1, v_1 \\ c_2, v_2 \\ \vdots \\ c_n, v_n \end{bmatrix} = \begin{bmatrix} R_1 \\ R_2 \\ \vdots \\ R_n \end{bmatrix}, \quad (3)$$

where $R_i = (N, c_i, v_i)$ ($i = 1, 2, \dots, n$) is defined as the sub-matter-element of R .

2.2. Extension Set Theory

2.2.1. Definition of Extension Set. Let U be the universe of discourse; then, an extension set \tilde{A} on U is defined as a set of ordered pairs as follows:

$$\tilde{A} = \{(v, y) \mid v \in U, y = K(v) \in (-\infty, \infty)\}, \quad (4)$$

where $y = K(x)$ is called the correlation function for extension set \tilde{A} . The $K(x)$ maps each element of U to a membership grade between $-\infty$ and ∞ . The higher degree and the more elements belong to the set. In a special condition, when $0 \leq K(x) \leq 1$, it corresponds to a normal fuzzy set. $K(x) \leq -1$ implies that the element x has no chance to belong to the set. When $-1 < K(x) < 0$, it is called an extension domain, which means that the element x still has a chance to become part of the set.

2.2.2. Definition of Correlation Function. The correlation functions have many forms dependent on application. If we set $V_o = \langle a, b \rangle$ and $V = \langle c, d \rangle$ being two intervals in the real number field, and $V_o \in V$, then the correlation function in the extension theory can be defined as follows:

$$K(v) = \frac{\rho(v, V_o)}{D(v, V_o, V)}, \quad (5)$$

where

$$D(v, V_o, V) = \begin{cases} \rho(v, V) - \rho(v, V_o), & v \notin V_o, \\ -1, & v \in V_o, \end{cases} \quad (6)$$

$$\rho(v, V_o) = \left| x - \frac{a+b}{2} \right| - \frac{b-a}{2},$$

$$\rho(v, V) = \left| x - \frac{c+d}{2} \right| - \frac{d-c}{2}.$$

The correlation function can be used to calculate the membership grade between x and V_o as shown in Figure 1.

2.3. Decision-Making Method for Solar Power System. Using the decision-making method for the solar power systems, it must have a software suit to simulate APGC, the maximum power, and the current of the solar power systems. Then, we can use the characteristics of solar power system to build the matter-element model of solar systems and to calculate the estimated index for selecting rank.

TABLE 1: Three different sorts of mathematical sets.

Compared item	Standard set	Fuzzy set	Extension set
Research objects	Data variables	Linguistic variables	Contradictory problems
Model	Mathematics model	Fuzzy mathematics model	Matter-element model
Descriptive function	Transfer function	Membership function	Correlation function
Descriptive property	Precision	Ambiguity	Extension
Range of set	$C_A(x) \in (0, 1)$	$\mu_A(x) \in [0, 1]$	$K_A(x) \in (-\infty, \infty)$

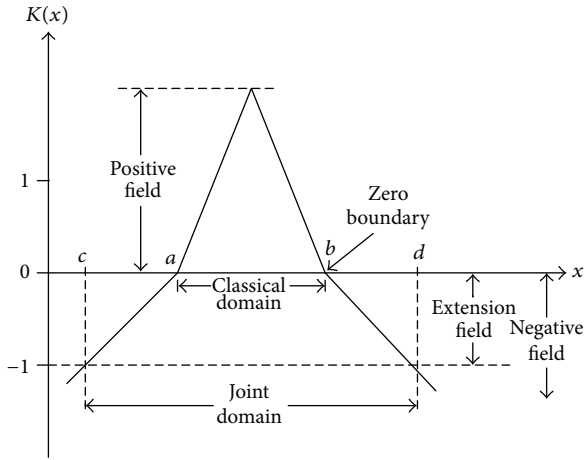


FIGURE 1: The proposed extended relation function.

2.4. *Test Conditions.* The paper is based on the simulated software to unify the location, area, the direction of harmonization, and the horizontal angle for the solar power system. It simulates all the conditions of each solar power system installed in the location of the latitude and longitude, respectively, (24, 9) and (120, 40), in Taichung. Then, it simulates the solar power system and the horizontal included angle is 23 degrees and the panel toward the south. The simulated total area of the solar power system is 50 square meters. There are established five groups of the matter-element model according to the characteristics which are the APGC, the maximum power, the maximum current, the total cost, and the total weight of the solar power systems.

The first three data statistics calculate from the commercial simulation software, the typical simulated results of the solar power system can be shown in Figures 2 and 3, there are easy to calculate the APCG, maximum power, and current of the tested solar system.

The two other data are provided from the producers of solar power systems. Table 2 shows the specification of different solar systems. Then, the paper uses the earlier 5 characteristics to create the matter-element model as shown in Table 3. Here, the A-class represents the best solar module. The opposite E-class represents the worst solar module. Table 3 shows that the c_1 is APGC, c_2 is the maximum power, c_3 is the total cost, c_4 is the maximum current, and c_5 is the total weight.

2.5. *The Proposed Extension Decision-Making Method.* This paper has been successfully using computer software to

TABLE 2: Specifications of the different PV modules.

PV samples	Characteristics				
	APGC (kwh/year)	Max. power (kw)	Cost (10^3 USD)	Max. current (A)	Weight (kg)
Module 1	4962	4.2	23.6	240	380
Module 2	4575	3.8	23.6	238	395
Module 3	11969	10.3	42.1	253	800
Module 4	3890	3.7	51.5	119	1030
Module 5	6998	6.2	30.1	174	644
Module 6	6629	5.6	24.8	330	608
Module 7	6685	6.0	27.7	341	608
Module 8	5251	4.3	44.1	288	662
Module 9	4528	4.1	40.8	131	836
Module 10	6833	6.2	26.8	363	886
Module 11	6286	5.1	52.3	220	420
Module 12	7255	6.3	29.7	178	570
Module 13	7858	6.7	29.3	186	532
Module 14	7812	6.3	30.9	356	600
Module 15	7915	6.2	32.7	356	601
Module 16	6543	5.7	32.2	324	672
Module 17	7284	6.4	23.5	127	812
Module 18	7415	5.5	30.7	332	550
Module 19	12614	10.8	47.3	257	800
Module 20	12297	10.5	42.4	255	800
Module 21	11094	9.5	49.0	172	1150
Module 22	5824	4.6	29.7	278	814
Module 23	4335	4.1	51.3	199	624
Module 24	7303	6.0	33.1	338	589
Module 25	3903	3.5	49.3	221	516
Module 26	8209	7.1	24.9	236	480
Module 27	4307	3.9	47.0	125	941
Module 28	6943	5.9	30.5	338	476
Module 29	10200	8.8	40.1	219	660
Module 30	2134	2.1	38.6	121	620

implement the proposed method for the selection of solar power systems; the details of the proposed method are shown as follows.

TABLE 3: Matter-element models of different classes.

Classes	Matter-element models
A-Class	$R1 = \left\{ \begin{array}{l} A \quad c1 \quad \langle 80, 100 \rangle \\ \quad \quad c2 \quad \langle 80, 100 \rangle \\ \quad \quad c3 \quad \langle 0, 20 \rangle \\ \quad \quad c4 \quad \langle 80, 100 \rangle \\ \quad \quad c5 \quad \langle 0, 20 \rangle \end{array} \right\}$
B-Class	$R2 = \left\{ \begin{array}{l} B \quad c1 \quad \langle 60, 80 \rangle \\ \quad \quad c2 \quad \langle 60, 80 \rangle \\ \quad \quad c3 \quad \langle 20, 40 \rangle \\ \quad \quad c4 \quad \langle 60, 80 \rangle \\ \quad \quad c5 \quad \langle 20, 40 \rangle \end{array} \right\}$
C-Class	$R3 = \left\{ \begin{array}{l} C \quad c1 \quad \langle 40, 60 \rangle \\ \quad \quad c2 \quad \langle 40, 60 \rangle \\ \quad \quad c3 \quad \langle 40, 60 \rangle \\ \quad \quad c4 \quad \langle 40, 60 \rangle \\ \quad \quad c5 \quad \langle 40, 60 \rangle \end{array} \right\}$
D-Class	$R4 = \left\{ \begin{array}{l} D \quad c1 \quad \langle 20, 40 \rangle \\ \quad \quad c2 \quad \langle 20, 40 \rangle \\ \quad \quad c3 \quad \langle 60, 80 \rangle \\ \quad \quad c4 \quad \langle 20, 40 \rangle \\ \quad \quad c5 \quad \langle 60, 80 \rangle \end{array} \right\}$
E-Class	$R5 = \left\{ \begin{array}{l} E \quad c1 \quad \langle 0, 20 \rangle \\ \quad \quad c2 \quad \langle 0, 20 \rangle \\ \quad \quad c3 \quad \langle 80, 100 \rangle \\ \quad \quad c4 \quad \langle 0, 20 \rangle \\ \quad \quad c5 \quad \langle 80, 100 \rangle \end{array} \right\}$

Step 1. Normalize the values of the characteristics into an interval between 0 and 100 as in (7). This process will be beneficial for estimation of solar systems. Consider

$$V_j^{\text{new}} = \left(\frac{V_j^{\text{old}} - V_{\min}}{V_{\max} - V_{\min}} \right) \times 100, \quad (7)$$

$$V_{\max} = \max \{V_j\}, \quad (8)$$

$$V_{\min} = \min \{V_j\}.$$

Step 2. Establish the matter-element model of every rank according to Table 3, where

$$R_i = \left\{ \begin{array}{l} \text{class} \quad c1 \quad v_{i1} \\ \quad \quad c2 \quad v_{i2} \\ \quad \quad c3 \quad v_{i3} \\ \quad \quad c4 \quad v_{i4} \\ \quad \quad c5 \quad v_{i5} \end{array} \right\}. \quad (9)$$

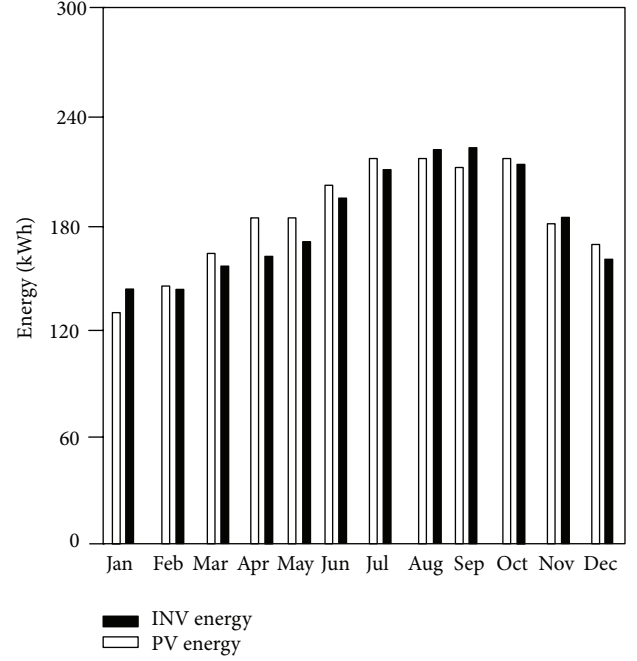
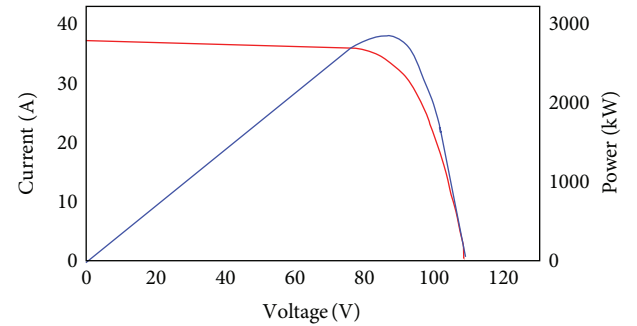


FIGURE 2: The typical APGC curves of the solar power system.



Corp.: SANYO
Module: HIP-55172
String (series \times parallel): 5×10
Capacity: 2.79kW

FIGURE 3: The typical maximum power and current curves of the solar power systems.

Step 3. Calculate the correlation index of every rank with the proposed extended correlation function as follows:

$$K_{ij} = \begin{cases} -\rho(v_i, V_{ij}), & v_i \in V_{ij}, \\ \frac{\rho(v_i, V_{ij})}{\rho(V_i, V_{pi}) - \rho(V_i, V_{ij})}, & v_i \notin V_{ij}, \end{cases} \quad (10)$$

$$i = 1, 2, \dots, 5; \quad j = 1, 2, \dots, 5.$$

Step 4. Set the weights of the estimated characteristics, W_{i1} , W_{i2} , W_{i3} , W_{i4} , and W_{i5} , depending on the importance of every characteristic in the estimated process of the user. In

this paper, the five weights are set at 0.3, 0.15, 0.3, 0.15, and 0.1, which means that the APGC and cost are more important than the other characteristics.

Step 5. Calculate the relation indexes for every rank as follows:

$$\lambda_i = \sum_{j=1}^5 W_{ij} K_{ij}, \quad i = 1, 2, \dots, 5. \quad (11)$$

Step 6. Normalize the values of the relation indexes into an interval between -100 and 100 as in (12). This process will be beneficial for the estimated process. Consider

$$\lambda'_i = \begin{cases} \frac{\lambda_i}{\lambda_{\max}} \times 100, & \lambda_i > 0, \\ \frac{\lambda_i}{|\lambda_{\min}|} \times 100, & \lambda_i < 0, \end{cases} \quad (12)$$

where

$$\lambda_{\min} = \min \{\lambda_i\}; \quad \lambda_{\max} = \max \{\lambda_i\}. \quad (13)$$

Step 7. Rank the normalized correlation indexes to estimate the rank of the tested solar system. Generally, the high correlation index implies that the solar power system has the high probability to belong to this class. Therefore, using the correlation index can be easy to determine the class of system that is most useful for the user and engineer.

3. Test Results and Discussion

The paper provides the decision-making method of solar power system that uses the MATLAB software to write the computing program. The testing results of the proposed method are shown in Table 4. It can observe the correlated index of various solar systems with the different rank, it should be noticed that the correlated index is based on the demanded conditions of the user. It can observe the correlated index of various solar power systems from Table 4. For example, module 1 can be a D-class solar power system due to large correlated index with the D-class, and module 19 is an A-class or better solar power system due to large correlated index with the A-class. On the contrary, the module 25 is an E-class or bad solar power system in the demanded conditions of the user. Table 5 compiles statistics of the top 5 according to A and E classes with correlated index the top 5 of the A-class are modules 19, 10, 20, 3, and 7, respectively, and the top 5 of the E-class include modules 4, 25, 9, 27, and 30, respectively. Therefore, the proposed EDMM is useful to determine the optimal solar power system based on the predetermined specifications of the user or solar system engineer.

4. Conclusion

The paper combines the commercial solar simulated software with the proposed EDMM to determine the optimal solar

TABLE 4: The correlation results of solar modules.

Sample	Rank				
	A	B	D	C	E
Module 1	-40	-76	38	14	-56
Module 2	-20	-79	10	12	-53
Module 3	46	-52	14	15	-80
Module 4	-100	-94	-54	-85	26
Module 5	-37	18	3	44	-29
Module 6	25	9	-53	10	-68
Module 7	37	11	-50	24	-40
Module 8	-60	22	100	-29	-46
Module 9	-76	-62	20	-28	9
Module 10	62	48	2	36	-36
Module 11	-8	-67	8	-19	-61
Module 12	-33	10	6	60	-31
Module 13	-17	-15	13	37	-36
Module 14	18	36	-53	43	-51
Module 15	17	50	-49	39	-53
Module 16	1	48	-36	12	-42
Module 17	-54	-62	-57	66	1
Module 18	5	24	-45	42	-46
Module 19	66	-77	-62	7	-91
Module 20	56	-60	19	11	-82
Module 21	12	-64	-27	-75	-72
Module 22	-39	17	42	2	-26
Module 23	-82	3	26	-59	-44
Module 24	8	42	-42	54	-49
Module 25	-53	-72	-32	-27	16
Module 26	31	-34	-58	30	-72
Module 27	-89	-80	17	-62	3
Module 28	20	17	-48	33	-46
Module 29	-29	24	-38	10	-66
Module 30	-84	4	-74	27	2

TABLE 5: The top 5 of A-class and E-class.

Ranks	A-class	E-class
1st	Module 19	Module 4
2nd	Module 10	Module 25
3rd	Module 20	Module 9
4th	Module 3	Module 27
5th	Module 7	Module 30

power system based on the predetermined specifications of the user or the engineer. The calculation of the proposed decision-making algorithm is also fast and very simple. It can be easily implemented by PC software. Test results show that the proposed method cannot only estimate the class of solar system, but it can also be applied to the selecting tools of other related renewable power systems such as wind power and full cells systems. The proposed method is also a new decision-making scheme for other engineering problems.

References

- [1] H. Wang, Y. Li, J. Wang, and Z. Wang, "Analysis of photovoltaic charging system based on MPPT," in *Proceedings of the Pacific-Asia Workshop on Computational Intelligence and Industrial Application (PACIIA '08)*, pp. 498–501, December 2008.
- [2] M. Taherbaneh and K. Faez, "Maximum power point estimation for photovoltaic systems using neural networks," in *Proceedings of the IEEE International Conference on Control and Automation ThC4-5 (ICCA '07)*, pp. 1614–1619, Guangzhou, China, June 2007.
- [3] M. Taherbaneh, H. G. Fard, A. H. Rezaie, and S. Karbasian, "Combination of fuzzy-based maximum power point tracker and sun tracker for deployable solar panels in photovoltaic systems," in *Proceedings of the IEEE International Conference on Fuzzy Systems (FUZZ '07)*, July 2007.
- [4] M. H. Wang, "A novel extension method for transformer fault diagnosis," *IEEE Transactions on Power Delivery*, vol. 22, no. 8, pp. 63–64, 2002.
- [5] M. H. Wang, "Application of extension theory to vibration fault diagnosis of generator sets," *IEE Proceedings*, vol. 151, no. 4, pp. 503–508, 2004.
- [6] W. Cai, "Extension management engineering and applications," *International Journal of Operations and Quantitative Management*. In press.
- [7] M. H. Wang and C. P. Hung, "Extension neural network and its applications," *Neural Networks*, vol. 16, no. 5-6, pp. 779–784, 2003.
- [8] M. H. Wang, Y. F. Tseng, H. C. Chen, and K. H. Chao, "A novel clustering algorithm based on the extension theory and genetic algorithm," *Expert Systems with Applications*, vol. 36, no. 4, pp. 8269–8276, 2009.

Research Article

Photovoltaic Power System with an Interleaving Boost Converter for Battery Charger Applications

Sheng-Yu Tseng¹ and Cheng-Tao Tsai²

¹Department of Electrical Engineering, Chang-Gung University, Taoyuan 33302, Taiwan

²Department of Electrical Engineering, National Chin-Yi University of Technology, Taiping 411, Taiwan

Correspondence should be addressed to Cheng-Tao Tsai, cttai@ncut.edu.tw

Received 20 June 2012; Accepted 11 September 2012

Academic Editor: Tapas Mallick

Copyright © 2012 S.-Y. Tseng and C.-T. Tsai. This is an open access article distributed under the Creative Commons Attribution License, which permits unrestricted use, distribution, and reproduction in any medium, provided the original work is properly cited.

This paper proposes a photovoltaic (PV) power system for battery charger applications. The charger uses an interleaving boost converter with a single-capacitor turn-off snubber to reduce voltage stresses of active switches at turn-off transition. Therefore, active switches of the charger can be operated with zero-voltage transition (ZVT) to decrease switching losses and increase conversion efficiency. In order to draw the maximum power from PV arrays and obtain the optimal power control of the battery charger, a perturbation-and-observation method and microchip are incorporated to implement maximum power point tracking (MPPT) algorithm and power management. Finally, a prototype battery charger is built and implemented. Experimental results have verified the performance and feasibility of the proposed PV power system for battery charger applications.

1. Introduction

Due to the continuous growth of the global energy demand for developing industry, it increases society awareness of environmental impacts from the widespread utilization of fossil fuels, leading to the exploration of renewable energy sources, such as PV arrays, wind energy, and so on. One of these sources is PV arrays energy, which is clean, quiet, and maintenance-free. However, due to the instability and intermittent characteristics of PV arrays, it cannot provide a constant or stable power output. Thus, a power converter (dc/dc converter or dc/ac converter) and MPPT algorithm are required to regulate its output power.

Several MPPT algorithms have been proposed [1–10]. Some of the popular MPPT algorithms use perturbation-and-observation method [1–3], incremental conductance method [4], constant voltage method [5, 6], β method [7], system oscillation method [8, 9], and ripple correlation method [10]. The perturbation-and-observation method requires the measurement of only a few parameters, thus it facilitates an MPPT control. As a result, it is often applied to the PV arrays for enhancing power capacity.

A typical PV power system is shown in Figure 1. The PV arrays usually need a battery charger to increase its utility rate. The research of this paper is only focused on PV arrays for battery charger applications. For charger design, many charging methods have been developed, such as the constant trickle current (CTC), constant current (CC), constant voltage (CV), hybrid CC/CV [11], and reflex charging methods [12–15]. The CTC method has a disadvantage that it has a longer charging time, the CC and CV are the simplest methods to battery charger, but both of them result in the situations of undercharge and overcharge. The hybrid CC/CV method can improve charging efficiency and charging time, but it has a disadvantage of difficult control. To reduce the charging time of the batteries, the reflex charging method is adopted in this paper. The method consists of a high positive pulse-charging current followed by a high current, short time negative pulse-discharging current, and a rest period. A high positive pulse-charging current can reduce the charging time and a negative pulse-discharging current is to reduce internal cell pressure and temperature of batteries. A rest period can provide the batteries with a reflex time in charging process.

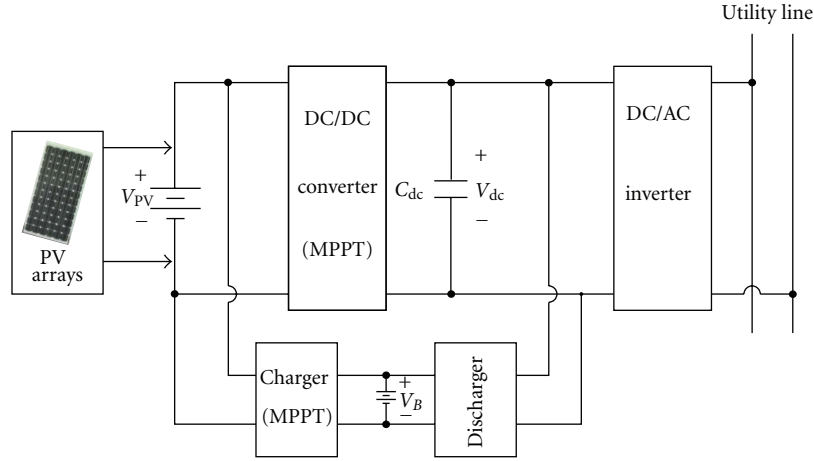


FIGURE 1: Block diagram of a typical PV power system.

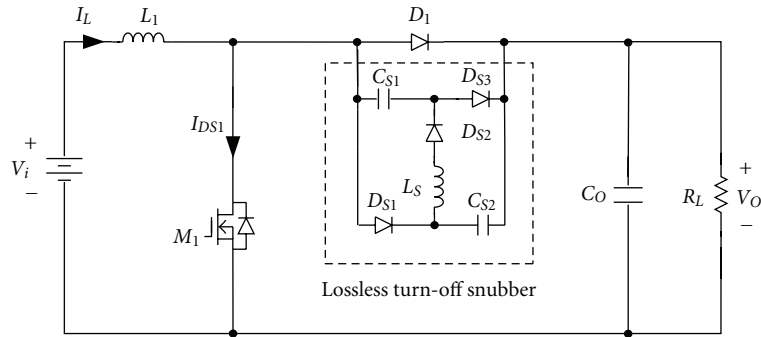


FIGURE 2: Topology of basic boost converter with a passive lossless turn-off snubber.

The basic switching power converters have six circuit structures, such as buck, boost, buck-boost, Cuk, Sepic, and Zeta converters. In order to obtain continuous input current for battery charger, the basic boost converter is widely used. However, it is operated under high switching frequencies resulting in high switching losses, noises, and component stresses. These drawbacks reduce power seriously and deteriorate in the performances of the basic boost converter. In order to alleviate the problems described previously, soft-switching technologies are introduced into the basic boost converter to reduce switching losses. Soft-switching technologies can be classified as passive and active soft-switching technologies. The passive technologies use only passive components to perform soft-switching operation [16–18]. The active technologies add one or more active switches along with other passive components to the basic switching power converters to perform soft-switching operation [19, 20]. For cost considerations, the proposed battery charger with passive soft-switching technologies is more attractive at low power level applications.

A basic boost converter with a passive lossless turn-off snubber for battery charger applications is usually adopted, as shown in Figure 2 [18], because it has a simple structure. However, the basic boost converter has a disadvantage that its output ripple current will swing over a wide range resulting

in a low battery life. In order to reduce output ripple current and increase power level, two sets of boost converters are incorporated with an interleaving fashion, as shown in Figure 3 [21]. Although interleaving boost converter with two sets of passive soft-switching circuits can also achieve soft-switching features, their component counts and cost are increased significantly. To overcome the previously discussed drawbacks, an interleaved boost converter with a single-capacitor turn-off snubber for battery charger applications is proposed, as shown in Figure 4. The proposed battery charger requires only a resonant capacitor C_S which is associated with inductors L_1 and L_2 to reduce switching losses of active switches.

2. Control Algorithm of the Proposed Charger

In order to achieve an optimal power control of battery charger, an MPPT algorithm and a power management unit are needed. These control algorithms are described as follows.

2.1. Topology of Battery Charger. The proposed charger includes an interleaving boost converter and a controller, as shown in Figure 5. Moreover, the controller adopts microchip to implement MPPT of PV arrays and battery

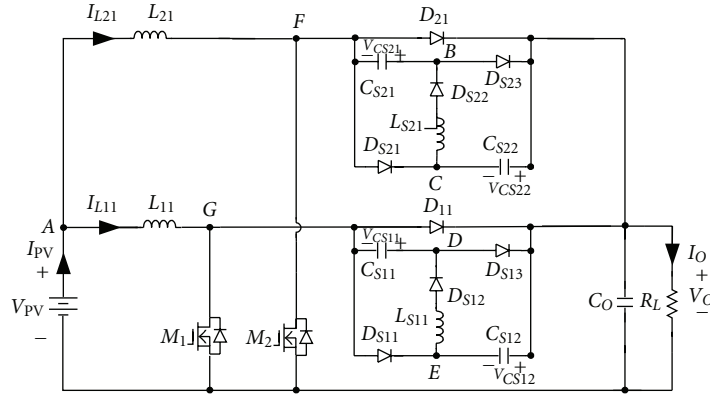


FIGURE 3: Topology of two sets of boost converters operated in an interleaving fashion.

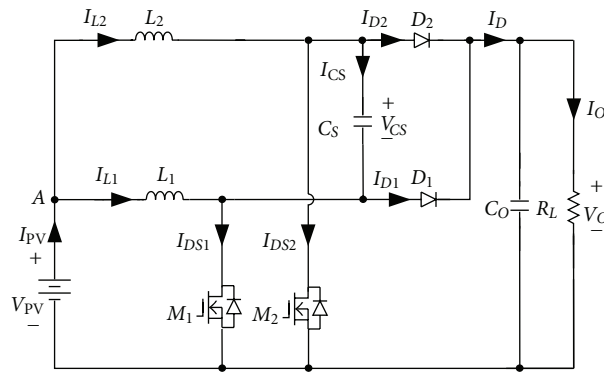


FIGURE 4: Topology of the proposed interleaving boost converter with a single-capacitor turn-off snubber for battery charger applications.

charging management. Therefore, the controller of the proposed battery charger can be divided into three units. They are MPPT operation, battery management, and power management units. The MPPT operation unit can implement the MPPT of PV arrays. The charging algorithm of battery charger is controlled with reflex charging method by battery management unit to reduce the charging time. In order to achieve the best energy utilization of the PV arrays, an MPPT with perturbation-and-observation method is integrated into an MPPT operation unit. Since the MPPT and charging algorithm must be associated to implement optimal control of battery charger, the power management unit is needed. To achieve optimal stability and safety for the proposed battery charger, the functions of under-voltage, over-current, and over-temperature protection circuits are required. All of the protection signals are also realized on a microchip.

2.2. MPPT Algorithm. Output characteristic variations of PV array depend on climatic conditions, such as temperature of PV arrays and insolation of sun. Its P-V curves at different insolation of the sun are shown in Figure 6. From Figure 6, it can be seen that each insolation level has a maximum power P_{max} , where P_{max1} is the maximum power at the largest insolation of sun while P_{max3} is the one at the least insolation of sun. Three maximum power points $P_{max1} \sim P_{max3}$ can be

connected by a straight line. Operational area on the right hand side of the straight line is defined as B area, while the one on the left hand side is defined as A area. Since output load connected in PV arrays increases, output voltage of PV arrays decreases. Therefore, when working point of PV arrays locates in A area, output load must decrease to make the working point to approach the maximum power point of PV arrays. On the other hand, when working point of PV arrays places on B area, output load must increase. Their operation conditions are shown in Figure 7. Figure 7(a) shows the working point located on A area, while Figure 7(b) illustrates the one located on B area. When working point locates on A area, the working point is changed from A_1 to maximum power point P_{max} at point A_6 through $A_2, A_3, A_4,$ and A_5 , as shown in Figure 7(a). When working point locates on B area, the working point is changed from B_1 to maximum power point P_{max} at point B_6 through $B_2, B_3, B_4,$ and B_5 , as shown in Figure 7(b). According to different operational area to increase or decrease output load, working point of PV arrays can be shifted to MPP.

In order to extract maximum power of PV arrays, a simple perturbation-and-observation method is adopted. Its flow chart is shown in Figure 8. In the MPPT flow chart, V_n and I_n are, respectively, new voltage and current of PV arrays, V_p and P_p separately represent its old voltage and power value, and $P_n(= V_n I_n)$ is the new power value of PV

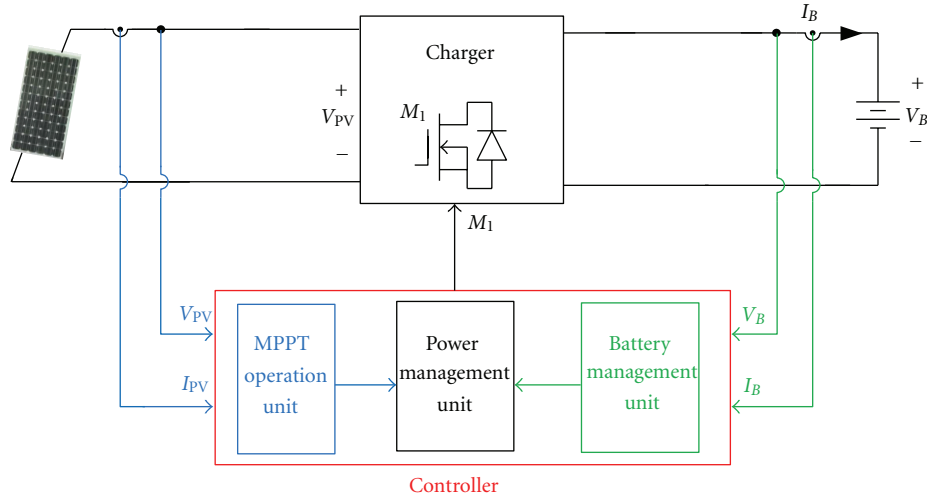
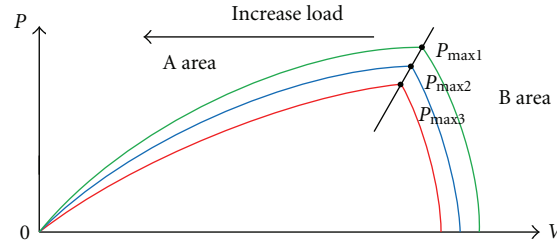


FIGURE 5: Block diagram of battery charger.

FIGURE 6: Plot of P - V curves for PV arrays at different insulations of sun.

arrays. According to flow chart of MPPT using perturbation-and observation-method, the first step is to read new voltage V_n and current I_n of PV arrays, and then to calculate new PV power P_n . The next step is to judge the relationship of P_n and P_p . According to the relationship of P_n and P_p and procedures of MPPT flow chart, the procedure enters to judge the relationship of V_n and V_p . When the relationship of V_n and V_p is decided, operational area of working point can be specified. According to control algorithm of MPPT, when the working point of PV arrays is located in A area, power system connected in PV arrays to supply load power must decrease output power to close the distance between working point and MPP of PV arrays. On the other hand, when the operating point is located in B area, PV power energy must be increased to approach maximum power point of PV arrays. Finally, the procedure of MPPT flow chart is returned to the first step to judge next maximum power point of PV arrays.

2.3. Power Management. The proposed charger is with a reflex charging method to reduce charging time, since the charging voltage and current of batteries must be limited for protecting battery life. The conceptual waveforms of charging current and voltage of battery charger with a reflex charging method are shown in Figure 9. Figure 9(a) shows reflex charging waveforms of battery charger under minimum battery voltage $V_{B(\min)}$, its $V_{B(\min)}$ is expressed as undercharge condition of battery voltage. Figure 9(b)

shows reflex charging waveforms of battery charger under maximum battery voltage $V_{B(\max)}$, its $V_{B(\max)}$ is expressed as overcharge condition of battery voltage. According to $V_{B(\min)}$ and $I_{B(\max)}$ or $V_{B(\max)}$ and $I_{B(\min)}$, the power limitation curve of battery charger can be obtained, as shown in Figure 9. When the maximum power $P_{PV(\max)}$ of PV arrays is larger or less than $P_{\max 1}$, the power operation point of PV arrays is traced as shown in Figure 10. As mentioned previously, the charging and discharging power of the proposed charger will be limited by power curve to extend battery life.

3. Derivation and Operational Principle of the Proposed Charger

In order to describe the merits of the proposed battery charger, its topology derivation and operational principles are briefly described as follows.

3.1. Derivation of the Proposed Charger. To reduce switching losses, a lossless turn-off snubber is inserted in a basic boost converter as shown in Figure 2. When switch M_1 is turned on, capacitors C_{S1} and C_{S2} are charged through inductor L_s and diode D_{S2} in a resonant manner. At the end of the resonant interval, capacitors C_{S1} and C_{S2} are charged to V_O and are clamped at V_O until switch M_1 is turned off. When switch M_1 is turned off, the charges stored

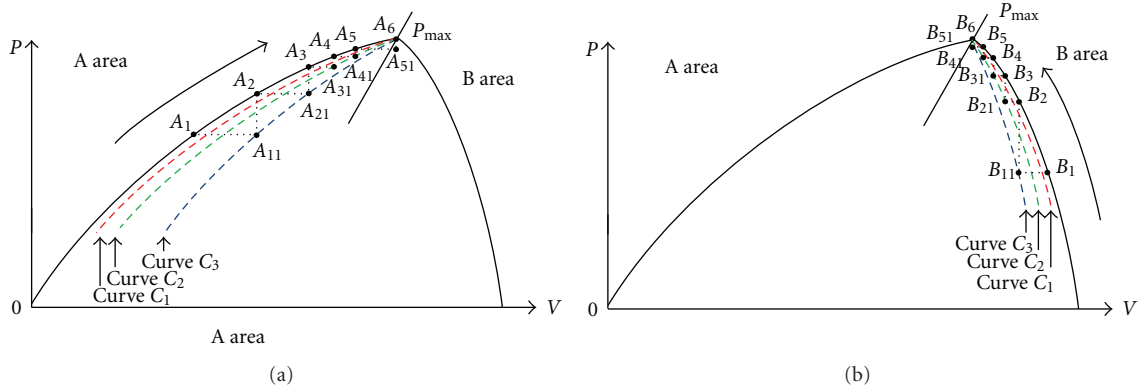


FIGURE 7: Illustration of PV arrays operated in (a) A area and (b) B area for MPPT.

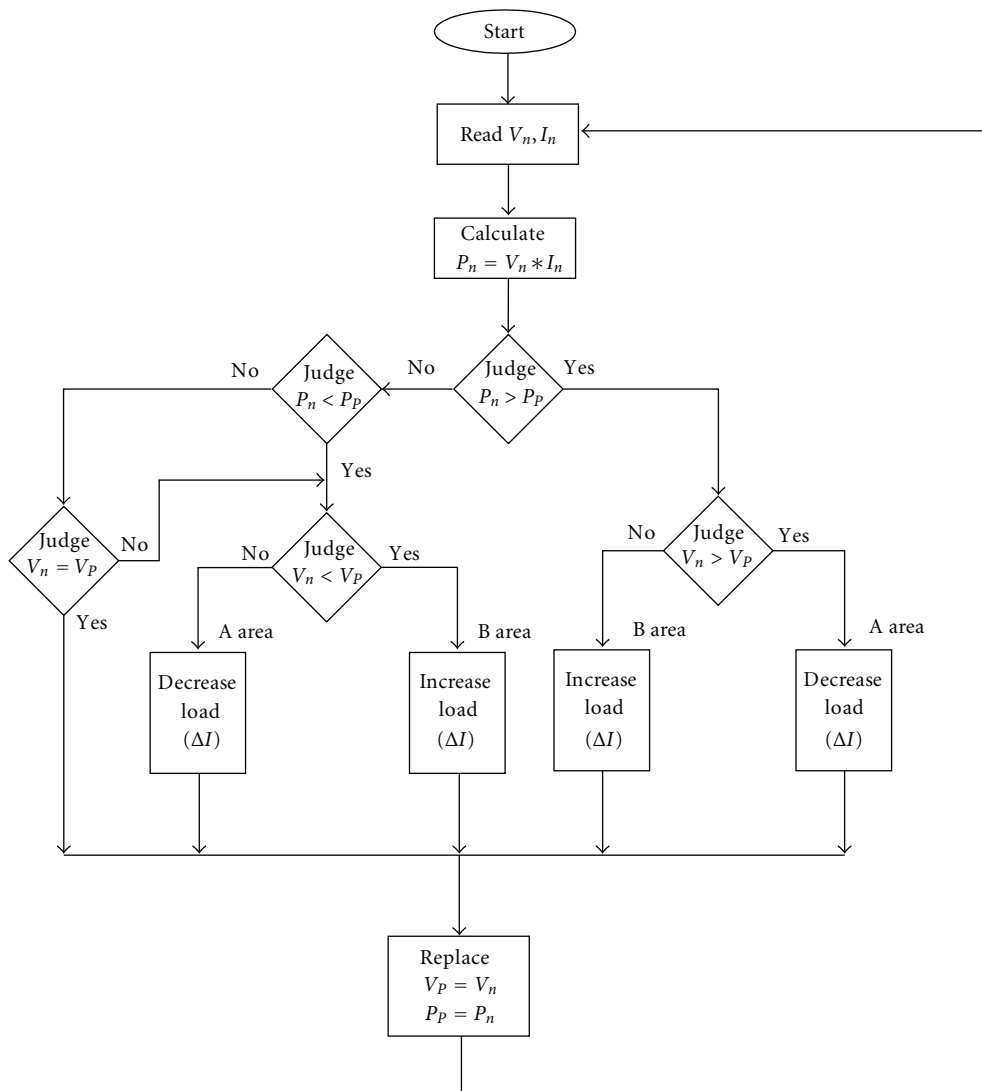


FIGURE 8: Flow chart of MPPT using perturbation-and-observation method for PV arrays system.

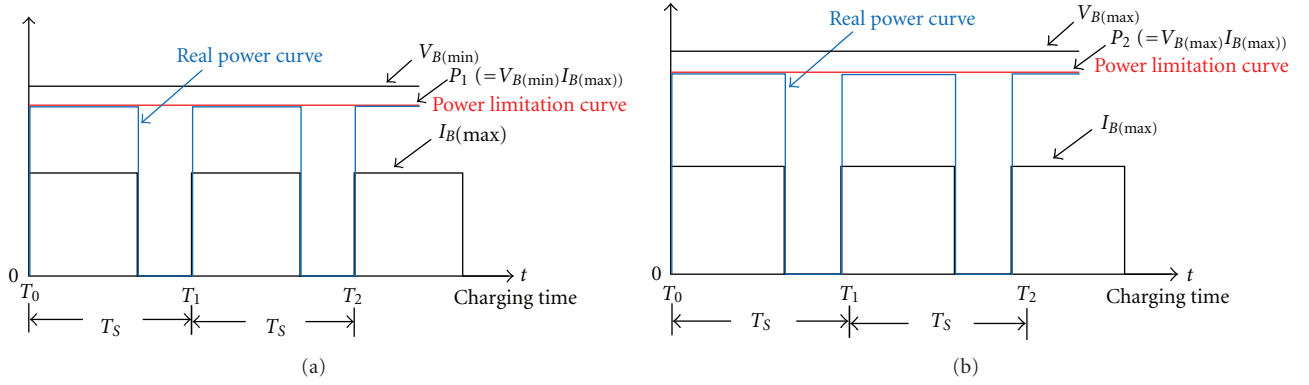


FIGURE 9: Conceptual waveforms of charging current, voltage and power for battery charger with reflex charging method (a) under the minimum battery voltage $V_{B(\min)}$ and (b) under the maximum battery voltage $V_{B(\max)}$.

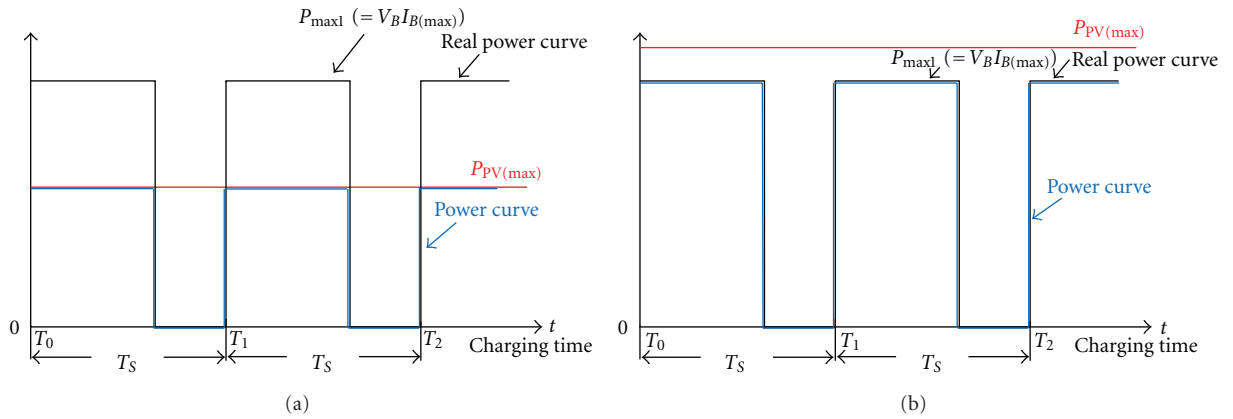


FIGURE 10: Conceptual power waveforms of PV arrays and battery charging power: (a) $P_{PV(\max)} \leq P_{\max 1}$ and (b) $P_{PV(\max)} \geq P_{\max 1}$.

in capacitors C_{S1} and C_{S2} are discharged to output load through diodes D_{S1} and D_{S3} , respectively. Thus, switch M_1 is turned off with zero-voltage transition (ZVT). As mentioned previously, although it can achieve the soft-switching feature, its output current ripple is relatively large for high current and low output voltage applications. Therefore, to reduce output current ripple, an interleaving scheme is usually adopted. In the following, the proposed interleaving boost converter with a single-capacitor snubber is derived.

Two lossless turn-off snubbers are used in an interleaving boost converter to reduce switching losses, as shown in Figure 3. To simplify circuit of Figure 3, voltages of capacitors C_{S12} and C_{S22} are replaced with dc voltages V_{CS12} and V_{CS22} , respectively. When voltages of capacitors C_{S12} and C_{S22} are replaced with dc voltages, the energies stored in capacitors C_{S12} and C_{S22} do not need to discharge their charges. Thus, diodes D_{S11} and D_{S21} can be removed, as shown in Figure 11(a). If voltage V_{CS12} or V_{CS22} is equal to $(V_O - V_{PV})$, nodes A, C, and E will have the same potential. Thus, they can be merged as node A, as shown in Figure 11(b). Based on the operational principle of an interleaving boost converters and the turn-off snubber, operational states of diode D_{11} (or D_{21}) is the same as diode D_{S23} (or D_{S13}) except that the operational duration of the turn-off snubber is operated

within resonant mode. Since the duration of resonant mode is much shorter than a period of the proposed converters, nodes F and D (or G and B) can be combined as the same node H (or I), as shown in Figure 11(c). It will not affect its original operational principle. Because inductor currents I_{L11} and I_{L21} are unidirectional in the derived converter, inductors L_{11} and L_{S21} connected with diode D_{S22} in series can be combined and replaced by inductor L_1 . Similarly, inductors L_{21} and L_{S11} and diode D_{S12} can be also merged as inductor L_2 , as shown in Figure 11(d). In Figure 11(c), since capacitors C_{S11} and C_{S21} and diodes D_{11} and D_{S23} or D_{21} and D_{S13} are, respectively, connected in parallel, they can be, respectively, incorporated as capacitor C_S and diode D_1 or D_2 . From Figure 11(d), it can be observed that the derived boost converter requires only a resonant capacitor C_S , which is associated with inductors L_1 and L_2 to function as a lossless turn-off snubber, reducing switching losses and component counts significantly. Therefore, Figure 11(d) is proposed for battery charger applications.

3.2. Operational Principle of the Proposed Charger. In Figure 4, the proposed battery charger with a single-capacitor turn-off snubber can achieve a ZVT feature for active switches. Operational modes of the proposed charger are divided

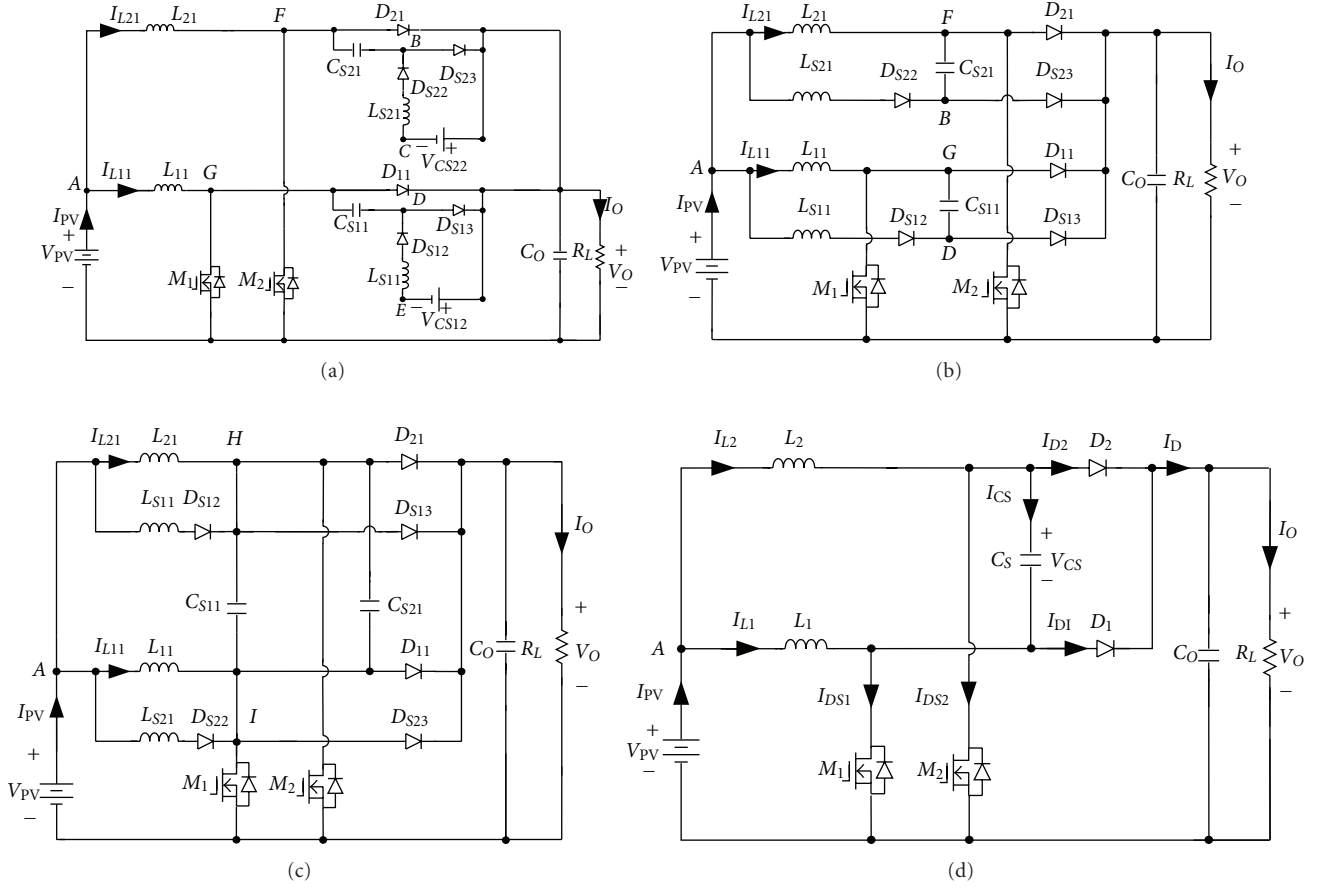


FIGURE 11: Derivation of the proposed battery charger with a single-capacitor turn-off snubber.

into ten modes, as illustrated in Figure 12, and their key waveforms are illustrated in Figure 13. In the following, each operational mode is described briefly.

Mode 1 (Figure 12(a); $t_0 \leq t < t_1$). Before t_0 , diode D_2 is in freewheeling, and inductor current I_{L2} is equal to diode current I_{D2} . At $t = t_0$, switch M_1 is turned on. The equivalent circuit at this time interval is shown in Figure 12(a), from which it can be found that switch current I_{DS1} is equal to the sum of capacitor current I_{CS} and inductor current I_{L1} . Since the interval of $t_0 \sim t_1$ is very short, inductor current I_{L1} is approximately equal to zero and capacitor voltage V_{CS} is close to zero. Thus, switch current I_{DS1} is approximately equal to capacitor current I_{CS} . During this time interval, the current I_{CS} is abruptly increased up to inductor current I_{L2} , and I_{D2} is abruptly decreased down to zero.

Mode 2 (Figure 12(b); $t_1 \leq t < t_2$). At time t_1 , capacitor current I_{CS} is equal to inductor current I_{L2} , and diode D_2 is reversely biased. At this time interval, snubber capacitor C_S resonates with inductor L_2 , and switch current I_{DS1} is just equal to the sum of resonant inductor current $I_{L2}(= I_{CS})$ and inductor current I_{L1} . At the same time, capacitor current

I_{CS} reaches its maximum value which can be expressed as follows:

$$I_{CS} = \frac{V_i}{Z_O}, \quad (1)$$

where Z_O is the characteristic impedance of L_2 - C_S or L_2 - C_S network, which is equal to $\sqrt{L_1/C_S}$ or $\sqrt{L_2/C_S}$.

Mode 3 (Figure 12(c); $t_2 \leq t < t_3$). When $t = t_2$, capacitor voltage V_{CS} is equal to V_O , and diode D_2 starts freewheeling through inductor L_2 . At the same time, switch M_1 is still in the on state. The switch current I_{DS1} is now equal to inductor current I_{L1} which increases linearly, while inductor current I_{L2} is decreased linearly.

Mode 4 (Figure 12(d); $t_3 \leq t < t_4$). At time t_3 , switch M_1 is turned off. Because inductor current I_{L1} must be continuous, capacitor C_S starts to discharge for sustaining a continuous inductor current. Thus, switch M_1 can be turned off with ZVT.

Mode 5 (Figure 12(e); $t_4 \leq t < t_5$). When time reaches t_4 , the voltage V_{CS} across capacitor C_S is discharged toward zero,

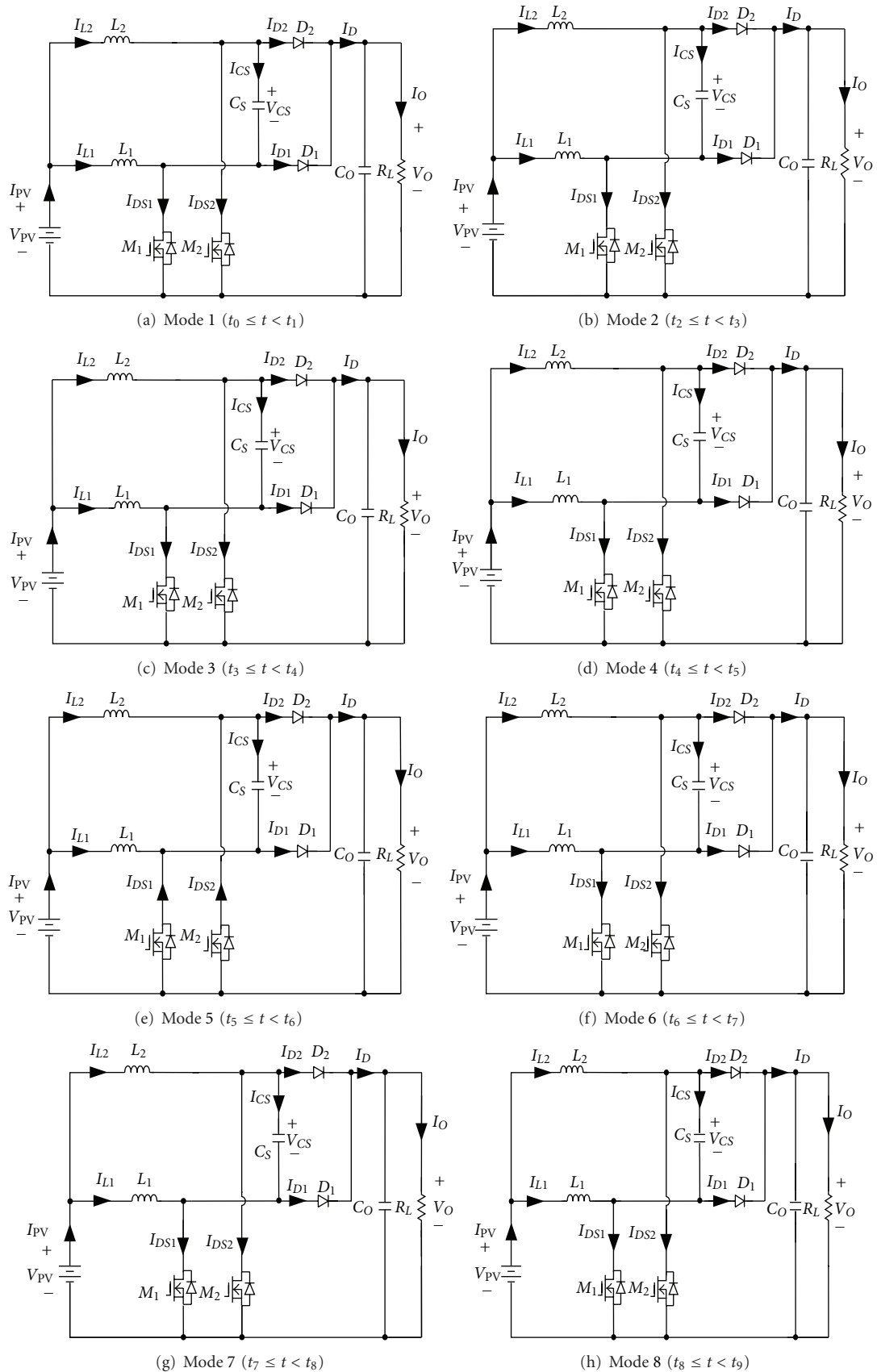


FIGURE 12: Continued.

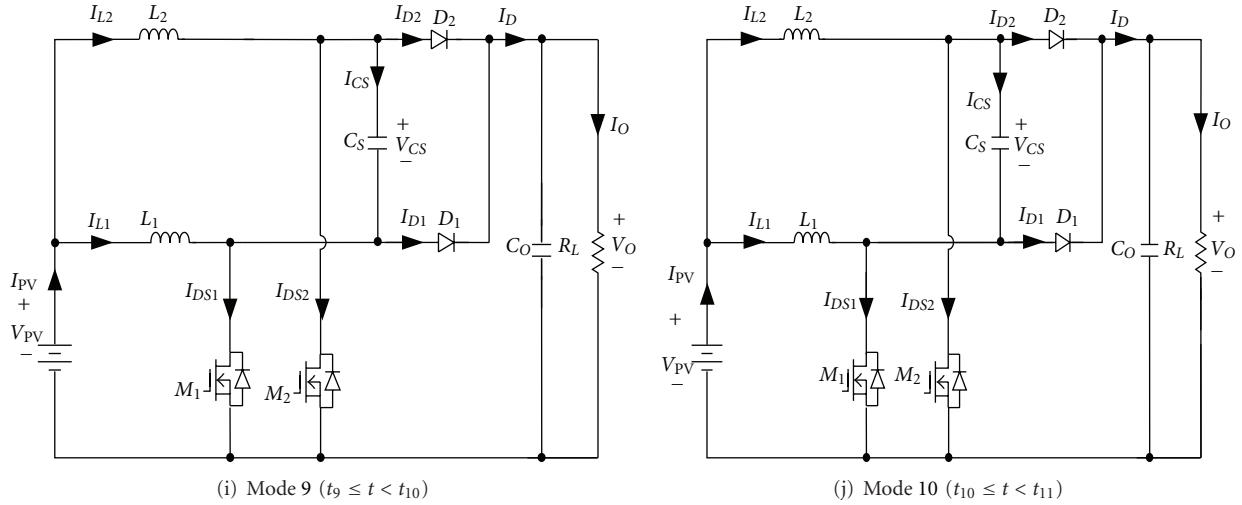


FIGURE 12: Operational modes of the proposed battery charger over one switching cycle.

and diode D_1 starts freewheeling. During this time interval, diodes D_1 and D_2 are in freewheeling through inductors L_1 and L_2 , respectively.

Mode 6 (Figure 12(f); $t_5 \leq t < t_6$). At time t_5 , diode D_1 is still in freewheeling, but diode D_2 stops freewheeling because inductor current I_{L2} drops to zero. In this moment, switch M_2 is turned on. Inductor current I_{L1} is equal to the sum of diode current I_{D1} and capacitor current $-I_{CS}$. Additionally, because the switch current I_{DS2} will flow through the low-impedance path of capacitor C_S , diode current I_{D1} will be dominated by the switch current I_{DS2} . That is, within this time duration, capacitor current $-I_{CS}$ is approximately equal to the switch current I_{DS2} . Capacitor current $-I_{CS}$ is abruptly increased up to inductor current I_{L1} , and I_{D1} is abruptly decreased down to zero.

Mode 7 (Figure 12(g); $t_6 \leq t < t_7$). At time t_6 , diode D_1 is reversely biased, and resonant network formed by capacitor C_S and inductor L_1 starts resonating. The switch current I_{DS2} is equal to the sum of inductor current I_{L1} ($= -I_{CS}$) and inductor current I_{L2} , and capacitor C_S is reversely charged.

Mode 8 (Figure 12(h); $t_7 \leq t < t_8$). At $t = t_7$, the capacitor voltage V_{CS} goes down to $-V_O$. The time interval lasts approximately a quarter of the resonant cycle. At the same time, capacitor current $-I_{CS}$ reaches its maximum value, which can be expressed by (1). During this mode, diode D_1 starts freewheeling, and inductor current I_{L2} is increased linearly.

Mode 9 (Figure 12(i); $t_8 \leq t < t_9$). At time t_8 , switch M_2 is turned off. Since the inductor current I_{L2} must be in smooth transition, capacitor voltage will drop to maintain a continuous inductor current. When $t = t_9$, capacitor voltage V_{CS} drops to zero.

Mode 10 (Figure 12(j); $t_9 \leq t < t_{10}$). During this time interval, diodes D_1 and D_2 are in freewheeling through

inductors L_1 and L_2 , and their currents I_{D1} and I_{D2} are decreased linearly. When switch M_1 is turned on again at the end of Mode 10, a new switching cycle will be recycled.

4. Control and Design of the Proposed Charger

In order to achieve optimal control of the proposed charger, the MPPT operation algorithm of PV arrays and reflex charging algorithm of battery must be considered. In the following, control and design of the proposed charger are described.

4.1. Control of the Proposed Charger. The proposed charger consists of an interleaving boost converter and controller. The controller adopts microchip of CY8C27443 made by Cypress Company. Block diagram of the proposed charger is shown in Figure 14. In Figure 14, the CY8C27443 microchip is divided into three units: MPPT, battery management, and power management units. In MPPT unit, the perturbation-and-observation method is adopted to trace maximum power point of PV arrays. The maximum power P_P of PV arrays can be decided. Moreover, battery management unit has four input signals (V_B , $V_{B(\max)}$, I_B , and $I_{B(\max)}$) where V_B is the battery voltage, $V_{B(\max)}$ is the set maximum battery voltage, I_B is the battery charging current, and $I_{B(\max)}$ is the set maximum battery charging current. According to four input signals, $P_B (= V_B I_B)$ and $P_{B(\max)} (= V_B I_{B(\max)})$ can be calculated. The P_B represents the present charging power of battery, while $P_{B(\max)}$ is the set maximum charging power. In addition, when V_B is equal to or greater than $V_{B(\max)}$, protection judgment makes output signal S_P from low to high value. The S_P is sent to PWM generator for shutdown PWM generator to avoid battery overcharge. In power management unit, a comparator is used to judge relationship of P_P and $P_{B(\max)}$. When $P_P (= P_{PV(\max)})$ is greater than $P_{B(\max)}$, signal S_1 is high and switch selector is operated to set $P_{\text{set}} = P_{B(\max)}$. When P_P is equal to or less than $P_{B(\max)}$, signal S_1 is low and switch selector is operated to set

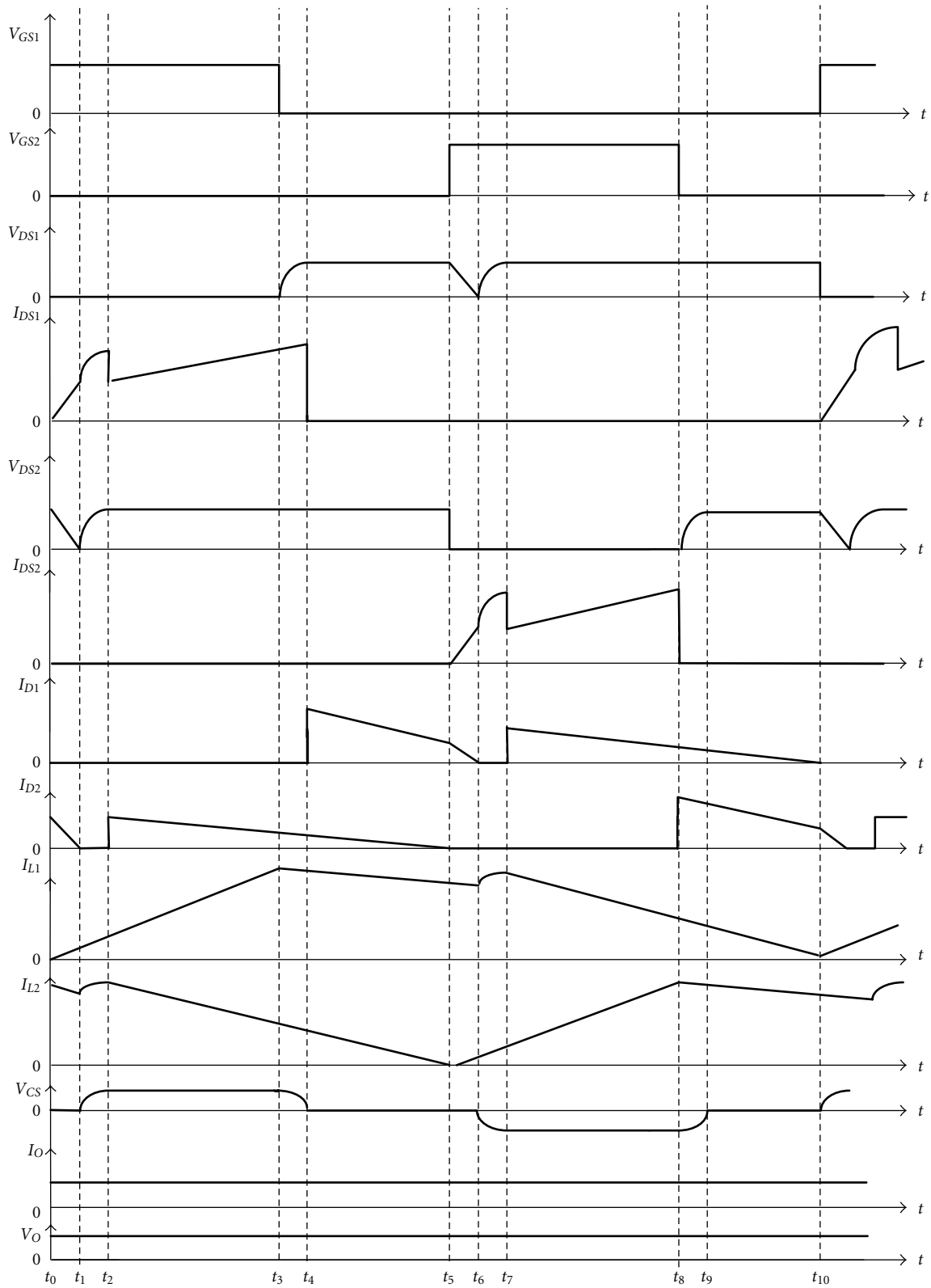


FIGURE 13: Key waveforms of the proposed battery charger operating over one switching cycle.

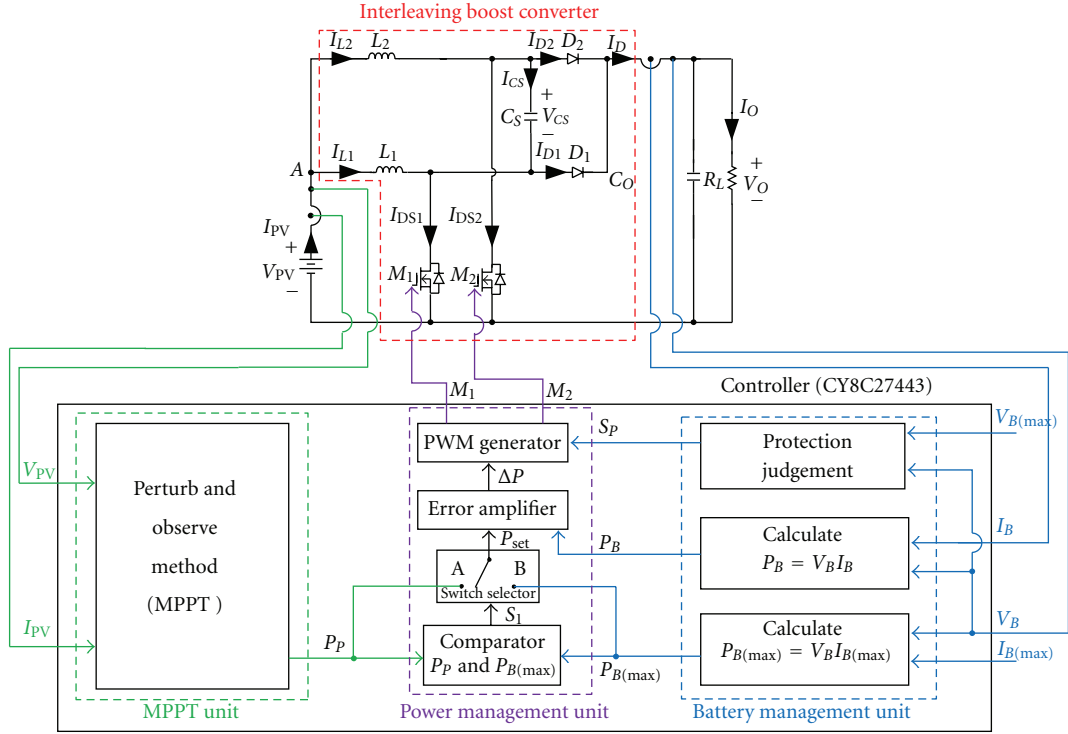


FIGURE 14: Block diagram of the proposed battery charger.

$P_{set} = P_B$. The P_{set} and P_B are sent to error amplifier to attain error value ΔP . When PWM generator attains ΔP , ΔP and triangle waves inside PWM generator attain PWM signals M_1 and M_2 via the comparator. The interleaving boost converter can change charging current I_B according to PWM signals M_1 and M_2 .

4.2. Design of the Proposed Charger. To realize the proposed soft-switching charger systematically, design of inductor L_1 or L_2 and the snubber C_S are presented as follows.

4.2.1. Design of Inductor L_1 or L_2 . Since the proposed charger is operated at the boundary of continuous conduction mode (CCM) and discontinuous conduction mode (DCM), the relationship between V_i and V_O can be attained with volt-second balance principle. Thus, transfer function $M(= V_O/V_{PV})$ can be expressed as

$$M = \frac{1}{1-D}, \quad (2)$$

where D is duty ratio of the proposed charger. When duty ratio D is determined by the relationship between V_{PV} and V_O , inductor L_1 or L_2 can also be expressed as

$$L_1 = L_2 = \frac{D(1-D)V_O}{2I_O} T_S, \quad (3)$$

where T_S is the switching cycle of the proposed charger and I_O is output current.

4.2.2. Design of Snubber Capacitor C_S . In the proposed charger, capacitor C_S resonates with inductor L_1 or L_2 to smooth out switch voltage at turn-off transition. The energy stored in C_S can be determined as

$$W_{CS} = \frac{1}{2} C_S V_O^2. \quad (4)$$

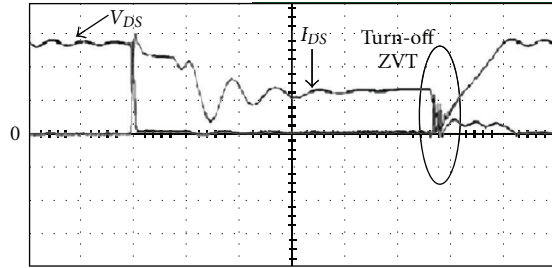
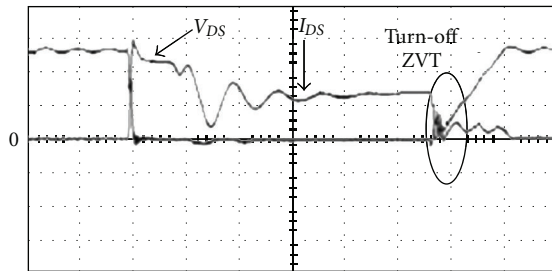
To completely eliminate the switch turn-off loss, the energy stored in capacitor C_S must be at least equal to the turn-off loss W_{Soff} . According to switching loss calculation of switch, W_{Soff} can be expressed by

$$W_{Soff} = \frac{t_{Soff}}{2} V_O I_{DP}, \quad (5)$$

where t_{Soff} is the falling time of switch at turn-off transition, V_O represents output voltage and I_{DP} is switch current at turn-off transition of switch. Therefore, capacitor C_S can be determined as

$$C_S \geq \frac{I_{DP}}{V_O} t_{Soff}. \quad (6)$$

The peak current I_{CS} of capacitor C_S should be limited to being less than the peak values of I_{DS1} and I_{DS2} , so it will not increase the current ratings of switches M_1 or M_2 . To eliminate turn-off loss W_{Soff} completely at different operation conditions, the time t_{Soff} is approximately equal to 200 ns in practical design considerations.

(a) (V_{DS1} : 50 V/div, I_{DS1} : 5 A/div, time: 1 μ s/div)(b) (V_{DS1} : 50 V/div, I_{DS1} : 5 A/div, time: 1 μ s/div)FIGURE 15: Measured voltage and current waveforms of (a) switch M_1 , and (b) switch M_2 in the proposed converters.

5. Measurements and Results

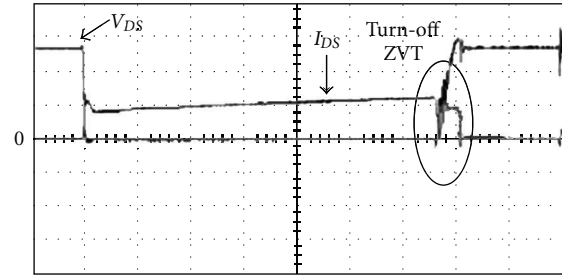
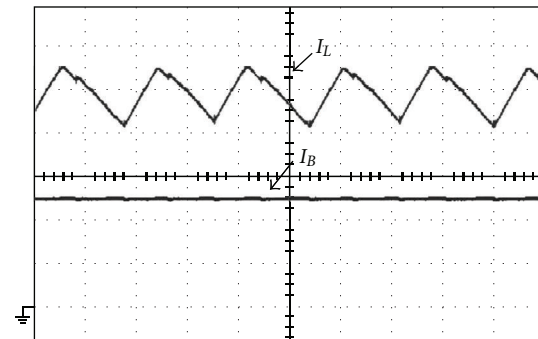
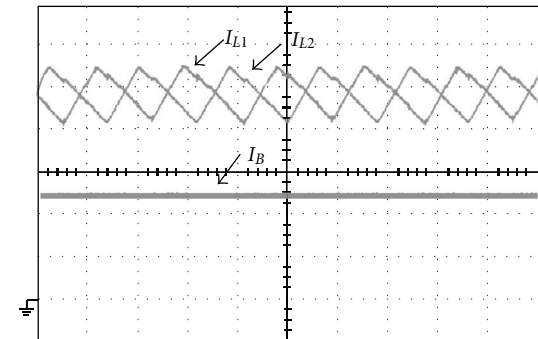
To verify the analysis and discussion, a PV system used to charge 48 V battery with the following specifications was implemented:

- (i) input voltage V_i : 34 ~ 42 V_{dc} (PV arrays),
- (ii) output voltage V_O : 44 ~ 54 V_{dc} (4 sets of 12 V battery connected in series),
- (iii) output maximum current $I_{O(max)}$: 10 A,
- (iv) output maximum power $P_{O(max)}$: 540 W.

From (6), value of snubber capacitor C_S can be calculated as 37 nF where I_{DP} is 10 A and V_O is 54 V. In our design sample, a capacitor with 39 nF is adopted. The components of power stage in the proposed boost converters are determined as follows:

- (i) M_1, M_2 : IRFP250,
- (ii) D_1, D_2 : MVUR1560,
- (iii) C_O : 470 μ F,
- (iv) L_1, L_2 : 30 μ H,
- (v) C_S : 39 nF,
- (vi) inductor core: EE-35.

The measured voltage and current waveforms of the active switches with the proposed single-capacitor snubber (as shown in Figure 4) and with two sets of turn-off snubbers (as shown in Figure 3) are shown in Figures 15 and 16, respectively. Although we can observe that each power switch is turned off with ZVT feature, there still exist significant differences. Compare with Figures 15 and 16, we can see

FIGURE 16: (V_{DS1} : 50 V/div, I_{DS1} : 5 A/div, time: 1 μ s/div). Measured voltage and current waveforms of switch in the interleaved boost converter with two sets of turn-off snubbers.(a) (I_L : 1 A/div, I_B : 5 A/div, time: 10 μ s/div)(b) (I_{L1}, I_{L2} : 1 A/div, I_B : 5 A/div, time: 10 μ s/div)FIGURE 17: Measured waveforms of inductor current I_L and charging current I_B of (a) single boost converter and (b) the proposed interleaving boost converter.

that the rise voltage curves of Figure 15 are smoother than those of Figure 16. The reason of this is that interleaving boost converter with two sets of turn-off snubbers, causes an abrupt energy on active switches and results in more switching losses. Figure 17(a) shows measured inductor current and charging current of the single boost converter with a turn-off snubber, and Figure 17(b) shows measured inductor current and charging current of the proposed interleaved boost converter with a single-capacitor turn-off snubber. From Figure 17, it can be seen that the proposed converter with a single-capacitor turn-off snubber has a lower ripple charging current I_B .

To make a fair comparison, the hardware components of the proposed charger and hard-switching boost charger

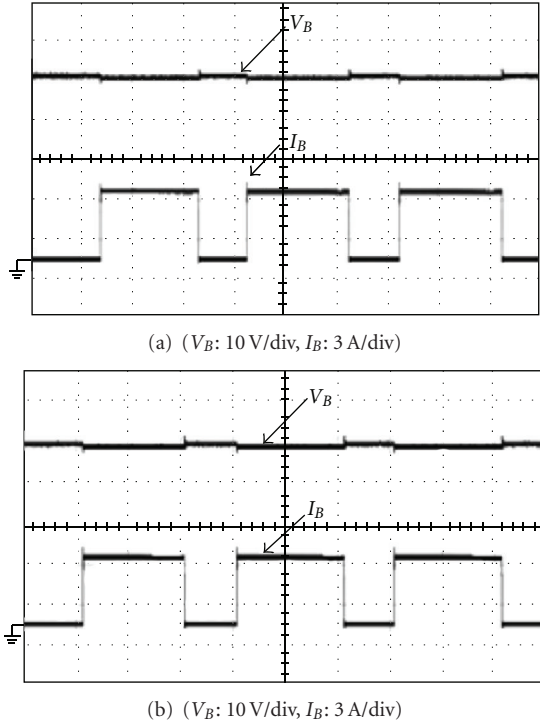


FIGURE 18: Battery voltage V_B and charging current I_B under step-load changes between 20% and 100% of full load of the discussed interleaving boost converters with (a) hard switching (b) a single-capacitor turn-off snubber.

are kept as the same as possible. Figure 18 shows the plots of output voltage and current waveforms of the two kinds of chargers under step-load changes between 20% and 100% with, respectively, rate of 1 kHz and a duty ratio of 50%. From Figure 18, it can be observed that although the proposed charger uses less component counts, it yields almost the same dynamic performance as those with complicated configurations. The comparisons between the efficiencies of the proposed charger and their counterparts are illustrated in Figure 19. It can be observed that the proposed charger cannot always yield higher efficiencies than the others under various operating conditions. It has a trend that, at higher output load, the proposed charger and the ones with two turn-off snubbers can yield higher efficiency, while at lower ones, the discussed charger with two sets of turn-off snubbers yields lower efficiency than the others. The reasons behind this are that at a fixed power level, a higher output load level will result in higher switch currents and the turn-off losses W_{Soff} will be much higher than the sum of the extra conduction loss W_{ES} and switching loss W_{Son} . Figure 20 shows the measured waveforms of battery voltage V_B and charging current I_B with pulse current charging method under repetitive rate of 1 s and duty ratio of 500 ms, as shown in Figure 14. Figure 20(a) shows those waveforms under $P_{PV(max)} = 50$ W, while Figure 20(b) illustrates those waveforms $P_{PV(max)} = 100$ W. From Figure 20, it can be seen that maximum pulse charging current $I_{O(max)}$, respectively, is limited 1 A (about 0.15 C) and

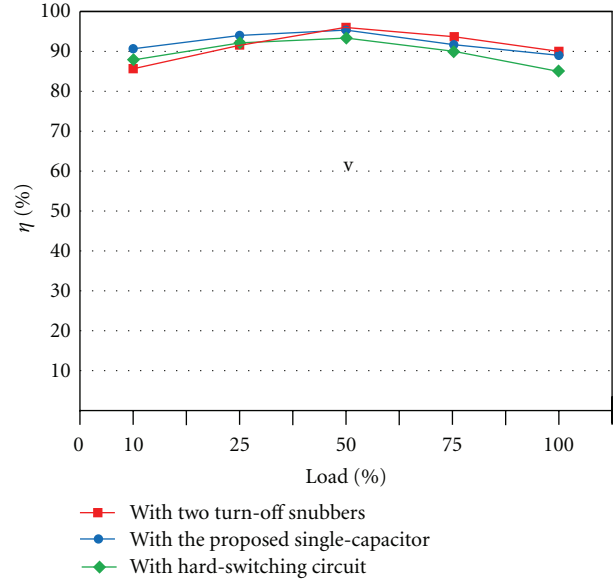


FIGURE 19: Comparison among efficiencies of the discussed interleaving boost converter with a single-capacitor turn-off snubber, hard switching, and two sets of turn-off snubbers from light load to heavy load.

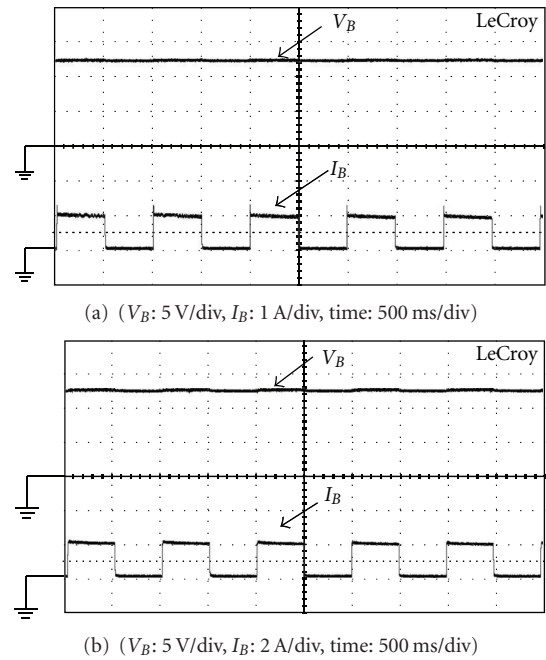


FIGURE 20: Measured waveforms of battery voltage V_B and charging current I_B with pulse current charging method: (a) $I_{B(max)} = 1$ A and (b) $I_{B(max)} = 2$ A.

2 A (about 0.3 C), where battery adopts lead-acid battery and capacity of each battery is 12 V/7 Ah and total battery voltage is 50 V. Measured waveforms of voltage V_{PV} , current I_{PV} and power P_{PV} of PV arrays with perturbation-and-observation method are used to implement MPPT. Figure 21(a) shows those waveforms under maximum power point $P_{PV(max)}$ at 100 W, while Figure 21(b) depicts those waveforms under

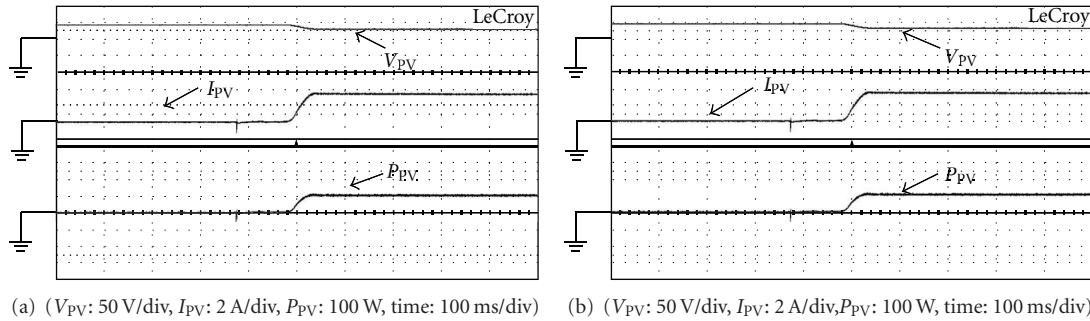


FIGURE 21: Measured waveforms of voltage V_{PV} , current I_{PV} and Power P_{PV} of PV arrays with perturbation- and-observation method to implement MPPT: (a) $P_{PV(\max)} = 100$ W, and (b) $P_{PV(\max)} = 200$ W.

$P_{PV(\max)}$ at 200 W. From Figure 21, it can be found that tracking time of PV arrays from zero to the maximum power point is about 40 ms.

6. Conclusions

In this paper, an interleaving boost converter with a passive snubber for battery charger applications is proposed. The proposed charger with a single-capacitor snubber to reduce voltage stresses of active switches at turn-off transition. Therefore, the conversion efficiency of the proposed charger can be increased significantly. In order to draw maximum power from the PV energy, a simple perturbation-and-observation method is incorporated to realize maximum power conversion. To verify the merits of the proposed charger, the operational principle, steady-state analysis, and design considerations have been described in detail. Additionally, from the experimental efficiency of the proposed charger, it has been shown that the proposed charger can yield higher efficiency at heavy load condition. An experimental prototype for a battery charger application (540 W, 54 V_{dc}/10 A) has been built and evaluated, achieving the efficiency of 88% under full load condition. Therefore, the proposed interleaving boost converter is relatively suitable for battery charger applications.

References

- [1] S. L. Brunton, C. W. Rowley, S. R. Kulkarni, and C. Clarkson, "Maximum power point tracking for photovoltaic optimization using ripple-based extremum seeking control," *IEEE Transactions on Power Electronics*, vol. 25, no. 10, pp. 2531–2540, 2010.
- [2] V. Agarwal, R. K. Aggarwal, P. Patidar, and C. Patki, "A novel scheme for rapid tracking of maximum power point in wind energy generation systems," *IEEE Transactions on Energy Conversion*, vol. 25, no. 1, pp. 228–236, 2010.
- [3] A. M. Subiyanto and S. Hussain, "Hopfield neural network optimized fuzzy logic controller for maximum power point tracking in a photovoltaic system," *International Journal of Photoenergy*, vol. 2012, Article ID 798361, 13 pages, 2012.
- [4] M. Taherbaneh, A. H. Rezaie, H. Ghafoorifard, K. Rahimi, and M. B. Menhaj, "Maximizing output power of a solar panel via combination of sun tracking and maximum power point tracking by fuzzy controllers," *International Journal of Photoenergy*, vol. 2010, Article ID 312580, 13 pages, 2010.
- [5] X. Weidong and W. G. Dunford, "A modified adaptive hill climbing MPPT method for photovoltaic power systems," in *Proceedings of the IEEE 35th Annual Power Electronics Specialists Conference (PESC '04)*, vol. 3, pp. 1957–1963, June 2004.
- [6] K. Kobayashi, H. Matsuo, and Y. Sekine, "An excellent operating point tracker of the solar-cell power supply system," *IEEE Transactions on Industrial Electronics*, vol. 53, no. 2, pp. 495–499, 2006.
- [7] S. Jain and V. Agarwal, "A new algorithm for rapid tracking of approximate maximum power point in photovoltaic systems," *IEEE Power Electronics Letters*, vol. 2, no. 1, pp. 16–19, 2004.
- [8] H. S. H. Chung, K. K. Tse, S. Y. R. Hui, C. M. Mok, and M. T. Ho, "A novel maximum power point tracking technique for solar panels using a SEPIC or Cuk converter," *IEEE Transactions on Power Electronics*, vol. 18, no. 3, pp. 717–724, 2003.
- [9] B. M. T. Ho and H. S. H. Chung, "An integrated inverter with maximum power tracking for grid-connected PV systems," *APEC*, vol. 3, pp. 953–962, 2004.
- [10] D. Casadei, G. Grandi, and C. Rossi, "Single-phase single-stage photovoltaic generation system based on a ripple correlation control maximum power point tracking," *IEEE Transactions on Energy Conversion*, vol. 21, no. 2, pp. 562–568, 2006.
- [11] A. A.-H. Hussein and I. Batarseh, "A review of charging algorithms for nickel and lithium battery chargers," *IEEE Transactions on Vehicular Technology*, vol. 60, no. 3, pp. 830–838, 2011.
- [12] F. Savoye, P. Venet, M. Millet, and J. Groot, "Impact of periodic current pulses on Li-Ion battery performance," *IEEE Transactions on Industrial Electronics*, vol. 59, no. 9, pp. 3481–3488, 2012.
- [13] L. R. Chen, "Design of duty-varied voltage pulse charger for improving Li-ion battery-charging response," *IEEE Transactions on Industrial Electronics*, vol. 56, no. 2, pp. 480–487, 2009.
- [14] Y. C. Chuang and Y. L. Ke, "High efficiency battery charger with a buck zero-current-switching pulse-width-modulated converter," *Interactive Electronic Technical Specification*, vol. 1, pp. 433–444, 2008.
- [15] L. R. Chen, C. M. Young, N. Y. Chu, and C. S. Liu, "Phase-locked bidirectional converter with pulse charge function for 42-V/14-V dual-voltage PowerNet," *IEEE Transactions on Industrial Electronics*, vol. 58, no. 5, pp. 2045–2048, 2011.
- [16] J. Yun, H.-J. Choe, Y.-H. Hwang, Y.-K. Park, and B. Kang, "Improvement of power-conversion efficiency of a DC—DC

- boost converter using a passive snubber circuit," *IEEE Transactions on Industrial Electronics*, vol. 59, no. 4, pp. 1808–1814, 2012.
- [17] C. A. Gallo, F. L. Tofoli, and J. A. C. Pinto, "A passive lossless snubber applied to the ACDC interleaved boost converter," *IEEE Transactions on Power Electronics*, vol. 25, no. 3, pp. 775–785, 2010.
- [18] C. Munoz, "Study of a new passive lossless turn-off snubber," *CIEP*, pp. 147–152, 1998.
- [19] B. R. Lin and H. Y. Shih, "ZVS converter with parallel connection in primary side and series connection in secondary side," *IEEE Transactions on Industrial Electronics*, vol. 58, no. 4, pp. 1251–1258, 2011.
- [20] T.-F. Wu, Y.-D. Chang, C.-H. Chang, and J.-G. Yang, "Soft-switching boost converter with a flyback snubber for high power applications," *IEEE Transactions on Power Electronics*, vol. 27, no. 3, pp. 1108–1119, 2012.
- [21] Y. K. Luo, Y. P. Su, Y. P. Huang, Y. H. Lee, K. H. Chen, and W. C. Hsu, "Time-multiplexing current balance interleaved current-mode boost DC-DC converter for alleviating the effects of right-half-plane zero," *IEEE Transactions on Power Electronics*, vol. 27, no. 9, pp. 4098–4112, 2012.

Research Article

On the Performance of Hybrid PV/Unitized Regenerative Fuel Cell System in the Tropics

Salwan Dihrab,¹ Tamer Khatib,² Kamaruzzaman Sopian,³
Habeb Al-Ani,³ and Saleem H. Zaidi³

¹Center of Renewable energy, Universiti Tenaga Nasional, Bangi 43000, Selangor, Malaysia

²Department of Electrical, Electronic & System Engineering, Faculty of Engineering & Built Environment, Universiti Kebangsaan Malaysia, Bangi 43600, Selangor, Malaysia

³Solar Energy Research Institute, Universiti Kebangsaan Malaysia, Bangi 43600, Selangor, Malaysia

Correspondence should be addressed to Tamer Khatib, tamer_khat@hotmail.com

Received 20 August 2012; Revised 21 October 2012; Accepted 31 October 2012

Academic Editor: Tapas Mallick

Copyright © 2012 Salwan Dihrab et al. This is an open access article distributed under the Creative Commons Attribution License, which permits unrestricted use, distribution, and reproduction in any medium, provided the original work is properly cited.

Solar hydrogen system is a unique power system that can meet the power requirements for future energy demands. Such a system uses the hydrogen as the energy carrier, which produces energy through the electrolyzer with assistance of the power from the PV during the sunny hours, and then uses stored hydrogen to produce energy through the fuel cell after sunset or on cloudy days. The current study has used premanufactured unitized regenerative fuel cells in which the electrolyzer and the fuel cell function within one cell at different modes. The system components were modeled and the one-day real operational and simulated data has been presented and compared. The measured results showed the ability of the system to meet the proposed load, and the total efficiency was about 4.5%.

1. Introduction

Photovoltaic (PV) power generation, which directly converts solar radiation into electricity, contains a lot of significant advantages, such as being inexhaustible and pollution-free, silent and with no rotating parts, and its size-independent electricity conversion efficiency. A positive environmental effect of photovoltaic is replacing electricity generated in a more pollutant way, or providing electricity where none was available before. While increasing the penetration of solar photovoltaic devices, various antipollution apparatuses can be operated by solar PV power, for example, water purification by electrochemical processing or stopping desert expansion by photovoltaic water pumping with tree implantation [1].

The hybrid PV/hydrogen systems have units producing hydrogen called electrolyzers, which are used to generate hydrogen with the assistance of the PV as an energy source. This hydrogen will be preserved in suitable storage medium before being converted to DC power through a unit called fuel cell. Fuel cells are electrochemical devices that convert

chemical energy, typically from hydrogen, directly into electrical energy. The introduction of fuel cell systems into the power generation market will not only supply clean renewable energy to millions of users, but it will help to reduce the dependence on oil [2].

Such a system includes a source of power (PV modules), a hydrogen generator (electrolyzer), a storage medium to store the hydrogen and hydrogen utilization units (fuel cell) which are able to make a continuous, and self-dependant or uninterruptable source of energy. The PV size should be designed properly, in order to have excess power over the load requirement. This excess power will be used to generate hydrogen through the generation units, and it will then utilize it after sunset or at a time of low solar irradiation. The load in this system will be powered in the short-term by the PV modules, and the hydrogen system will act as a long-term supplier. An illustration of short- and long-term supplying is shown in Figure 1.

The modeling of a PV-powered hydrogen generation system is needed to solve the electrical equations for the PV and the DC/DC converters (if they exist) and the electrochemical

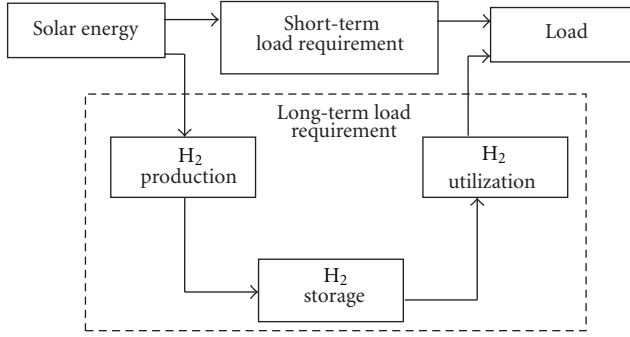


FIGURE 1: Long- and short-term power supplying for solar hydrogen systems [3].

equation for the electrolyzers. Fischer [4] compared the experimental results of a small system consisting of a solar cell generator, water electrolysis, and power conditioning with calculated results of a system simulation model, while Vidueira et al. [5] examined the performance of the solar hydrogen system for producing hydrogen via an electrolysis generator, in order to satisfy the hydrogen consumption of the first two fuel cell buses in Madrid. Some other researchers used various software to simulate the system performance, such as Park et al. [6, 7], who used (PSCAD/EMTDC) software to simulate a hydrogen production system performance.

Galli and Stefanoni [8] investigated and tested some commercial solar-hydrogen technologies, preliminary performance results, and the control of the system for solar-powered regenerative fuel cell system in Italy, while Hedström et al. [9] did so in Sweden, Abaoud and Steeb [10] in the German-Saudi bilateral program HYSOLAR, Voss et al. [11] in Germany, Lutfi and Veziroğlu [12] in Pakistan, Chaparro et al. [13] in Spain, and Little et al. [14] in UK. Torres et al. [15] also simulated a PV-hydrogen-fuel-cell hybrid system in Mexico.

The main objective of this paper is to present the performance of a hybrid PV/unitized regenerative fuel cell system under Malaysian weather conditions. A PV/unitized regenerative fuel cell system is built in the laboratories of the solar energy research institute (SERI)/Universiti Kebangsaan Malaysia. The results presented in this paper are based on a real operation conditions. The comparison between the operational and simulated data is also presented in this paper.

2. System Description

The proposed system mainly consists of two major subsystems, which are the PV modules (Kyosera, KC85T) located outdoor and the hydrogen system located inside the lab. The main components of the system used in this work are 3 same oriented PV modules (the method used by Markvart [16] is based on the maximum operating current, and the lowest solar irradiation was used to predict how many modules needed to be used) with 87 W maximum power and 0.65 m² active area, unitized regenerative fuel cell (URFC), gases storages and water tanks, humidifiers, water traps, DC/DC converter (WD150-400), maximum power point tracker

(MPPT) (STECA PR 1010) to ensure maximum PV power output, and bus bar to transfer the current either from the PV to the load and electrolyzer in the sunny hours or from the fuel cell to the load during the sunset. The system starts in the morning, when the PV current is high enough to power the load, while the excess current sends power to URFC stack, which works in electrolysis mode, receiving water from small water pump. The generated gases are then sent to the storage tanks. When the PV current fails to power the load, the system will then switch to fuel cell mode after purging the lines with nitrogen. The humidifiers used for fuel cell mode were PERMA PURE MH Series humidifiers which are shell and tube moisture exchangers that allow the transfer of water vapor between a liquid water supply and a flowing gas stream. Water is absorbed into the walls of the Nafion tube and transferred to the dry gas stream. This transfer is driven by the difference in partial pressures of water vapor on opposing sides. Deionized water was filled into the tank which is equipped with heater (2 kW) to heat up the water to the desired temperature through the temperature controller. Nitrogen for purging was used when switching from electrolyzer mode to fuel cell mode and at system shutdown time at which the nitrogen supplies to both hydrogen and oxygen piping line using solenoid valve. The solenoid valves will open and allow nitrogen to flow through the fuel and oxidant. A schematic of the hydrogen system is shown in Figure 2.

The laboratory was equipped with a fuel cell test station capable of measuring the stack temperature, hydrogen and air flow rate measurement, and the stack operating current and voltage. The subsystem contains humidification bottles for the fuel cell mode to humidify the reactant gases. The humidification can be bypassed if a dry gas feed into the stack is desired. The gas flow rates are controlled manually by a set of valves for each side of the stacks. Moreover, a data acquisition system was incorporated to generate polarization curves and time history of the stacks performance, the temperature at various locations in the system, and the solar irradiation.

3. System Modeling

3.1. *PV Module.* The model given by Duffie and Beckman [17] was used to model the PV modules' current and voltage output. At fixed temperatures and solar radiation, the current-voltage characteristic of a PV module can be modeled using

$$I = I_L - I_D = I_L - I_0 \left(e^{(V+IR_s)/a} - 1 \right) - \frac{V + IR_s}{R_{sh}}. \quad (1)$$

The power is given by

$$P_{PV} = IV. \quad (2)$$

In most cases, the shunt current can be ignored because the shunt resistance is so high that the term goes to zero, particularly for monocrystalline solar cells, so (1) becomes

$$I = I_L - I_D = I_L - I_0 \left(e^{(V+IR_s)/a} - 1 \right) \quad (3)$$

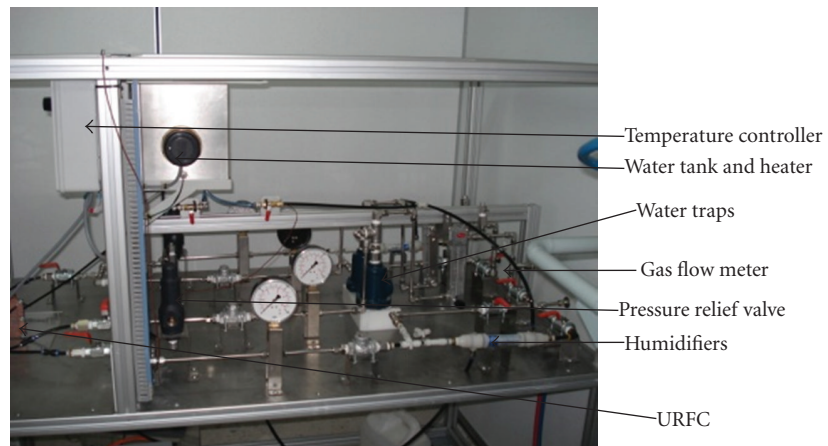
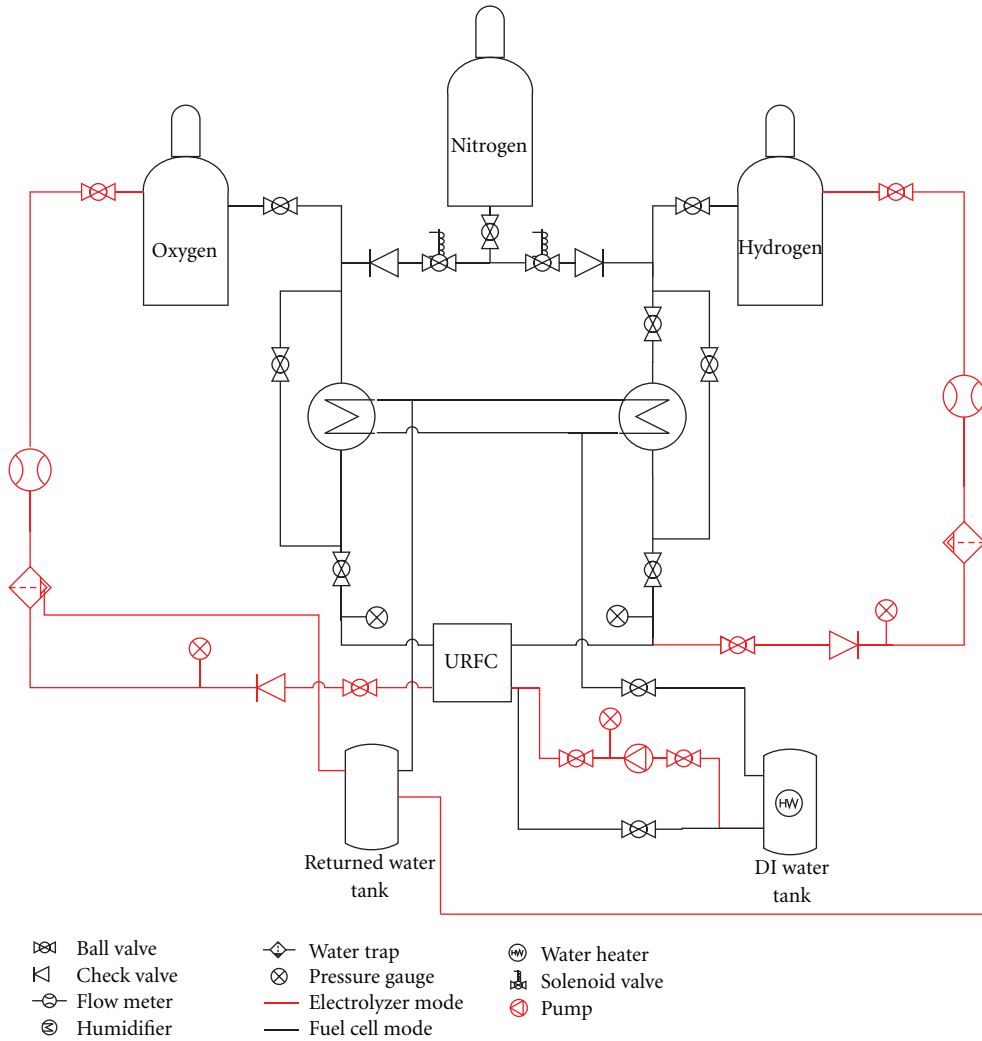


FIGURE 2: The hydrogen system prototype.

and in terms of voltage becomes

$$V = a \cdot \ln\left(\frac{I_L - I + I_o}{I_o}\right) - IR_s. \quad (4)$$

The values of I_L , I_o , V_{oc} , and the parameter a are functions of the cell temperature. The model presented by Duffie and

Beckman [17] was used to find these parameters and consequently the operating voltage at any load current.

3.2. *Electrolyzer Mode.* The electrode kinetics of an electrolyzer modeled using the semiempirical current-voltage relationships is presented by Ulleberg [18]. The basic form

TABLE 1: Electrolyzer mode parameters.

Parameter	Value	Unit
r_1	9.5×10^{-5}	$\Omega \cdot \text{m}^2$
r_2	-4.7×10^{-7}	$\Omega \cdot \text{m}^2 \cdot ^\circ\text{C}^{-1}$
s_1	0.1689	V
s_2	0.0008	$\text{V} \cdot ^\circ\text{C}^{-1}$
s_3	-1.33×10^{-5}	$\text{V} \cdot ^\circ\text{C}^{-2}$
t_1	0.33	$\text{m}^2 \cdot \text{A}^{-1}$
t_2	5.48	$\text{m}^2 \cdot \text{A}^{-1} \cdot ^\circ\text{C}$
t_3	242	$\text{m}^2 \cdot \text{A}^{-1} \cdot ^\circ\text{C}^2$

of the I - V curve is given by (5), and that curve varies for a given temperature:

$$U_{\text{el}} = U^o - \frac{RT}{nF} \ln(P_{\text{H}_2} \cdot P_{\text{O}_2}^{0.5}) + \frac{r}{A} I + s \log\left(\frac{t}{A} I + 1\right). \quad (5)$$

Ulleberg and Mørner [19] used the following equations to count the temperature dependence of the ohmic resistance (r) and the overvoltage coefficients (s and t):

$$t = t_1 + \frac{t_2}{T} + \frac{t_3}{T^2},$$

$$r = r_1 + r_2 T, \quad (6)$$

$$s = s_1 + s_2 T + s_3 T^2.$$

The electrolyzer used in this study had been tested under different operating temperatures, and with and without ohmic losses to predict the ohmic losses (as well as the rest of the losses). The results are then plotted, and, through curve fitting, the parameters can be found. Table 2 listed the overpotential parameters for the electrolyzer. Once the eight parameters for the electrolyzer mode were found, (5) can be used to describe the I - U for the stack. Table 1 listed the electrolyzer mode parameters.

3.3. Fuel Cell Mode. The current-voltage characteristics of a PEM fuel cell used in this study are an empirical equation used by Ulleberg [20] that takes overvoltages due to activation into account. However, the concentration losses were neglected since the operating current density was lower than 200 mA/cm^2 . The following equation was used to predict the fuel cell mode voltage as a function of the current density:

$$U_{\text{fc}} = U_o - b \log i - ri. \quad (7)$$

The open-circuit voltage can be measured or calculated from

$$U_o = E_{\text{rev}} + b \log i_o. \quad (8)$$

Table 2 listed the real operation results for the URFC working on the fuel cell mode at two different cell temperatures and 1 bar pressure fully humidified hydrogen and oxidants.

In order to simulate the performance of the system, the electric and thermoelectric equations of each part of the system were solved using MATLAB code. The input parameters were the solar irradiation and location parameters

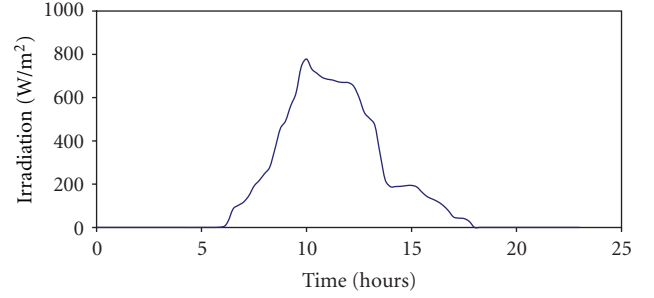


FIGURE 3: Solar irradiation for the selected day (November 19, 2009).

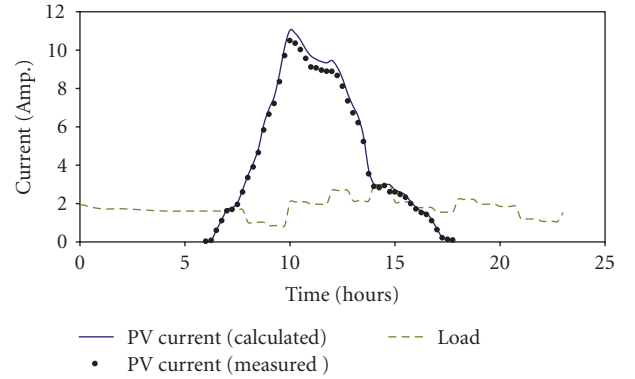


FIGURE 4: PV current output and load current for the selected day (November 19, 2009).

(whether data), proposed load profile, regenerative fuel cell specifications, and the hydrogen and oxygen tanks specifications. The DC/DC controller efficiency was set to 95%.

4. Results and Discussion

Among the testing days, a relatively low solar radiation day was selected, on which the total daily radiation was about 4.1 kWh (refer to Figure 3). The system first turned on the electrolyzer mode ELM to generate hydrogen. Figure 4 shows the measured and simulated PV current output and the current given to the load. It's clear to see that the current from the PV during the sunny hours was much higher than the load current, and therefore the excess current goes to the stack to generate hydrogen. The simulated and measured data was almost with relatively low error, especially at a low operating current, and slightly increased when the current increased due to nonconsiderable ohmic losses for the simulation data.

The electrolyzer current keeps increasing as the PV current increases and then decreases till reaching to zero at about 4 PM. At that time, the stack switched to fuel cell mode FCM after purging the stack with inert nitrogen. The fuel cell mode current is higher than the load current and the load voltage is 12 V DC , while the fuel cell mode voltage is less than 6 V . Because of this the stack should generate a higher current to meet the power required for the load after

TABLE 2: Fuel cell mode parameters.

T, °C	Oxygen				Air			
	$E_{rev.}$ V	U_o V	$b,$ mV/dec	$i_o,$ mA/cm ²	$E_{rev.}$ V	U_o V	$b,$ mV/dec	$i_o,$ mA/cm ²
30	1.18	1.028	86.6	0.0016	1.17	0.972	91.1	0.0012
70	1.17	0.999	71.8	0.0035	1.16	0.962	79	0.0028

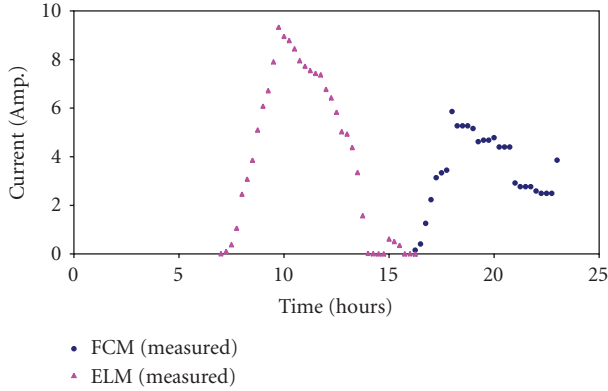


FIGURE 5: Fuel cell and electrolyzer mode measured current.

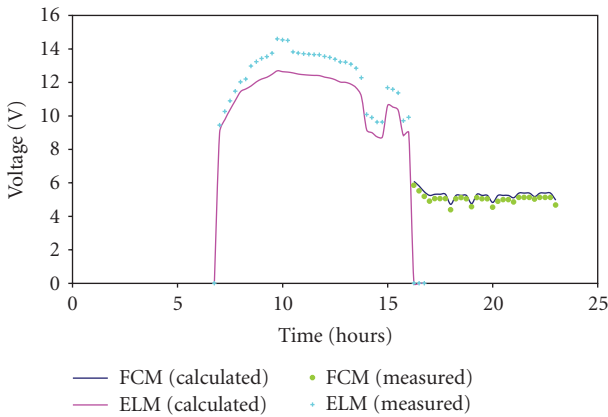


FIGURE 6: Fuel cell mode voltage and electrolyzer mode voltage.

DC/DC controls the voltage to the desired load amount. Figure 5 shows the stack current for the electrolyzer and fuel cell mode.

The Fuel cell and electrolyzer mode voltage are shown in Figure 6. The voltage of the stack during the fuel cell mode is around 6 V (7 cells stack). The measured electrolyzer voltage was slightly higher than the simulated values because the PV output voltage was slightly higher than the electrolyzer required voltage. The bus bar current available at the system is either from the PV current or from the stack through the fuel cell mode. Figure 7 shows the bus bar current distribution for the selected day.

The variation of the stored hydrogen inside the hydrogen tank is shown in Figure 8. The initial pressure value was set at 1 bar. The simulation results showed acceptable predictable values comparing to the real data, with a RMS error of

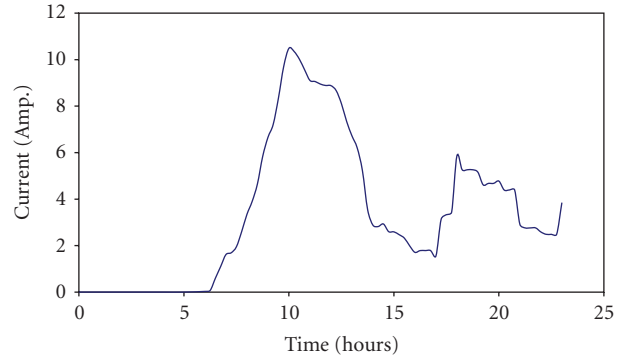


FIGURE 7: Measured fuel cell and electrolyzer mode bus available current.

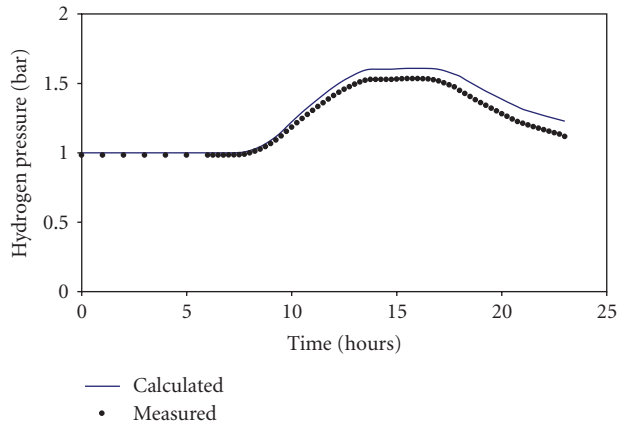


FIGURE 8: Simulated and measured hydrogen tank pressure.

0.07 bars. This was mainly because the gases were assumed to behave as an ideal gas and the real amount of the produced and consumed amount of hydrogen was not the same as the simulated values.

The summary of the full measured results for the selected day is shown in Figure 9 and all the results are listed in Table 3.

5. Conclusion

The following can be concluded from the current study.

- (1) The load will be powered by the PV array at the solar time, and the extra power will go to the electrolyzer to produce hydrogen. After sunset, or at the time of low irradiation, this stored hydrogen will be used to power the load through the fuel cell.

TABLE 3: Summary of the selected day measured and simulation results.

System	Simulated	Measured	
Solar input	4.08	4.08	kWh/m ²
PV output	0.83	0.78	kWh
PV efficiency ^a	10.3	9.7	%
User load	0.37	0.37	kWh
PV to load ^b	28.85	31.43	%
Load powered by PV ^c	65.26	66.94	%
FCM power	0.13	0.12	kWh
FCM operating hours	7	7	hr
Total H ₂ consumed ^d	0.25	0.27	kWh
FCM energy efficiency ^e	50.1	45.35	%
ELM power	0.46	0.51	kWh
ELM operating hours	9	9	hr
Total H ₂ produced	0.39	0.35	kWh
ELM energy efficiency ^f	84.48	68.98	%
Total system Efficiency ^g	4.55	4.55	%
Round trip efficiency ^h	42.31	31.28	%

^a PV output to the solar input.

^b (Load – Fuel cell mode power)/PV output.

^c (Load – Fuel cell mode power)/load.

^d Based on HHV for hydrogen.

^e Fuel cell mode power to the hydrogen consumed.

^f Hydrogen produced to the electrolyzer mode power.

^g Load to the solar input.

^h Fuel cell mode efficiency and electrolyzer mode efficiency.

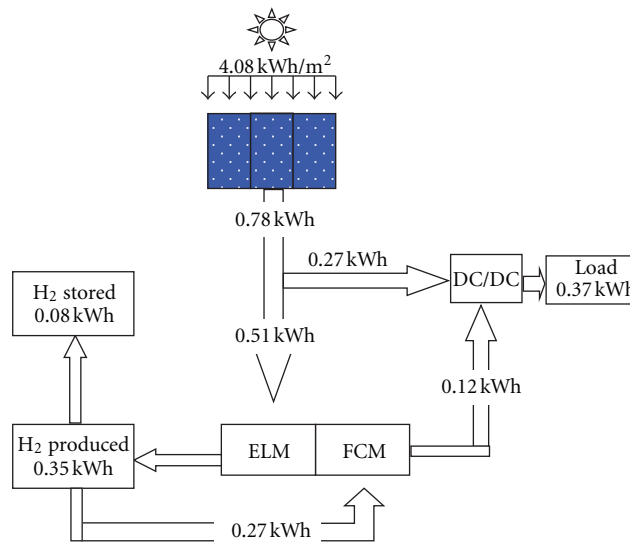


FIGURE 9: Summary of measured data for the selected day.

(2) Comparing the simulated results with measured data shows the ability of the cell modeling to predict the cell performance with an acceptable level of error. The difference between the measured and simulated data increased as the operating current increases.

(3) The performance of the stack works on electrolyzer or fuel cell mode was slightly lower when compared with the discrete electrolyzer and fuel cell, which

is an expected result since the membrane electrode assembly catalysts were chosen based on compromise between fuel cell and electrolyzer mode performance.

Abbreviations

a: Curve fitting parameter Volts
b: Tafel constant mV/dec
E: Voltage V

F : Faraday's constant, 96485 Amp · sec/mol
 G : Solar irradiance W/m²
 I : Current Amp
 I_o : Diode reverse saturation current Amp
 i : Current density Amp/cm²
 N^o : Molar flow rate mol/sec
 N_C : No. of cell in the stack
 n : No. of electron in the reaction (2)
 P : Power W
 P : Partial pressure atm
 R : Resistance ohm
 R : Gas constant kJ/kg · K
 r : Parameter related to ohmic resistance
 ohm · m²
 s : Coefficient for overvoltage V
 t : Coefficient for overvoltage m²/Amp
 T : Temperature K
 U : Fuel Cell or electrolyzer Voltages V
 V : PV voltage V.

Subscripts

c : Cell
 D : Diode
 el : Electrolyzer
 fc : Fuel cell
 H_2 : Hydrogen
 L : Light
 O_2 : Oxygen
 o : Exchange current density
 oc : Open circuit
 s : Series
 sh : Shunt
 sc : Short circuit
 ref : Reference
 rev : Reversible
 T : Tilted.

Acknowledgments

The authors would like to thank the Solar Energy Research Institute (SERI), Universiti Kebangsaan, Malaysia, for their invaluable support. Sincere gratitude should be sent to the Ministry of Science, Technology and Innovation (MOSTI), Government of Malaysia, for providing funds for the research under the IRPA Project no. 03-01-02-SF0329.

References

- [1] K. Ro, "Two-loop controller for maximizing performance of a grid-connected photovoltaic-fuel cell hybrid power plant," in *Electrical Engineering*, Faculty of the Virginia Polytechnic Institute and State, Blacksburg, Va, USA, 1997.
- [2] T. A. Nergaard, "Modeling and control of a single-phase, 10 kW fuel cell inverter," in *Electrical Engineering*, Faculty of the Virginia Polytechnic Institute and State, Blacksburg, Va, USA, 2002.
- [3] J. Pettersson, B. Ramsey, and D. Harrison, "A review of the latest developments in electrodes for unitised regenerative polymer electrolyte fuel cells," *Journal of Power Sources*, vol. 157, no. 1, pp. 28–34, 2006.
- [4] M. Fischer, "Review of hydrogen production with photovoltaic electrolysis systems," *International Journal of Hydrogen Energy*, vol. 11, no. 8, pp. 495–501, 1986.
- [5] J. M. Vidueira, A. Contreras, and T. N. Veziroglu, "PV autonomous installation to produce hydrogen via electrolysis, and its use in FC buses," *International Journal of Hydrogen Energy*, vol. 28, no. 9, pp. 927–937, 2003.
- [6] M. Park, D. H. Lee, and I.-K. Yu, "PSCAD/EMTDC modeling and simulation of solar-powered hydrogen production system," *Renewable Energy*, vol. 31, no. 14, pp. 2342–2355, 2006.
- [7] M. Park, H. R. Seo, D. H. Lee, and I. K. Yu, "Characteristics analysis of a PV-AF-SPE system under several irradiation conditions," *Renewable Energy*, vol. 34, no. 3, pp. 499–503, 2009.
- [8] S. Galli and M. Stefanoni, "Development of a solar-hydrogen cycle in Italy," *International Journal of Hydrogen Energy*, vol. 22, no. 5, pp. 453–458, 1997.
- [9] L. Hedström, C. Wallmark, P. Alvfors, M. Rissanen, B. Stridh, and J. Ekman, "Description and modelling of the solar-hydrogen-biogas-fuel cell system in GlashusEtt," *Journal of Power Sources*, vol. 131, no. 1-2, pp. 340–350, 2004.
- [10] H. Abaoud and H. Steeb, "The German-Saudi hysolar program," *International Journal of Hydrogen Energy*, vol. 23, no. 6, pp. 445–449, 1998.
- [11] K. Voss, A. Goetzberger, G. Bopp, A. Häberle, A. Heinzel, and H. Lehmborg, "The self-sufficient solar house in Freiburg—results of 3 years of operation," *Solar Energy*, vol. 58, no. 1–3, pp. 17–23, 1996.
- [12] N. Lutfi and T. N. Veziroglu, "Solar-hydrogen demonstration project for Pakistan," *International Journal of Hydrogen Energy*, vol. 17, no. 5, pp. 339–344, 1992.
- [13] A. M. Chaparro, J. Soler, M. J. Escudero, E. M. L. De Ceballos, U. Wittstadt, and L. Daza, "Data results and operational experience with a solar hydrogen system," *Journal of Power Sources*, vol. 144, no. 1, pp. 165–169, 2005.
- [14] M. Little, M. Thomson, and D. Infield, "Electrical integration of renewable energy into stand-alone power supplies incorporating hydrogen storage," *International Journal of Hydrogen Energy*, vol. 32, no. 10-11, pp. 1582–1588, 2007.
- [15] L. A. Torres, F. J. Rodríguez, and P. J. Sebastian, "Simulation of a solar-hydrogen-fuel cell system: results for different locations in Mexico," *International Journal of Hydrogen Energy*, vol. 23, no. 11, pp. 1005–1009, 1998.
- [16] T. Markvart, *Solar Electricity*, John Wiley & Sons, New York, NY, USA, 1994.
- [17] J. A. Duffie and W. A. Beckman, *Solar Engineering of Thermal Processes*, John Wiley & Sons, New York, NY, USA, 2nd edition, 1991.
- [18] O. Ulleberg, "Modeling of advanced alkaline electrolyzers: a system simulation approach," *International Journal of Hydrogen Energy*, vol. 28, no. 1, pp. 21–33, 2003.
- [19] O. Ulleberg and S. O. Mørner, "TRNSYS simulation models for solar-hydrogen systems," *Solar Energy*, vol. 59, no. 4–6, pp. 271–279, 1997.
- [20] O. Ulleberg, *Stand-alone power systems for the future: optimal design, operation & control of solar-hydrogen energy systems [Ph.D. thesis]*, Norwegian University of Science and Technology, Trondheim, Norway, 1998.

Research Article

Optical Design of a Solar Dish Concentrator Based on Triangular Membrane Facets

Hongcai Ma,^{1,2} Guang Jin,¹ Xing Zhong,¹ Kai Xu,¹ and Yanjie Li^{1,2}

¹ Changchun Institute of Optics, Fine Mechanics and Physics, Chinese Academy of Sciences, Changchun 130033, China

² Graduate University of the Chinese Academy of Sciences, Beijing 100039, China

Correspondence should be addressed to Guang Jin, jing@ciomp.ac.cn

Received 30 June 2012; Revised 13 October 2012; Accepted 17 October 2012

Academic Editor: Kalvala Srinivas Reddy

Copyright © 2012 Hongcai Ma et al. This is an open access article distributed under the Creative Commons Attribution License, which permits unrestricted use, distribution, and reproduction in any medium, provided the original work is properly cited.

The design of a solar dish concentrator is proposed based on triangular membrane facets for space power applications. The facet concentrator approximates a parabolic surface supported by a deployable perimeter truss structure, which originates from a large aperture space antenna. For optimizing the number of facets rows and focal-diameter ratio of the concentrator, Monte Carlo ray-tracing method is utilized to determine optical performance of the concentrator, and the system root-mean-square (RMS) deviation is considered in this design procedure. A 600-facet concentrator with focal-diameter ratio of 1.1 will achieve 83.63% of radiative collection efficiency over a 15 cm radius disk located in the focal plane, with a mean solar concentration ratio exceeding 300. The study in this paper is helpful for the development of the membrane facet concentrator.

1. Introduction

Space-based solar energy is an attractive energy source with a huge potential application for the space solar power and support of various spacecrafts. Researchers have focused on researching the large aperture concentrator as the key component for space-based concentrator photovoltaic (CPV) system collecting space-based solar radiation onto a high-efficiency photovoltaic cells [1, 2]. To reduce volume and mass of space-based CPV systems while maximizing efficiency of the photovoltaic cells, there has been long interest in the development of membrane dish concentrators for space power applications. As lightweight, inexpensive, high-performance structures, they are excellent candidates for space-deployable collectors as well as cost-effective terrestrial energy sources. For the terrestrial use, the proposed design of ellipsoidal polyester membrane facets has much better performances than a multifacet dish concentrator consisting of identical circular, and the simulated membrane shape was experimentally verified [3]. A large-span solar parabolic trough concentrator is designed based on a multilayer polymer mirror membrane mounted on a rotatable concrete structure [4]. For the use in space, an inflatable prototype for

the Deployable Solar Concentrator has been developed [5]. Especially, L'Garde has developed power antenna concept, and this new technology utilizes an inflatable membrane reflector to concurrently concentrate solar energy for space electrical power generation, while acting as an antenna with large aperture and high gain [6]. Similarly, many reflector antennas with a mesh membrane surface and a deployable perimeter truss, such as AstroMesh antenna [7, 8] and deployable modular mesh antenna [9], divide the reflector surface into triangular flat facets. While the above antenna configurations are also adaptive to be used as concentrators, they had not been explored for solar power generation applications.

This paper deals with the optical design of a lightweight solar concentrator with triangular membrane flat facets as potential low-cost alternate for space solar power generation applications. The focal radiation flux distributions are calculated by the Monte Carlo ray-tracing method. To obtain the desired radiative collection efficiency and mean solar concentration ratio, we investigate on the minimal number of facets of the concentrator when varying focal-diameter ratio (F/D) of the concentrator under consideration of both the system RMS deviation and the random surface error.

2. Concentrator Geometry

Generally, the deployable membrane antennas consist of cable network supplemented with a membrane, tension ties, perimeter truss, and rear net. For simplicity, we only consider the forming process for a membrane surface. The number and size of triangle facets of the membrane surface are determined by layout of nodes. To minimize the number of nodes, a net with coinciding three-band nodes is adopted in this paper [10]. The layout of nodes is shown as Figure 1(a). For the circular aperture, the membrane is divided into m equal sectors and N equally spaced concentric circles, and there are $m \times n$ nodes in the n th concentric circles lying on equally spaced radian length of $2\pi/(mn)$. Then the horizontal nodes are mapped onto the desired parabolic surface giving the shape of membrane after deformation. In reality, the horizontal nodes of membrane are pulled down by cable to the mapped positions of nodes, and then the nearby three nodes comprise a triangle membrane facet. The mapping procedure used for generating the triangular-facet membrane surface is shown in Figure 1(b). The ideal deformed membrane is approximately parabolic in shape and consists of many triangular flat planes, but in reality each plane becomes deformed due to cable tension, membrane tension, membrane size, and surface curvature which is related to focal length. The ideal forming process for a membrane surface has only been considered in this paper. In the final surface, the number of triangular facets t and nodes j are

$$\begin{aligned} t &= mN^2, \\ j &= mN^2 + 1, \end{aligned} \quad (1)$$

and numerical description of the deformed membrane given by the positions of nodes on the parabolic surface is derived as

$$P_{\text{nodes}} = \begin{pmatrix} x_{n,i} \\ y_{n,i} \\ z_{n,i} \end{pmatrix} = \begin{pmatrix} n \frac{D}{2N} \cos \left[(i-1) \frac{2\pi}{mn} \right] \\ n \frac{D}{2N} \sin \left[(i-1) \frac{2\pi}{mn} \right] \\ \frac{(x_{n,i} + y_{n,i})}{4F} \end{pmatrix} \quad 1 \leq i \leq mn, \quad (2)$$

where n is the number of concentric circles where the nodes are located, i represents the i th node in the anticlockwise direction in the n th concentric circle, D is the aperture diameter, and F is the nominal focal length of the concentrator.

For the solar concentrator based on a triangular membrane facets, in this paper we assume the requirements for the radiation flux on a circular target are that radiative collection efficiency $\eta_c = 80\%$, at a high mean concentration ratio of at least $C_{\text{mean}} = 300$; meanwhile, the concentrator geometry is refined by selecting the minimum number of facets rows N , and the F/D ratio is varied to get the desired radiation flux as high as possible.

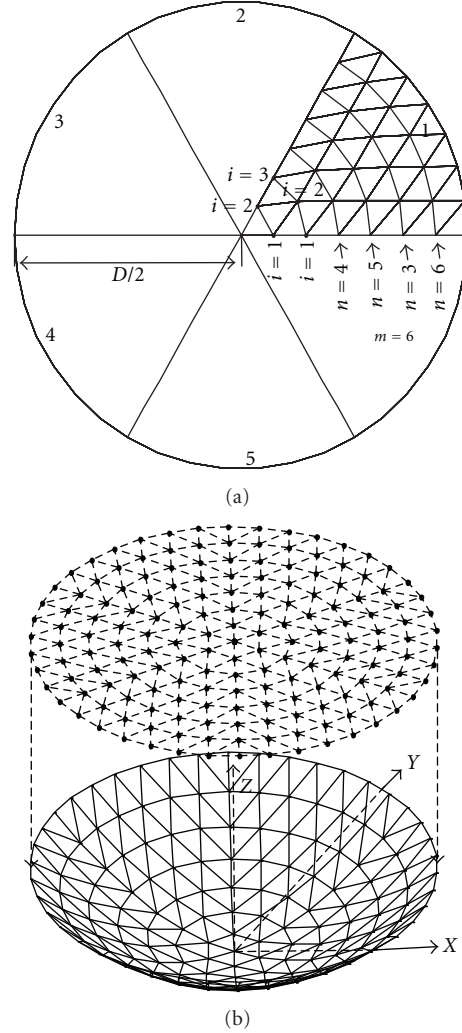


FIGURE 1: Flat-facet concentrator: (a) a layout of nodes with $m = 6$ and $t = 294$ facets, placed in $N = 7$ rows and (b) the mapping procedure for generating the triangular facets membrane surface.

3. Monte Carlo Ray-Tracing Method

In Monte Carlo ray-tracing method, the average radiation flux on the target \bar{q} and the area-weighted mean solar concentration C_{mean} on a circular disk target are defined as

$$\begin{aligned} \bar{q} &= \frac{\pi \sum_{m=1}^{N_{\text{target}}} q_m (r_m^2 - r_{m-1}^2)}{\pi R_{\text{target}}^2}, \\ C_{\text{mean}} &= \frac{\bar{q}}{I_0}, \end{aligned} \quad (3)$$

where q_m is the radiation flux received by the m th discrete annular element, r_m is the radius of the m th discrete annular element, N_{target} is the number of discrete annular elements on the circular target, $R_{\text{target}} = 0.15$ m is the radius of the circular target disk, and I_0 is the incident direct solar flux in space.

Incident rays are distributed over the triangular elements in proportion to the projected element areas. The angular distribution of the launched rays is modeled by

TABLE 1: Parameters of the simulated concentrator.

Parameters	Numerical value
Concentrator aperture	$D = 6$ m
Focal-diameter ratio	$F/D = 0.4 \sim 1.6$
Incident direct solar flux	$I_0 = 1309.2$ W/m ²
Target size	$R_{\text{target}} = 0.15$ m
Receiver type	Flat, without shadowing
Number of facets	$N = 9, 10, 11, 12$
Half-cone angle of sun disk	$\theta_{\text{sun}} = 4.65$ mrad
Surface error	$\sigma_s = 0, 10$ mrad
Reflectivity of facets	1
equal sectors divided	$m = 6$

the “pillbox-sunshape”, which represents the ideal solar disk with uniform brightness in half-cone angle θ_{sun} . In order to take into account the random surface error combining with membrane wrinkling at the facets, a Gaussian distribution (expressed in milliradians) is assumed for the angular deviation of the reflected rays with respect to the nominal direction of reflection [11]. The latter is given by the specular law of reflection in which triangular-facets normal vectors are derived from the node triples positions. The receiver is considered without shadowing the incident solar energy. Table 1 summarizes the parameters of the membrane facet concentrator.

4. Optical Design of Triangular-Facets Concentrator for the System

The accuracy requirements of deployable antenna with a perimeter truss structure are often specified by the system RMS deviation δ_{rms} of the actual triangular flat facets surface from the desired parabolic surface. While we could vary the F/D ratio of the concentrator originated from the deployable antenna to get the focal radiation flux as high as possible, the allowable RMS deviation limits the satisfying range of F/D ratios. Thus, the RMS deviation is considered for this analysis. For a given value of δ_{rms} , the maximal triangular facet length L and the facet rows N are given by [12]

$$\begin{aligned} \frac{L}{D} &= \sqrt{8\sqrt{15} \frac{\delta_{\text{rms}}}{D} \frac{F}{D}}, \\ N &= \frac{D}{2L}. \end{aligned} \quad (4)$$

According to the practical limitation of the allowable RMS deviation $\delta_{\text{rms}} = 0.36$ mm [13], the relationships between the facet rows N and the minimum F/D ratio are shown by the curve in Figure 2. In Figure 2, the F/D ratios satisfying the requirement of the RMS deviation are on the upper right zone of the curve, and there are satisfying F/D ratios for $N = 9, 10, 11,$ and 12 , respectively. The satisfying range of F/D ratios enlarges when the facet rows N increases. With the concentrator divided into an enough large number of small facets, all range of F/D ratios is satisfying. This relationship offers restricted limits for the F/D ratio selected

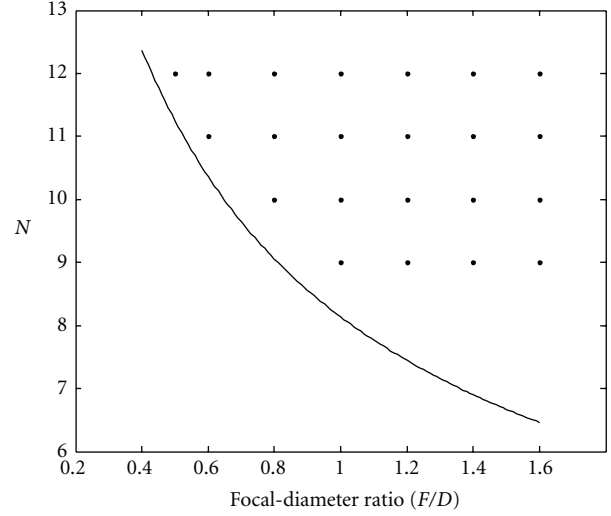


FIGURE 2: The dependence of the number of facet rows N on minimum F/D ratio with the allowable RMS deviation $\delta_{\text{rms}} = 0.36$ mm.

for different facet rows N in the following optimization procedure of the flat-facet concentrator.

Figures 3(a) and 3(b) show that the variation of radiative collection efficiency with F/D ratio when the random surface error σ_s is 0 and 10 mrad, respectively, for the facet rows N of 9, 10, 11, and 12. Both figures illustrate that the larger the number of facets, the higher the collection efficiency. By comparing (a) and (b), it is shown that the collection efficiency η_c is slightly lower in the presence of random surface error for the same facet rows N value. For instance, by comparison of the case with and without the surface error, the average decreasing amount is only 0.1% from 0.4 to 1.6 of F/D ratio. In addition, an optimal F/D ratio which corresponds to the highest collection efficiency exists for each facet rows N as the horizontal line shows; however, the optimal F/D ratio decreases with the increase of facet rows N . For instance, for a concentrator with $N = 10$, the collection efficiency η_c increases from 67.7% to 85.27% for the F/D ratio increasing from 0.4 to 1.1 and with N increasing from 9 to 12, the optimal F/D ratio decreases from 1.3 to 1.1. Furthermore with the F/D increasing beyond the optimal F/D ratio, the collection efficiency decreases more obviously with random surface error than without random surface error, for example the average decrease is 0.3% with surface error of 10 mrad and 0.15% without random surface error when F/D ratio increases from 1.1 to 1.6 for $N = 10$.

Similarly, Figures 4(a) and 4(b) show the variation of the mean concentration ratio C_{mean} with the F/D ratio for several facet rows N values when the random surface error σ_s is 0 and 10 mrad, respectively. The mean concentration ratio C_{mean} exhibits similar dependence on F/D ratio as the collection efficiency does (Figure 3). The mean concentration ratio also increases with the increasing number of facet rows N . With the surface error increasing from 0 to 10 mrad, the mean concentration ratio C_{mean} appreciably decreases. When $N = 10$, $F/D = 1.1$, the mean concentration ratios are 340.9, 333.5, respectively, both exceeding 300.

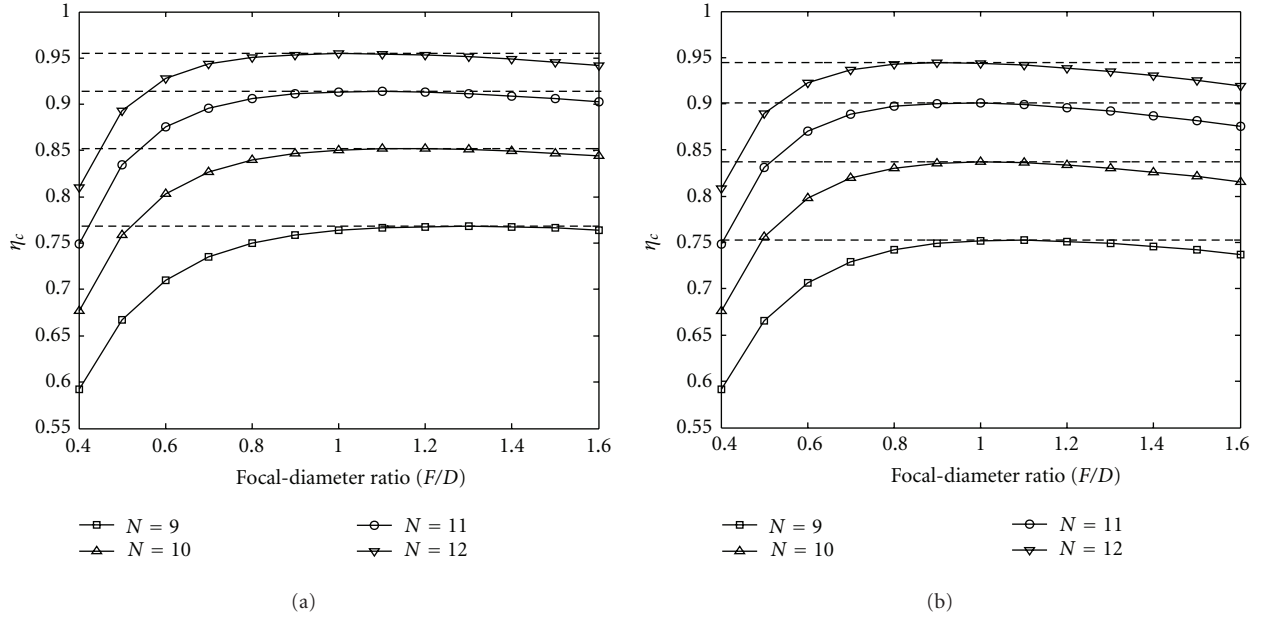


FIGURE 3: The dependence of radiative collection efficiency η_c on F/D ratio with the random surface error σ_s of (a) 0 mrad and (b) 10 mrad.

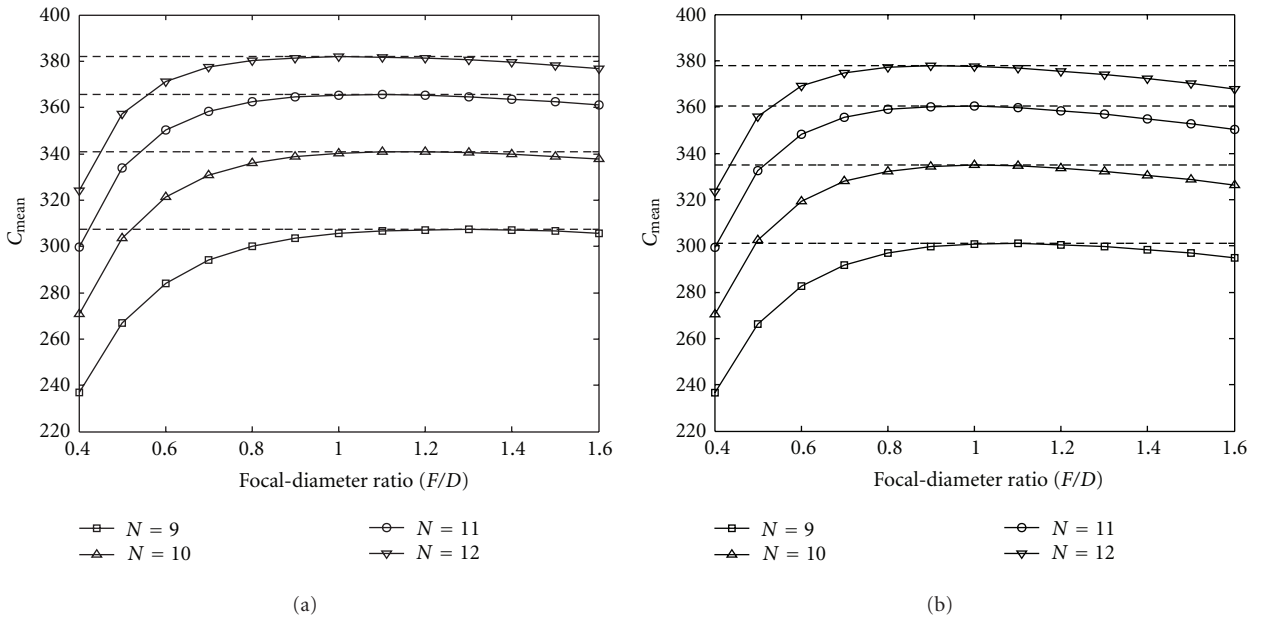


FIGURE 4: The dependence of the area-weighted mean solar concentration C_{mean} on F/D ratio with the random surface error σ_s of (a) 0 mrad and (b) 10 mrad.

In the case keeping concentrator aperture D constant, the existence of the optimal F/D ratio for each facet rows is discussed in more detail. When the F/D ratio increases, the concentrator implies a reflected solar cone with more angular divergence. Therefore, the image on the receiver increases. But, on the other hand, a smaller F/D ratio also implies larger RMS deviation, which increases the image size. Therefore, the observed optimal F/D ratio is the result of a trade-off between these two effects.

Based on the above analysis, the selection of the optimal facet rows N and F/D ratio is determined by both the desired

flux and allowable RMS deviation δ_{rms} . The procedure of optimization design can be described in the following steps: firstly, the minimum number of facet rows N is obtained according to the requirements of radiation flux; secondly, the appropriate range of F/D ratio is derived from the allowable RMS deviation δ_{rms} ; finally, the F/D ratio is scanned over the range satisfying the requirement of the RMS deviation to achieve the highest radiation flux under the consideration of the random surface error. Based on this design procedure, the obtained optimal facet rows $N = 10$ and F/D ratio = 1.1 result in radiative collection efficiency of 83.63% at a mean

concentration ratio of 333.5 for a 15 cm radius target with the surface error of 10 mrad, which fulfills well the design requirements.

5. Conclusions

We have identified the optical performance of a solar concentrator based on triangular membrane facets for energy collection. The concentrator approximates an ideal parabolic with triangular flat facets supported by a deployable perimeter truss structure, which originates from a large aperture space antenna. An optical design procedure to the membrane facet concentrator has been developed. The number of facet rows N and focal-diameter ratio (F/D) was optimized by Monte Carlo ray-tracing method, in which the radiative collection efficiency and area-weighted mean concentration ratio were calculated. Under consideration of the allowable RMS deviation $\delta_{\text{rms}} = 0.36$ mm and a random surface error combing with membrane wrinkling of 10 mrad, a 600-facet concentrator will achieve 83.63% of radiative collection efficiency over a 15 cm radius disk located in the focal plane, with an area-weighted mean concentration ratio of 333.5. The solar concentrator based on triangular membrane facets is a promising option for the development of a cost-effective space photovoltaic solar energy generation.

Acknowledgment

The financial support provided by National Basic Research Program of China with Grant no. 2010CB227101 is greatly appreciated.

References

- [1] M. J. O'Neill, M. F. Piszczor, M. I. Eskenazi et al., "Ultra-light stretched Fresnel lens solar concentrator for space power applications," in *Proceedings of the SPIE's 48th Annual Meeting*, pp. 5179–5117, San Diego, Calif, USA, August 2003.
- [2] L. S. Mason, "A solar dynamic power option for space solar power," NASA/TM 1999-209380, 2000.
- [3] G. Zanganeh, R. Bader, A. Pedretti et al., "A solar dish concentrator based on ellipsoidal polyester membrane facets," *Solar Energy*, vol. 86, pp. 40–47, 2012.
- [4] R. Bader, A. Pedretti, and A. Steinfeld, "A 9-m-aperture solar parabolic trough concentrator based on a multilayer polymer mirror membrane mounted on a concrete structure," *Journal of Solar Energy Engineering*, vol. 133, no. 3, Article ID 031016, 2011.
- [5] G. Grossman and G. Williams, "Inflatable concentrators for solar propulsion and Dynamic Space Power," *Journal of Solar Energy Engineering*, vol. 112, no. 4, pp. 229–236, 1990.
- [6] D. Lichodziejewski and C. Cassapakis, "Inflatable power antenna technology," in *Proceedings of the AIAA 99-1074 37th Aerospace Sciences Meeting and Exhibit (AIAA '99)*, January 1999.
- [7] K. Ando, J. Mitsugi, and Y. Senbokuya, "Analyses of cable-membrane structure combined with deployable truss," *Computers and Structures*, vol. 74, no. 1, pp. 21–39, 2000.
- [8] N. M. Awlad Hossain, C. H. Jenkins, and L. Hill, "Analysis of a membrane modified perimeter-truss mesh antenna," in

Proceedings of the UV/Optical/IR Space Telescopes: Innovative Technologies and Concepts, pp. 259–270, SPIE, Bellingham, Wash, USA, August 2004.

- [9] S. P. Chodimella, J. Moore, J. Otto, and H. Fang, "Design evaluation of a large aperture deployable antenna," in *Proceedings of the AIAA/ASME/ASCE/AHS/ASC Structures, Structural Dynamics, and Materials Conference*, vol. 6624, Newport, RI, USA, May 2006.
- [10] G. Tibert, *Deployable tensegrity structures for space applications [Ph.D. thesis]*, Stockholm, 2002.
- [11] A. Rabl, *Active Solar Collectors and Their Applications*, Oxford University Press, New York, NY, USA, 1985.
- [12] P. K. Agrawal, M. S. Anderson, and M. F. card, "Preliminary design of large reflectors with flat facets," *IEEE Transactions on Antennas and Propagation*, vol. AP-29, no. 4, pp. 688–694, 1981.
- [13] M. W. Thomson, "AstroMesh deployable reflectors for ku and ka band commercial satellites," in *Proceedings of the 20th International Communication Satellite Systems Conference and Exhibit (AIAA '02)*, Montreal, Canada, May 2002.

Research Article

Performance of Grid-Connected Photovoltaic System in Two Sites in Kuwait

Ali Hajiah,¹ Tamer Khatib,² K. Sopian,³ and M. Sebzali¹

¹ Kuwait Institute for Scientific Research (KISR), Safat 13109, Kuwait

² Department of Electrical, Electronic & System Engineering, Faculty of Engineering & Built Environment, Universiti Kebangsaan Malaysia, Bangi 43600, Malaysia

³ Solar Energy Research Institute, Universiti Kebangsaan Malaysia, Bangi 43600, Malaysia

Correspondence should be addressed to Tamer Khatib, tamer.khat@hotmail.com

Received 13 September 2012; Revised 14 October 2012; Accepted 15 October 2012

Academic Editor: Tapas Mallick

Copyright © 2012 Ali Hajiah et al. This is an open access article distributed under the Creative Commons Attribution License, which permits unrestricted use, distribution, and reproduction in any medium, provided the original work is properly cited.

This paper presents an assessment of the electricity generated by photovoltaic (PV) grid-connected systems in Kuwait. Three years of meteorological data are provided for two main sites in Kuwait, namely, Al-Wafra and Mutla. These data and a PV grid-connected system mathematical model are used to assist a 100 kW_p grid-connected PV system proposed for both sites. The proposed systems show high energy productivity whereas the annual capacity factors for Mutla and Al-Wafra are 22.25% and 21.6%, respectively. Meanwhile the annual yield factors for Mutla and Al-Wafra are 1861 kWh/kW_p/year and 1922.7 kWh/kW_p/year, respectively. On the other hand the cost of the energy generated by both systems is about 0.1 USD/kWh which is very close to the price of the energy sold by the Ministry of Electricity and Water (MEW). Furthermore the invested money is recovered during the assumed life cycle time whereas the payback period for both sites is about 15 years. This work contains worthwhile technical information for those who are interested in PV technology investment in Kuwait.

1. Introduction

Based on the fact that PV systems are clean, environment friendly, and secure energy sources, PV system installation has played an important role worldwide. However, the drawback of PV systems is the high capital cost as compared to conventional energy sources. Therefore, many research works are carried out currently focusing on optimization of PV systems [1]. Grid-connected PV systems can be divided into two parts: building integrated PV systems (BiPV) and distribution generation PV (DGPV) systems. BiPV systems usually supply a specific load and inject the excess energy to the grid. On the other hand the DGPV systems inject the whole produced energy to the grid without feeding any local load. The grid-connected systems can consist of a PV array only as an energy source, or another energy source can be in cooperation with the PV array such as wind turbine, diesel system, or a storage unit [2].

PV system size and performance strongly depend on metrological variables such as solar energy, wind speed,

and ambient temperature and, therefore, to optimize a PV system, extensive studies related to the metrological variables have to be done [3]. The importance of the meteorological data in sizing PV systems lies in the fact that the PV modules output energy strongly depends on the available solar energy and the ambient temperature, while the wind turbines (in case of hybrid PV/Wind systems) output power is a function of the available wind speed.

The performance of a PV module strongly depends on the sun light conditions. Standard sunlight conditions on a clear day are assumed to be 1000 watt of solar energy per square meter and it is sometimes called “one sun” or a “peak sun.” Less than one sun will reduce the current output of a PV module by a proportional amount [1]. Furthermore, cell temperature, T_c , is an important factor in determining the performance of PV cells. The increase in cell temperature decreases PV module’s voltage linearly, while increasing cell temperature increases PV module’s current. The effect of cell temperature on PV modules performance depends on PV cells manufacturing. However, increasing cell temperature by

TABLE 1: Monthly mean of daily solar radiation and ambient temperature for Al-Wafra and Mutla sites.

Month	Mutla station		Al-Wafra station	
	Solar radiation	Temperature	Solar radiation	Temperature
JAN	319 (W/m ²)	14.3 (°C)	326 (W/m ²)	14.7 (°C)
FEB	325 (W/m ²)	19.4 (°C)	351 (W/m ²)	19.9 (°C)
MAR	446 (W/m ²)	23.1 (°C)	494 (W/m ²)	23.4 (°C)
APR	484 (W/m ²)	28.6 (°C)	473 (W/m ²)	24.9 (°C)
MAY	512 (W/m ²)	37.8 (°C)	568 (W/m ²)	37.2 (°C)
JUN	546 (W/m ²)	42.2 (°C)	629 (W/m ²)	42.9 (°C)
JUL	599 (W/m ²)	42.5 (°C)	624 (W/m ²)	44.3 (°C)
AUG	604 (W/m ²)	42 (°C)	578 (W/m ²)	43.6 (°C)
SEP	565 (W/m ²)	36.9 (°C)	564 (W/m ²)	40.8 (°C)
OCT	514 (W/m ²)	31.6 (°C)	459 (W/m ²)	33.7 (°C)
NOV	423 (W/m ²)	20.2 (°C)	387 (W/m ²)	26 (°C)
DEC	378 (W/m ²)	18.9 (°C)	319 (W/m ²)	18.3 (°C)
AV.	476 (W/m ²)	29.79 (°C)	481 (W/m ²)	30.8 (°C)

1 Celsius, C, degree decreases PV modules voltage by 0.085–0.123 V. On the other hand, increasing cell temperature by 1 C increases PV modules current by 0.0026–0.0032 A [1]. Based on this, increasing cell temperature by 1 C degree decreases PV module's power by 0.5–0.6%. In general, most of PV modules are being tested at 25 C degrees; thus, a different output power is expected when PV modules are working under different climate conditions. As for wind speed, the wind turbine output energy depends on the amount of wind power which hits the blades of a wind turbine. Therefore, to predict the energy produced by a wind turbine located in a specific location, a comprehensive study of the wind speed characteristic for this location must be done.

In general, the most common optimization methodology that is followed by the researchers starts by defining a specific area, and then a time series data for solar energy, ambient temperature, and wind (in case of hybrid PV/wind system) must be obtained. After that, the calculation of optimum tilt angle is conducted by modeling the solar energy on a tilt surface. Then based on the nature of the PV system (standalone, grid, or hybrid) the calculation of system energy sources (PV array battery, wind turbine, and diesel generator) optimum capacity is done. Finally, the size of the inverter in the PV system is calculated optimally.

However, according to a World Bank report published in 2010, the electricity production (MWh) in Kuwait was reported at 57082 GWh in 2010 [4]. This energy is totally generated by fossil fuel (64.4% oil sources and 35.7% natural gas), while the alternative energy sources including solar, wind, hydro-, and nuclear ones are not used at all [5]. Based on this, the Kuwaiti government has set recently the most ambitious target for using renewable energy in the Gulf region. The new Kuwaiti government renewable energy policy aims to generate 10% of its electricity from sustainable sources by 2020. The Kuwaiti government is trying to free up oil for export and expand its generation capacity to support increased tourism, manufacturing, and home building in a \$112-billion development program. However, renewable energy is a new subject for Kuwait, and that is why there is

a lack of information regarding the suitability of renewable energy sources for Kuwait's weather [6].

Kuwait is a desert country with high numbers of sun shining hour per day and, therefore, the use of PV grid-connected systems for electricity generation is promising at this country. Based on this, the main objective of this paper is to assist the electricity generated by PV grid-connected systems located at two main sites in Kuwait, namely, Al-Wafra and Mutla. This assessment—which is done using technical and economical criteria—provides worthwhile information for those who are interested in PV system installation at Kuwait. This work is done based on real meteorological data for the period 2009–2011. These data are provided by the Kuwait National Meteorological Network (KNMN) at KISR.

2. Solar Energy Potential in the Selected Sites

In this paper weather profiles for two sites located in Kuwait, namely, Mutla and Al-Wafra are analyzed. Mutla is located at latitude N 29° 22' 54'' and longitude 47° 37' 50''. Meanwhile Al-Wafra is located at latitude: 28° 37' 01'' and longitude 48° 00' 29''. The analyzed weather profiles contain solar radiation and ambient temperature data for three years (2009–2011). Figure 1 shows the mean hourly solar radiation for both sites. From the figure, both sites have almost the same solar radiation profile whereas it reaches the maximum value (1000 W/m²) in the summer time (June–August) while the minimum mean value is usually happening in the winter time (November–February). However both sites are desert sites with high clearness index along the year and, therefore, most of global solar radiation recorded consisted of direct solar radiation. On the other hand, Figure 2 shows the ambient temperature profile for both sites. The ambient temperature for both sites is in the range of 10–50°C with peak value in the summer time and minimum value in the winter time.

Table 1 shows the monthly mean daily solar radiation and ambient temperature for Al-Wafra and Mutla sites. The average ambient temperature for both sites is 28.78°C, and

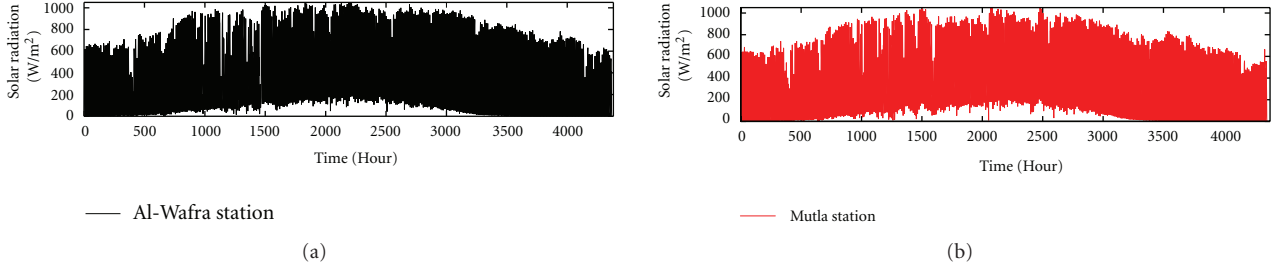


FIGURE 1: Hourly solar radiation profile for Al-Wafra and Mutla sites.

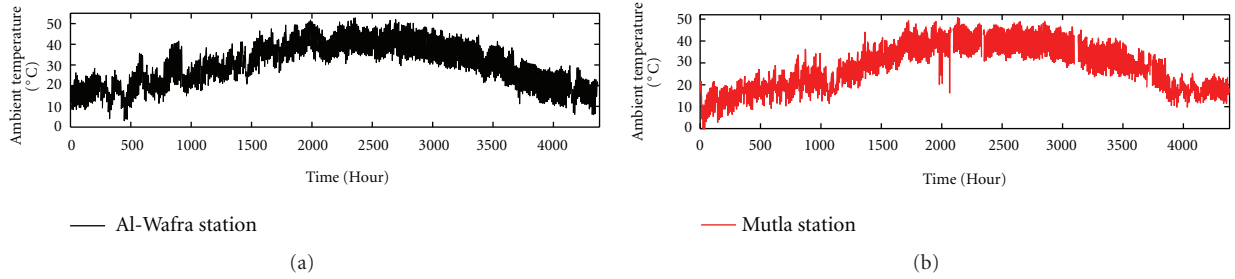


FIGURE 2: Ambient temperature profiles for Al-Wafra and Mutla sites.

30.8°C, respectively. On the other hand the average solar radiation for Mutla site is 476 W/m². This means that the annual mean daily solar energy received at this site is 5.712 kWh/m² (the peak sunshine hours is 5.7). As for Al-Wafra, the annual mean daily solar radiation is 481 W/m² which leads to that the annual mean daily solar energy is 5.772 kWh/m² (the peak sunshine hours is 5.8). Based on this, both sites have high solar energy potential and it is expected that PV systems productivity will be high as compared to other renewable energy alternatives.

3. PV Grid-Connected System Model

Figure 3 shows the typical component of a grid-connected system consisting of a PV array, DC-AC inverter and a grid interconnection point. Based on this, the mathematical model of the PV grid-connected system must contain the mathematical model of the PV array as well as the inverter [7].

3.1. PV Array Mathematical Model. The output power of a PV array depends on the available solar radiation (G) and the ambient temperature (T). The output power of a PV array increases linearly as the solar radiation increases and decreases as the ambient temperature increases. Thus, the instantaneous output power of a PV array [1] can be given by

$$P_{PV}(t) = P_{Peak} \left(\frac{G(t)}{G_{standard}} \right) - \alpha_T [T_c(t) - T_{standard}], \quad (1)$$

where $G_{standard}$ and $T_{standard}$ are the standard test conditions for solar radiation and cell temperature, respectively, and α_T

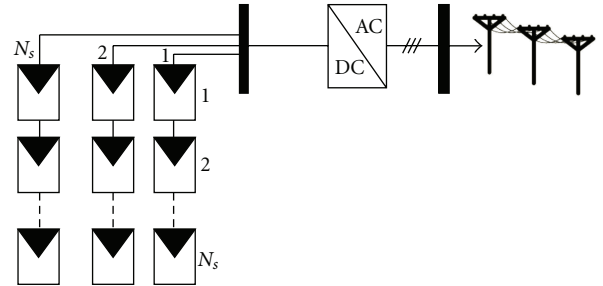


FIGURE 3: PV grid-connected system components.

is the temperature coefficient of the PV module power which can be obtained from the datasheet [1]. P_{peak} is the rated power of the PV array while T_c is the cell temperature and it is given by

$$T_c(t) - T_{ambient} = \frac{T_{standard}}{800} G(t). \quad (2)$$

To extract maximum power from a PV array which is under varying weather and load conditions, maximum power point trackers (MPPTs) are used. Such a device ensures maximum power operation of PV array and in this case the PV array is assumed to be operating at maximum power output, P_{peak} . However, based on (1), the calculation of PV array output power requires solar radiation and ambient temperature records, and, therefore, hourly solar radiation and ambient temperature records for the adopted sites have been obtained.

3.2. *Inverter Mathematical Model.* The efficiency of an inverter [1] is calculated by

$$\eta(t) = \frac{P_{in}(t) - P_{Loss}(t)}{P_{in}(t)}, \quad (3)$$

where $P_{in}(t)$ and $P_{Loss}(t)$ are the instantaneous input power and power loss during the conversion.

Ignoring the wire efficiency, the input power to the PV system is the output power of the PV module. The P_{Loss} is not constant but depends on many conditions which make it difficult to be calculated. Thus, an alternative model for inverter efficiency needs to be developed in order to estimate the inverter's output power.

Figure 4 shows an efficiency curve for a commercial inverter obtained from the datasheet. The curve describes the inverter's efficiency (in percent) in terms of input power and inverter rated power.

The efficiency curve can be described by a power function as follows:

$$\eta = c_1 \left(\frac{P_{PV_{input}}}{P_{INV_{Rated}}} \right)^{c_2} + c_3, \quad \frac{P_{PV_{input}}}{P_{INV_{Rated}}} > 0, \quad (4)$$

$$\eta = 0, \quad \frac{P_{PV_{input}}}{P_{INV_{Rated}}} = 0,$$

where P_{PV} and P_{INV_c} are PV module output power and inverter's rated power, respectively, while c_1 – c_3 are the model coefficients.

A MATLAB fitting tool can be used for calculating the developed inverter model coefficients, c_1 – c_3 . Therefore, samples of the inverter's efficiency curve shown in Figure 4 must be taken for the purpose of curve fitting using the MATLAB fitting tool. Intensive number of samples must be taken for a specific part of the curve as in zone B, less intensive number of samples are taken from the zone A, while few samples are taken from the zone C as described in Figure 4.

4. PV Grid-Connected Evaluation Criteria

To judge the feasibility of a grid-connected PV system, technical and economical evaluation criteria can be applied. In this paper technical criteria, namely, capacity factor and yield factor are applied. On the other hand, the cost of energy produced by the system (CoE) and the payback period are used as economical evaluation criteria.

The yield factor (YF) is defined as the annual, monthly, or daily net AC energy output of the system divided by the peak power of the installed PV array at standard test conditions (STC) and it is given by [7]

$$YF = \frac{E_{PV}(\text{kWh/year})}{PV_{WP}(\text{kWp})}. \quad (5)$$

This factor assists the productivity of a PV array under certain weather conditions. On the other hand, the capacity factor (CF) is defined as the ratio of the actual annual energy output to the amount of energy the PV array would generate

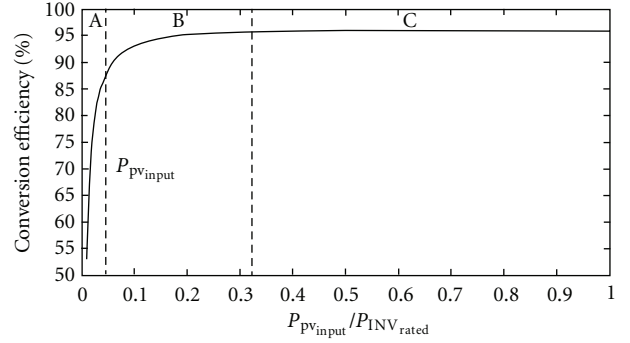


FIGURE 4: Typical efficiency curve for an inverter.

if it operated at full rated power (P_r) for 24 h per day for a year [7]:

$$CF = \frac{Y_F}{8760} = \frac{E_{PV_{annual}}}{P_R * 8760}. \quad (6)$$

This factor evaluates the usage of the PV array. However, the economical evaluation criteria, the life cycle cost, unit cost, and payback period criteria are used, and the life cycle cost is given by

$$LCC = C_{capital} + \sum_1^n C_{O\&M} R_{PW} + \sum_1^n C_{replacement} R_{PW} - C_{salvage} R_{PW}. \quad (7)$$

The capital cost ($C_{capital}$) of a project includes the initial capital expense for equipment, the system design, engineering, and installation. This cost is always considered as a single payment occurring in the initial year of the project, regardless of how the project is financed. Maintenance ($C_{O\&M}$) is the sum of all yearly scheduled operation and maintenance (O&M) costs. However, equipment replacement costs are not included. O&M costs include such items as an operator's salary, inspections, insurance, property tax, and all scheduled maintenance. Replacement cost ($C_{replacement}$) is the sum of all repair and equipment replacement cost anticipated over the life of the system. The replacement of a battery is a good example of such a cost that may occur once or twice during the life of a PV system. Normally, these costs occur in specific years and the entire cost is included in those years. The salvage value ($C_{salvage}$) of a system is its net worth in the final year of the life cycle period. It is common practice to assign a salvage value of 20 percent of original cost for mechanical equipment that can be moved. This rate can be modified depending on other factors such as obsolescence and condition of equipment. Future costs must be discounted because of the time value of money. One dollar received today is worth more than the promise of \$1 next year, because the \$1 today can be invested and earn interest. Future sums of money must also be discounted because of the inherent risk of future events not occurring as planned. Several factors should be considered when the period for

an LCC analysis is chosen. First is the life span of the equipment. PV modules should operate for 20 years or more without failure. However, twenty years is the normal period chosen to evaluate PV projects [1]. Finally the R_{PW} subscript indicates the present worth of each factor. The formula for the single present worth (R_{PW}) of a future sum of money (F) in a given year (N) at a given discount rate (I) is

$$R_{PW} = \frac{F}{(1+I)^N}. \quad (8)$$

After calculating the LCC, the unit cost of the energy produced by the system can be calculated as follows:

$$\text{CoE} = \frac{\text{LCC}}{\sum_1^n E_{PV}}. \quad (9)$$

The payback period can be calculated as follows:

$$\begin{aligned} \text{PBP} &= \frac{C_{\text{capital}}}{\text{Saving}_{\text{Annual}} * R_{PW}} \\ &= \frac{C_{\text{capital}}(\text{USD})}{E_{PV_{\text{Annual}}}(\text{kWh/year}) * \text{CoE}(\text{USD/kWh}) * R_{PW}}. \end{aligned} \quad (10)$$

5. Results and Discussion

In this paper a 100 kWp grid PV system is assumed to be installed at each site. The modelled PV module specifications are shown in Table 2. As for the inverter, a 100 kW inverter is used. The conversion efficiency model of the used inverter can be described as follows:

$$\begin{aligned} \eta &= -0.3253 \left(\frac{P_{PV}}{P_{INV_R}} \right)^{-1.143} + 97.49, \quad \frac{P_{PV}}{P_{INV_R}} > 0, \\ \eta &= 0, \quad \frac{P_{PV}}{P_{INV_R}} = 0. \end{aligned} \quad (11)$$

Table 3 shows the assumed units cost for the PV system in calculating the LCC, CoE, and PBP. The life cycle time of the PV system is assumed to be 20 years.

5.1. Al-Wafra Site. Figure 5 shows the monthly mean daily energy generated (kWh/month) by the system. The annual energy generation by the system is 192.270 MWh. According to this the final yield factor for this system is 1922.7 kWh/kWp/year. Meanwhile the average capacity factor is 22.25%. As for the performance of the inverter, a performance factor for the inverter is defined in this paper. This performance factor equals to the ratio of the annual mean daily conversion efficiency to the rated efficiency provided by the manufacturer. Based on this the performance factor of the used inverter is 96.4%. However, the LCC of the proposed system for Al-Wafra is 371000 USD. This means that the unit cost of this system is 0.0965 USD/kWh and the payback period is 15.6 years.

TABLE 2: PV modules specifications.

PV module type	KYOCERA (KC200GT)
PV module capacity	200 Wp
Maximum current	7.10
Maximum voltage	16.9
Open circuit voltage	21.5
Short circuit current	7.45
Efficiency ($G > 200 \text{ W/m}^2$)	12.75%
Efficiency ($G < 200 \text{ W/m}^2$)	14.5%
Temperature coefficient of power	$-3.9 \times 10^{-3}/^\circ\text{C}$

TABLE 3: PV system units cost.

Unit	Price
PV array	3.8/Wp USD
Inverter 100 kWp	32,000.00 USD
O&M	500 USD/year
Salvage	20% of the capital cost
Wires and circuit breakers	7,000.00 USD
Support structure	5,000.00 USD
Civil work and transportation	3,000.00 USD
Cost of kWh in Kuwait	0.10 USD

5.2. Mutla Site. The mean monthly daily energy generated (kWh/month) by the system is shown in Figure 6. The annual energy generation by the system is 186.11 MWh. Meanwhile, the capacity factor for this system is 21.6% and the final yield factor is 1861 kWh/kWp/year. The performance factor of the used inverter is 95.9%. As for the system cost, the LCC of the proposed system for Al-Wafra is 371000 USD. In addition, the unit cost of this system is 0.0997 USD/kWh and the payback period is 16.1 years.

5.3. Systems Productivity Evaluation. As mentioned before, the yield factor and the capacity factor criteria are used to assist the productivity of the proposed systems. In general the capacity factor is used to assist the usage of a power source. The CF is ratio of the energy generated by these sources to the maximum energy that could be generated according to the source's ratings and for 24 hours. However, for a PV power source the sun is only available for 12 hours a day and thus the ideal CF is 0.5 due to the unavailability of sun during the night. In addition to that, the maximum real CF is slightly lower than 0.5 due to the energy conversion losses [8–10]. In general the typical CF for a PV array is in the range of 0.15–0.4 [8–10]. However, in this paper the maximum CF is 0.4557 after considering the assumed energy conversion losses. Figure 7 shows the monthly mean daily CF for both sites. The CF values for both systems are in the range of (0.15–0.31) which means that both system's operation are in the typical operation zone.

On the other hand, the yield factor measures the productivity of the PV system. However, there is no typical range for the yield factor because this factor is a location-dependant factor. That is to say, each county (climate zone)

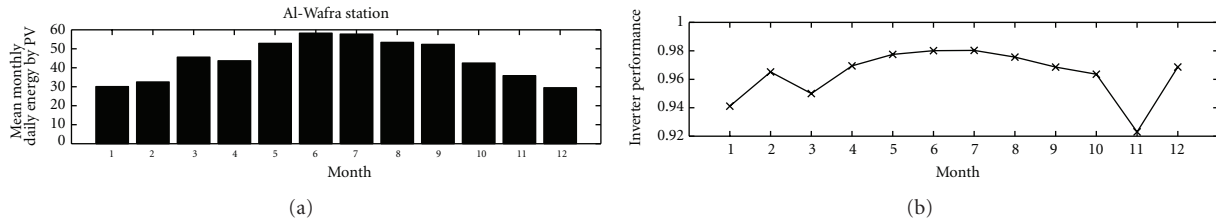


FIGURE 5: PV system performance at Al-Wafra site.

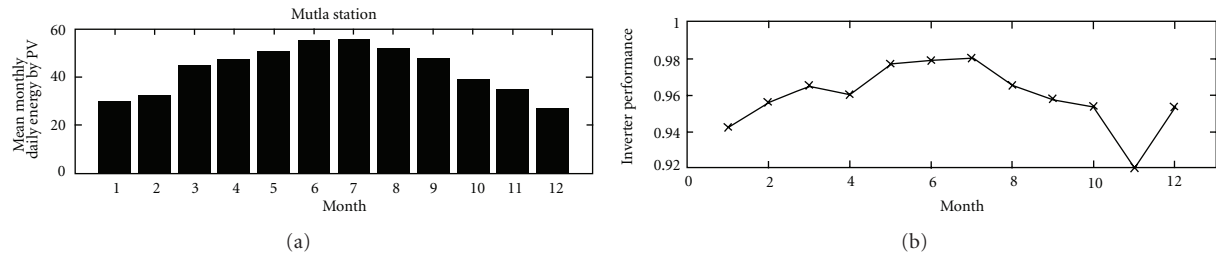


FIGURE 6: PV system performance at Mutla site.

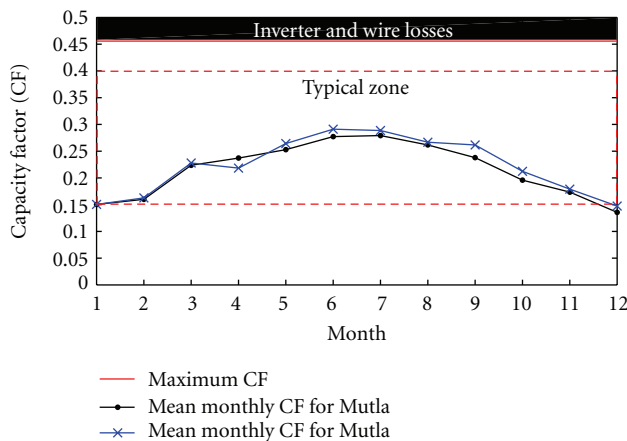


FIGURE 7: Monthly mean daily CF for Al-Wafra and Mutla sites.

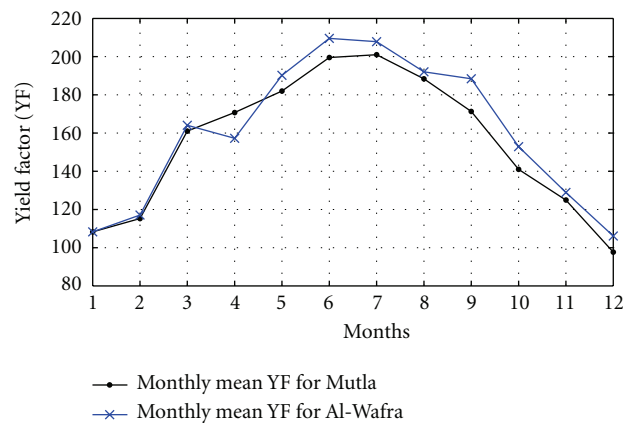


FIGURE 8: Monthly mean daily YF for Al-Wafra and Mutla sites.

has its own typical yield factor. In [10] the typical field factors for 6 countries are reported. The typical YF for Germany is in the range of 400–1300 kWh/kWp/year, while it is in the range of 470–1230 kWh/kWp/year for Japan. Furthermore, the typical yield factor for The Netherlands, Italy, Switzerland, and Israel are 400–900, 450–1250, 450–1400, and 740–2010 kWh/kWp/year, respectively. As for Kuwait, Figure 8 shows the range of the YF for both systems. The monthly mean of YF for Mutla is in the range of 97–201 kWh/kWp/month; meanwhile it is in the range of 106–209 for Al-Wafra. However, as mentioned before, the annual YF for Mutla and Al-Wafra are 1861 kWh/kWp/year and 1922.7 kWh/kWp/year, respectively. This proves that the PV technology in Kuwait has almost the best performance when compared to the countries reported by [10].

6. Conclusion

In this paper the performance of a 100 kWp grid-connected PV systems was studied for two sites, namely, Al-Wafra and Mutla in Kuwait. The proposed systems showed high energy productivity whereas the annual capacity factors for Mutla and Al-Wafra were 22.25% and 21.6%, respectively. Meanwhile the annual yield factor for Mutla and Al-Wafra were 1861 kWh/kWp/year and 1922.7 kWh/kWp/year, respectively. On the other hand the cost of the energy generated by both systems was about 0.1 USD which is very close to the price of the cost of energy sold by the Kuwaiti electricity company. Furthermore the invested money is recovered during the assumed life cycle time whereas the payback period for both sites was about 15 years. Such a work is helpful for PV technology investments in Kuwait.

References

- [1] R. P. Mukund, *Wind and Solar Energy*, CRC Press, 1999.
- [2] M. A. Eltawil and Z. Zhao, "Grid-connected photovoltaic power systems: technical and potential problems-a review," *Renewable and Sustainable Energy Reviews*, vol. 14, no. 1, pp. 112–129, 2010.
- [3] T. Khatib, "A review of designing, installing and evaluating standalone photovoltaic power systems," *Journal of Applied Sciences*, vol. 10, no. 13, pp. 1212–1228, 2010.
- [4] Ministry of Electricity & Water (MEW), *Electrical Energy. Edition 36A*, Statistics Dept. & Information Center, Ministry Of Electricity & Water, 2011.
- [5] The World Bank, ".,," The World Bank Annual Report, 2010.
- [6] A. H. Abdullah, A. A. Ghoneim, and A. Y. Al-Hasan, "Assesment of grid-connected photovoltaic systems in the Kuwaiti climate," *Renewable Energy*, vol. 26, no. 2, pp. 189–199, 2002.
- [7] E. Kymakis, S. Kalykakis, and T. M. Papazoglou, "Performance analysis of a grid connected photovoltaic park on the island of crete," *Energy Conversion and Management*, vol. 50, no. 3, pp. 433–438, 2009.
- [8] G. Privitera, A. R. Day, G. Dhesi, and D. Long, "Optimising the installation costs of renewable energy technologies in buildings: a linear programming approach," *Energy and Buildings*, vol. 43, no. 4, pp. 838–843, 2011.
- [9] B. Rezaie, E. Esmailzadeh, and I. Dincer, "Renewable energy options for buildings: case studies," *Energy and Buildings*, vol. 43, no. 1, pp. 56–65, 2011.
- [10] A. McEvoy, T. Markvart, and L. Castaner, *Practical Handbook of Photovoltaics: Fundamentals and Applications*, Elsevier, New York, NY, USA, 2011.

Research Article

Economical Feasibility of Utilizing Photovoltaics for Water Pumping in Saudi Arabia

Ahmet Z. Sahin¹ and Shafiqur Rehman²

¹Department of Mechanical Engineering, King Fahd University of Petroleum and Minerals, Dhahran 31261, Saudi Arabia

²Center for Engineering Research, Research Institute, King Fahd University of Petroleum and Minerals, Dhahran 31261, Saudi Arabia

Correspondence should be addressed to Ahmet Z. Sahin, azsahin@gmail.com

Received 15 June 2012; Revised 3 September 2012; Accepted 4 September 2012

Academic Editor: Daniel Chemisana Villegas

Copyright © 2012 A. Z. Sahin and S. Rehman. This is an open access article distributed under the Creative Commons Attribution License, which permits unrestricted use, distribution, and reproduction in any medium, provided the original work is properly cited.

Energy and water are the two major need of the globe which need to be addressed for the sustenance of the human beings on this planet. All the nations, no matter most populous, developed and developing need to diversify the means and ways of producing energy and at the same time guarding the environment. This study aims at techno economical feasibility of producing energy using PV solar panels and utilizing it to pump-water at Dhahran, Riyadh, Jeddah, Guriat, and Nejran regions in Saudi Arabia. The solar radiation data from these stations was used to generate electricity using PV panels of 9.99 kW total capacity. Nejran region was found to be most economical in terms of minimal payback period and cost of energy and maximum internal rate of return whereas PV power production was concerned. Water-pumping capacity of the solar PV energy system was calculated at five locations based on the PV power production and Goulds model 45J series of pumps. Monthly total and annual total water pumping capacities were determined. Considering the capital cost of combined solar PV energy system and the pump unit a cost analysis of water pumping for a well of 50 m total dynamic head (TDH) was carried out. The cost of water pumping was found to vary between 2 and 3 US\$/m³.

1. Introduction

Solar energy is a clean source of energy, and it does not risk human lives, environment, and economic disasters which may include oil and coal sludge spills, coal mine and devastating gas pipeline explosions, unforeseen nuclear accidents, and water supply contamination from natural gas fracking. Its utilization promotes better health through decreased coal plant emissions pollution.

Water pumps, powered by photovoltaic (PV) panels, are being used frequently to pump water for domestic usage, to irrigate crops and landscape, to cattle, and provide potable water. The advantage of using solar energy for pumping the water is that major quantities of water are required during day time and that too during time when the sun is on top of our head, and during these times the PV panels produce maximum energy and hence the water quantity. These solar pumps can be installed anywhere no matter it is a valley,

remotely located farms, forest, or locations which are difficult to reach and are not connected to national electric grid. The utilization of solar water pump in developing countries is providing a workable solution to meet water needs of the people. At the same time, one can also save the environment by avoiding or minimizing the burning of fossil fuel for energy generation. The solar water-pumping technology is commercially available, has-proven record of reliability, require, minimal skilled manpower once in operation, and operation and maintenance cost is also very minimal and affordable.

Kingdom of Saudi Arabia is blessed with high intensities of solar radiations and longer durations of sunshine hours and vast open land with gentle topographical features in most of it and complex terrain in some part of it. According, Rehman et al. [1] global solar radiation varies between a minimum of 1.63 MWh/m²/y at Tabuk and a maximum of 2.56 MWh/m²/y at Bisha while mean value remained as

2.06 MWh/m²/y. The sunshine duration varied between 7.4 and 9.4 h with an overall mean of 8.89 h or about a total of 3245 h in a year. The specific yield was found to vary from 211.5 to 319.0 kWh/m² with a mean of 260.83 kWh/m² [1]. The dwellings are spread all over the Kingdom with major concentrations in Dhahran on the eastern coast, Riyadh in the central part, Jeddah on the west coast, Guriat in the north most, and Nejran in the south part. Most of the major cities are connected to national electricity grid and the network of national and provincial highways. Still there are remote areas and smaller cities and towns which are not yet connected to national electricity grid and are dependent on power supply from diesel generating power stations and have isolated grids. Some of these dwellings are located in mountainous region where it is not only difficult to lay the grid but also economically prohibitive. Availability of water for domestic use and drinking purposes is a great challenge in such areas and areas which are far from the main cities or industrial regions. Ground water is available in most of these areas but they require electricity and equipment to pump the water for domestic usage, irrigation, and cattle.

Water pumping has regularly been a technical challenge, solving the problems of drinking water supply and regular irrigation was a prerequisite for the development of civilization in many of the ancient empires [2]. The PVPs are being installed worldwide, and there were approximately 10,000 such systems in 1993 which reached to almost six times that is, 60,000 units in 1998, [3]. The ongoing efforts on performance improvement and modeling [4–9], system sizing and optimization [10–14], and performance of PV systems [15] on the basis of experimental measurements have resulted in commercially acceptable, economically affordable, and easily maintainable with least possible expertise. These developments have led and are contributing to the improvement of the lives of remotely located dwellings.

J. S. Ramos and H. M. Ramos [16] used a pump of 154 W powered by a solar array of 195 watt peak (W_p) to pump water for village having ten families and consuming 100 L of water each with 6-day immunity period and 2% permissible loss of load at a cost of 1.06 €/m³ and capital investment of 3019 €. Ould-Amrouche et al. [17] stated that the utilization of PV water-pumping systems helped both in improving the living conditions in remote areas and keeping the environment clean. Mahmoud and El-Nather [18] conducted the economical feasibility of using photovoltaic (PV) technology to pump the ground water in comparison with using diesel units. Their study proved that PV-battery system was economical compared to the diesel system. According to Kaldellis [19] the PV water-pumping systems (PVPs) are environmentally friendly solution and contribute substantially to the satisfaction of remote communities' water consumption needs.

PV-powered water-pumping systems have been installed and are operational in various parts of the globe including Arabian countries, and some of these installation dates back to early 1990s. Some of these studies and installations have been reported in the literature like Bhave [20] for India, Alawaji et al. [21] for the Kingdom of Saudi Arabia, Hammad [22] for Jordan, Al Suleimani and Rao [23]

TABLE 1: Geographical coordinates of meteorological stations considered in this study.

Location	Latitude, (°N)	Longitude, (°E)	Elevation, (m)
Dhahran	26.3	50.2	17
Riyadh	24.7	46.7	620
Jeddah	21.7	39.2	17
Guriat	31.4	37.7	504
Nejran	17.6	44.4	1212

TABLE 2: Global solar radiation on horizontal surface (kWh/m²/d).

Month	Dhahran	Riyadh	Jeddah	Guriat	Nejran
Jan	3.57	3.76	4.53	3.14	5.71
Feb	4.42	4.63	5.32	3.96	6.60
Mar	5.13	5.38	6.18	5.04	6.98
Apr	6.03	6.19	6.88	6.15	7.43
May	7.03	7.15	7.17	7.10	7.65
Jun	7.73	7.87	7.12	7.95	7.87
Jul	7.26	7.59	7.04	7.76	7.22
Aug	6.97	7.15	6.53	6.92	7.14
Sep	6.45	6.34	6.17	5.92	7.53
Oct	5.33	5.47	5.56	4.41	7.09
Nov	4.00	4.22	4.60	3.26	6.37
Dec	3.28	3.52	4.15	2.80	5.65
Annual	5.60	5.78	5.94	5.37	6.94

for Oman, Al-Karaghoul and Al-Sabounchi [24] for Iraq, Manolakos et al. [25] for Greece, Kordab [26] for ESCWA member countries, Meah et al. [27] for, Sutthivirode et al. [28] for Thailand, and Chueco-Fernández and Bayod-Rújula [29] for Chile. In Saudi Arabia, the work has been reported on various aspects of solar energy such as radiation data prediction and estimation [30–37], photovoltaic-based cost of solar energy by generation Rehman et al. [38], availability of solar radiation and sunshine duration by Aksakal and Rehman [39], photovoltaic electricity for irrigation Rehman et al. [40] desert camping Al-Ali et al. [41], and solar radiation and sunshine duration maps by Mohandes and Rehman [42].

2. Input Data and Assumptions

The geographical coordinates and elevation above mean sea level of all the locations being considered in the present work are listed in Table 1. The global solar radiation values are summarized in Table 2 for Dhahran, Riyadh, Jeddah, Guriat, and Nejran. The isolated grid PV power system with 9.99 kW of installed capacity is considered for all the locations being reported in this paper. The PV systems consist of 54 modules of 185 W each with rated efficiency of 14.8%, module frame area of 1.24 m², nominal operating cell temperature of 45°C, temperature coefficient of 0.40%, and an inverter of 10 kW capacity with 90% efficiency. The miscellaneous losses in energy yield process are taken as 1%. For financial analysis, the capital cost is taken as 8US\$ per W_p with 25 years of

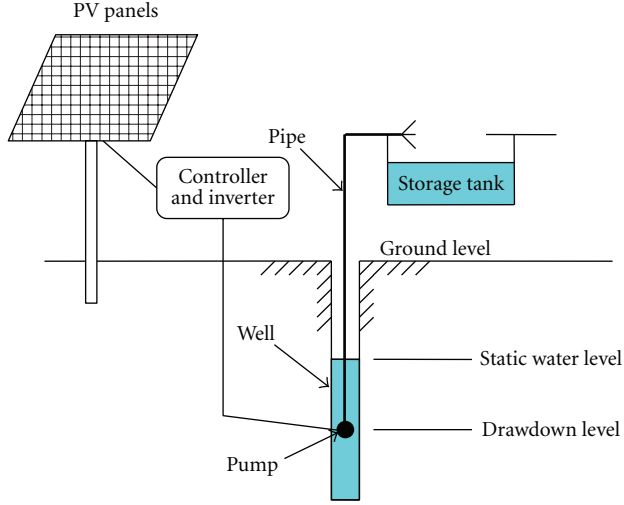


FIGURE 1: Schematic view of the solar photovoltaic water-pumping system.

operating life, inflation rate of 2%, debt interest rate of 7.0%, debt ratio of 70%, and debt term of 10 years. The total capital cost was calculated to be US\$79,920, and it is assumed that it remains the same irrespective of location of the station. The total area covered by the PV panes was worked out to be 68 m². The schematic view of the solar PV water-pumping system considered in this work is shown in Figure 1.

3. Seasonal Variation of Solar Radiation on Horizontal Surface

Long-term monthly average global solar radiation intensities on daily basis for Dhahran, Riyadh, Jeddah, Guriat, and Nejran are summarized in Table 2. Highest intensities of 7.73, 7.87, 7.95, and 7.87 kWh/m²/d were observed in the month of June at Dhahran, Riyadh, Guriat, and Nejran, respectively and of 7.17 kWh/m²/d in May at Jeddah. It is also evident that relatively higher intensities were observed during April to September period which also correspond to higher-demand period for both power and water. Highest annual mean solar radiation intensity of 6.94 kWh/m²/d was found at Nejran.

4. Solar Energy, Energy Density, and Greenhouse Gases Emission Analysis

The energy produced a PV array and delivered to the grid is estimated as follows:

$$E_P = S\eta_P\bar{H}_t, \quad (1)$$

where S is the area of the array, \bar{H}_t is the daily total radiation on tilted surface, and η_P is the average efficiency of the PV array. The produced energy (E_P) is reduced by taking into consideration the miscellaneous PV array losses, (λ_p) and

TABLE 3: Values of PV module-related variables.

PV module type	η_r (%)	NOCT (°C)	β_p (%/°C)
Monocrystalline silicon (Mono-Si)	13.0	45	0.40
Polycrystalline silicon (Poly-Si)	11.0	45	0.40
Amorphous silicon (a-Si)	5.0	50	0.11
Cadmium telluride (CdTe)	7.0	46	0.24
Copper indium diselenide (CIS)	7.5	47	0.46

other power conditioning losses (λ_c). These losses are taken into consideration using the following equation:

$$E_A = E_P(1 - \lambda_p)(1 - \lambda_c), \quad (2)$$

where E_A is the PV array energy available to the load and the battery, if in use. The overall efficiency η_A is defined as follows:

$$\eta_A = \frac{E_A}{SH_t}. \quad (3)$$

In (1), the average efficiency of the PV array (η_P) which is a function of average temperature of the PV module T_c is estimated using the following equation:

$$\eta_P = \eta_r[1 - \beta_p(T_c - T_r)], \quad (4)$$

where η_r is the PV module efficiency at reference temperature T_r ($= 25^\circ\text{C}$) and β_p is the temperature coefficient for module efficiency. The module temperature T_c is related to the mean monthly ambient temperature T_a through Evan's [43] formula as given below:

$$T_c - T_a = (219 + 832\bar{K}_t) \left(\frac{\text{NOCT} - 20}{800} \right), \quad (5)$$

where NOCT is the nominal operating cell temperature and \bar{K}_t the monthly mean clearness index. The values of η_r , NOCT, β_p , and depend on the type of PV module considered. For standard technologies and module the values of these variables are summarized in Table 3. The efficiency of photovoltaic cells varies with their operating temperature. Most cell types exhibit a decrease in efficiency as their temperature increases.

The monthly total energy estimated using (1) to (5) for all the locations is summarized in Table 4. This table also includes the energy density per unit area of the PV panel in kWh/m². At Dhahran and Riyadh the maximum energy of 1.569 and 1.596 MWh was observed in the month of October while at Jeddah (1.573 MWh), Guriat (1.517 MWh), and Nejran (2.057 MWh) in the months of March, August, and November, respectively. Similarly, the highest values of energy density of 23.07, 23.47, 23.13, 22.31, and 30.25 kWh/m² corresponding to Dhahran, Riyadh, Jeddah, Guriat, and Nejran occurred in the months of October, October, March, August, and November, respectively. Based on annual total energy output, maximum energy of 19.59 MWh was produced at Nejran while a minimum of 16.325 MWh at Dhahran, as can be seen from Table 4.

TABLE 4: Annual energy delivered and energy density for all the stations under consideration.

Month	Dhahran		Riyadh		Jeddah		Guriat		Nejran	
	MWh	kWh/m ²								
Jan	1.303	19.16	1.362	20.03	1.536	22.59	1.288	18.94	1.961	28.84
Feb	1.277	18.78	1.326	19.50	1.443	21.22	1.230	18.09	1.768	26.00
Mar	1.383	20.34	1.435	21.10	1.573	23.13	1.472	21.65	1.719	25.28
Apr	1.319	19.40	1.336	19.65	1.417	20.84	1.444	21.24	1.464	21.53
May	1.354	19.91	1.353	19.90	1.324	19.47	1.478	21.74	1.325	19.49
Jun	1.313	19.31	1.312	19.29	1.195	17.57	1.463	21.51	1.198	17.62
Jul	1.318	19.38	1.347	19.81	1.250	18.38	1.509	22.19	1.204	17.71
Aug	1.416	20.82	1.428	21.00	1.298	19.09	1.517	22.31	1.343	19.75
Sep	1.505	22.13	1.461	21.49	1.384	20.35	1.493	21.96	1.628	23.94
Oct	1.569	23.07	1.596	23.47	1.540	22.65	1.401	20.60	1.966	28.91
Nov	1.341	19.72	1.408	20.71	1.404	20.65	1.206	17.74	2.057	30.25
Dec	1.227	18.04	1.312	19.29	1.439	21.16	1.184	17.41	1.957	28.78
Annual	16.325	240.07	16.677	245.25	16.804	247.12	16.685	245.37	19.590	288.09

TABLE 5: Summary of greenhouse gases avoided as a result of PV power utilization for water pumping in Saudi Arabia at different locations.

Location	GHG (tCO ₂)/year	Gasoline saved (L/year)	During life time of the plant	
			(tCO ₂)	L
Dhahran	3.3	1,420	82.5	35,500
Riyadh	3.4	1,451	85.0	36,275
Jeddah	3.4	1,462	85.0	36,550
Guriat	3.4	1,452	85.0	36,300
Nejran	4.0	1,704	100.0	42,600
Average	3.5	1,498	87.5	37,445

As a result of utilization of solar energy for water pumping in Saudi Arabia, on an average of 3.5 tons of CO₂ gas could be avoided from entering into the local atmosphere annually, as given in Table 5. Equivalently at Dhahran, Riyadh, Jeddah, Guriat, and Nejran a total of 1,420, 1,451, 1,462, 1,452, and 1,704 liters of gasoline could be saved from burning for energy production annually. On an average, during the life time of the PV panels in operation, in this case 25 years, around 87.5 tons equivalent of greenhouse gasses could be avoided from entering into the local atmosphere, or 37,445 liters of gasoline could be saved from burning.

5. Economical Analysis of Solar Energy Production

The pretax internal rate of return (IRR) on equity (%) and assets (%), which represents the true interest yield provided by the project equity and assets over its life before income tax, is calculated using the pre-tax yearly cash flows and the project life and included in Table 6. In the present case, IRR has been calculated on a nominal basis that is including inflation. For a project to be considered financially acceptable, IRR is expected to be equal to or greater than the required rate of return of the investor. The simple

payback (year) is the duration of time that it takes for a proposed project to recoup its own initial cost, out of the income or savings it generates. The simple payback method is the indicator that how desirable is the investment. Lesser the payback period better will be the investment. From economical analysis, it is evident that Nejran is the best location for the utilization of PV solar energy with maximum internal rate of return (IRR) of 14.0% and plant capacity of 22.4% and minimum simple payback period of 9.7 years and cost of energy of 16.32 US¢/kWh compared to other stations used in the present work. The other remaining locations are very near to each other whereas cost of energy and other economical indicators are concerned.

The effect of initial investment cost on cost of energy (COE) was also studied to check on the sensitivity. The initial investment costs of 8, 7, 6, 5, 4, 3, and 2US\$ per peak watt (W_p) were considered while keeping all other interest rates the same. The resulting COE values for all the locations and initial investment rates are compared in Figure 2. It is evident that as the initial investment cost goes down, the COE also responds in the same manner. A decrease of US\$1 per W_p in the initial investment cost (i.e., 7US\$ instead of 8US\$) causes a decrease of 12.5% in COE (i.e., 17.13 US¢/kWh instead of 19.58 US¢/kWh), and, for further decrease of 1US\$, the COE decreased to 14.69 US¢/kWh or a decrease of 16.7%.

TABLE 6: Summary of internal rate of return (IRR) and cost of energy (COE) for all the stations considered in the present work.

Location	Pretax IRR (%)		Payback period (years)		Cost of energy (US¢/kWh)	Plant capacity factor (%)
	Equity	Assets	Simple	Equity		
Dhahran	10.3	3.2	11.7	13.1	19.582	18.7
Riyadh	10.7	3.5	11.4	12.9	19.169	19.1
Jeddah	10.9	3.5	11.3	12.8	19.024	19.2
Guriah	10.7	3.5	11.4	12.9	19.160	19.1
Nejran	14.0	5.2	09.7	11.1	16.319	22.4
Average	11.3	3.8	11.1	12.6	18.651	19.7

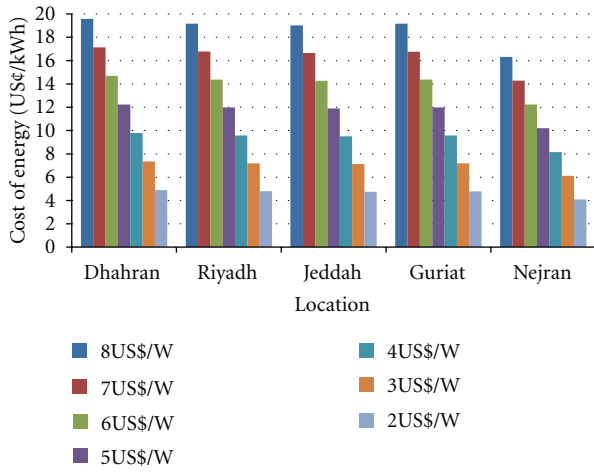


FIGURE 2: Effect of capital cost on cost of energy generated from 9.99 kW installed capacity PV power plant in Saudi Arabia.

6. Performance of Solar-Energy-Based Water Pumping

6.1. *Water-Pumping Analysis.* The power required for pumping water from underground $P_{hyd}(W)$ can be determined by the expression

$$P_{hyd} = \rho g H Q (W), \quad (6)$$

where ρ is the density of water (kg/m^3), g is the gravitational acceleration (m/s^2), H is the total head (m), and Q is the volumetric flow rate of water (m^3/s). Assuming that the density and the gravitational acceleration do not vary significantly, the product HQ is found to be directly proportional to the pumping power requirement. HQ may be considered as the pumping capacity rate. Thus the equation can be rewritten as

$$HQ = \frac{P_{hyd}}{\rho g} (\text{m}^4/\text{s}) \quad (7)$$

to determine the pumping capacity rate HQ in m^4/s for any given available power $P_{hyd}(W)$. Once the total head H (m) is available, the volumetric flow rate of water that can be pumped from underground Q (m^3/s) can be calculated. This expression indicates that a hydraulic power of $P_{hyd} = 1 W$ is equivalent to a pumping capacity rate of $8.8 \text{ m}^4/\text{day}$. For

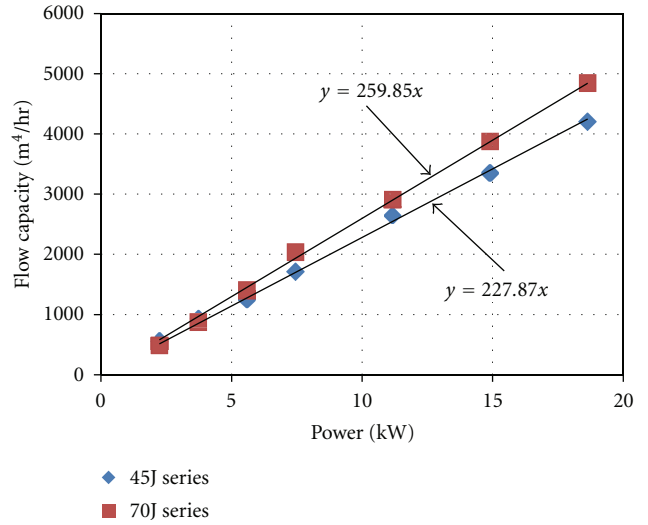


FIGURE 3: Flow capacity rate as function of pump size for two series of pumps.

the determination of the total pumping capacity for a given period of time, this equation can be written as

$$HQ t = \frac{P_{hyd} \times t}{\rho g} (\text{m}^4), \quad (8)$$

where time t is time (s). Accordingly, a hydraulic energy ($P_{hyd} \times t$) of 1 kWh (i.e., 3600 kJ) is equivalent to a pumping capacity ($HQ t$) of 367 m^4 . On the other hand, the required pump size $P(W)$ can be determined from

$$P = \frac{P_{hyd}}{\eta} = \frac{\rho g H Q}{\eta}, \quad (9)$$

where η is the pump efficiency.

6.2. *Water-Pumping Capacity.* Twelve models of water pumps at different sizes from Goulds Pump Company were selected in the present work. Six of these are from 45J series, and the remaining six are from 70J series high-capacity flat bowl 6-inch submersible pumps. Detail specifications of these pumps are given in Tables 7(a) and 7(b). The nominal flow rate of these pumps at best efficiency ranges from 45 to 70 GPM, and their motor size ranges from 3 to 25 HP. Depth of water for which the pumps operate ranges from

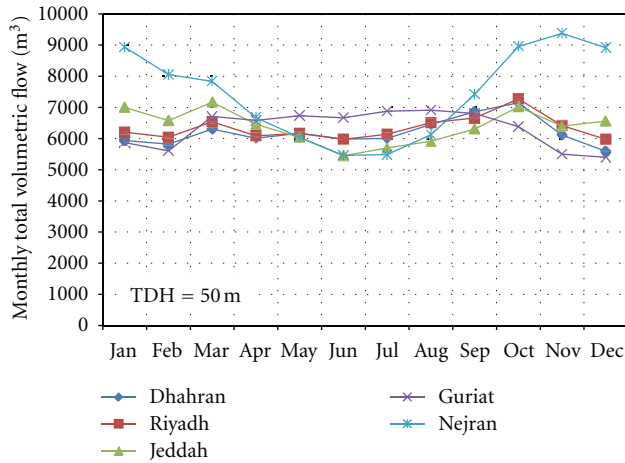


FIGURE 4: Monthly total volumetric flow of water from a well with total dynamic head of 50 m using solar PV-operated Goulds model 45J series pump for five different sites in Saudi Arabia.

100 to 1350 feet. Nominal flow capacity rate of each pump (in m^4/hr) is also given in the last column in Table 7.

Figure 3 shows the nominal flow capacity rate variation of the pumps at best efficiency point as function of the power consumption. As can be seen from this figure, the nominal flow capacity rate is almost linear with the power (or size) of the pump in each series of pumps. The least squares fit line for the data is shown on the figure for each series. The slopes of the lines are slightly different from each other as a result of different efficiencies of pumps. 70J series pumps are slightly more efficient (62% max) than the 45J series pumps (60% max). Accordingly, the relationship of nominal flow capacity rate and the power for each series of pumps can be expressed as follows:

$$\text{Flow capacity rate (m}^4/\text{hr)} = 227.87 \times \text{Power (kW)} \text{ for 45J series}$$

$$\text{Flow capacity rate (m}^4/\text{hr)} = 259.85 \times \text{Power (kW)} \text{ for 70J series.}$$

The flow rate in m^3/hr is obtained by dividing the flow capacity rate with the total dynamic head (TDH).

Monthly total volumetric flow of water from a depth of 50 m total dynamic head using solar PV-operated Goulds model 45J series pumps is shown in Figure 4. The maximum efficiency of the pumps in this series is 60%. Monthly total volumetric flow of water shows fairly uniform variation throughout the year except for the Nejran site. In Nejran site the volumetric flow is found to be considerably higher during the winter months as compared with that during the summer months. This is due to the high solar energy availability during the winter months in the site of Najran. Referring to Table 4, the yearly average solar electric power generation from the solar PV panels considered in the five sites, namely, Dhahran, Riyadh, Jeddah, Guriat, and Nejran is 1.86, 1.90, 1.92, 1.90, and 2.24 kW, respectively. Therefore the most suitable pump model for the solar PV energy generator is the 45J03 model that comes with 5 hp (2.24 kW) motor

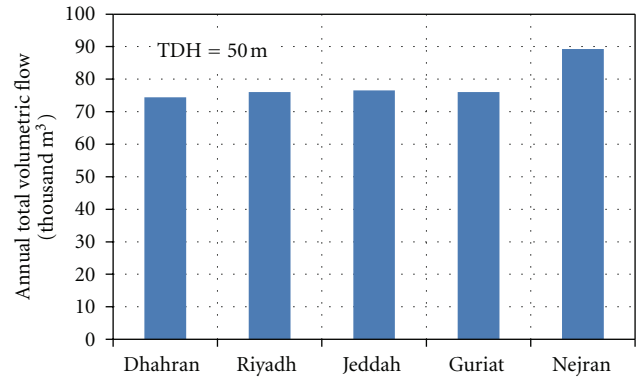


FIGURE 5: The annual total volumetric flow of water from a well with total dynamic head of 50 m using solar PV-operated Goulds model 45J series pump for five different sites in Saudi Arabia.

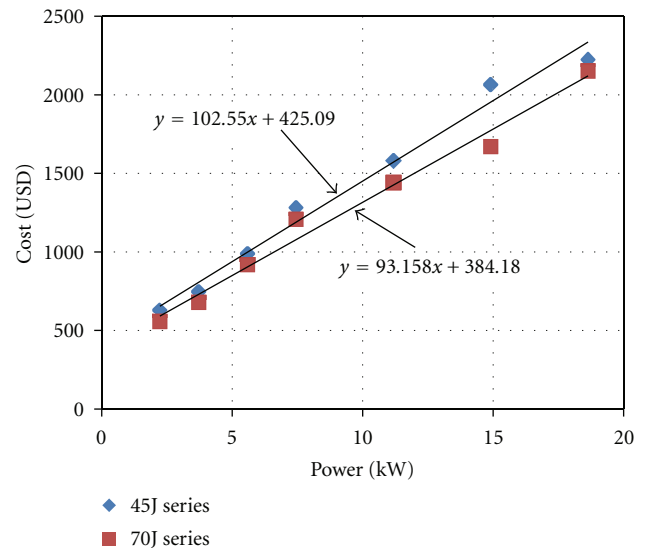


FIGURE 6: Cost of pumps as function of the pump size (power) for two series of pumps.

and efficiently operates with a TDH of 54.58 m as can be seen from Table 7(a). This is the reason why the TDH is fixed to be 50 m in Figure 4. The annual total volumetric flow of water for the same solar PV energy generator is shown in Figure 5 for the five sites considered. The variation of the annual total volumetric flow among the sites considered is minimal except for the case of Nejran site where the annual total volumetric flow is about 18% more than the other sites.

Figure 6 shows the cost (price) of water pumps considered in this study. The price of water pumps is found to increase with the size of the pumps. The variation shows a nearly linear trend for both series of pumps considered. This trend can be expressed in first-order approximation for both the pump series as

$$\text{Price (\$)} = 102.55 \times \text{Power (kW)} + 425.09 \text{ for 45J series}$$

$$\text{Price (\$)} = 93.158 \times \text{Power (kW)} + 384.18 \text{ for 70J series of pumps.}$$

TABLE 7

(a) Specifications of Goulds water pumps 45J series considered

Model	Price (USD)	Flow rate (GPM)	Power (hp)	TDH (feet)	Flow rate (m ³ /hr)	Power (kW)	TDH (m)	Flow capacity rate (m ⁴ /hr)
45J03	630	45	3	180	10.22175	2.2368	54.864	560.8061
45J05	745	45	5	300	10.22175	3.728	91.44	934.6768
45J07	987	45	7.5	400	10.22175	5.592	121.92	1246.236
45J10	1280	45	10	550	10.22175	7.456	167.64	1713.574
45J15	1580	45	15	850	10.22175	11.184	259.08	2648.251
45J20	2065	45	20	1075	10.22175	14.912	327.66	3349.259
45J25	2226	45	25	1350	10.22175	18.64	411.48	4206.046

Data at best efficiency (%60).

(b) Specifications of Goulds water pumps 70J series considered

Model	Price (USD)	Flow rate (GPM)	Power (hp)	TDH (feet)	Flow rate (m ³ /hr)	Power (kW)	TDH (m)	Flow capacity rate (m ⁴ /hr)
70J03	556	70	3	100	15.9005	2.2368	30.48	484.6472
70J05	680	70	5	180	15.9005	3.728	54.864	872.365
70J07	919	70	7.5	290	15.9005	5.592	88.392	1405.477
70J10	1208	70	10	420	15.9005	7.456	128.016	2035.518
70J15	1443	70	15	600	15.9005	11.184	182.88	2907.883
70J20	1670	70	20	800	15.9005	14.912	243.84	3877.178
70J25	2152	70	25	1000	15.9005	18.64	304.8	4846.472

Data at best efficiency (%62).

TABLE 8: Cost of solar PV water pumping from a well with 50 m TDH.

Location	Cost of water pumping with TDH = 50 m (US¢/m ³)
Dhahran	2.69
Riyadh	2.63
Jeddah	2.61
Guriat	2.63
Nejran	2.24
Average	2.56

Considering both of the relationships, a representative linear relation applicable for all the pump can be obtained by

$$\text{Price (\$)} = 98 \times \text{Power(kW)} + 405. \quad (10)$$

Considering the pump model 45J03, a cost of USD630 is added to the capital cost of solar PV system. Therefore the cost of water produced from a well of 50 m TDH becomes 2.69, 2.63, 2.61, 2.63, and 2.24 US¢/m³ for Dhahran, Riyadh, Jeddah, Guriat, and Nejran, respectively, as shown in Table 8. The average pumping cost of water per cubic meter is found to be 2.56 US¢.

7. Conclusions

An economical feasibility study was carried out in relation to producing electrical energy using PV solar panels for pumping underground water at Dhahran, Riyadh, Jeddah, Guriat, and Nejran sites in Saudi Arabia. A solar PV energy generation system producing 9.99 kW of electrical energy

was considered. The electrical energy generated was used to calculate the underground water-pumping capacity at each of the five sites. The following conclusions can be derived from the present work.

- (i) The annual total energy output was found to be the maximum (19.59 MWh) at Nejran site while it was a minimum (16.325 MWh) at Dhahran site.
- (ii) The Nejran site was found to be most economical in terms of minimal payback period and cost of energy and maximum internal rate of return.
- (iii) Goulds model 45J series of pumps were found to be suitable to be integrated with the solar PV energy generation system.
- (iv) Based on the solar PV electrical energy generation, monthly total water-pumping capacities were found to be nearly uniform throughout the year except for the Nejran site. Considerably higher water production capacity was observed during the winter months in Nejran.
- (v) Annual total water-pumping capacities were almost equal in all the sites considered except for the Nejran site where the water-pumping capacity was %18 higher.
- (vi) The cost analysis of water pumping system indicated that, for a well of 50 m total dynamic head (TDH), the cost of water pumping vary between 2 and 3 US¢/m³ in all the five sites in Saudi Arabia.

Acknowledgment

The authors would like to acknowledge the support provided by King Abdulaziz City for Science and Technology (KACST) through the Science and Technology Unit at King Fahd University of Petroleum and Minerals (KFUPM) for funding this work through project no. 09-ENE779-04 as part of the National Science, Technology and Innovation Plan.

References

- [1] S. Rehman, M. A. Bader, and S. A. Al-Moallem, "Cost of solar energy generated using PV panels," *Renewable and Sustainable Energy Reviews*, vol. 11, no. 8, pp. 1843–1857, 2007.
- [2] W. Bucher, "Aspects of solar water pumping in remote regions," *Energy for Sustainable Development*, vol. 3, no. 4, pp. 8–27, 1996.
- [3] R. Barlow, B. McNeils, and A. Derrick, "Solar pumping: an introduction and update on the technology, performance, costs, and economics," World Bank technical paper no.168, Intermediate technology publications and the World Bank, Washington, DC, USA, 1993.
- [4] A. J. van Staden, J. Zhang, and X. Xia, "A model predictive control strategy for load shifting in a water pumping scheme with maximum demand charges," *Applied Energy*, vol. 8, pp. 4785–4794, 2011.
- [5] S. Sallem, M. Chaabene, and M. B. A. Kamoun, "Energy management algorithm for an optimum control of a photovoltaic water pumping system," *Applied Energy*, vol. 86, no. 12, pp. 2671–2680, 2009.
- [6] Z. Şen and Ş. M. Cebeci, "Solar irradiation estimation by monthly principal component analysis," *Energy Conversion & Management*, vol. 49, no. 11, pp. 3129–3134, 2008.
- [7] M. Xu, R. V. N. Melnik, and U. Borup, "Modeling anti-islanding protection devices for photovoltaic systems," *Renewable Energy*, vol. 29, no. 15, pp. 2195–2216, 2004.
- [8] H. Kawamura, K. Naka, N. Yonekura et al., "Simulation of I-V characteristics of a PV module with shaded PV cells," *Solar Energy Materials and Solar Cells*, vol. 75, no. 3-4, pp. 613–621, 2003.
- [9] M. C. Fedrizzi, F. S. Ribeiro, and R. Zilles, "Lessons from field experiences with photovoltaic pumping systems in traditional communities," *Energy for Sustainable Development*, vol. 13, no. 1, pp. 64–70, 2009.
- [10] D. B. Nelson, M. H. Nehrir, and C. Wang, "Unit sizing and cost analysis of stand-alone hybrid wind/PV/fuel cell power generation systems," *Renewable Energy*, vol. 31, no. 10, pp. 1641–1656, 2006.
- [11] A. Hamidat and B. Benyoucef, "Mathematic models of photovoltaic motor-pump systems," *Renewable Energy*, vol. 33, no. 5, pp. 933–942, 2008.
- [12] X. Gong and M. Kulkarni, "Design optimization of a large scale rooftop photovoltaic system," *Solar Energy*, vol. 78, no. 3, pp. 362–374, 2005.
- [13] M. S. S. Ashhab, "Optimization and modeling of a photovoltaic solar integrated system by neural networks," *Energy Conversion & Management*, vol. 49, no. 11, pp. 3349–3355, 2008.
- [14] W. De Soto, S. A. Klein, and W. A. Beckman, "Improvement and validation of a model for photovoltaic array performance," *Solar Energy*, vol. 80, no. 1, pp. 78–88, 2006.
- [15] A. H. Arab, F. Chenlo, K. Mukadam, and J. L. Balenzategui, "Performance of PV water pumping systems," *Renewable Energy*, vol. 18, no. 2, pp. 191–204, 1999.
- [16] J. S. Ramos and H. M. Ramos, "Solar powered pumps to supply water for rural or isolated zones: a case study," *Energy for Sustainable Development*, vol. 13, no. 3, pp. 151–158, 2009.
- [17] S. Ould-Amrouche, D. Rekioua, and A. Hamidat, "Modelling photovoltaic water pumping systems and evaluation of their CO₂ emissions mitigation potential," *Applied Energy*, vol. 87, no. 11, pp. 3451–3459, 2010.
- [18] E. Mahmoud and H. El-Nather, "Renewable energy and sustainable developments in Egypt: photovoltaic water pumping in remote areas," *Applied Energy*, vol. 74, no. 1-2, pp. 141–147, 2003.
- [19] J. K. Kaldellis, E. Meidanis, and D. Zafirakis, "Experimental energy analysis of a stand-alone photovoltaic-based water pumping installation," *Applied Energy*, vol. 88, pp. 4556–4562, 2011.
- [20] A. G. Bhave, "Potential for solar water-pumping systems in India," *Applied Energy*, vol. 48, no. 3, pp. 197–200, 1994.
- [21] S. Alawaji, M. S. Smiai, S. Rafique, and B. Stafford, "PV-powered water pumping and desalination plant for remote areas in Saudi Arabia," *Applied Energy*, vol. 52, no. 2-3, pp. 283–289, 1995.
- [22] M. A. Hammad, "Characteristics of solar water pumping in Jordan," *Energy*, vol. 24, no. 2, pp. 85–92, 1999.
- [23] Z. Al Suleimani and N. R. Rao, "Wind-powered electric water-pumping system installed in a remote location," *Applied Energy*, vol. 65, no. 1, pp. 339–347, 2000.
- [24] A. Al-Karaghoul and A. M. Al-Sabounchi, "A PV pumping system," *Applied Energy*, vol. 65, no. 1-4, pp. 145–151, 2000.
- [25] D. Manolakos, G. Papadakis, D. Papantonis, and S. Kyritsis, "A stand-alone photovoltaic power system for remote villages using pumped water energy storage," *Energy*, vol. 29, no. 1, pp. 57–69, 2004.
- [26] M. Kordab, "Priority option of photovoltaic systems for water pumping in rural areas in ESCWA member countries," *Desalination*, vol. 209, no. 1–3, pp. 73–77, 2007.
- [27] K. Meah, S. Fletcher, and S. Ula, "Solar photovoltaic water pumping for remote locations," *Renewable and Sustainable Energy Reviews*, vol. 12, no. 2, pp. 472–487, 2008.
- [28] K. Sutthivirode, P. Namprakai, and N. Roonprasang, "A new version of a solar water heating system coupled with a solar water pump," *Applied Energy*, vol. 86, no. 9, pp. 1423–1430, 2009.
- [29] F. J. Chueco-Fernández and A. Bayod-Rújula, "Power supply for pumping systems in northern Chile: photovoltaics as alternative to grid extension and diesel engines," *Energy*, vol. 35, no. 7, pp. 2909–2921, 2010.
- [30] S. Rehman and M. Mohandes, "Estimation of diffuse fraction of global solar radiation using artificial neural networks," *Energy Sources A*, vol. 31, no. 11, pp. 974–984, 2009.
- [31] S. Rehman and M. Mohandes, "Artificial neural network estimation of global solar radiation using air temperature and relative humidity," *Energy Policy*, vol. 36, no. 2, pp. 571–576, 2008.
- [32] S. Rehman and T. O. Halawani, "Global solar radiation estimation," *Renewable Energy*, vol. 12, no. 4, pp. 369–385, 1997.
- [33] S. Rehman and T. O. Halawani, "Development and utilization of solar energy in Saudi Arabia—review," *Arabian Journal for Science and Engineering*, vol. 23, no. 1, pp. 33–46, 1998.

- [34] S. Rehman, "Solar radiation over Saudi Arabia and comparisons with empirical models," *Energy*, vol. 23, no. 12, pp. 1077–1082, 1998.
- [35] M. Mohandes, S. Rehman, and T. O. Halawani, "Estimation of global solar radiation using artificial neural networks," *Renewable Energy*, vol. 14, no. 1–4, pp. 179–184, 1998.
- [36] S. Rehman, "Empirical model development and comparison with existing correlations," *Applied Energy*, vol. 64, no. 1–4, pp. 369–378, 1999.
- [37] S. Rehman and S. G. Ghorri, "Spatial estimation of global solar radiation using geostatistics," *Renewable Energy*, vol. 21, no. 3–4, pp. 583–605, 2000.
- [38] S. Rehman, M. A. Bader, and S. A. Al-Moallem, "Cost of solar energy generated using PV panels," *Renewable and Sustainable Energy Reviews*, vol. 11, no. 8, pp. 1843–1857, 2007.
- [39] A. Aksakal and S. Rehman, "Global solar radiation in North-eastern Saudi Arabia," *Renewable Energy*, vol. 17, no. 4, pp. 461–472, 1999.
- [40] S. Rehman, A. A. Shash, and O. S. B. Al-Amoudi, "Photovoltaic technology of electricity generation for desert camping," *International Journal of Global Energy Issues*, vol. 26, no. 3–4, pp. 322–340, 2006.
- [41] A. R. Al-Ali, S. Rehman, S. Al-Agili, M. H. Al-Omari, and M. Al-Fayez, "Usage of photovoltaics in an automated irrigation system," *Renewable Energy*, vol. 23, no. 1, pp. 17–26, 2001.
- [42] M. Mohandes and S. Rehman, "Global solar radiation maps of Saudi Arabia," *Journal of Energy and Power Engineering*, vol. 4, no. 12, pp. 57–63, 2010.
- [43] D. L. Evans, "Simplified method for predicting photovoltaic array output," *Solar Energy*, vol. 27, no. 6, pp. 555–560, 1981.